Geophysical Characterization of a

Neal Hot Springs, Oregon, USA

Colorado School of Mines

Imperial College London

June 2011

Abstract

Neal Hot Springs is an active geothermal area that is also the proposed location of a binary power plant, which is being developed by US Geothermal Inc. To date, two production wells have been drilled and an injection well is in the process of being completed. The primary goal of this field camp was to provide a learning experience for students studying geophysics, but a secondary goal was to characterize the Neal Hot Springs area to provide valuable information on the flow of geothermal fluids through the subsurface. This characterization was completed using a variety of geophysical surveying methods including: potential fields, deep seismic exploration, vertical seismic profiling, passive seismic monitoring, shallow seismic exploration, direct current resistivity and self potential. Each method designed survey lines that ran mostly perpendicular to the proposed fault structures to provide the best resolution in the data. In addition to these lines, a small grid was created by students to survey with a variety of methods (electrical and potential field methods). This grid location was chosen because warm fluids were found to be upwelling in the area.

Each of these data sets were processed and analyzed by students to determine a unifying solution that best describes the subsurface. After careful observation of the surface geology, as well as the results of each method, it has been determined that there is a primary horst structure just east of Neal Hot Springs. This horst structure is igneous in composition and is fractured throughout. Additionally, there is one major fault (Fault A) with significant offset that was discovered by the gravity, magnetics, and Warm Spring surveys inside the greater horst body. Each of these fractures, along with the fault that binds the horst block on the west side at Neal Hot Springs, is believed to have fluid flow; however, only the Hot Springs have hot fluids. It was also determined that a minor fault structure (Fault B), on the east side of Fault A, was the path for the Warm Spring flow. While the paths of both the major flows were discovered (i.e. the Warm Spring and Neal Hot Springs), the heat source for these flows was not discovered. Further geophysical analysis would need to be completed in order determine the actual source.

Contents

Figures

Tables

Equations

Glossary

CSM	Colorado School of Mines
ICL	Imperial College London
BSU	Boise State University
EM	Electromagnetic
DC	Direct current
SP	Self potential
VSP	Vertical Seismic Profiling
m	Meters
^{0}C	Degrees Celcius
MW	Megawatts
DOE	Department of Energy
Ma	Million years ago
km	Kilometers
NE	North East
GPS	Global Positioning Satellite
DS10	Deep Seismic Line 1
DS20	Deep Seismic Line 2
DS30	Deep Seismic Line 3
HS01	Shallow Seismic Line 1000
HS02	Shallow Seismic Line 2000
HS03	Shallow Seismic Line 3000
DC1	DC Resistivity Line 1
NAD	North American Datum
UTM	Universal Transverse Mercador
N	North
S	South
E	East
W	West
kHz	KiloHertz
mS/m	Meter*Seimens per Meter
Hz	Hertz
A	Amperes
dB/dt	Change in magnetic field over time
$\mu V/m^2$	Microvolts per square meter
NNW	North-North-West
SSE	South-South-East
DC2	DC Resistivity Line 2
DC3	DC Resistivity Line3
DC4	DC Resistivity Line 4
DC5	DC Resistivity Line 5

DC6	DC Resistivity Lint 6
DGPS	Differential Global Positioning Satellite
Ohm-m	Ohm meters
s	Seconds
ms	Milliseconds
mV	Millivolts
CSAMT	Controlled Source Audio Magnetotellurics
$CuSO_4$	Copper Sulfate
USGS	US Geological Survey
TWT	Two way time
QC	Quality Control
DBS	Deconvolution before stack
CMP	Common midpoint
NMO	Normal moveout
DAS	Deconvolution after stack
DMO	Dip moveout
RMS	Root mean Squared

Acknowledgements

The students of the 2011 Field Camp would like to thank the following parties for their help and support. This field camp could not have been such a success without it.

… for Their Financial Backing

US Department of Energy

Colorado School of Mines

Imperial College London

Boise State University

Global Geophysical/Rutt Bridges donations through SEG Foundation Project of special merit

… for the Use of Equipment

CGGVeritas

Sercel

Colorado School of Mines

Boise State University

Geosoft

UBC-GIF Inversion Algorithms

… for Their Help While in the Field

Vale Elementary School

US Geothermal Inc.

Dan Kunz

Ian Warren

Scott Nichols

Bill Teplow

US Geothermal Inc. – Tour of Raft River

Vale High School

US Bureau of Land Management

Local Land Owners

Ashley, Cole and Dick Jordan

Tom McElroy

City of Vale and the Community

Brent Barton

Kat and the Sagebrush Saloon

Rachel Johnson

… for Their Time and Teaching

USGS

Jonathon Glen (Noah, Keith)

Spencer Wood & Mark Ferns

Virginia Gellerman

… Our Staff and Professors

Michael Batzle

Andre Revil

Helmut Jakubowicz

Lee Liberty

Kasper Van Wijk

Dawn Umpleby

Brian Passerella

Robert Raynolds

Paul Odin

Rich Krahenbuhl

John McDonald

Terry Young

… and all the Additional Help We Received

Yaoguo Li

Leon Folks

Andy Kass

Jeff Shoffner

Marios Karaoulis

… Our Teaching Assistants

Joyce Hoopes

Kristen Pierce

Gareth Collins

Ashley Fish

Cici Martinez

Roxy Frary

Kyle Lindsay

Shaun Finn

Thomas Blum

The following students collaborated on the acquisition of the data and the production of this report:

Colorado School of Mines (CSM)

Kendra Johnson
Patricia Littman
Camriel Coleman
Meghan Helper
Gordon Osterman
Travis Pitcher
Chelsea Newgord
Qamar Bukamseen
Kelly Zimmerman
Bethany Behrens
Matthew Fackler
Joe Capriotti
Nick Kramer
Lillian Comegys

Boise State University (BSU)

Scott Havens
Jason Jennings
Jason Compton
Andrew Peterson
Hank Hetric
Katie Carlisle
Clint Colwell

Imperial (ICL)

Oluniyi (John) Akinsola
Aisha Al-Bulushi
Venera Batyrkhan
Myriam Cuylaerts
Adebola Daramola
Edafe Perekowei Edivri
James Alexander Elgenes
Joanna Halliday
Rassa Herabat
Gritsadapong Leaungvongpaisa
Oliver Nicholls
Jonny Chigbo
Tepy Septyana
Akela Silverton
Ghulam Subhani
Bisma Suleman
Thitisorn Thitipattanakul
Joanna Wallis
Colin Coulson Ward
Matthew Aidan Whaley

Disclaimer

The contents of this report serve to document survey activities carried out at Neal Hot Springs, Oregon, USA by students from the Colorado School of Mines, Imperial College London and Boise State University. The acquisition, processing and interpretation of these survey data are primarily intended as a learning exercise and to serve as an introduction to practical geophysical techniques in the field and raw data handling. The aforementioned schools do not guarantee the accuracy or validity of the data obtained or the interpretations and conclusions subsequently presented in this document.

1. Introduction

From May 16th to May 27th 2011, forty one students from three different universities including Colorado School of Mines, Imperial College London, and Boise State University conducted a geophysical field camp at Neal Hot Springs, close to Vale, Oregon, USA.

The selected survey site at Neal Hot Springs is an active geothermal area. Geophysical methods are used to characterize subsurface anomalies, and can be used to characterize active geothermal areas. The field camp conducted a variety of geophysical survey methods, with the intention of developing current understanding of the subsurface structure, fluid dynamics and processes operating in this area.

The geophysical survey techniques employed over the course of the field camp included:

- Potential fields: Gravity, magnetism, and electromagnetism (EM)
- Resistivity: Direct current (DC) and self potential (SP)
- Deep seismic reflection
- Shallow seismic reflection
- Lacustrine seismic reflection
- Vertical seismic profiling (VSP)
- Passive seismic monitoring
- Controlled Source Audio Magnetotellurics
- Paleomagnetics

This report details the acquisition methodology, processing, interpretation and integrated analysis of the data acquired over the Neal Hot Springs survey site. Additionally, this report recommends further steps that could be taken to continue research into and development of this geothermal area for power generation.

1.1 Objectives

The main objective of this field camp was to introduce students to geophysical field methods, and provide them with hands on experience of acquisition of a variety of geophysical

data, data processing, interpretation, and integration and analysis of a multiple of data types. A secondary objective of this field camp was to validate the hypothesized working geothermal system through geological understanding and geophysical prospecting. In addition to mapping the main fracture zone, tracing fluid motion was also targeted by several geophysical techniques. This field camp also tests the value of geophysical prospecting for geothermal energy.

1.2 Methodology

Surveys were designed to identify anomalies in the subsurface; these are most clearly and accurately delimited in geophysical data where a survey line bisects the anomaly perpendicular to its longitudinal plane. Geological mapping of the area anticipates the subsurface structure to feature an uplifted horst block bounded by normal faults, featuring surface hot springs and underlying hot brine upwelling at the fault planes. Accordingly, in the case of linear anomalies such as the fault planes, survey lines should ideally run perpendicular to the strike of the fault.

The main survey site focused on identifying the western fault plane and associated fluid motion, this being the fault over which the Neal Hot Springs is believed to lie. Survey design was restricted by terrain or access concerns; for example, deep seismic surveying was restricted to the main dirt roads running though the site in order to limit environmental damage caused by the Vibroseis trucks. Terrain was less of a concern for resistivity and self potential surveys, and many of the shorter survey lines surveyed by these methods were planned to run perpendicular to the strike of the fault regardless of terrain and vehicular access. The potential field methods are capable of covering uneven terrain and can be completed rapidly; these surveys covered all survey lines.

An additional survey area was located adjacent to the “warm spring”, lying to the east of the main survey site, on the other side of the hypothesized horst block. This area is referred to as the “Warm Spring” site. This survey was constructed as a 100m by 280m grid for shallow survey methods including EM, gravity, magnetics, resistivity and self potential. The grid is orientated such that the lines run parallel and perpendicular to the anticipated fault plane.

All of the survey lines and areas were planned to incorporate overlapping tie in points so that data could be corrected and resolved to one central point. This is critical to eliminating noise from instrumental drift when analyzing the data.

2. Background

2.1 Location

The Neal Hot Springs geothermal area is located in Malheur County, Oregon about 90 miles northwest of Boise. Figure 2-1 shows the location of Neal Hot Springs, which is just west of Ontario, Oregon, marked with a green dot.

Figure 2-1 Regional Map Showing the Location of Neal Hot Springs [*Google Earth, 2011*]

The potential of the Neal Hot Springs site as a geothermal resource was first identified by Chevron Minerals in 1979. A single well was drilled, penetrating a depth of 859.5m when a massive loss of circulation of drill fluids occurred. This loss of fluid circulation is interpreted to indicate that the well bore had penetrated the fault zone associated with the geothermal

system. Further study estimated the reservoir temperature to be 155 C to 160°C, and the distal source temperature to be 175°C to 180°C [*US Geothermal Inc, 2007*].

2.2 Geothermal Development

Neal Hot Springs is located northwest of Vale, Oregon. Vale has long been reputed for its warm-water wells and hot springs. Vale has taken advantage of its geothermal resources since the early 1900's; however, its initial use was restricted to residential and commercial space heating [*Wisian et al, 1996*]. In 1981, Lakeview became the site of Oregon's first geothermal power plant. There are currently six active geothermal projects in Oregon: Newberry Volcano, Crump Geyser, Neal Hot Springs, Paisley, and two projects located at Klamath Falls. The geothermal resources of Neal Hot Springs are the result of the interaction between meteoric water and local faults, but a majority of the geothermal areas in Oregon are believed to be the result of magmatic activity in coincidence with the Cascade Range [*Gannett, 1988*].

Surface expressions of geothermal activity include hot springs, steam vents, geysers, boiling mud pots, and silicified rocks. These surface expressions are typically located near volcanoes or earthquakes [*Duffield and Sass, 2003*]. According to Duffield and Sass [2003], the molten rock within volcanoes directly heats the water, while the fractured rock associated with earthquake zones allows the deep circulation of water. These zones make up less than 10% of the Earth's surface, but they are prime areas for the exploitation of geothermal energy [*Duffield and Sass, 2003*].

In 1921, the first successful geothermal power plant was built by John D. Grant to generate electricity, but it wasn't until 1960 that the first large-scale geothermal power plant, the Geysers reservoir, began operation [*EERE website, 2011*]. Geothermal power plants typically harness geothermal resources that contain rather high temperatures. Geologically active/younger volcanoes or zones with high heat flow are desirable locations for this temperature requirement. The geothermal gradient, which describes the proportional rate of temperature increase with depth to the rate heat escapes to the surface, is used to discern these zones of high heat flow [*Duffield and Sass, 2003*]. Industrial power generation generally becomes feasible with temperatures in the zone of interest ranging from 200-320˚C. After a

geothermal reservoir is discovered, it is tapped using water that naturally reaches the surface or is brought to the surface by drilled wells.

2.2.1 Geothermal Power Plants

An electrical-grade hydrothermal system uses temperatures greater than 100-150˚C. There are three types of electrical-grade hydrothermal systems: hot-water, vapor-dominated, and moderate-temperature [*Duffield and Sass, 2003*]. Hot-water systems are located over porous and permeable rock saturated with 200˚C water. The water partly boils to steam as it rises up the production well, where the steam is then directed to a turbine generator to produce electricity. Vapor dominated hydrothermal systems are in place when the pore spaces of rocks are filled with steam rather than water. In this system the steam can be routed directly into the turbines. Vapor systems are highly sought after because of their simplicity, but they are rarer than their hot water counterparts. The moderate-temperature hydrothermal systems (binary systems) do not have the capacity to directly produce steam. Instead, the hot water from the subsurface is used to boil a secondary fluid whose steam is then used to drive the turbine generators [*Duffield and Sass, 2003*].

Between 1980 and 1982, the world's first operational binary geothermal power plant in the world was constructed and tested at the Raft River site [*US Geothermal Inc., 2007*]. Although the power plant at Raft River produced only 7 megawatts (MW) yearly, its contribution to technology was highly valuable. There are now 12 operating binary cycle plants in the western United States. They produce a total of 184 MW yearly. The geothermal reservoir at Raft River has a predicted capability of 110 MW yearly production level. The fluids in the reservoir at Raft River have a low non-condensable gas unit, low salinity, and dissolved content between 1200 and 6800 parts per million. The temperature is 135-150^{0}C at depths between 1350 and 1850 meters. The fluid that is converted into steam to run through the turbines is isopentane, which has a boiling point at 85^{0}C [*US Geothermal Inc., 2007*]. A project very similar to Raft River is planned for Neal Hot Springs, which is set to be completed by the end of 2011. However, at Neal Hot springs R134A refrigerant will be used as the secondary fluid instead of isopentane.

Also, the secondary fluid will be air cooled at Neal Hot Springs unlike Raft River where it is cooled in evaporation ponds.

Initial investigation of the Neal Hot Springs area was carried out by Chevron Minerals in 1979 during a period of high oil prices and concerns over future energy supply. However, despite the initial success of the investigation, no subsequent development of the area was carried out.

US Geothermal Inc. began acquiring interests in the geothermal prospect in 2006, and currently hold a series of long term leases of the geothermal rights to 9.6 square miles at Neal Hot Springs. Two production wells have been successfully drilled; one completed in May 2008, finding fluid flow and brine temperatures of 141.6°C at 702.6m, and another in October 2009 finding temperatures of 141.1°C at 882.7m [*Clutter,T., 2010*].

Following the grant of a Conditional Use Permit by Malheur County Planning Commission in 2009, US Geothermal Inc. is in the process of constructing a binary cycle geothermal power plant with a capacity of 26 MW. The project is financially backed by the US Department of Energy (DOE). Upon completion of the power plant, the power output will be sold to Idaho Power Company under a 25 year power purchase agreement [*Clutter,T., 2010*]. The agreement provides for the sale up to 25 MW per year. Figure 2-2 shows the proposed layout of the US Geothermal power plant.

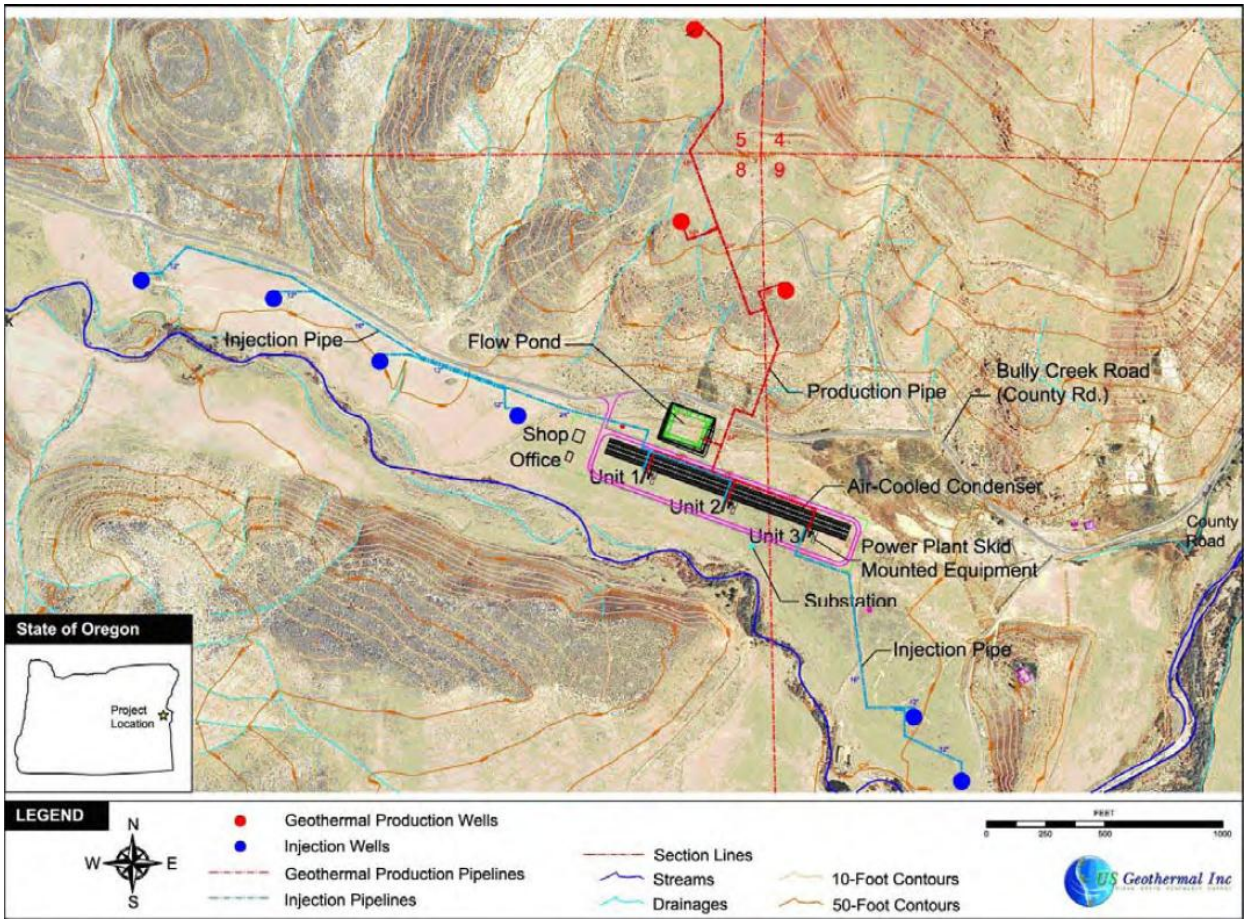

Figure 2-2 Neal Hot Springs Power Plant [*US Geothermal Inc. Website, 2011*]

2.3 Survey history

Developing geothermal energy requires an immense initial investment, especially when drilling new production and injection wells. Therefore, correct well placement is required in order to optimize the value of the project. According to US Geothermal Inc., gravity and magnetic data from a survey completed in 2007 were utilized to locate the production wells [*US Geothermal Website*]. No other geophysical techniques were completed at this site prior to the geophysical field camp in 2011. The 2007 gravity data along with a current 3D density inversion over the site have provided additional, prior information during the interpretation of summer field geophysical data in this report. The 2007 gravity data are illustrated in Figure 2.-3, and a coarse 3D generalized density inversion of these data, performed by CSM during Field Camp 2011, is shown in Figure 2-4.

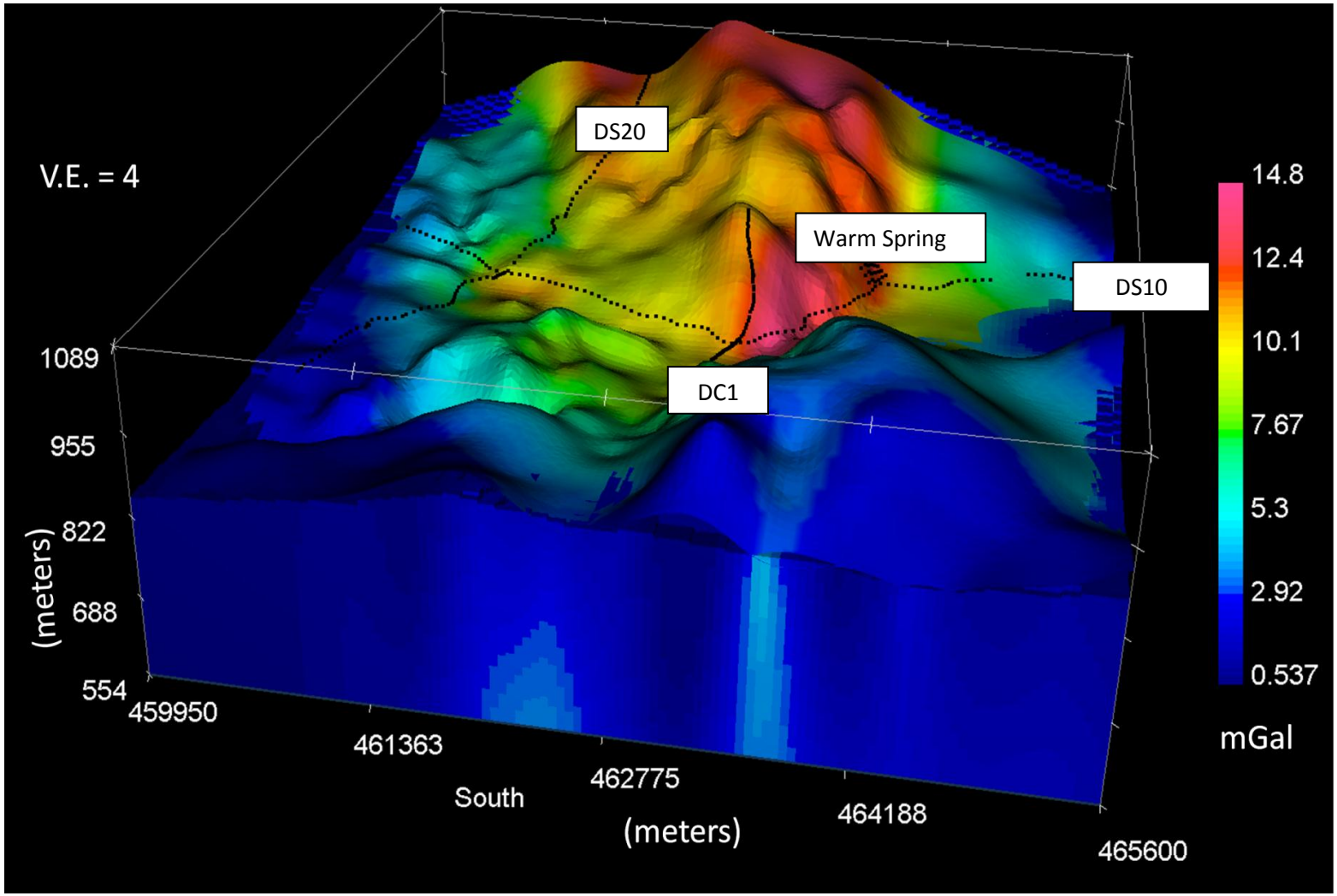

Figure 2-3 Gravity Data [*Geothermal, Inc. 2007*], 250 station spacing around Neal Hot Springs.GZINV3D, created at UBC-GIF based on [*Li and Oldenburg, 1998*]

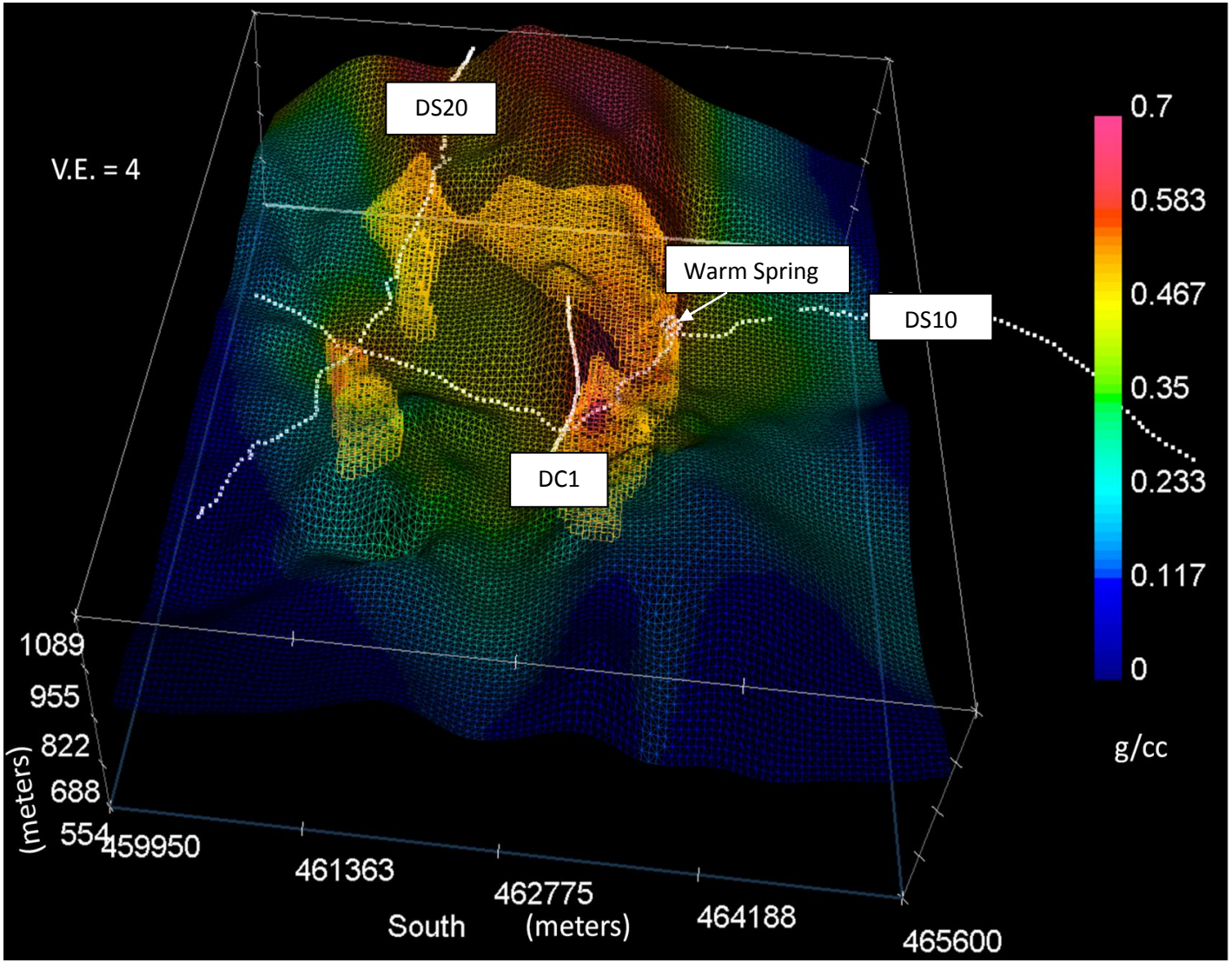

3D Generalized Density Inversion, volume rendered showing densest structures. GZINV3D [*Li & Oldenburg, 1998*], Teaching License for CSM-CGEM by UBC-GIF

From the inversion in Figure 2-3, it can be seen that there is a high density body located just east of the Neal Hot Springs site, which extends and widens to the north and eventually curves around to the west. This is the proposed location of the igneous horst block, which provides more information indicating that Neal Hot Springs is the result of a fault. This inversion provides merit to the survey lines that were determined by the 2011 Field Camp. DC1 follows right along the fault, while DS10 clearly intersects it. Additionally, the Warm Spring site appears to be located right near a secondary high density anomaly indicating that that location is also in the vicinity of a fault on the opposite side of the horst block.

3. Geology

3.1 Regional Geology

The origin of the Colombia Plateau and Snake River plain, which is shown in Figure 3-1, is a highly debated subject. The theories that attempt to explain the creation of these large scale features can be grouped into two categories defined by the primary driving force; (1) a deep mantle plume and (2) a shallow mantle plume combined with rifting. Within the deep mantle plume group, theories vary from a simple vertical plume to a plume complicated by the subduction and overriding of a convergent plate boundary, according to Geist and Richards [*1993*]. The second group, described by Christiansen [*2002*], maintains that a shallow plume combined with tectonic extension is a sufficient driving force to create the massive volcanic units of the Colombia Plateau and the Snake River plain. On a large scale, the physical manifestation of the tectonic rifting is the Idaho-Oregon graben—a dominating feature that strikes roughly north-south. Overall, the area surrounding Vale, OR is a geologically complex region whose origin has wide-spread controversy.

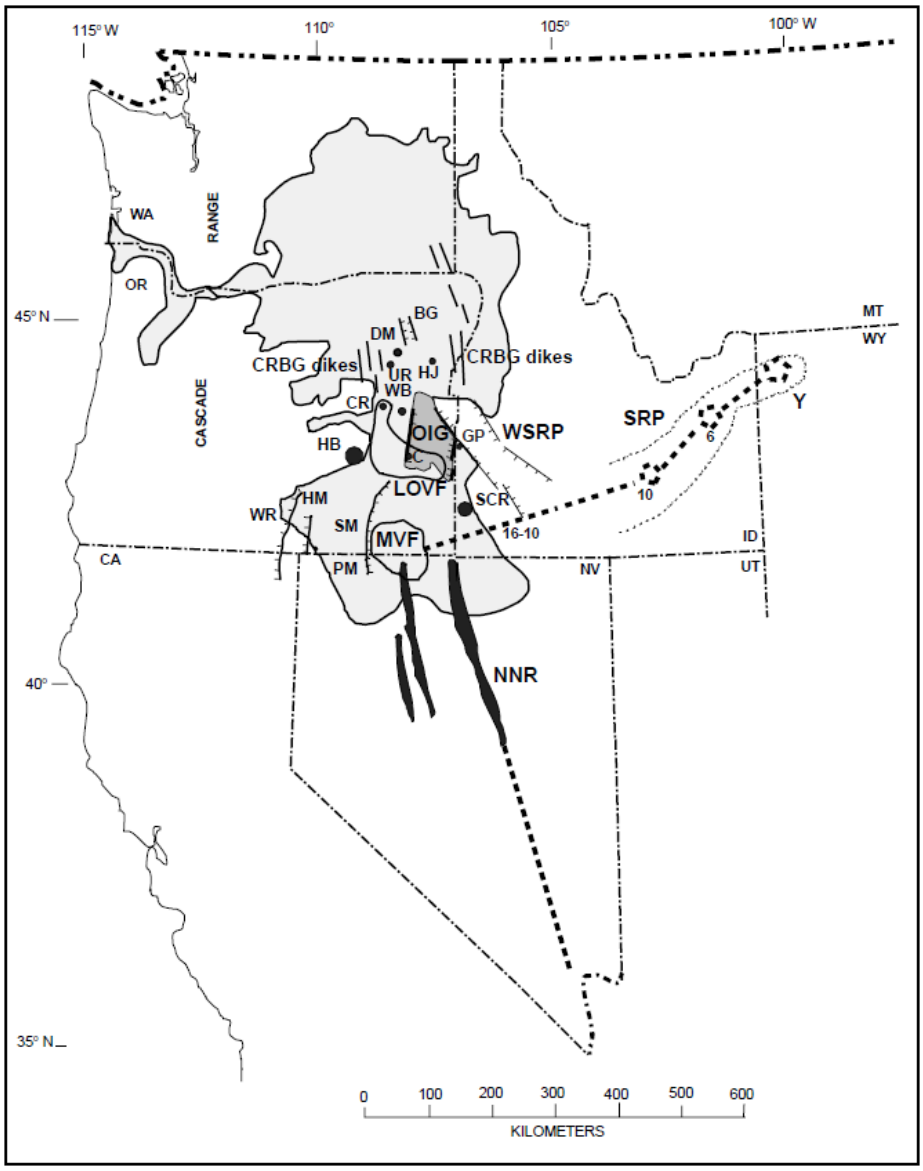

Figure 3-1 Regional Map Showing the Oregon-Idaho Graben (OIG)

Figure 3-1 labeling: the Columbia River Basalt Group (CRBG dikes), the Northern Nevada Rift (NNR), and the Western Snake River plain (WSRP). Additional symbols shown are: BG—Baker graben; C—Crowely; CR—Castle Rock; DM—Dooley Mountain; GP—Graveyard Point; HB—Harney basin; HJ—Huntington Junction; HM—Hart Mountain; LOVF—Lake Owyhee volcanic field; MVF—Mc-Dermitt volcanic field; PM—Pueblo Mountains; SM—Steens Mountain; SCR—Silver City Reservoir; Y—Yellowstone Plateau; WA—Washington; OR—Oregon; ID—Idaho; MT—Montana; WY—Wyoming; UT—Utah; NV—Nevada; CA—California. Numbers displayed along the Snake River plain (SRP) show the age progression of rhyolitic volcanism. [*Cummings et al, 2000*]

3.2 Stratigraphy and Sedimentology

3.2.1 Overview

The stratigraphy and sedimentology of the Oregon-Idaho graben and western Snake River plain are influenced by the extensional structure of the region as well as frequent volcanic activity. Rift basins, also known as grabens and half-grabens, are responsible for a specific sedimentary stratigraphy known as tripartite. The Snake River down warp is characterized by this tripartite stratigraphy [*Camp et al, 2003*]. According to Schlishe and Withjack, tripartite stratigraphy is a cyclical succession of fluvial to lacustrine deposition. This sequence is controlled by the sediment supply, basin capacity, and volume of water as illustrated in Figure 3-2. The first example would result in fluvial sedimentation, the second example would result in shallow lacustrine sedimentation, and the third example would result in deep lacustrine sedimentation. Tripartite stratigraphy shows the evolution of different depositional environments in a basin. In conjunction with this mechanism, the volcanic rocks of the region form the surface geology as seen in Figure 3-3, and Table 3-1 shows the color indices for the surface geology [*Couch et al, 1975*].

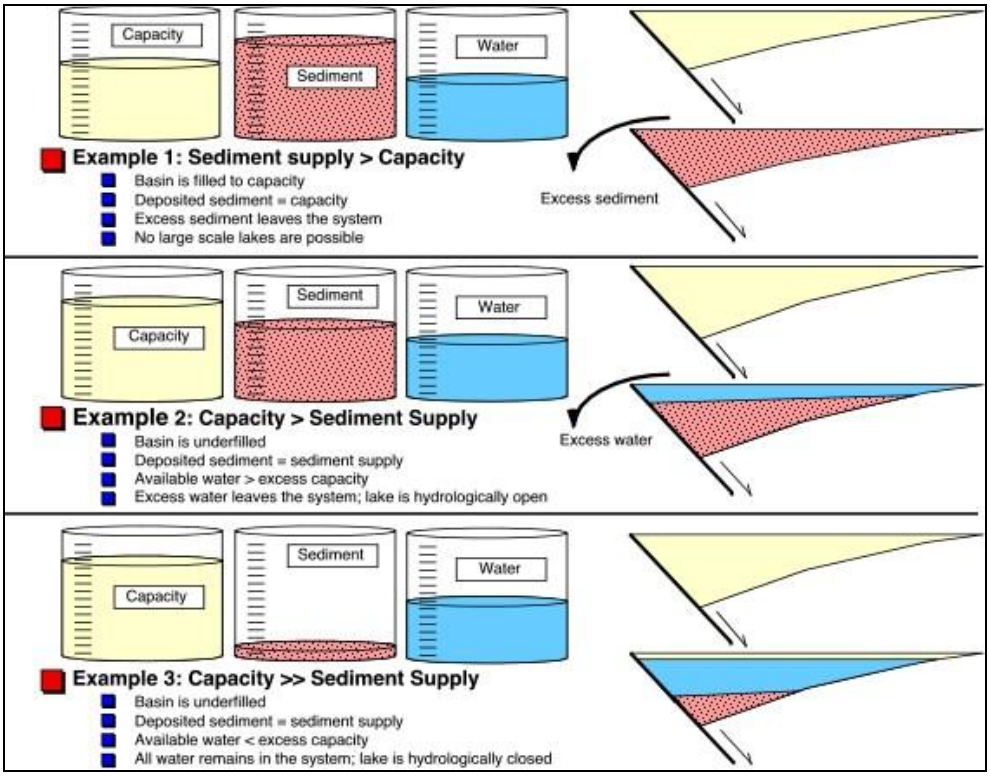

Figure 3-2 Tripartite Stratigraphic Deposition [*Schlishe and Withjack, 1999*]

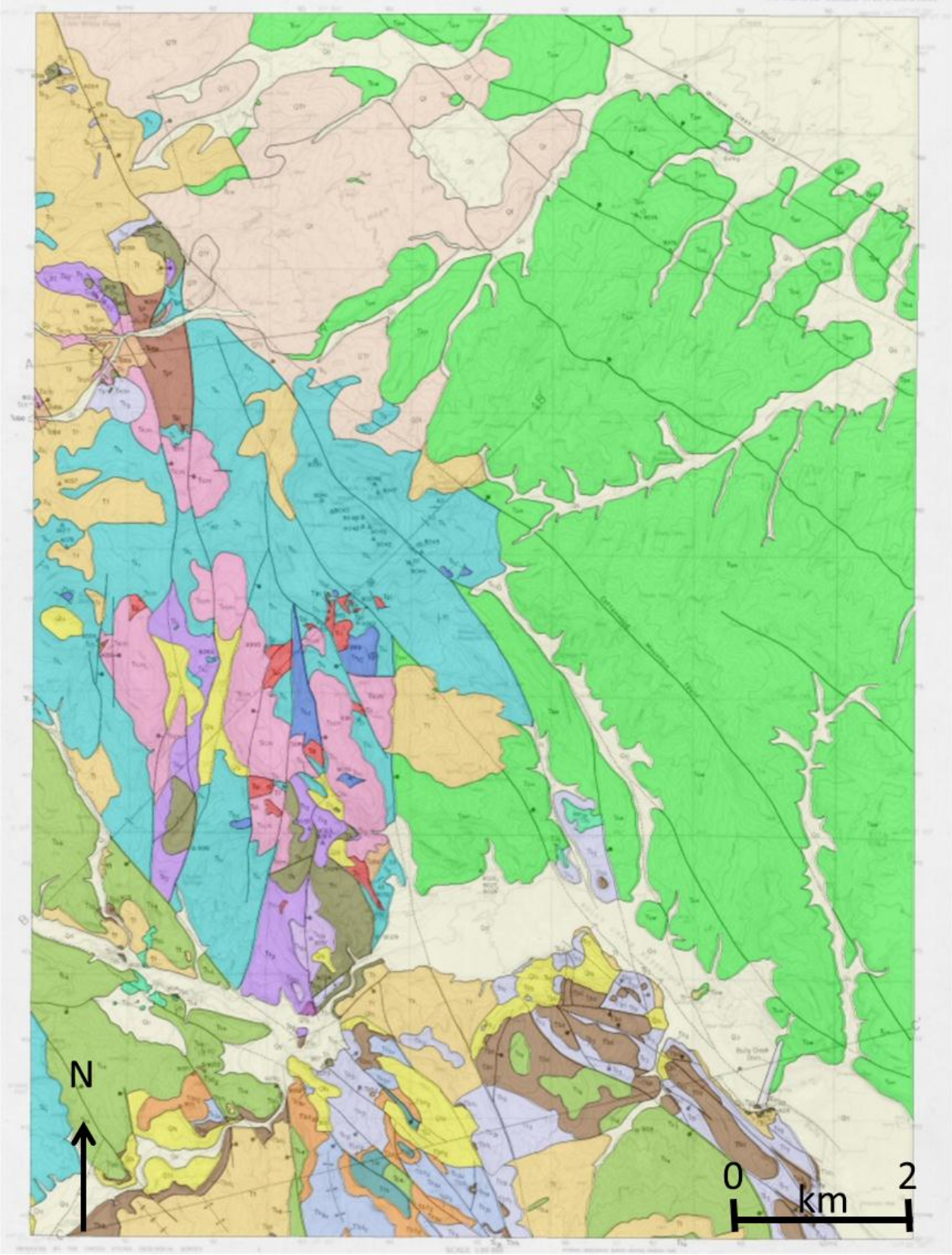

Figure 3-3 Surface Geology of Neal Hot Springs Region

Table 3-1 List of Color Schemes for Figure 3-3

Unit	Color	Rock type	Age
Qa		Alluvium	Ho
QTs		Siliceous sinter	Ho
Qls		Landslide deposits	Ho
Qf		Youngest Alluvial Fan deposits	Q
QTf		Older alluvial fan deposits	Q and/or Plio
Tf		Oldest alluvial fan deposits	Plio and/or Mio
Tsw		Sedimentary rocks of the western Snake River Plain	Plio and/or u.Mio
Ts4		Youngest sedimentary rocks	u. Mio
Tls		Limestone	u. Mio
Tds		Dacite scoria	u. Mio
Tba		Basaltic andesite and andesite	u. Mio
Tba2		Basaltic andesite and andesite	u. Mio
Tba1		Basaltic andesite and andesite	u. Mio
Tch		Chalcedony veins	u.to m. Mio
Ts3		Younger sedimentary rocks	m. Mio
Ts3u		Younger sedimentary rocks, upper	m. Mio
Ts3l		Younger sedimentary rocks, lower	m. Mio
Tlr		Littlefield Rhyolite	m. Mio
Th		Hunter Creek Basalt	m. Mio
Ts2		Older sedimentary rocks	m. Mio
Twt		Welded tuff	m. Mio
Tai		Andesite dikes	m. Mio
Trcm		Rhyolite of Cottonwood Mountain	m. Mio
Tri		Rhyolite intrusions	m. Mio
Ts1		Oldest sedimentary rock	m. Mio
Tpt		Palagontici tuff breccia	m. Mio
Toba		Older basaltic andesite and andesite	m. Mio

Mark Ferns and Spencer Wood provided a generalized sketch of the stratigraphy of the Neal Hot Springs geothermal study area (Figure 3-4). According to Ferns and Wood [*2011*], the western Snake River plain sediments, and upper layer of olivine basalt, form the sediments of the Idaho group. Drip Springs silicified sediment and Vines Hill andesites comprise the Oregon-Idaho graben fill. Littlefield rhyolite, Cottonwood Mountain rhyolite, Dinner Creek tuff, and Malheur Gorge basalt create the basement rock. The correct thicknesses of the stratigraphy are provided in Figure 3-5. The Malheur Gorge basalt, Dinner Creek tuff, and Hunter Creek basalts are the product of tholeiitic flood-basalt volcanism during the middle Miocene [*Camp et al, 2003].* The volcanic rocks of this region show an evolutionary trend through the increase in silica and iron content. This creates a pattern of the tholeiitic basalts overlain by rhyolitic lava flows. The andesitic flows, such as Vines Hill, may have been the product of the once-basaltic caldera center's collapse [*Wood and Ferns, 2011*].

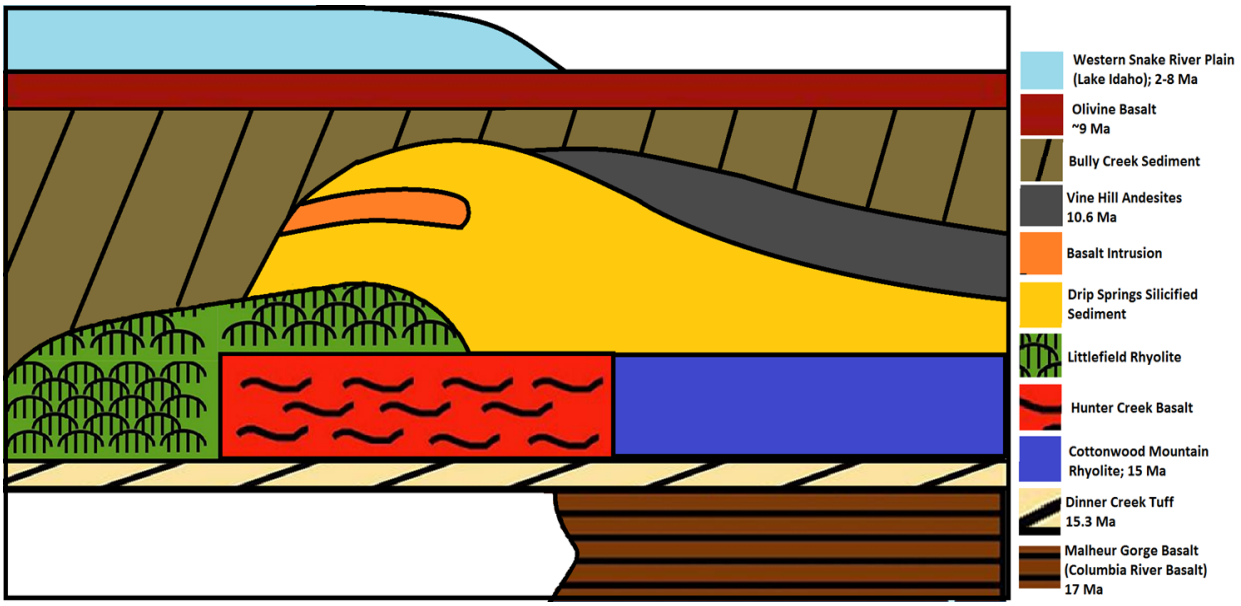

Figure 3-4 Stratigraphic Sketch of Neal Hot Springs Area (not drawn to scale) [*Wood and Ferns, 2011*]

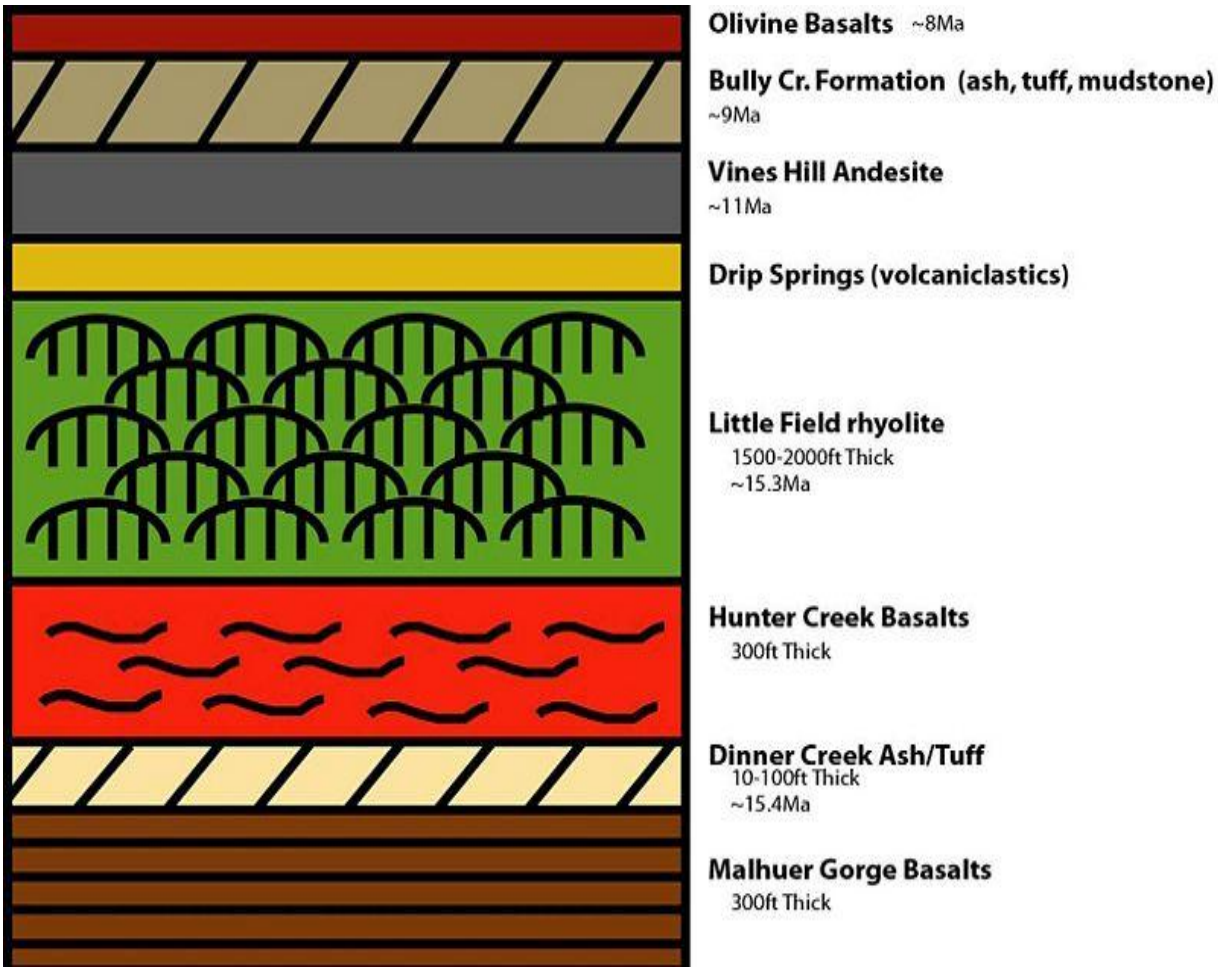

Figure 3-5 Stratigraphic Column of Neal Hot Springs Geology [*Geophysics Department Boise State University, 2011*]

The Malheur Gorge basalts, regionally known as the Columbia River basalts (CRB), are combined with voluminous ash flows contemporaneously erupted from four nearby calderas to represent the oldest volcanic rocks of our study region. The volcanic episode began approximately 15 million years ago (Ma) and was ended by 5 Ma [*Wisian et al, 1996*]. This gives the CRB a Miocene to Pliocene age. The Malheur Gorge basalt of our study area was measured at about 16.5 Ma. The deposition of the Malheur Gorge basalt occurred before the initial subsidence which created the Oregon-Idaho graben [*Cummings et al, 2000*]. The Malheur Gorge is a combination of tholeiitic basalt and mafic pyroclastic deposits [*Camp et al, 2003; Cummings et al, 2000*] Tholeiitic basalt is a fine-grained, mafic rock with a high content of iron ore and low content of silica.

The Dinner Creek ash flow tuff was laid down approximately 15.3 Ma. It creates a 3-30.5m ledge, or rim rock, everywhere in the area. According to Camp et al [*2003*] the Dinner Creek tuff

originates from a caldera near Castle Rock or Westfall Butte. It is a densely welded ignimbrite, or pyroclastic density current [*Camp et al, 2003*], with pumice inclusions that have been flattened into glass by the overlying rock. Cummings et al [*2000*] describe the Dinner Creek Tuff as a "weakly peralkaline (aluminum deficient]) rhyolite that erupted from a vent north or northwest of the (Oregon-Idaho) graben".

The Hunter Creek basalt reaches thicknesses of 9m at Neal Hot Springs. This is the final tholeiitic basalt in the Neal Hot Springs stratigraphy, and it erupted at the end of the Dinner Creek ash flow deposition, commonly creating tachylytic lenses, or glassy mafic inter-beds, of the two layers [*Camp et al, 2003*]. The age of the Hunter Creek basalt has been measured at about 15.4 Ma.

Cottonwood Mountain rhyolite erupted from the western margin of the Oregon-Idaho graben at 15.2 Ma [*Cummings et al, 2000*]. According to Cummings et al, the rhyolite of Cottonwood Mountain erupted during initial subsidence of the Oregon-Idaho graben. It is characterized as plagioclase-phyric and can reach thicknesses over 200m.

The Littlefield Rhyolite has a thickness ranging 460-610m in the Neal Hot Springs area. The Littlefield rhyolite is a common intrusion at fault zones in the Oregon-Idaho graben [*Cummings et al, 2000*]. It is reported to have erupted from several vents including the Simmons Gulch [*Cummings et al, 2000*].

The Drip Springs sediment is a clastic sedimentary rock classified as an Oregon-Idaho graben fill. The Drip Springs and Bully Creek sediments follow typical tripartite stratigraphy, containing arkosic channel sandstone, tuffaceous floodplain sandstone, siltstone, and mudstone with cross-bedding structures and other indicators of a fluvial depositional system [*Cummings et al, 2000*]. The sediments of the Bully Creek unit include ashes, tuffs, and diatomite, or silica remnants of aquatic plants [*Ferns and Wood, 2011*]. According to Cummings et al [*2000*], there was a period of basalt hydrovolcanism in the Oregon-Idaho Graben at 14.3 to 12.6 Ma that distinguishes the two sedimentary layers. This is referenced in the stratigraphic sketch (Figure 3-5). Between 13.1 and 12.5 Ma arkosic fluvial sediments of the Drip Springs interacted with geothermal systems to create silica-sinter deposits and talus breccias [*Cummings et al, 2000*].

From 12.6 to 10.5 Ma sedimentation increased, resulting in primarily fluvial deposition with large amounts of volcanic detritus [*Cummings et al, 2000*].

The Vines Hill andesite erupted at 10.6 Ma from vents flanking both sides of the Oregon-Idaho graben [*Cummings et al, 2000*]. The Vines Hill andesite is dark gray in color.

The Idaho group, of Pliocene age, is composed of siltstones, gravel, sand, clay, and ash varying in thickness from as much as 1.5km thick to 0.3km thick [*Wisian et al, 1996; Long and Kaufmann, 1980*]. The Idaho group is not solely sedimentary in origin; there are tuffs and basalt layers in the oldest section [*Long and Kaufmann, 1980*], as indicated by the diked olivine basalt in the stratigraphic sketch. The Idaho Group has been split into three formations: the Chalk Butte Formation, the Grassy Mountain Basalt Formation, and the Kern Basin Formation. Both the Chalk Butte and Kern Basin are composed of tuffaceous claystone, siltstone, sandstone, and conglomerate, with some fresh-water limestone present in the Chalk Butte [*Bowen and Blackwell, 1975*]. The sedimentary layers of the Idaho group (the Chalk Butte and Kern Basin) are of lacustrine and fluvial sedimentation [*Raynolds, 2010*].

3.2.2 Field Observations

Stratigraphy and sedimentology was observed in the Neal Hot Springs survey site. The surface geology was correlated with a well log from Neal Hot Springs Well 8 to create a cross section (Figure 3-6). The cross section strikes at 040°; A to A' follows South to North. There were several different lithologies marked: siliceous sinter, lacustrine or fluviatile sediments, and volcanic rocks.

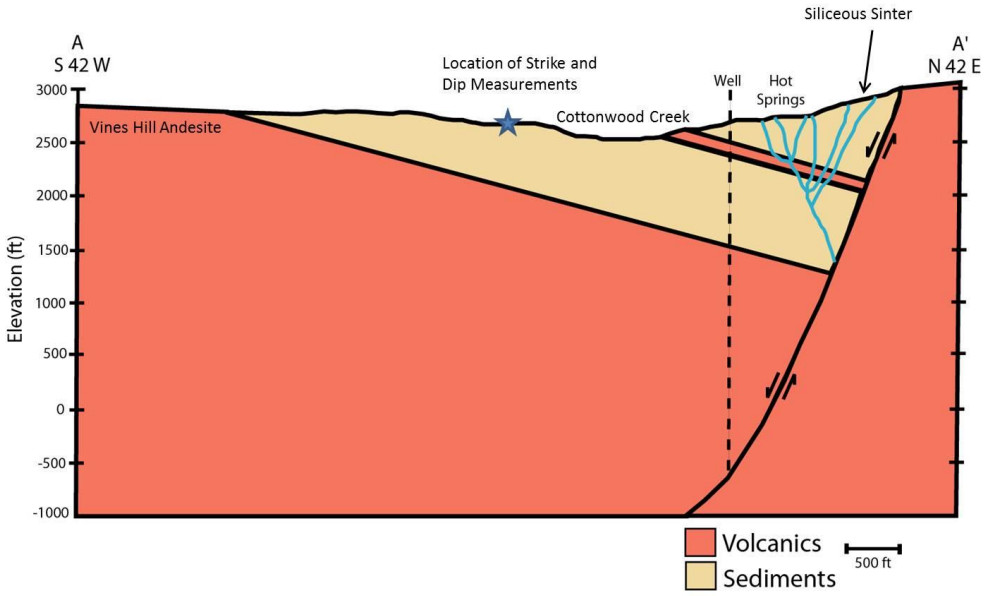

Figure 3-6 Annotated Cross Section of the Neal Hot Springs Study Area

The siliceous sinter indicated is a product of hydrothermal alteration. Hot water traveling upwards dissolves constituents in the surrounding rock and creates lateral and vertical zones of alteration. Siliceous sinter is a surficial product of this process; it typically overlies rock saturated with mercury or sulfur. The siliceous sinter, part of the Drip Springs Formation, forms a carapace at several other locations to the east of the present hot springs, and these outcrops were interpreted as a manifestation of the Neal Hot Springs' migration. In one of these eastward locations breccias with chalcedony and some opaline were present. This would be representative of a deeper zone of alteration.

The surface morphology running parallel to Cottonwood Creek indicates a less resistant underlying lithology. Here this is assumed to be the sedimentary package observed farther south on the cross section. This strata contained unconsolidated laminations of clay and silt with abundant fossils indicating a lacustrine depositional system. A noticeable white ash bed was also included in this package. From this marker bed a strike and dip of 345°, 14° NE was measured.

Behind the sedimentary sequence, an outcrop of Vine Hill andesite was noted. The cross section depicts the volcanic rocks dipping underneath the sedimentary strata towards the fault,

creating a half-graben. These assumptions were correlated with the well log from Neal Hot Springs Well 8.

The stratigraphy gained from well logs is a valuable resource for the creation of cross sections. The well logs from Neal Hot Springs Well 8 (NHS-8), Well 2 (NHS-2), Well 1 (NHS-1), and Well 5 (NHS-5) were donated by U.S. Geothermal Inc. for use in this project and are shown in Figure 3-7. Schematic stratigraphic columns were created by Dr. Robert Raynolds (Figure 3-8). These columns closely resemble the stratigraphy depicted by the cross section.

Figure 3-7 Relative Location of Wells in Neal Hot Springs Area and Generalized Cross Section

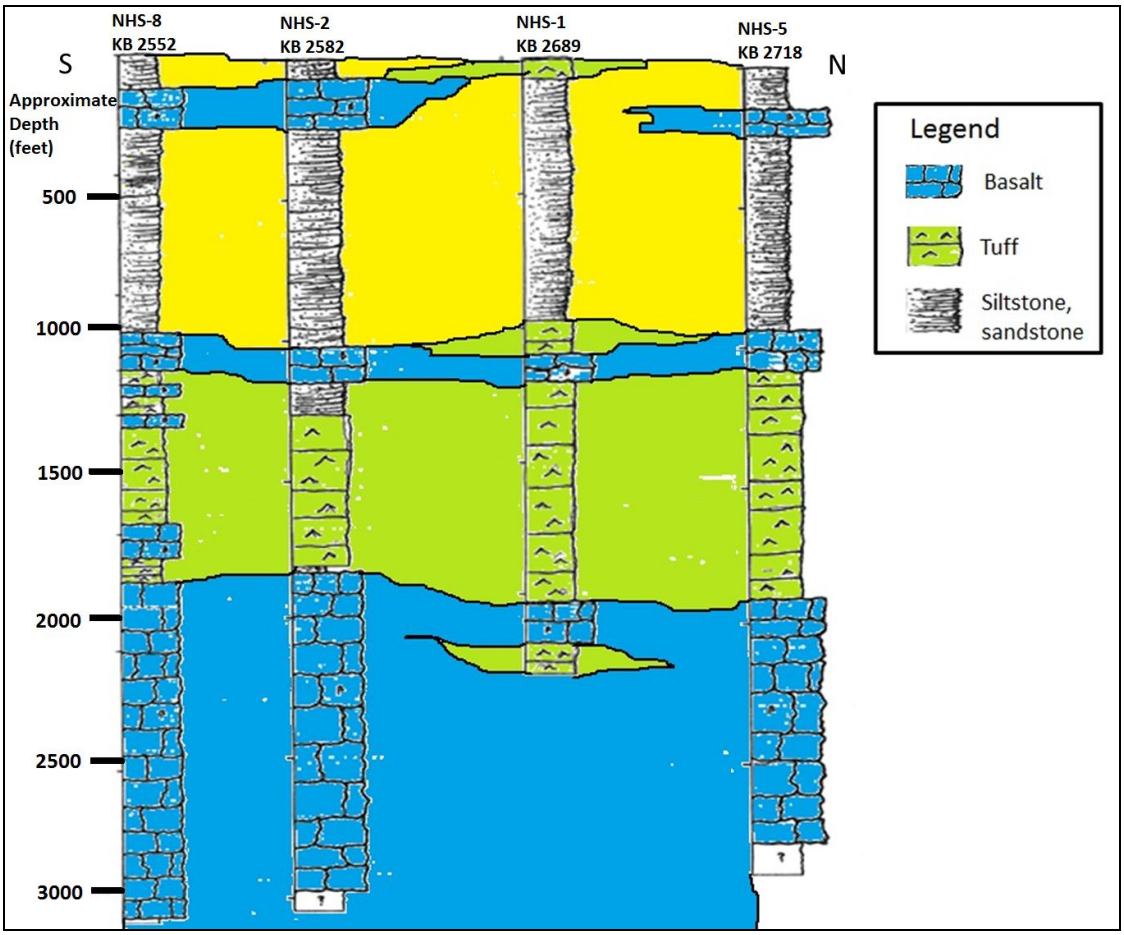

Figure 3-8 Interpreted Stratigraphic Columns from wells NHS-8, NHS-2, NHS-1, and NHS-5 (left to right)

[*Adapted from Raynolds, 2011*]

3.3 Structural Geology

3.3.1 Oregon-Idaho Graben

The Oregon-Idaho graben lies on a north-south trend within the middle Miocene back arc rift system [*Cummings et al, 2000*]. Cummings et al [*2000*] associate this north-south trend as the margin between the Continental Margin and accretionary terraces. Extending from southern Nevada to southeastern Washington, the subsidence of the Oregon-Idaho graben closely followed the most voluminous of tholeiitic basalt eruption 15.4 Ma [*Cummings et al, 2000*]. As a result of prolonged subsidence, intragraben faults were formed leading to rejuvenated volcanism and, consequently, the formation of sub-basins [*Cummings et al, 2000*]. Subsidence rates waned by 12.6 Ma [*Cummings et al, 2000*]. The Oregon-Idaho graben contains structural trends of major northwestern-striking faults with minor north-striking and east-

northeast-striking faults. In addition to these faults, east-west horst and graben mechanisms instigated right lateral strike-slip movement. Deformation places these episodes of faulting in the lower to middle Miocene. Lack of deformation in the upper Miocene olivine basalts restricts this time period [*Camp et al, 2003*].

3.3.2 Study Area

In the immediate vicinity of the Neal Hot Springs, tilted fault blocks were generated from the initial subsidence of the Oregon-Idaho graben. This area is bounded on the east by a northwest-southeast trending fault; however, evidence of lithological displacement across the fault has not been observed (Figure 3-9). The eastern horst is composed of the volcanic basement including the Hunter Creek Basalt and Cottonwood Rhyolite. The western graben, or downthrown block, is covered by younger sedimentary units of the Western Snake River plain [*BSU, 2011*] (Figure 3-10).

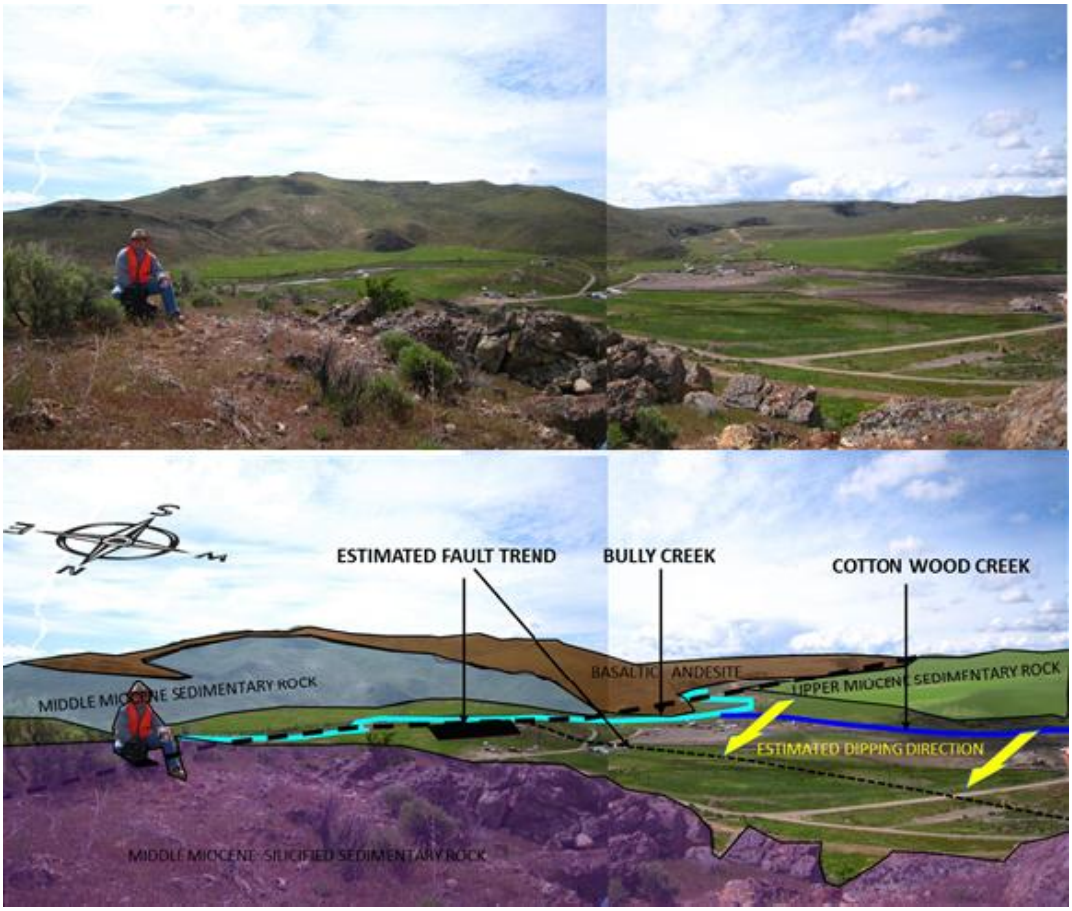

Figure 3-9 General Structure of the Field Area

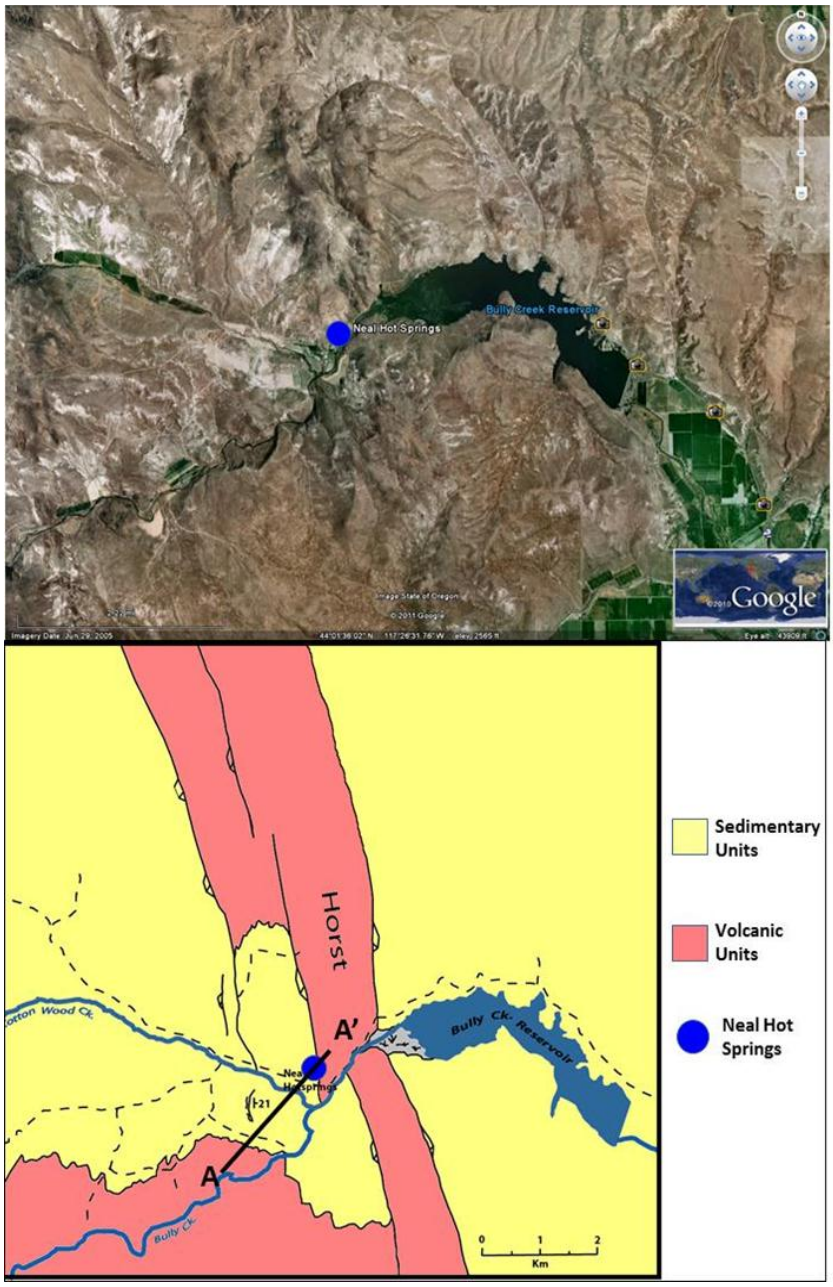

Figure 3-10 Satellite Image and Geological Map at Neal Hot Springs. Cross section A-A' is shown on geological map.

The 040° cross section previously discussed displays a southwestern dipping fault. This fault is interpreted as the primary structure responsible for the upwelling of geothermal fluids. Bully Creek may also be associated with another fault [*Raynolds, 2011*]. As a result of the structural interpretation, an east-west line and north-south line were implemented for the geophysical surveys.

3.4 Geological Implications

The geological interpretation of this region is pertinent for several reasons. Not only are the maps and cross sections used to create models in geophysical processing techniques such as gravity, but they may also be used to identify possible geothermal reservoirs or fluid flow conduits. Forward modeling and inversion modeling, two important geophysical processing techniques, involve the creation of geologic models and will be discussed in subsequent sections. When analyzing a stratigraphic column or cross section, potential reservoirs may be located within sedimentary units or at the interface between volcanic and sedimentary or other volcanic layers [*Ferns and Wood, 2011*]. Faults are recognized as a plane of weakness along which fluids may circulate, but they may also act as seals by juxtaposing permeable layers against impermeable ones thus creating a reservoir. Also, two features of rhyolite domes are of importance when evaluating a subsurface for fluid flow conduits or reservoirs. The interiors of rhyolite domes freeze and form cooling fractures, and the bottom of volcanic layers may represent permeable rubble flows. The stratigraphy and structure of a region must not be discounted to reach logical conclusions.

4. Surveying

Accurate surveying of the Neal Hot Springs area was perhaps one of the most critical processes completed at this field camp. The position information is critical to be able to accurately assess the models created by each method. Additionally, coherent survey information over the entire site is necessary for various methods to be able to integrate data sets and analysis. For the surveying of Neal Hot Springs, two Trimble differential global positioning satellite (DGPS) systems were used to collect data over the DS10, DS20, and DS30 lines, the HS01, HS02, and HS03 lines, the DC1 line, and the Warm Spring survey lines. The GPS positions of the other DC resistivity lines were collected using a handheld GPS. The handheld GPS units had an average accuracy of 3m, which is not precise in comparison with the DGPS units; however for the purposes of the resistivity and self potential methods it was sufficient.

To interpret missing data points, or incorrectly labeled points, a digital elevation model with a 10m pixel resolution was referenced. ArcGIS software was then used to get the GPS coordinates of the missing and incorrect points from the digital elevation model. Maps were generated using ArcGIS software which utilized the NAD 1983 UTM Zone 11N projection and USGS base maps as references.

The DGPS system from Colorado School of Mines was a base station/rover pair with survey grade accuracy. This DGPS is shown in Figure 4-1. The initial step in every DGPS survey was to set up the base station at a location that was within the line of sight of a fair amount of points. The rover unit is then coupled with the base station receiver. This coupling ensures that as the rover is moved to a variety of locations it will continue to communicate with the base station via radio to achieve positioning with centimeter accuracy. The operator moves to the location of the flag and marks the location with the GPS over a time interval to stack the position location and increase further accuracy.

Figure 4-1 Rover and Base Station for DGPS

The GPS unit from Boise State University was a mapping grade rover with data that was corrected in a post-processing program that referenced the many GPS base stations that were setup at the passive seismic stations. These base stations had access to more satellites and allowed the GPS data to be corrected to centimeter accuracy as well.

5. Potential Fields

5. Potential Fields

5.1 Acquisition

5.1.1 Gravity

Within the main survey area, gravity data were acquired along 3 lines, corresponding with deep seismic lines DS10 and DS20 and resistivity line DC1. These are indicated in Table 5-1 below. Additional gravity data were acquired over the Warm Spring site.

Gravity readings were taken at regular intervals along each line as indicated in Table 5-1. The data were acquired using a Scintrex CG-5 gravimeter and a Lacoste and Romberg (L and R) gravimeter.

Table 5-1 Gravity Survey Lines

Line No.	DS10	DS20	DC1
Sample Interval	60m	60m	20m
No. samples	202	101	64
Line length	12km	6km	1280m

All objects exert a gravitational force on all surrounding objects that is proportional to their mass. This force is measureable; gravimeters measure the displacement of a suspended mass from the vertical due to the presence of excess mass or anomalous subsurface densities. In order to obtain accurate readings, both the Scintrex CG5 and L and R gravimeters must be leveled to ensure the maximum displacement from the vertical is recorded. This is converted and corrected to a relative gravity measurement; by comparison with a local gravity benchmark, the absolute gravity at a point can be calculated. Figure 5-1 shows the lines that gravity surveys were completed on.

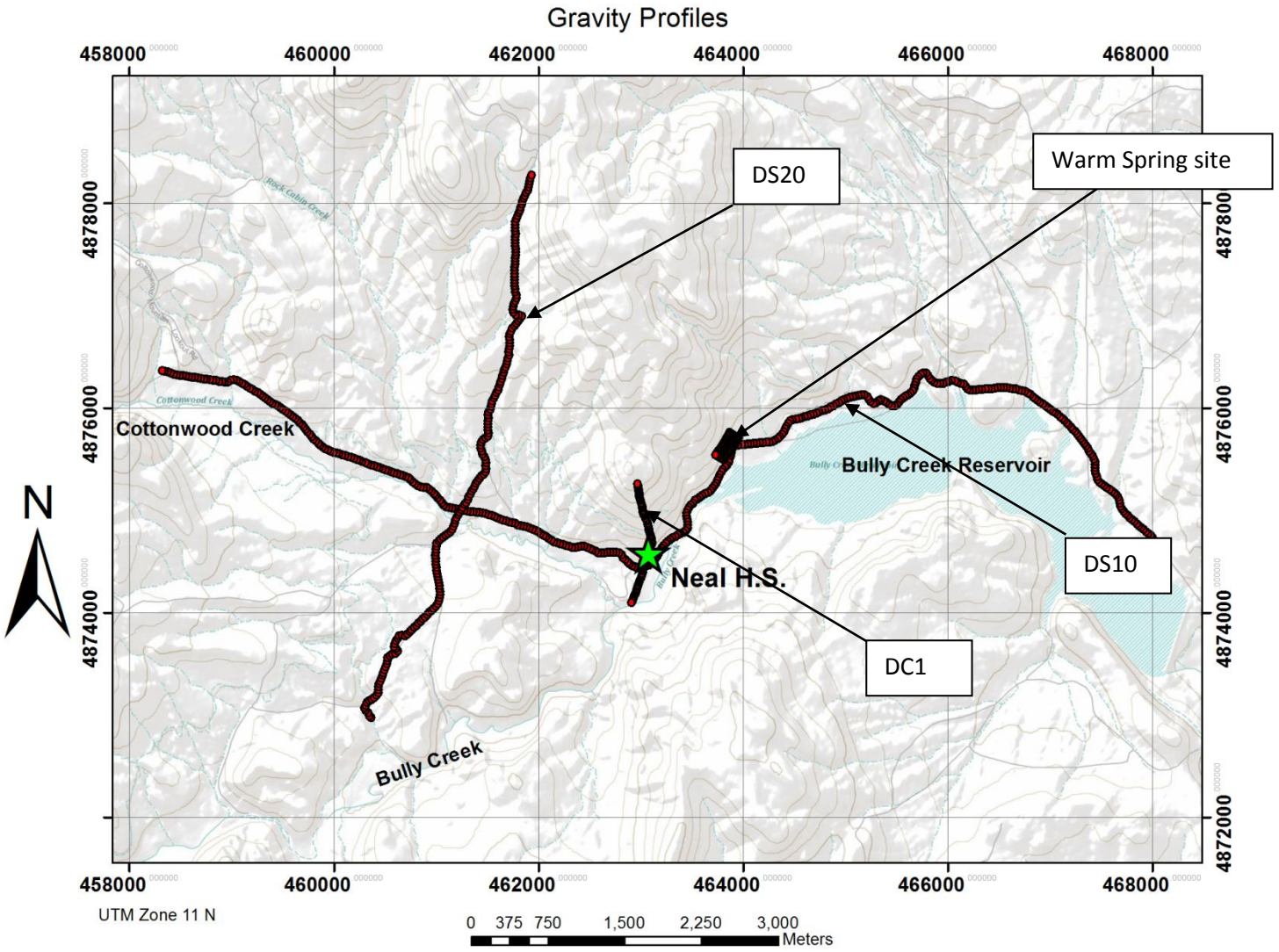

Figure 5-1 Survey Lines for Gravity Measurements

The Scintrex CG5 and L and R gravimeters operate on similar principles, but use different systems. The Scintrex CG5 operates using a fused quartz system, where a mass is balanced using a spring and electrostatic force. The position of the mass is altered by variations in gravity; the displacement of the mass is proportional to the gravitational variation. The magnitude of the electrostatic force required to return the mass to a neutral position is proportional to the displacement of the mass, and therefore proportional of the gravitational variation. Figure 5-2 shows the operation of the Scintrex CG5 Gravimeter

Figure 5-2 Operation of Scintrex CG5 Gravimeter

The L and R gravimeter does not depend on a quartz system but is instead composed entirely of metal, making it much more durable than the Scintrex CG5. However, it is less accurate than the Scintrex CG5. Figure 5-3 below is a simplified diagram of how the L and R gravimeter operates. When a measurement is being recorded, the hinge releases and the displacement of the mass is measured giving indication to the change in gravity.

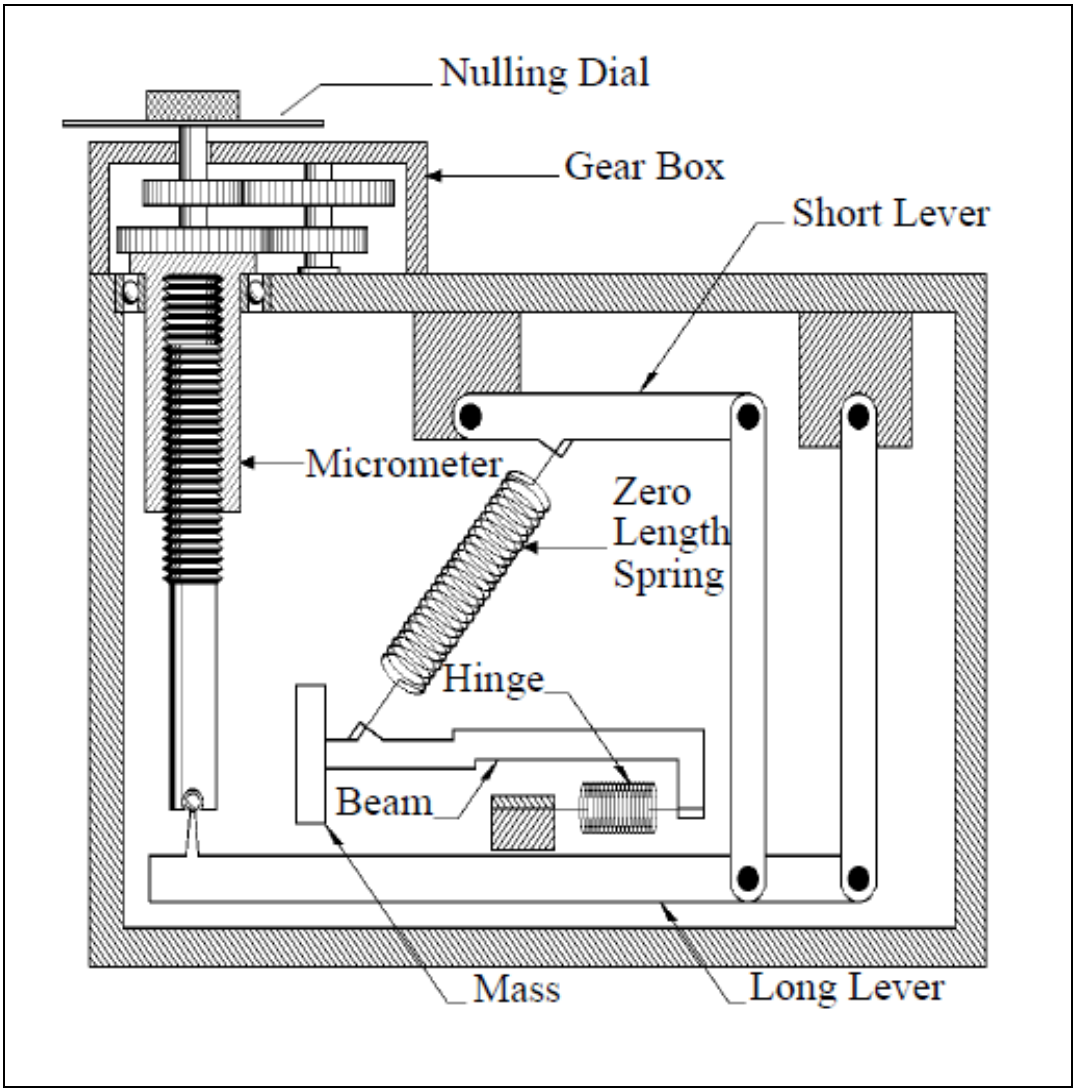

Figure 5-3 L and R Gravimeter [*Reynolds, 2003*]

5.1.2 Magnetics

Magnetics data were acquired along deep seismic lines DS10 and DS20, the resistivity line DC1, as well as other small areas, as shown by

Figure 5-4, including the Warm Spring site. Each magnetic data set was acquired continuously over all surveyed lines at a sampling rate of 1Hz. The magnetometers used incorporated a GPS system, allowing positioning markers to be made at regular intervals in the data records.

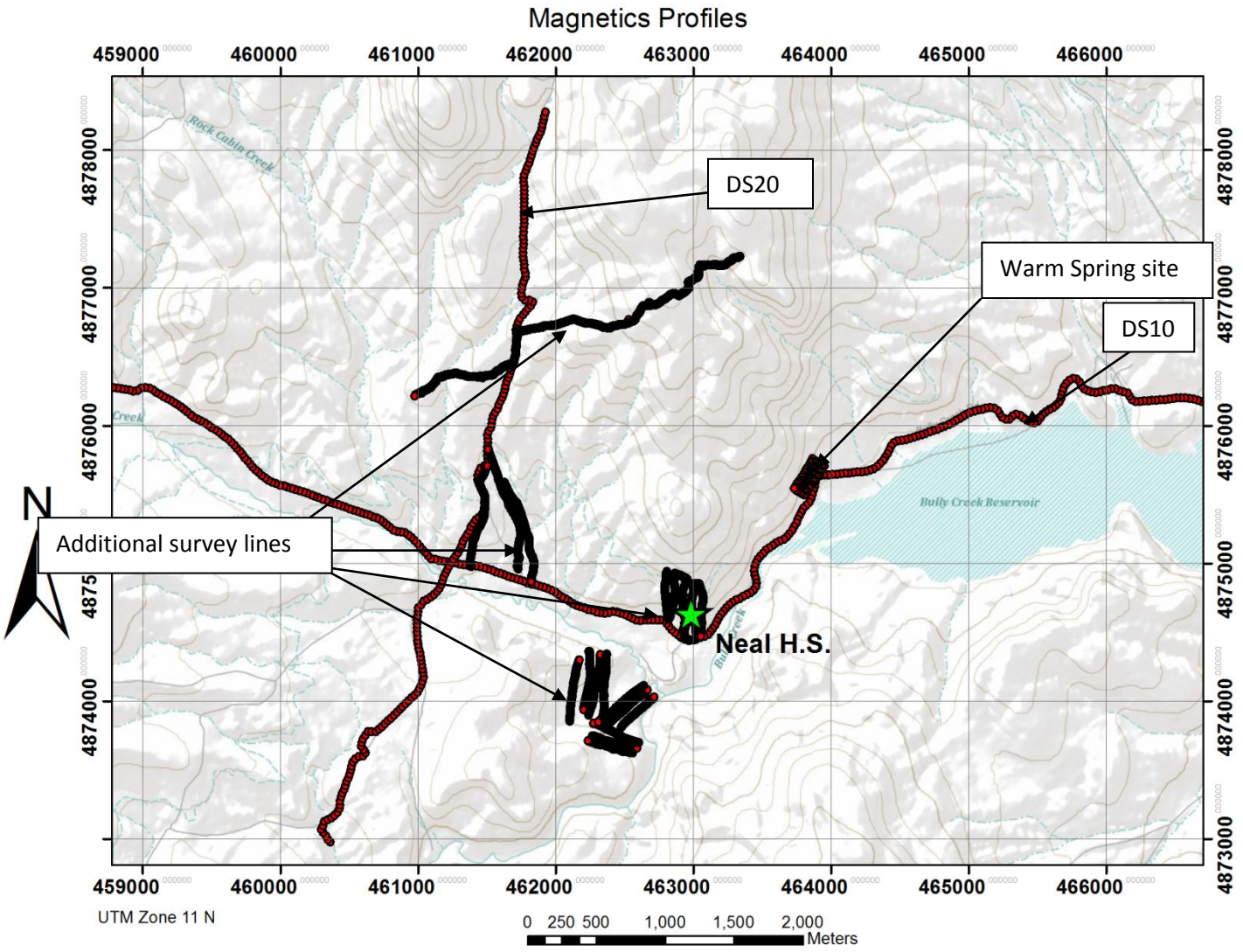

Figure 5-4 Map Showing Magnetics Survey Line

The magnetic data were collected using two cesium vapor magnetometers; one (supplied by BSU) measured the total magnetic field strength at each sample point, and the other was a vertical gradiometer (supplied by CSM), measuring the vertical gradient in the magnetic field strength. A proton precession magnetometer was installed at a static location as a base station to monitor diurnal variation in the Earth's magnetic field throughout the survey duration.

The cesium vapor magnetometers take advantage of the nine different energy states of the cesium atom. The equipment utilizes atoms that contain sublevels with magnetic energy. These sublevels must be suitably spaced in order to measure Earth's magnetic field which is relatively weak [*Telford et. al, 1990*].

Proton precession magnetometers contain a proton rich fluid. A polarizing magnetic field is applied to the fluid, and the protons align to this field. When the polarizing field is abruptly removed, the protons process to align to the Earth's magnetic field at the surveyed point. The frequency of this proton precession is measureable and proportional to magnetic field strength [*Telford et. al., 1990*].

The BSU magnetometer measured the total field strength The magnetic field strength is proportional to magnetic susceptibility, and once the data is corrected for diurnal variation, the magnetic susceptibility of the subsurface underlying the sample point can be found.

The CSM magnetometer measured the vertical gradient in magnetic field strength by sampling magnetic field strength at two points, vertically offset by 1m, and finding the difference. Acquisition of the vertical gradient is shown in Figure 5-5. This gradient allows estimation of the variation in magnetic susceptibility of the subsurface with depth. Using a gradiometer, rather than a magnetometer measuring total field strength, has the advantage of requiring fewer corrections to be made to the data during processing, and may provide more accurate results. The data produced by the magnetics survey remain as relative rather than absolute measurements of magnetic field strength and magnetic susceptibility.

Figure 5-5 Acquisition of Magnetic Data

5.1.3 Electromagnetics

5.1.3.1 Frequency Domain Electromagnetics

Controlled source electromagnetic surveys in the frequency domain were carried out over deep seismic lines DS10 and DS20 and resistivity line DC1, and in addition at the Warm Spring site. These lines are indicated in

Figure 5-6 below.

Controlled source electromagnetic surveys rely on artificial electrical and magnetic fields generated for the purpose of the survey. Two frequency domain EM tools were used, EM31 and EM34. Surveys were carried out with both tools over all lines shown in

Figure 5-6. The two tools, on account of their different operating frequency ranges, investigate to different subsurface depths.

5. Potential Fields

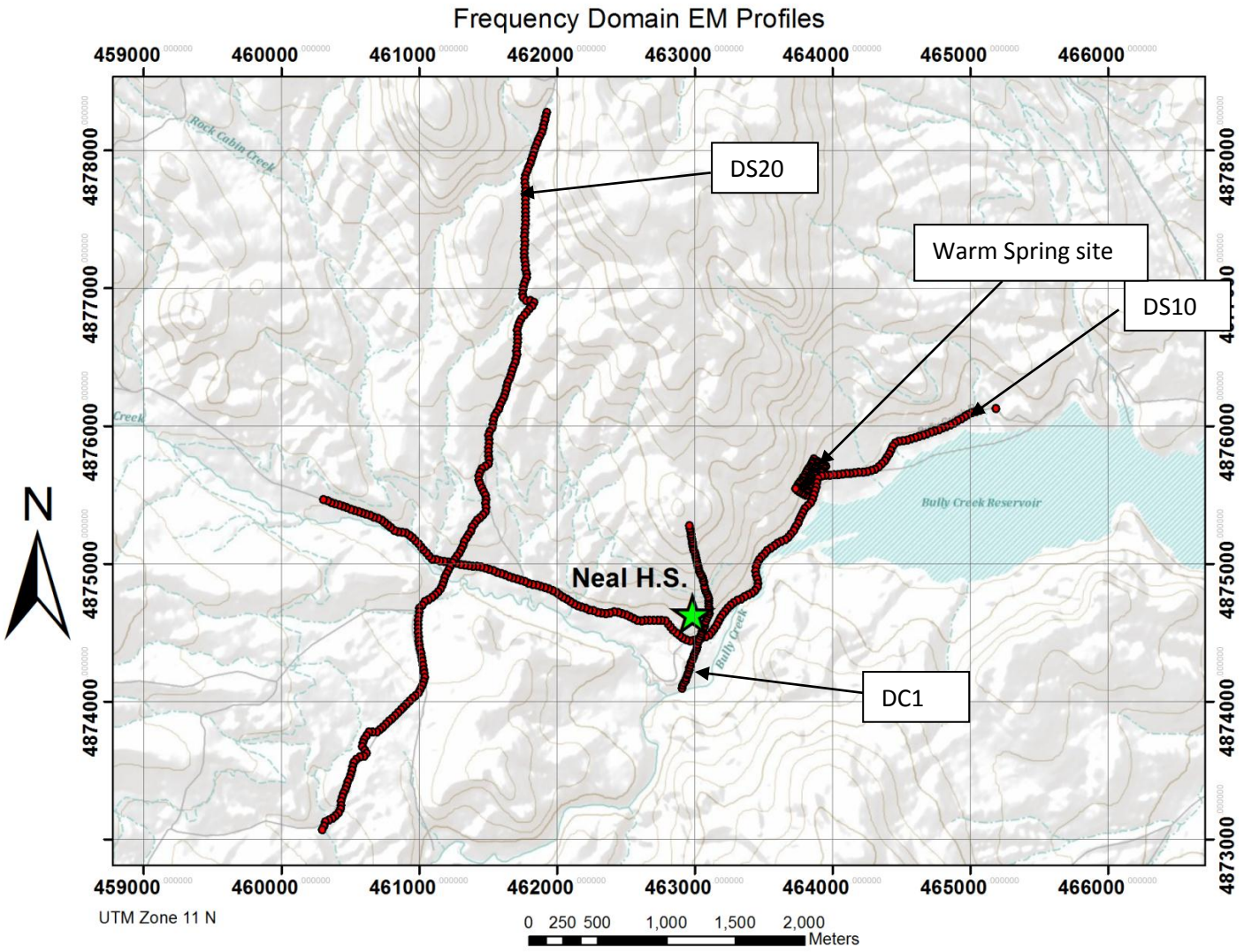

Figure 5-6 Frequency Domain Acquisition Line

Both the EM31 and EM34 operate on similar principles; an alternating current at a known frequency passed through a coil of wire (the transmitter coil) generates a primary electromagnetic field. This primary field induces a secondary field in the subsurface. This secondary field in turn induces an alternating flow of current in a second coil of wire (the receiver coil). The secondary field also induces alternating currents in electrically conductive bodies in the subsurface; these 'eddy currents' modify the phase and amplitude of the electromagnetic field measured at the receiver coil, allowing these anomalous bodies to be detected and their relative conductivity calculated.

The EM31 device features a transmitter coil and a receiver coil mounted on opposite ends of a rod with an intercoil separation of 3.7m. The EM31 can be configured to measure the vertical or horizontal secondary field; for the purposes of this field camp, it was configured to measure the vertical component of the induced electromagnetic field with a horizontal co-planar configuration. The primary field at the transmitter coil is generated by a constant alternating current at a frequency of 9.8 kHz. The receiver coil measures the in-phase in parts per thousands of the modified field; this is useful for detecting the presence of metals and the quadrature (terrain conductivity) in meter*Siemens/meter (mS/m). The tool is calibrated, prior to surveying, in an area of non-conductivity. The tool requires a single operator, who should be free from any electrically conductive material. In order to measure the vertical field, the rod is held in a horizontal position, and the operator walks at a constant speed between each station. In the case of the horizontal co-planar configuration, the depth of investigation for this tool is about 6m. Figure 5-7 shows the EM31 in use.

Figure 5-7 Acquisition Using the EM31 Device

The EM34 tool features larger transmitter and receiver coils than the EM31. Similarly, the EM34 must be calibrated in an area of non-conductivity prior to commencing the survey, such that 0 mS/m is measured in the absence of conductive materials. The two coils are connected by a cable of known length; in this case a 20m cable. The separation distance between the coils, dictated by the length of this cable, influences the depth of investigation, and remained constant during this survey. The EM34 was operated by placing the transmitter coil 20m in front of the receiver coil with a horizontal co-planner configuration (i.e. coils are placed horizontally on the ground). With a 20m coil separation, the depth of investigation of this method was approximately 10-15m.

Measurements were made at intervals of 30m on the surveyed lines. Where conductive bodies are present, fluctuations in the reading of the order of 10 mS/m are observed on both

the EM31 and EM34. Where observed during acquisition, the presence of conductive materials, such as power lines, and any distinctive geology were noted, as these can have a potentially significant effect on the data recorded on both recording devices.

5.1.3.2 Time Domain Electromagnetics

The survey was carried out using five 100m by 100m, 1 dimensional central loop soundings 100m apart. The third sounding location was also used as a fixed loop survey with two measurements taken 25m inside and 25m outside of the loop along the profile. The central loop sounding is acquired by locating the receiver at the center of the square 100m by 100m loop. The survey was carried out along the third resistivity line (DC3) and was centered at the inferred location of the fault zone. 15 repetitions at each station were collected. Figure 5-8 shows the locations of the soundings

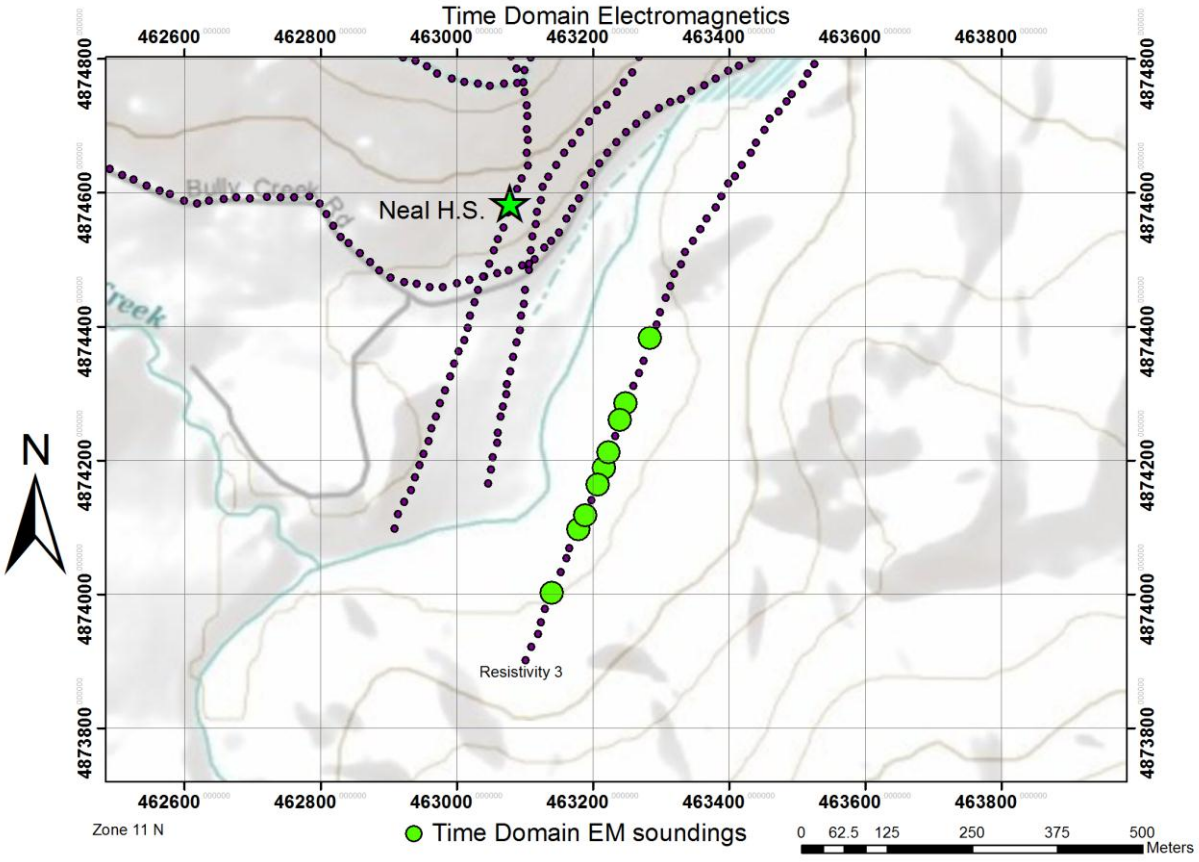

Figure 5-8 Location of the TEM Soundings

The EM-47 Transmitter, shown in Figure 5-9, outputs a bipolar square wave. In this survey's setup, a 7.5Hz repetition rate, a 2A current in the loop, and a current ramp off of about 6 micro seconds was used. With this 100m by 100m loop, the upper limits in sounding depths were being reached at about 150m. It is more commonly used to measure near surface conductivity anomalies in depth using smaller loop sizes and higher repetition rates.

Figure 5-9 EM47 Receiver (Left) and Transmitter (Right) [*Geonics Website*]

The PROTEM receiver can be used with a very wide range of transmitters and survey setups. It measures the rate of decay of an induced magnetic field along 3 axes. The receiver coil is a 3-component air-cored loop. The receiver measured 20 time gates, geometrically spaced, after the primary current from the EM-47 was switched off. To accurately monitor the decay rate the receiver coil has a very wide bandwidth of 270 kHz. Because of the relatively low signal from the decay, the data were stacked at each data point over 15 seconds.

5.1 Processing

5.1.1 Gravity Data

In order to process gravity data, measurements must first be converted into the correct units, corrected for instrument drift, and different lines and instruments must be correlated.

The Lacoste and Romberg gravimeter (L&R) raw data is comprised of unitless counter readings that must be converted to milligals (mGals). Each individual L&R has a unique conversion sheet to translate counter readings into gravity data. The conversion sheet is contained in the appendix. The sheet shows direct conversions for every counter reading multiple of 100, and an interval factor applicable to other values. The Scintrex CG-5 raw data is already in units of mGals, although the values are still relative gravity readings.

Gravimeters drift gradually from their original calibration over their lifetimes. To mitigate the effect of instrumental drift on accuracy, a base station is designated at the beginning of an acquisition period. Base station readings are taken intermittently throughout surveying and at the start and end of each day. In processing, data is corrected such that base station values read the same, assuming a linear drift with respect to time. The assumption is valid as long as the base station is visited at minimum every three hours for the L&R, and every four hours for the Scintrex CG-5 (CG-5).

At Neal Hot Springs, the first flag on the main line (flag 1001) was chosen as the base station. The CG-5 visited 1001 at the start and end of each day, and used a local base station for surveying far from the main line. A reading was taken every three hours to verify that the drift was accurately accounted for. The L&R also used a local base station, at which readings were taken roughly two hours apart. Lines that took more than one session to complete were tied together by overlapping the two segments. The last one or two data points for the first segment were repeated to further improve data quality.

Once local base station corrections are applied, the different lines are correlated using the main base station. The Neal Hot Springs CG-5 data were adjusted by comparing the base station measurements at the beginning of each day with the first measurement at the beginning of data acquisition. Every data point in a day's file was shifted by the difference between the two measurements such that all main base stations show the same number.

Because both the L&R and CG-5 are used to display relative change in gravity, the trend along a line will be similar for different instruments, but the values may be very different. To make combining the two instruments' data useful, at least one location is measured using both instruments. The measurements are compared, and another shift is applied in the same manner as the base station. Here, the L&R values were increased to match the range of the CG-5.

Next, the data were organized into the four survey lines: DS10, DS20, DC1, and Warm Spring survey. The data were saved as .txt files to be imported to the modeling software, Geosoft's Oasis Montaj, which is able to consider both gravity and magnetics in its

interpretation of a region. The program applies several more corrections to the data. The first is a terrain correction, which weights the effect of the topography on different data points. An existing regional digital elevation map generated by Colorado School of Mines professors and graduate students was used for the Neal Hot Springs data. The free-air and Bouguer anomaly corrections are applied simultaneously. The free-air correction adjusts for the elevation alone and assumes the only material between the observation point and sea level is air. In other words, the theoretical amount by which gravity would change based on this increased radius from data point to the center of the Earth is cancelled. The Bouguer correction is similar to free-air, but assumes all mass between the data point and sea level to be a homogenous mass at a certain density. Equations with explanations for corrections can be found in Appendix B section a. Once all corrections have been applied, the remaining value represents the gravitational anomaly at the observation point. At this stage, a forward modeling is performed, which generates a color-coded gravity map that is ready for interpreting.

5.1.2 Magnetics Data

The processing flow for the magnetics data was as follows:

1) A diurnal correction was applied.
2) The surveyed DGPS co-ordinates were merged with the data.
3) The data were used to iteratively forward model the subsurface.

The following software was used to process the data: Microsoft Excel, Magmap2000, and Geosoft Oasis Montaj. The raw data from the cesium vapor magnetometers was in a binary file and the raw proton precession data was stored in a STN file.

The data were subject to an initial quality control check in Magmap2000. The data were corrected for errors made during acquisition (e.g. incorrect dates in data from the proton precession magnetometer). Correct time and date information in the datasets is vital for correlating between datasets and with the GPS data. As previously discussed, the base station data were acquired by a static proton precession magnetometer. These data were de-spiked to eliminate noisy data points that were unlikely to reflect variation in the Earth's magnetic field.

The diurnal correction was applied using Magmap2000. The diurnal correction effectively removed the effects of the background magnetic field by subtracting the diurnal variation recorded at the base station from the data recorded by the cesium vapor magnetometer. The corrected data were imported into Microsoft Excel and matched with the GPS positioning data, as these were not correlated during acquisition. GPS coordinates were recorded for every station (at 30m intervals along the surveyed lines), and interpolated between stations.

The corrected and positioned data were imported into Geosoft Oasis Montaj. The data were plotted to produce 1D profiles of magnetic field strength along the surveyed lines. The data were subject to further quality control, and noisy data and outliers were eliminated. Outliers include any anomalous spikes in the profile not likely caused by subsurface expressions.

The causative subsurface structure of the magnetic data observed was then iteratively forward modeled in Geosoft Oasis Montaj. The model was constrained by the magnetic data and independent knowledge of the subsurface to produce a final image.

5.1.3 Frequency Domain Electromagnetic Data

Processing frequency domain electromagnetic data begins with the association of GPS coordinates to the EM-31 and EM-34 readings. A quality check of the readings resulted in the removal of extreme conductivity readings associated with the EM-34 acquisition. Those readings are believed to be representative of surface noises (e.g. DC cables, fences, or running water). The apparent conductivities from the EM-34 data were plotted against station numbers to quality check the trends in the data. Contour maps of apparent conductivities from EM-34 and EM-31 were produced using Surfer. For EM-31 data, smoothing was required.

5.1.4 Time Domain Electromagnetic Data

The raw data from the PROTEM receiver is output in the form of time gates vs. a Geonics number that is related to the voltage reading from the receiver coil. It must be converted to a time in microseconds vs. the change in the magnetic field over time (dB/dt). This converted reading is in units of microvolts per square meter ($\mu V/m^2$). The manual for the PROTEM receiver lists the locations in time of the time gates corresponding to each frequency. The frequency was chosen to be 7.5Hz and maintained throughout the survey, therefore the

proper time gates at the proper locations were able to be identified. To convert from Geonics' number to $\mu V/m^2$, Equation 5-1 was used.

Equation 5-1 Time Domain Conversion [*Li, 2011*]

$$\frac{dBi}{dt} = \frac{19.2 * Vi}{EA * 2^n}$$

Where *Vi* is the Geonics number, *EA* is the effective area of loop (*EA* = 31.4m^2), and *n* is the gain (*n*=1).

After applying this correction to all data, the 15 records, which were taken at each station, were averaged together to further reduce noise and obtain a single record. To estimate the error in the measurements, the standard deviation of the 15 records was added to a percentage of the averaged value at each time gate.

The EM1DTM program was used to invert the data at each station to obtain conductivity values in the units of Siemens per meter (S/m) as a function of depth. As a starting conductivity model, a total of 50 layers with a maximum depth of 400m were used. The forward modeling was run with an L-curve inversion type assuming horizontally layered structures and an infinite half space.

5.2 Results

5.2.1 Gravity

The DS10 line was divided into two sections, east and west, to aid in gravity and magnetic interpretation of the region. Dividing the line allowed for the data to be correlated along nearly linear profiles, which further improved interpretations of the subsurface geology. This division was located at the center of the Neal Hot Springs. The eastern-most measurements of the DS10 line were removed from the modeled data due to insignificant features.

The gravity data for the western segment of the DS10 line illustrated the presence of two relatively dense bodies within the subsurface. However, the eastern positive anomaly was better represented in the eastern segment. These data highs were attributed to a denser material nearer the surface, most likely basalt. The shallow character of the basalts is the result of faulting. The gravity readings increase as they approach the center of Neal Hot Springs. The gravimeter detected the presence of the second massive body within the subsurface.

The dominant geological features of the west DS10 line were two listric normal faults and the variation in bodies they create beneath the surface. The eastern fault was shared with the eastern segment of the DS10 line; this fault was the conduit of the Neal Hot Springs. This focal point of the system was unfortunately the break-point between the two survey lines as it was the point where the 2D assumption failed. The western fault did not travel as close to the surface, but it could possibly act as a conduit of hot water, similar to other faults in the region. The gravitational and magnetics joint interpretation of the western segment of the DS10 line is depicted in Figure 5-10 below. The model followed all assumptions made while creating it, and produced a result with two massive bodies in locations that correlate with the collected gravity data.

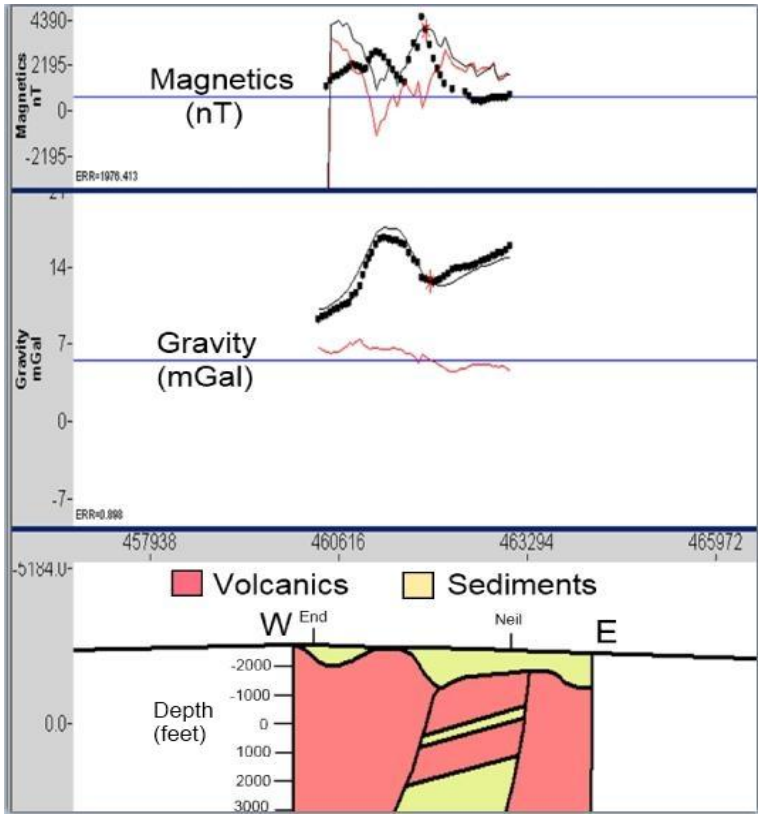

Figure 5-10 Western Portion of DS10 Line

The eastern segment of the DS10 line began at the Neal Hot Springs and ended along the road near the center of Bully Creek Reservoir. The surface geology of the line consisted mainly of sediments, but the interpretation revealed significant volcanic material located at shallow

depths below the surface. The gravity data showed a higher gravitational anomaly to the west, which gradually decayed toward the east. This was explained by the presence of an extensional fault system. The relatively higher subsurface location of the basaltic horst resulted in a higher gravity reading because it was denser than the surrounding sediments. As the survey moved east along the profile, the gravity measurements lessened because the basalt was farther down and there was an increased amount of lower density sediments overlying it.

The gravity data alone does not give a simple understanding as to the movement of water in the system; however, when coupled with magnetic data, the two give a solid indication as to the geological structures of the subsurface and how water may be extracted. The gravity and magnetic data helped to image the subsurface lithology and locate primary faults. Because faults can act as conduits of fluids, the identification of fault locations aided the interpretation of where hot water could be targeted in the system. Figure 5-11, below, depicts a cross-section view of the eastern segment of the DS10 line. The joint model produced from the gravity and magnetic data shows the faulted horst system. It should be noted, however, that the horst block out crops at the surface in the field, but a layer of sediment was added to fit the model more accurately.

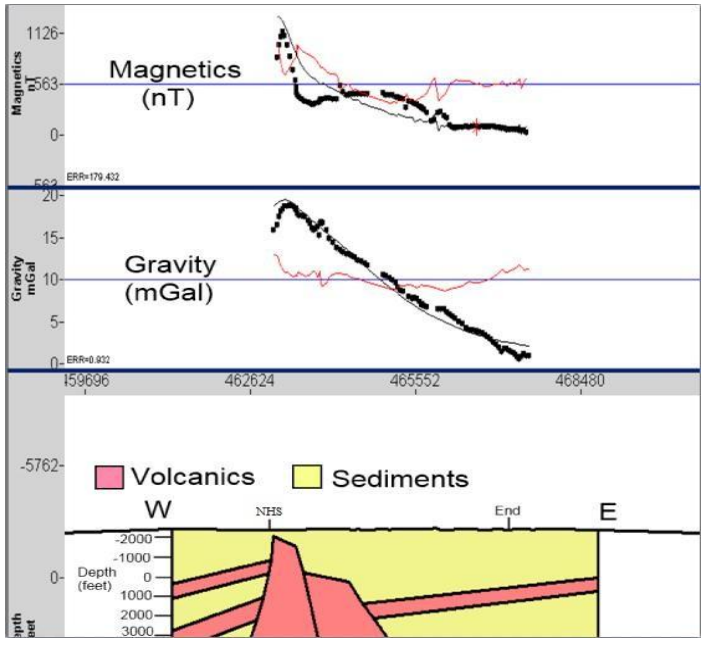

Figure 5-11 Eastern Portion of DS10 Line

The DS20 line ran orthogonally to the DS10 line, and intersected it directly in the middle of one of the main geological features in the subsurface. Based upon a cross-section view of the 2007 data once again, a geological model was constructed to represent the region. The gravity and magnetics data on the DS20 line was quite simple to correlate, as the general trend was a large body becoming deeper beneath the surface toward the south, connected at depth. On the very right side, a normal fault cuts through the area, creating an offset in the subsurface lithology, and causing the block to the right to fall even farther beneath the surface. Therefore, the data shows a steady, gradual decay of the gravitational anomaly. The top of the fault continues in a different direction, causing a basaltic intrusion to rise to the surface as an outcrop. This is all represented in Figure 5-12.

The model below showed a very impressive fit for both the gravity and magnetics data, fitting the general trend with little alteration. Each individual cusp in the collected data could not be fit without seriously altering the interpretation. There could have been small layers of sediment or other volcanic rocks that were built into the model but would have also made sense. If the model were to fit the data exactly, the noise would have been built into the model as well, which is something to be avoided. The type of forward modeling used to interpret the data was non-unique, so the best result is shown below in Figure 5-12.

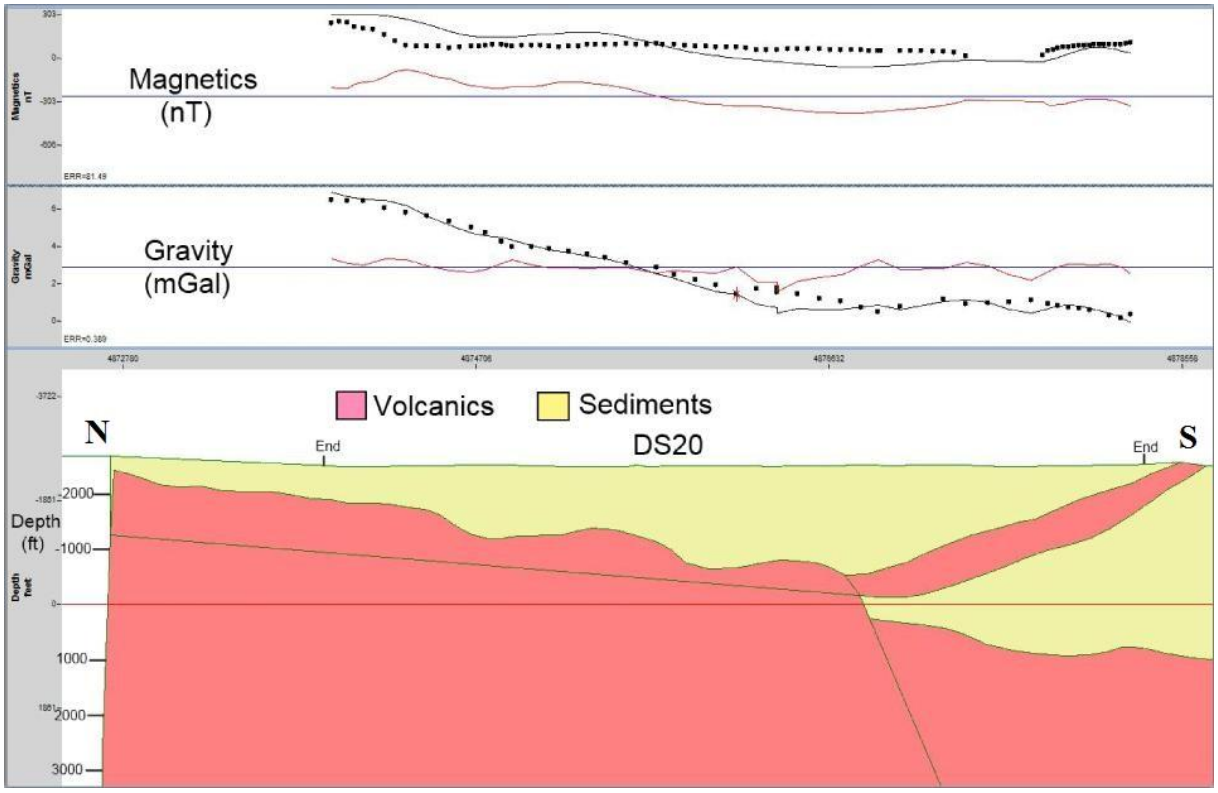

Figure 5-12 Interpretation of DS20 Line

5.2.2 Magnetics

The final image of the subsurface geology was obtained by coupling and running forward modeling on the gravity and magnetic data. Forward modeling involves the creation of a geological cross section under the magnetic and gravity profiles. In order to do the forward modeling of the data, the profile lines were all processed separately. Because of the orientation of the primary seismic line, it was divided into two sections to make the interpretation more intuitive. This division is located at the Neal Hot Springs. The cross sections were then formed by manually inputting features into Geosoft representative of stratigraphic layers observed at the surface and predicted subsurface structures. Inversion results from a previously conducted 3D gravity survey gave indication as to the subsurface structures which guided the forward modeling. The geological units were assigned density and magnetic susceptibility values to generate gravity and magnetics curves (respectively) which, after adjustment of the cross section, aligned with the acquired data.

The resulting images show three boxes. The top box contains the magnetic data, the middle contains the gravity data, and the bottom contains the geological image. The black dots in the gravity and magnetic boxes represent the collected data. The black line represents the magnetic and gravity data expected from the generated geological cross section shown in the third box. The red line represents the error.

While the forward-modeling densities from the western part of the main seismic line (DS10) show a close fit to the gravity data (Figure 5-10), the magnetics data were not well-supported by the predicted magnetic susceptibility values. The results from the eastern portion of this profile follow the general trend of the magnetics data, but the overall product does not match. However, the two positive magnetic anomalies in this profile were given consideration in the forward-modeling process. The resulting cross section illustrates a package of western-dipping volcanic and sedimentary rocks interpolated between two listric faults. The central magnetic spike was interpreted as an effect of the western-most normal fault. The exteriors of both faults are characterized by large volumes of basalt. The second positive magnetic anomaly was the effect of the outcropping western basalt structure. This interpretation coincides with the known geology. Prior to geophysical surveying, predictions were made concerning the location and orientation of the fault with respect to the geothermal system. The hanging wall of normal faults is typically more fractured, thus making it an ideal conduit for fluid flow. The Neal Hot Springs is a surface manifestation of geothermal fluids travelling up the eastern fault in the west DS10 profile. This fault may be identified as the westernmost fault in the eastern DS10 profile as well (Figure 5-11).

The eastern section DS10 illustrates a horst transected by an additional normal fault (Figure 5-11). On either side of the horst are western dipping volcanic and sedimentary strata. The curve generated by the magnetic susceptibility values better fit the magnetic data along this profile. The dominating feature of the eastern DS10 magnetic data is a magnetic spike similar to the prominent spike of the western DS10 magnetic data. This was again interpreted as a fault and illustrated in the geological section. The local extensional area may be viewed by overlaying

the two sections along the common listric fault. The en echelon faulting array discernable from map view is now accompanied by a reasonable subsurface structure.

5.2.3 Frequency Domain Electromagnetic Data

A map of the apparent conductivity from the EM-31 data is shown in Figure 5-13. Large contrasts in conductivity can be observed at three primary locations: one near the intersection of DS10 and DS20, one at the intersection of DS10 and DC1 and one on the east side of DS10. These contrasts are generally interpreted as faults associated with the larger horst structure. The first two anomalies flank the primary horst structure, which contains high resistivity volcanic rocks extending from Neal Hot Springs and line DC1 to the eastern side of DS10. The edges of this horst structure are the normal faults that are believed to have heated water flowing up them. There are minor variations in the conductivity of the horst structure between these two anomalies, which may be caused by smaller fault structures, within the horst, that were down thrown and have more recently filled with sediments. Both of these interpreted faults coincide with structures seen in the DC resistivity and SP results seen in Section 6. The third low conductivity anomaly near the intersection of lines DS10 and DS20 correlates with a high density body seen in the 2007 Gravity that was inverted in Section 2. This anomaly may be a continuation of a larger horst structure for the area, but it is surely associated with volcanic material. Close to this low conductivity anomaly, there is also a very high conductivity anomaly; this could be associated with fluid flow along an additional fault or it may be caused by a buried metallic object.

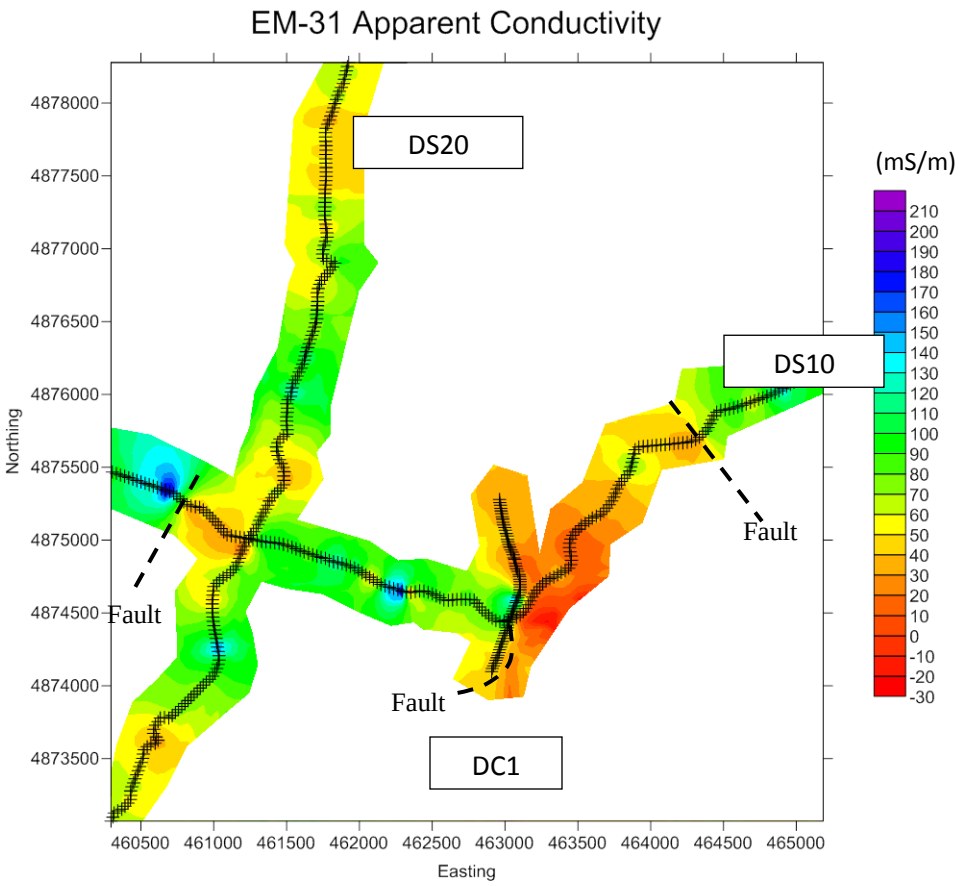

Figure 5-13 Map of EM-31 Data ,the color scale represents apparent conductivities in mS/m.

The EM-34 measures the apparent conductivity dictated by the soil and fluid conductivity and saturation. The figures below display the apparent conductivity plots versus station numbers along DS10, DS20, and DC1. Though abrupt anomalies are observed, field notes indicate that those anomalies are due to surrounding metal objects. On the plots, general trends can be identified and interpreted. Figure 5-14, Figure 5-15, and Figure 5-16 show the general trends observed by the EM-34 data along lines DS10 and DS20, respectively. A map of all acquired EM-34 data is displayed in Figure 5-17. The map confirms the trends observed in the EM-31 data.

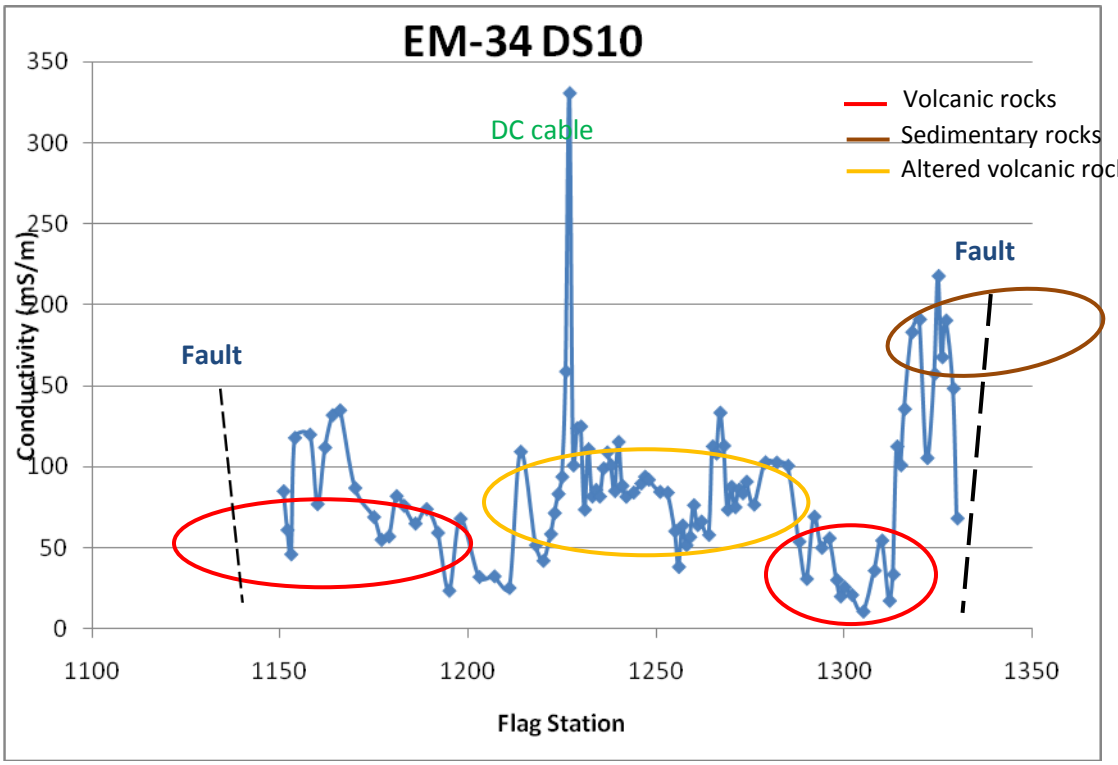

Figure 5-14 EM-34 Conductivity Measurements Along Line DS10

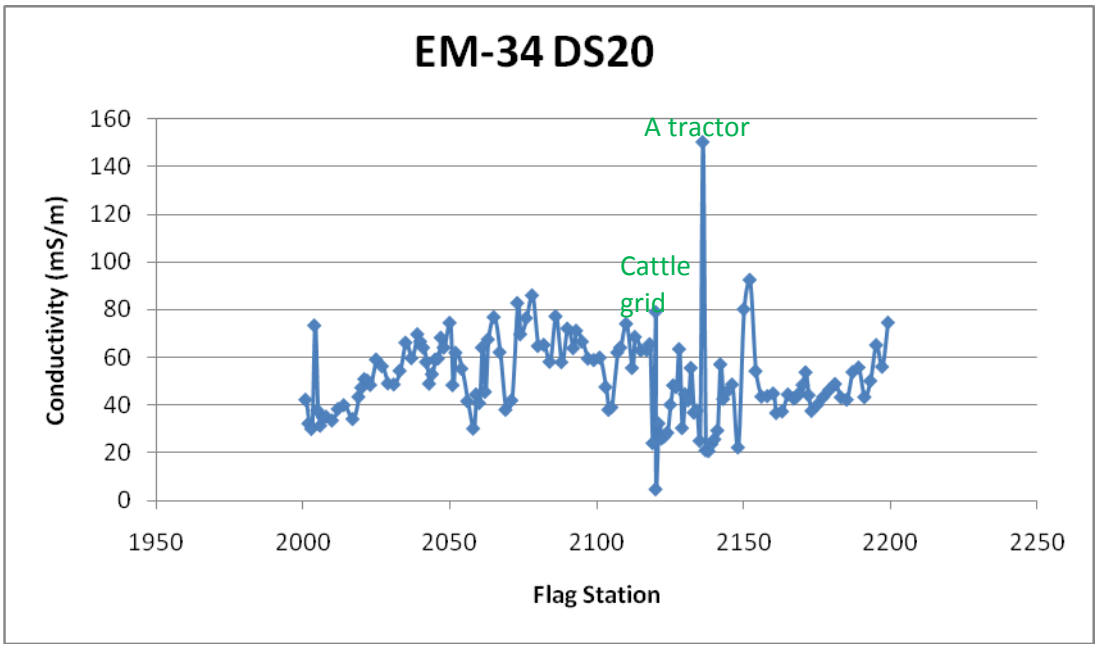

Figure 5-15 EM-34 Conductivity Measurements Along Line DS20

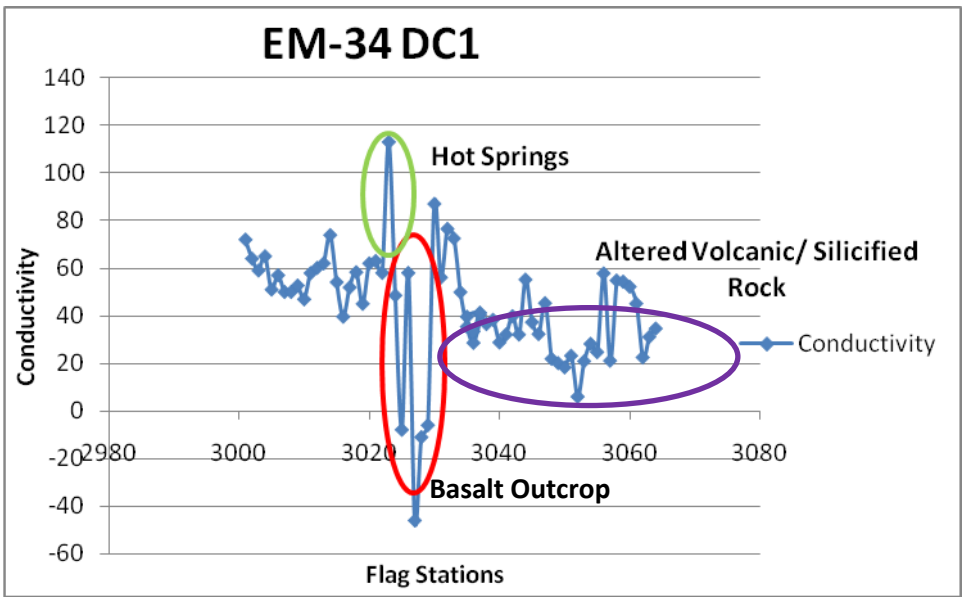

Figure 5-16 EM-34 Conductivity Data Along Line DC1

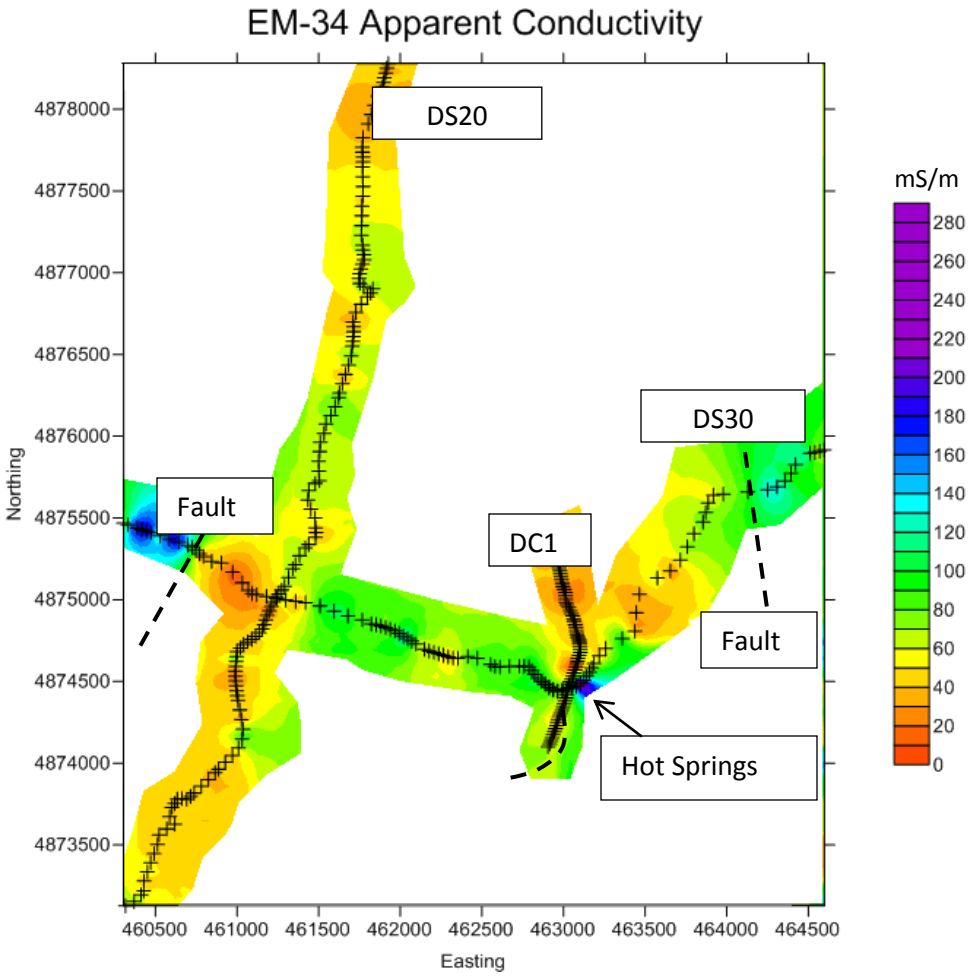

Figure 5-17 Map of EM-34 Data

5.2.4 Time Domain Electromagnetic Data

The data after roughly the 11th time gate becomes very noisy and effectively limits the depth of investigation. The most accurate data is that closest to the surface, and it becomes increasingly less meaningful as depth increases.

Some soundings are more accurate than others, and the central loop soundings at 0, 100m, 200m, and 300m are most accurate at depth because of the stronger signal at these locations. In those locations the largest depth seen is around 150m. The offset soundings done outside the loop are accurate to 75m, and the offset soundings done inside the loop are accurate to 100m. Figure 5-18 shows a schematic of the TEM array design.

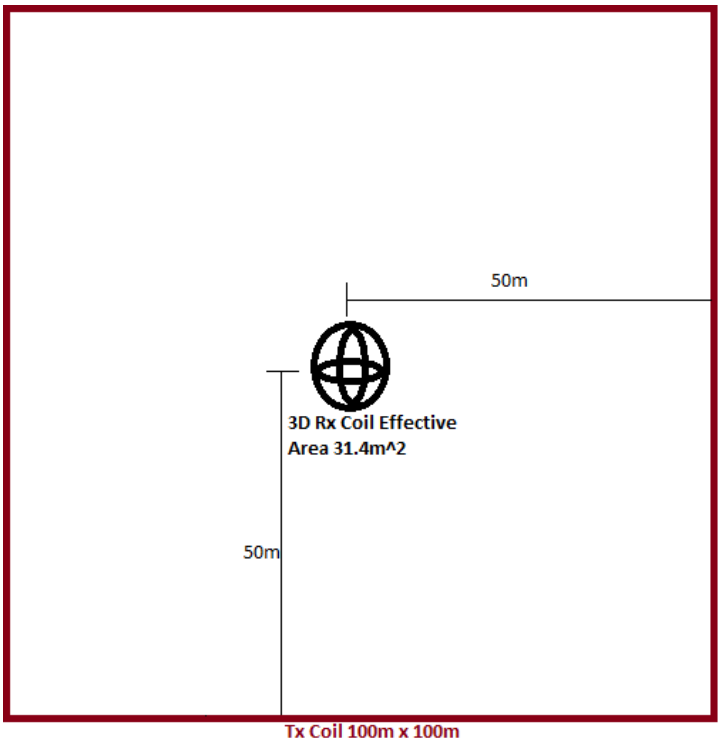

Figure 5-18 Array Design for TEM Sounding

The central loop sounding done at 400m was completely noise-dominated due to a bad transmitter current. The bad transmitter current was most likely the result of a dying battery. Figure 5-19 shows the results from the inversion along the profile. At the central loop sounding at 300m along the profile, the transition from conductive to resistive areas indicates the fault zone crossing through the sounding at a depth of 90m. This does not show in the sounding at 275m, thus the fault has a mostly vertical dip.

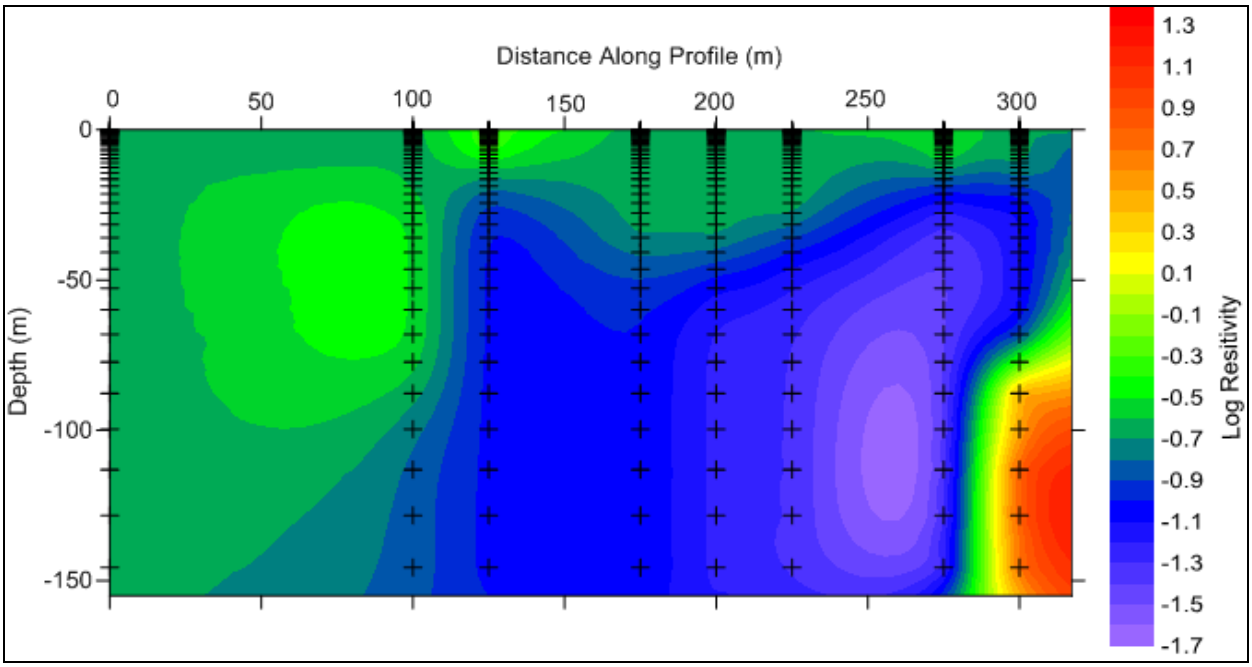

Figure 5-19 Results from TEM Inversion Along the Profile

This interpretation reveals the inaccuracy of assuming a 1D horizontally layered Earth, a requirement for inversion. Hoekstra and Blohm [*1990*] shows that the 1D inversion yields accurate depths to structures in a non-horizontally layered medium; however, the conductivity values become skewed.

6. Electrical Methods

Resistivity surveys were carried over 6 survey lines within the main survey area, named DC1-6, shown in Figure 6-1. Wenner arrays, as shown in Figure 6-2, were used on survey lines DC1, DC2, DC3, DC4 and DC6. A Dipole-Dipole array (Figure 6-3) was used on survey line DC5, which corresponded with the central section of DC4. The survey geometry for each survey line is summarized in Table 6-1.

Table 6-1 Resistivity Survey Geometry

Survey Line	DC1	DC2	DC3	DC4	DC5	DC6
Array Type	Wenner	Wenner	Wenner	Wenner	Dipole-Dipole	Wenner
Line Length	1260m	1260m	1260m	5400m		1600m
Electrode Spacing	20m	20m	20m	20m	20m	20m
No. Electrodes	64	64	64	270		80

Survey lines DC1, DC2 and DC3 were orientated perpendicular to anticipated strike of the major NNW SSE fault. Survey lines DC4, DC5 and DC6 run parallel to the main road running though the site, approximately parallel to the fault zone, and tie lines DC1-3 together.

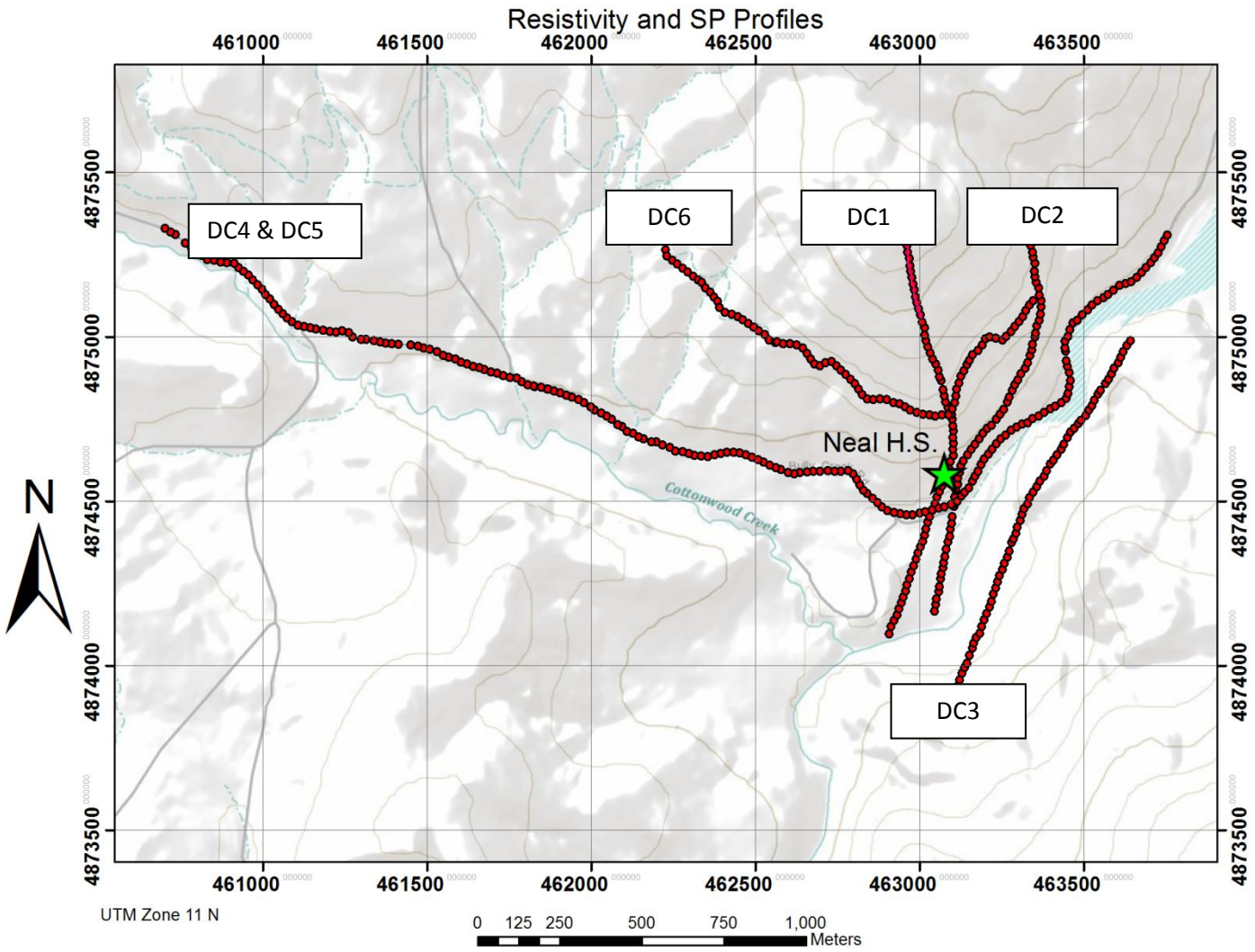

Figure 6-1 Profile Lines for Resistivity and Self Potential Methods

6.1 Acquisition

6.1.1 DC Resistivity

An ABEM SAS 4000 system was used for all surveys. When using the Wenner array (Figure 6-2), the system sequentially injected current into the ground between two electrodes (electrodes A and B in Figure 6-2) at varying offsets and positions along the array. It then measured the current passing though the subsurface between two electrodes positioned symmetrically between the injection electrodes (electrodes M and N in Figure 6-2).

When using the Dipole-Dipole array, the injection electrodes remain static, and the measurement electrodes are increasingly offset from the injection electrodes, maintaining a constant spacing between the measurement electrodes, as seen in Figure 6-3.

As seen in both Figure 6-2 and Figure 6-3, the electrode arrays sample varying midpoints and subsurface depths according to the electrode positioning and spacing. This allows construction of a 2D subsurface resistivity profile following processing and inversion of the data.

DGPS coordinates and elevations were recorded at every electrode position. Four measurement stations were missed on lines DC3 and DC4 due to cable length limitations.

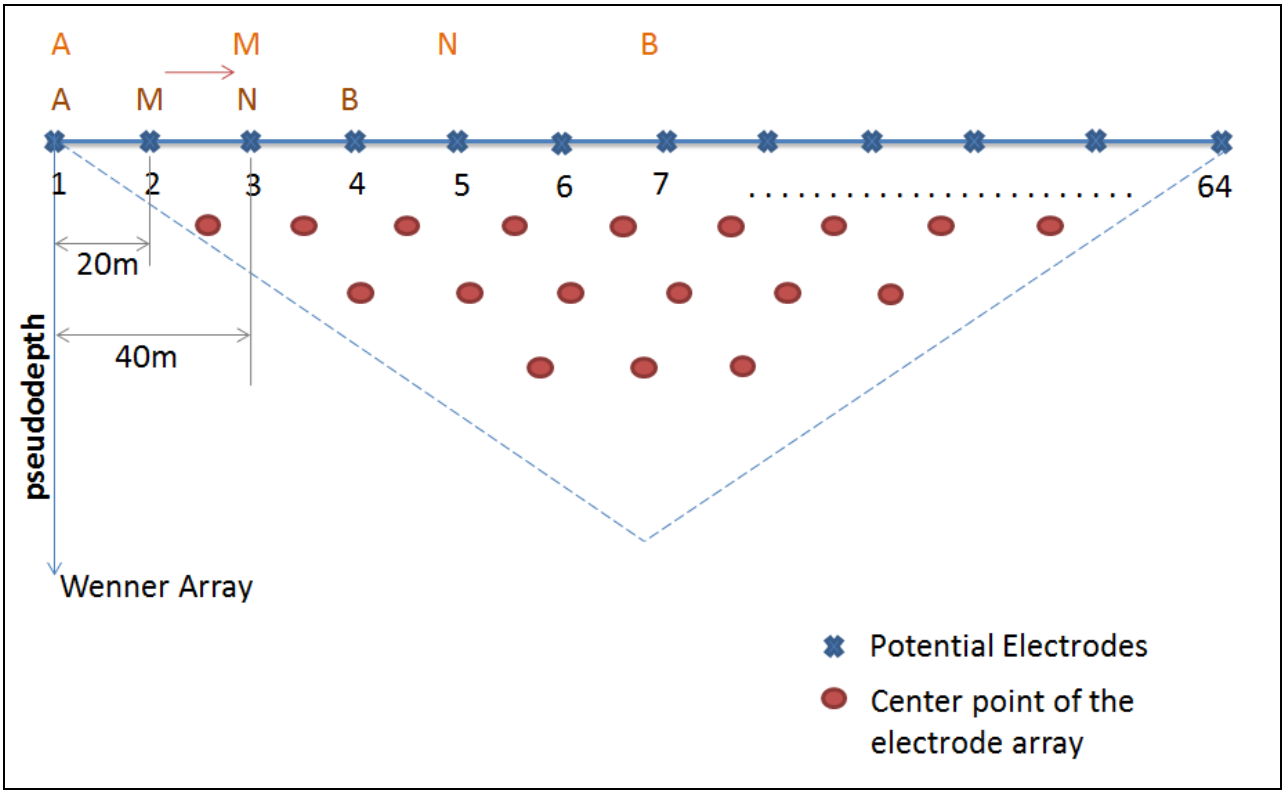

Figure 6-2 Wenner Array Acquisition Setup for Neal Hot Springs

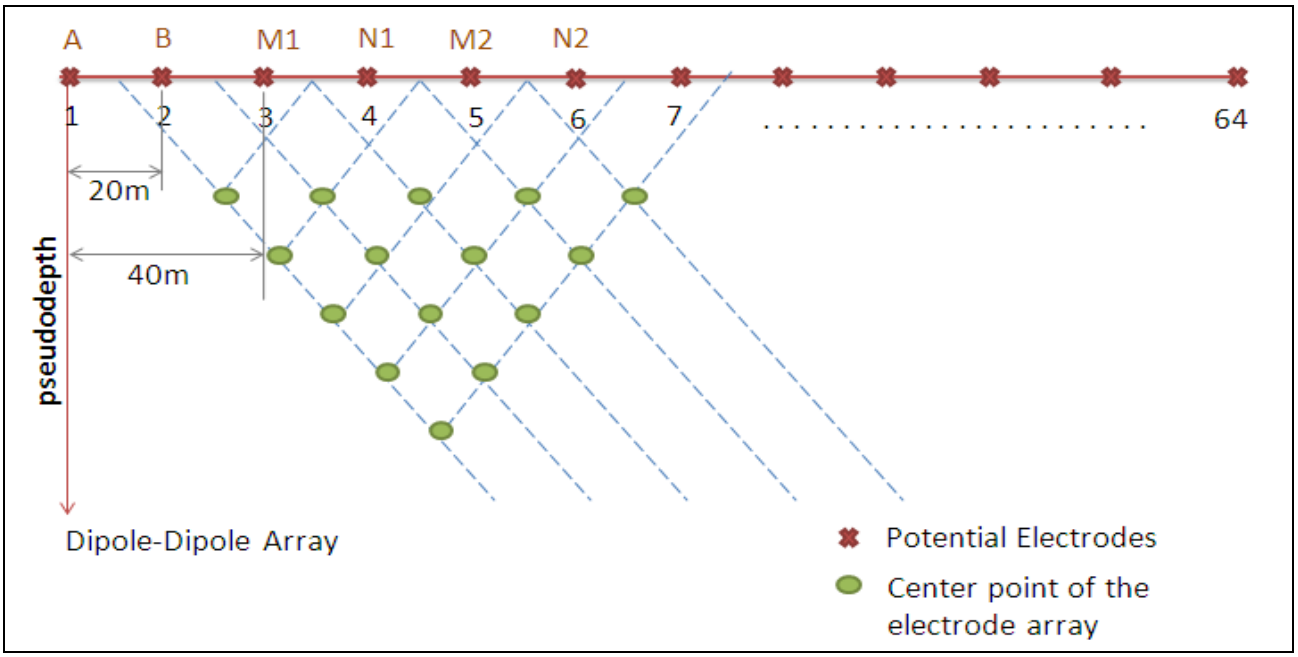

Figure 6-3 Dipole-Dipole Array Acquisition for Neal Hot Springs

6.1.2 Self Potential

Five SP profiles were obtained along the same lines as the resistivity survey; lines DC1-6 (excluding line DC5) as shown in Figure 6-1, orientated perpendicular and sub-parallel to the fault plane.

The self potential array utilized a pair of non-polarizing petiau electrodes (that do not generate their own SP effects). The electrodes are comprised of lead/lead chloride, bentonite, and a microporous extremity composed of a low-permeability wood. A high impedence millivoltmeter measured the electrical potential between the reference electrode, placed at the beginning of each profile, and the moving electrode. The moving electrode was progressively offset from the reference electrode at intervals of 20m. Where multiple reference points were used along a profile, a reference correction was made to correct for variations in the reference electrode and match points along the same SP profile. [*Barde-Cabusson, 2011*]. This reference correction process is illustrated in Figure 6-4.

The subsurface sampled by the majority of SP profiles in this area were partially saturated with river water. This is not ideal, as it increases noise levels in the data, however, it was considered that sufficient data samples were acquired to constrain the data and accurately analyze the data and model the conductivity of the subsurface.

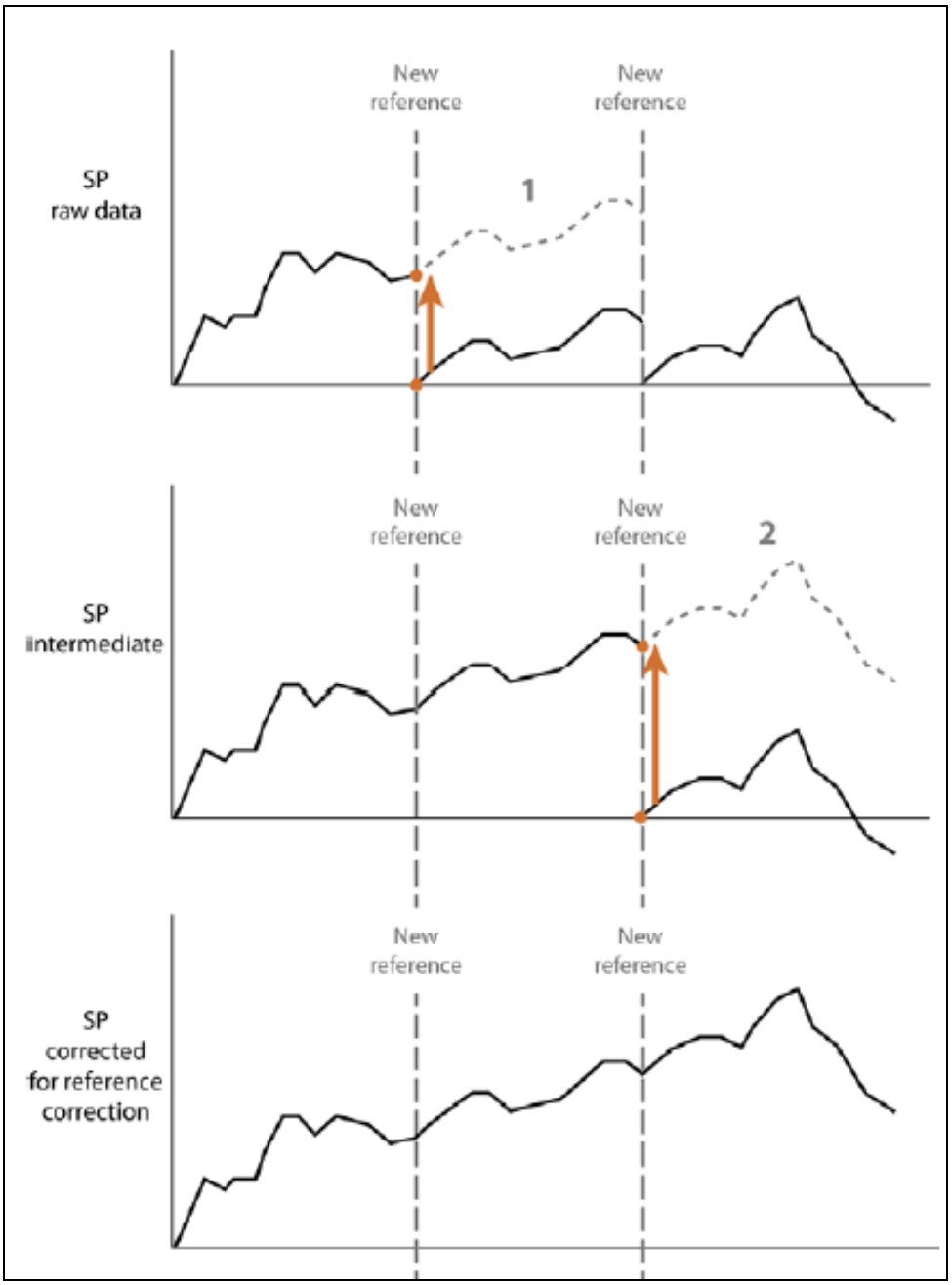

Figure 6-4 Reference Correction Done Along Profile 4 [*Barde-Cabusson, 2011*]

6.2 Processing

6.2.1 DC Resistivity

The raw resistivity data were recorded in binary format and converted to .dat format using RS23. RES2DINV was used to invert the data. The data were inverted using a least squares method algorithm and a robust inversion. The robust inversion was underdetermined and

produced an over-smoothed model of the resistivity of the subsurface along the surveyed profiles. The data were then corrected for topography across the profile by applying the surveyed station elevations to the data. Erroneous data points were eliminated. Resistivity data typically exhibit a smoothly varying profile in nature. Some inversion parameters were adjusted to insure the best results were acquired.

6.2.2 Self Potential Data

All self potential profiles were tied into the resistivity profile from survey line DC1 with tie in points on lines DC3, DC4 and DC6. Survey lines DC1 and DC2 had the same reference electrode. The data were not corrected for drift, as the measurements required for drift correction were not made on SP lines DC2, DC3 or on parts of DC4 and DC6. Where data were available, the magnitude of the correction was small enough to be considered negligible. Each profile was plotted in MS Excel with respect to distance along the profile line and the corrected self potential. The profiles were compiled, gridded and contoured in Surfer. The contour plot was generated with a Kriging interpolation, based on semi-variogram fitted to the data. See Appendix B for information on Kriging interpolation and variograms.

6.3 Results

6.3.1 Least Square Resistivity Inversion Results with Self Potential Analysis

The determination of the electrical resistivity distribution through DC tomography is useful for the quantitative study of ground water flow in geothermal areas. It gives information on the architecture of the sub surface. Self potential (SP) data will identify areas in which ground water is flowing. These two sources of information, when taken together, can help define the GEOMETRY of an existing hydrothermal system.

The inversion process was an inverse modeling procedure in which the apparent resistivity values were converted into resistivity tomogram that could be used for geological interpretation. A number of parameters were varied to produce the best possible result. Inversions, using three and five iterations, were performed on the data gathered during the acquisition process at Neal Hot Springs. Least square inversion (L2 norm) was used throughout [*Locke, 2011*]. The RMS error was a key measurement in determining the acceptability of an inversion result. The range of acceptable values on the inversions was taken as 0-15% (except for profile 5). The change in layer thickness parameter was kept at 10%. A minimum value was placed on the damping parameter at 0.015 in order to avoid instability in the model. A reference model was not utilized in the inversion process.

Data points corresponding to systematic and random noise were removed prior to running to the inversions. Table 6-2 states the parameter values used in each inversion. In the following analysis interpretations are made on what the vertical and lateral discontinuities, evident in the profiles, pertain to.

Table 6-2 Parameter Values

Profile	Damping Factor	Constraint	No. of Iterations	RMS error (%)
1	0.02-0.22	Standard	5	10.76
2	0.03-0.22	Standard	5	6.36
3	0.15-0.16	Standard	5	10.27
4	0.03-0.02	Standard	4	9.0
5	0.08-0.3	Standard	6	23.9
6	0.015-0.16	Standard	5	9.1

Results of Line DC1

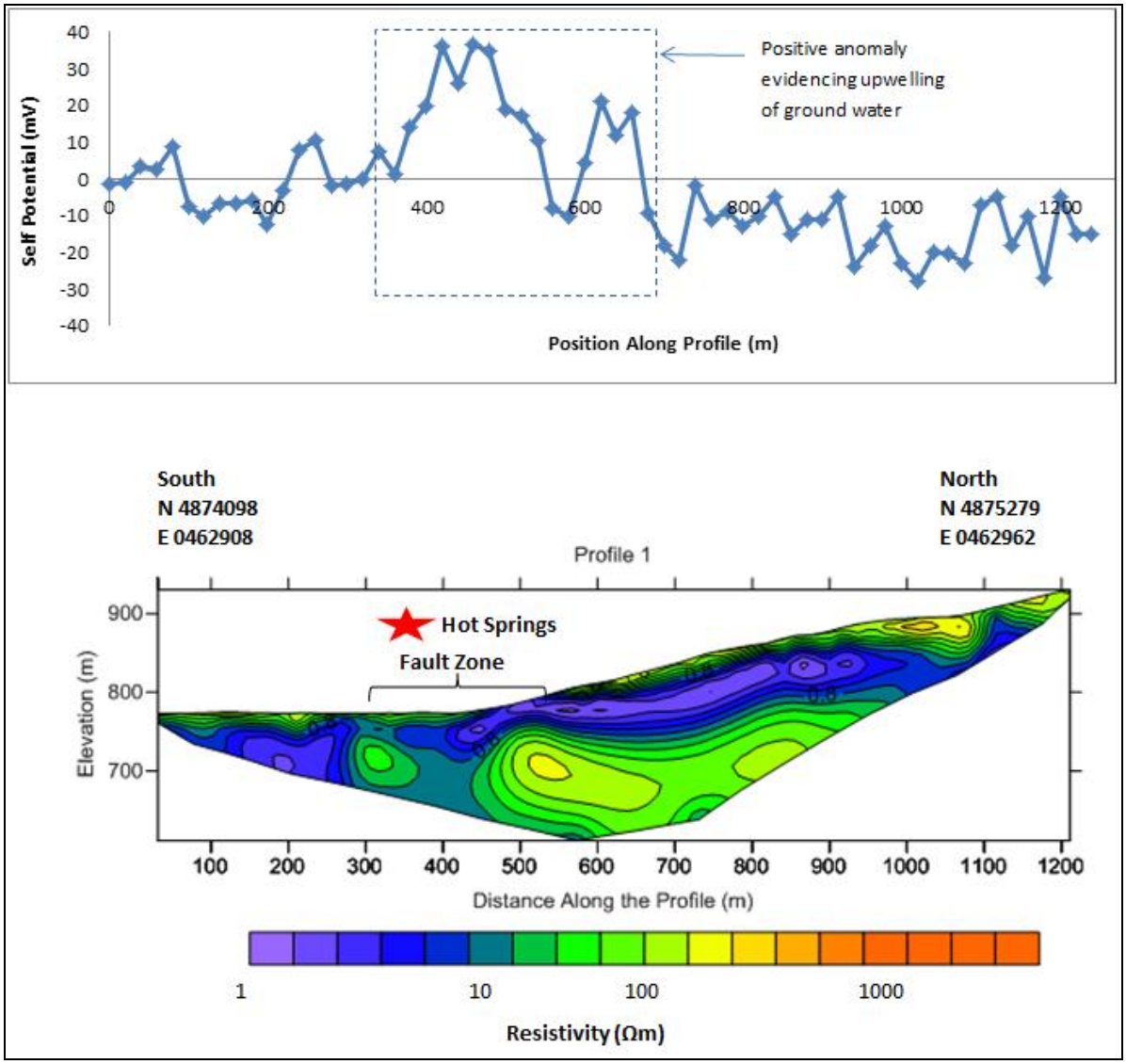

Figure 6-5 DC1 SP Results (Top) and DC Resistivity Results (Bottom)

Observations of Figure 6-5:

- Layer of low resistivity evident in near surface between 350m and 1050m
- Underlying layer of higher resistivity between 450m and 950m
- No clear evidence of fault
- Main maximum positive SP anomaly at 400–500m. This main peak coincides with the location of the Hot Springs
- Negative SP anomaly at approx. 600m and 700m respectively

Results of Line DC2

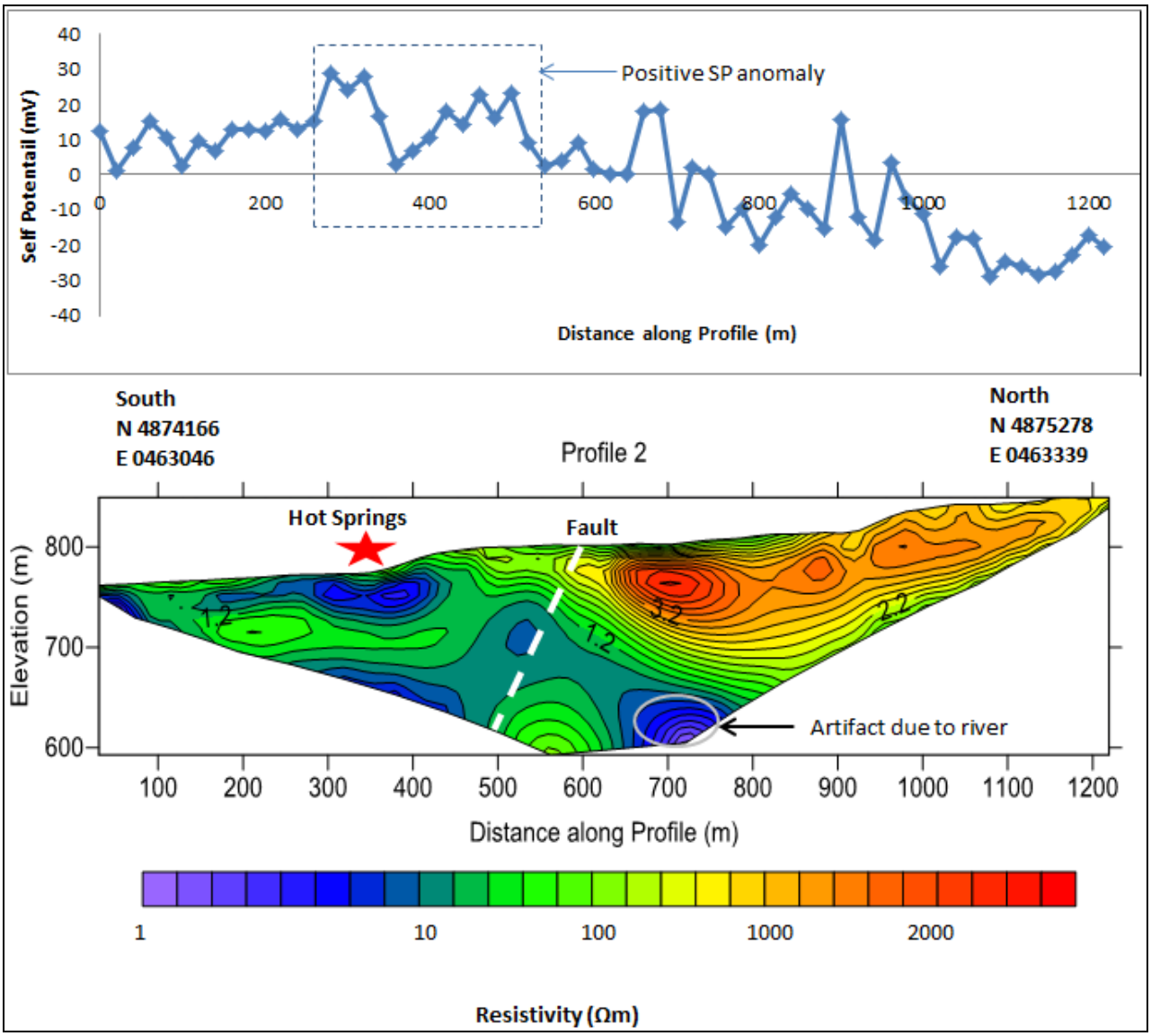

Figure 6-6 DC2 SP Results (Top) and DC Resistivity Results (Below)

Observations of Figure 6-6:

- Higher resistivity revealed in area East of profile 1 beyond 700m
- There is a clear change from low to high resistivity from west to east across the profile
- Maximum SP peak of 30 mV located at approximately 300m. This coincides directly with a low resistivity region and the location of the hot springs.

Results of Line DC3

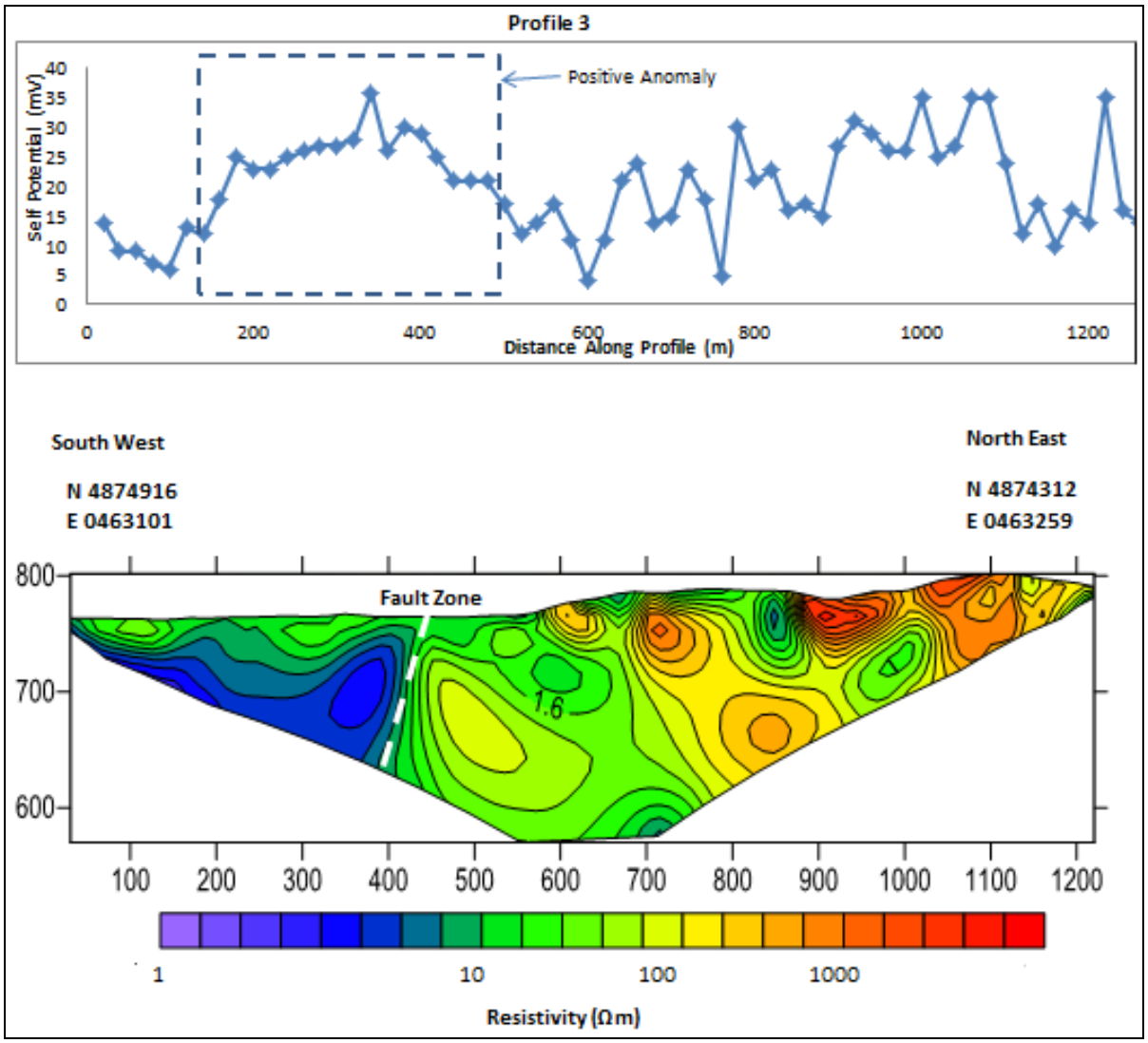

Figure 6-7 DC3 SP Results (Top) and DC Resistivity Results (Bottom)

Observations of Figure 6-7:

- At 400m there is a clear vertical discontinuity in resistivity.
- Resistivity generally increases along the profile. There is variable near surface resistivity in the later part of the profile.
- Further North along the profile there is another distinct discontinuity in resistivity, moving from a region of lower to higher resistivity

Results of Line DC4

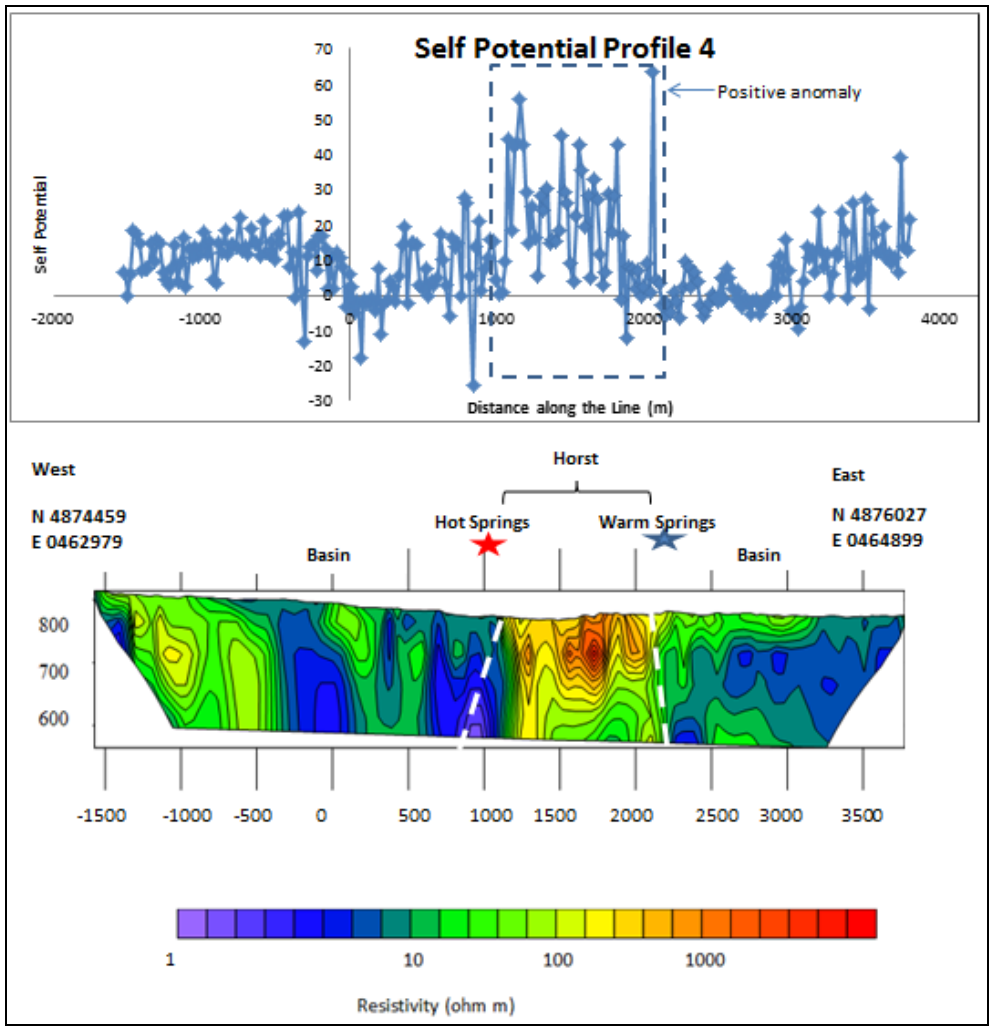

Figure 6-8 DC4 SP Results (Top) and DC Resistivity Results (Bottom) (-1500m from each electrode spacing to get the value to fit the res2D profile)

Observations of Figure 6-8:

- The hot springs was located at 463077/4874585 and the Warm Spring at 463918/4875636, to the west and east of the horst-like structure respectively
- Large positive SP anomaly associated with the highly resistive horst like structure bounded by possible faults
- To the west of the profile the resistivity was fairly high
- Further along the profile, to the far East, the resistivity decreases

Results of Line DC5

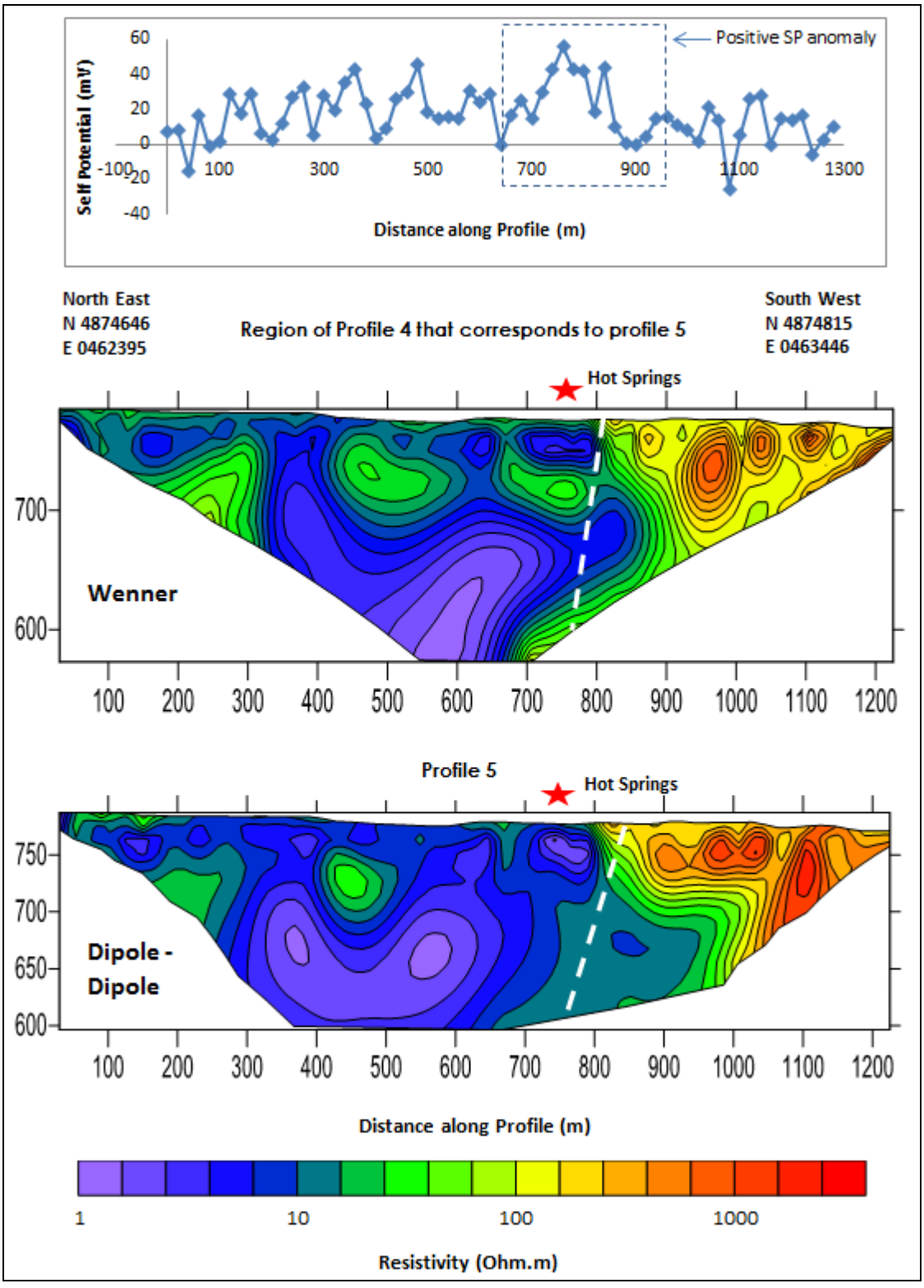

Figure 6-9 Profile 5 Resistivity (top) and SP (below) results

Observations of Figure 6-9:

- The Wenner and Dipole-Dipole arrays produce very similar results (with a distinct change in resistivity at 450 m) indicating that a change in the acquisition configuration does not drastically affect the result.
- However, there appears to be more structure in the Wenner array than in the Dipole-Dipole array.
- At deeper depths, the Wenner array showed much lower resistivity than the Dipole-Dipole configuration

Results of Line DC6

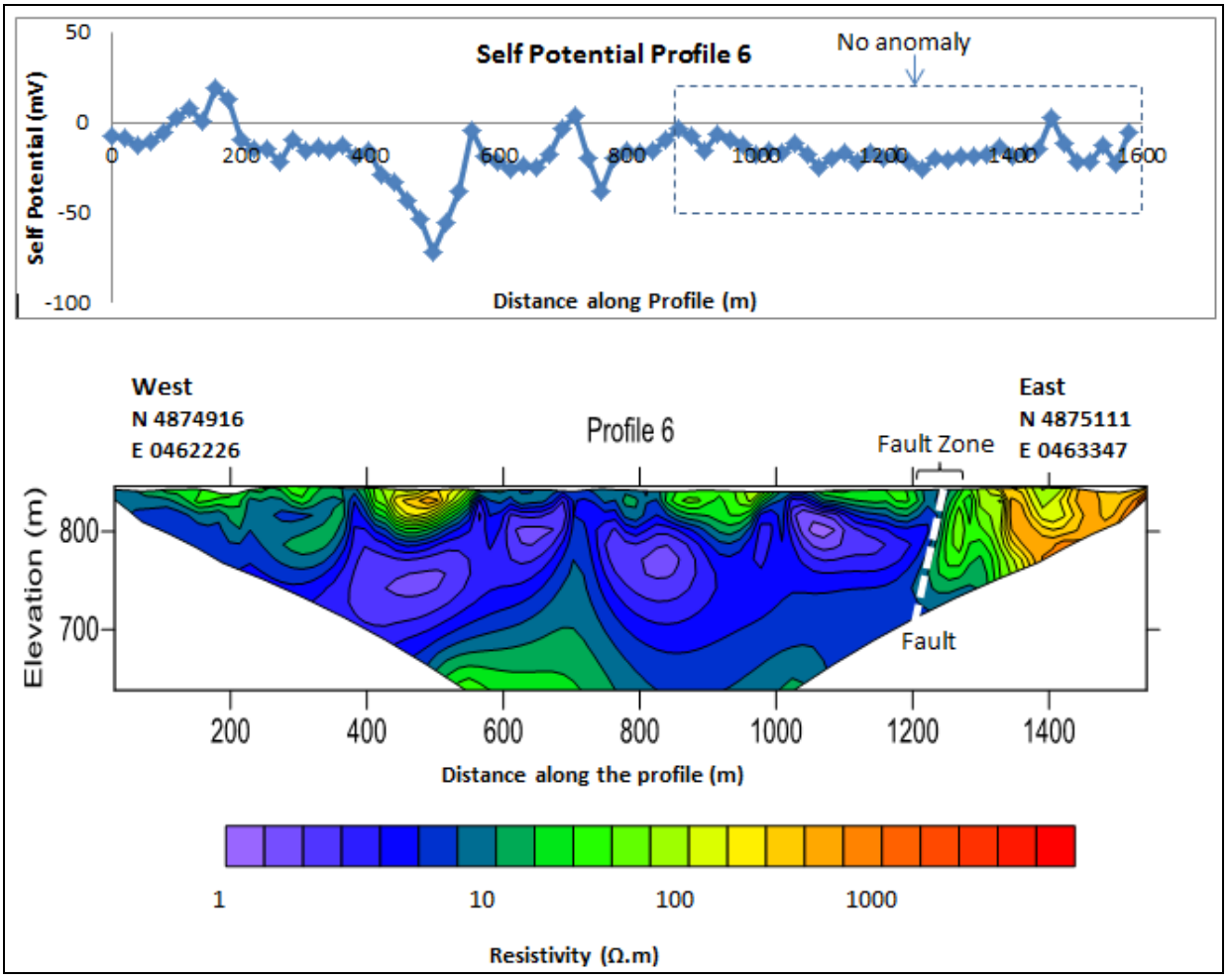

Figure 6-10 Profile 6 Resistivity (top) and SP (below) results

Observations of Figure 6-10:

- Thick layer of low resistivity along center of profile, generally negative anomaly along the profile
- There are four points of distinctly low resistivity on the profile that coincide with negative spikes in the SP plot
- From 1300m onwards there is an area of higher resistivity
- From 800m onwards the profile is flat. Localized artifact at approximately 450-500m

6.3.2 Resistivity Sections and SP Graphical Interpretations

In line DC1 there is a highly conductive layer near the surface. Varying hypotheses were generated to explain the shallow conductive zone (between 350m and 1050m) detected along this line (Figure 6-5). A plume of conductive material may have infiltrated the unconsolidated material. It should be noted that this profile was in close proximity to the river which may possibly have an influence on the resistivity measurements. The anomaly could also be due to an area of different sediment type; a contact between the overlying sediments and underlying volcanic rocks is illustrated. DC1 was thus interpreted to lie almost parallel to the fault which serves as the contact between the sediments and volcanic rocks. Saturated sediment could also account for the conductive anomaly. The more saturated the rock, the more conductive the shallow zone. The maximum penetration depth of the resistivity measurements is directly proportional to the length of cable and inversely proportional to the subsurface conductivity [*Powers, 2007*]. Thus, the conductive zone is only limited to the uppermost 60m of the resistivity section in DC1.

A maximum positive anomaly at 400m coincided directly with the hot springs on DC1 and the SP anomaly corresponds to ground water flow. Generally in this area, the positive anomalies relate to upwelling water and the negative anomalies relate to areas of ground water recharge. The self-potential, resistivity and temperature data collected along DC1 were combined to help in delineating the orientation of the profile relative to the location of the

fault boundary, which marks the contact between volcanic and sedimentary rocks. Figure 6-11 shows this delineation.

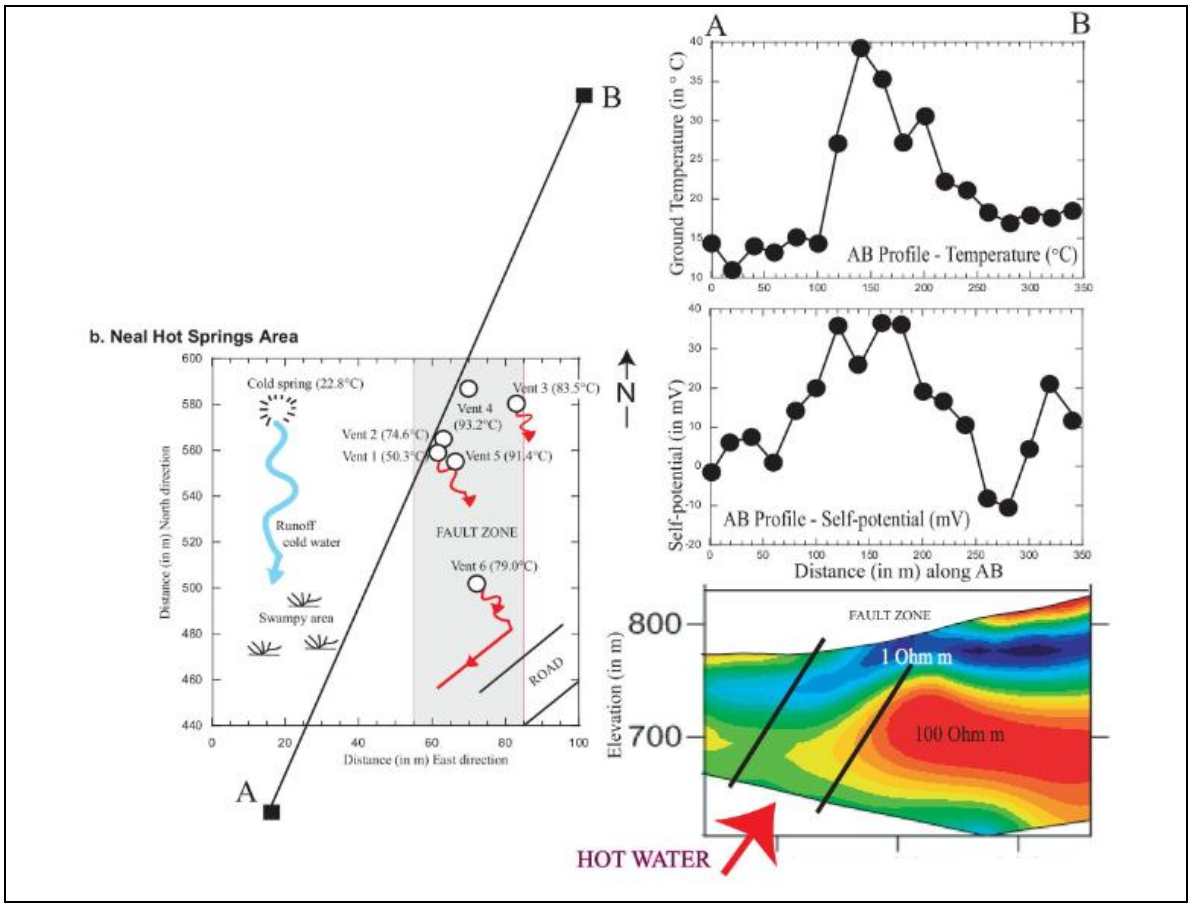

Figure 6-11 Temperature, Self Potential, and Resistivity of a Section of Profile DC1

The fault zone is less apparent in DC1 due to the orientation, because DC1 is not only parallel to the orientation of the fault but also lies on the fault boundary, However, there are some traces of the fault zone apparent in the resistivity profile. The self potential shows that there is an upwelling of water in this region, which further indicates that the fault zone is in the vicinity. The temperatures were measured at 30 cm depth and were between 30-40^{0}C in the area over the self potential anomaly, and therefore over the fault zone. This upwelling of hot water and the associated SP and resistivity anomalies indicate that there are hot fluids upwelling in the fault zone at Neal Hot Springs.

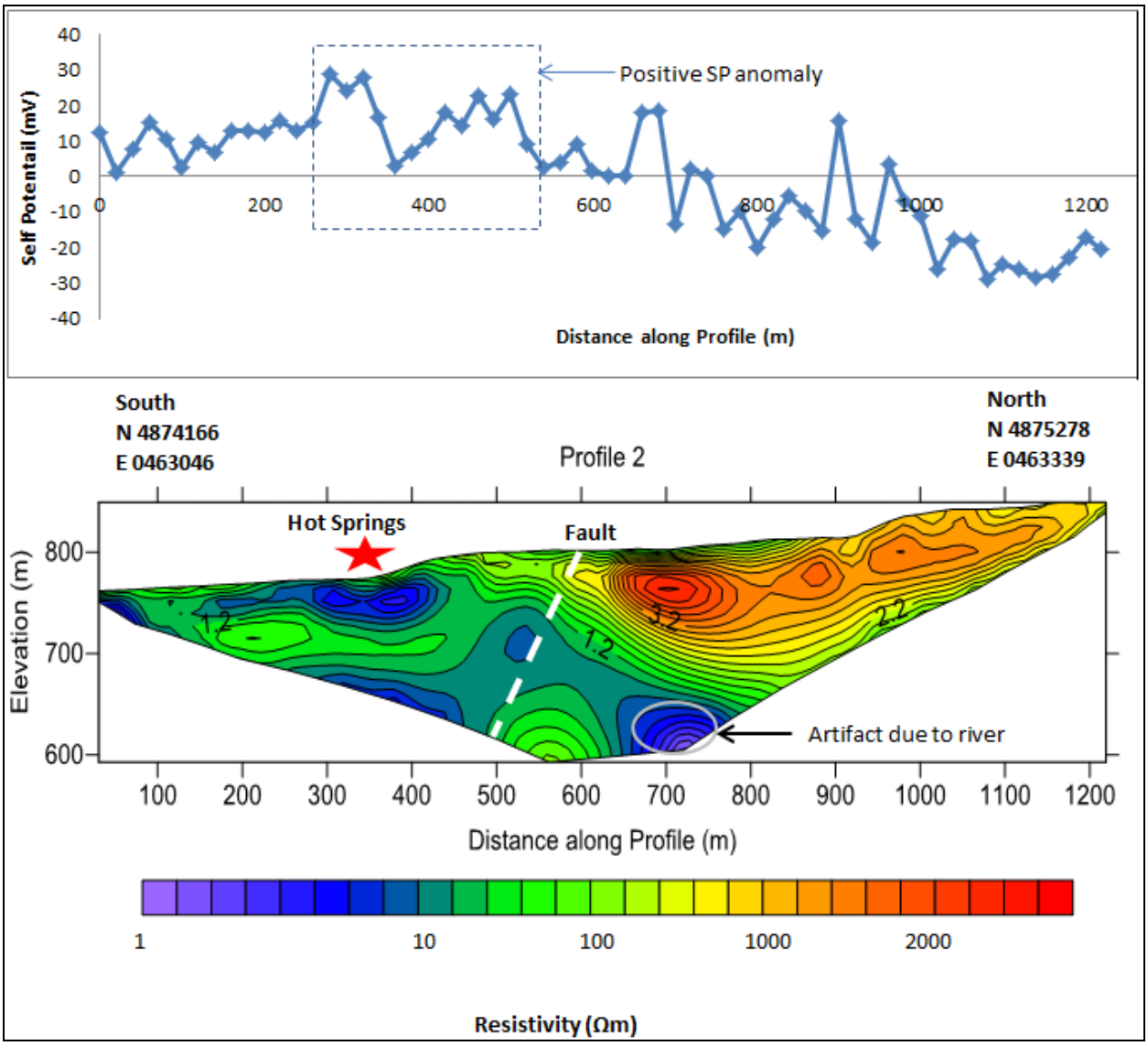

Figure 6-12 Results of DC2

A maximum positive anomaly at 300m also coincided directly with the hot springs on profile DC2 (Figure 6-12). During the resistivity data acquisition, the presence of this river may have led to part of the current flowing into the river resulting in the lower part of the resistivity section, in profile DC2, to be more conductive than usually expected. The orientation of the contact between the more resistive and less resistive rocks on DC2 (Figure 6-12) appears to be in a NW-SE direction. However, after combining all the datasets and analyzing them with the geological interpretation, it was deduced that the orientation of this contact is trending in a fairly N-S direction.

The orientation of DC3 is perpendicular to the fault. This profile best illustrates the structures and contacts evident in the area. On the Southwest part of DC3, there is a large area of low resistivity due to the presence of water in the study area. This correlates with the maximum SP anomaly in this region (Figure 6-13). The general increase in resistivity towards the north along DC3 is due to the presence of volcanic material. However, possible micro-faults may have broken up the volcanic material to the east causing fluctuations in the resistivity data. This fluctuation was also observed on the graphical representation of the SP data. The most distinct change in resistivity was observed at ~400m and this marks the location of a fault. The presence of this fault was confirmed by combining the results of the TEM, resistivity, and self-potential surveys along DC3.

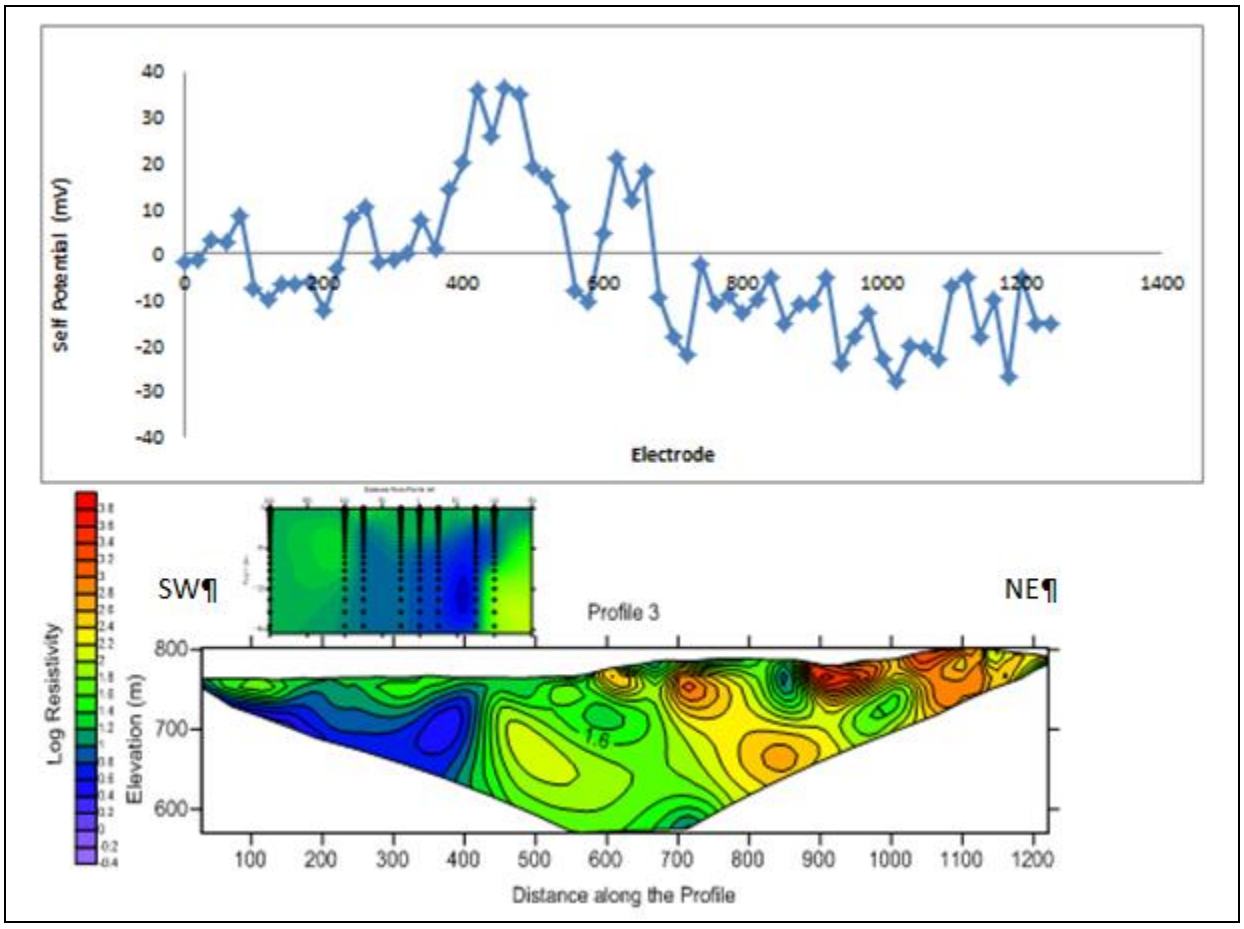

Figure 6-13 The TEM, Resistivity, and Self Potential along a Section of DC3. The TEM profile is converted to resistivity and adheres to the same color scale as the resistivity profile

The time domain survey intersects the third resistivity and self-potential profiles directly over the region believed to correspond to the fault (Figure 6-13). In the TEM survey, there is a highly conductive body at the end of the profile. This body is believed to correspond to the movement of water. The high conductivity zone in the TEM data aligns with the fault location in the resistivity data. This region is also associated with a positive self-potential anomaly, indicating the upward flow of water. The three surveys solidify the location of the fault and the presence of upwelling water.

The longest of all the profiles acquired, DC4, was taken along line DS10. This profile was ~5.5km long and two clear discontinuities in the resistivity reveal a horst-like structure that is made up of volcanic material surrounded by sedimentary material. The high resistivity area - the horst structure - is attributable to the upwelling of water from the subsurface while the low resistivity area is attributable to the recharge of water in the surrounding sediments. Subsequently, the high resistivity area corresponds to a region of a large positive SP anomaly while the low resistivity area corresponds to the slightly negative SP anomaly (Figure 6-8). This horst-like structure is interpreted to be bounded by a fault to the west (just west of Neal Hot Springs) and a fault to the east (just east of the Warm Spring), marked by distinct changes in the resistivity. This is corroborated by the distinctly higher SP values at these locations and over the horst area (Figure 6-8). To the west of the profile the resistivity was fairly high due to the presence of volcanic rock outcropping. Also, further east along the profile the resistivity decreases due to the presence of water reservoir rock associated with the nearby damn.

A comparison between the Wenner and Dipole-Dipole array was taken along the road (DC5 and a section of DC4). A clear difference in the resistivity at depth between the Dipole-Dipole and Wenner arrays can be explained by the weak signal strength at depth with the Dipole-Dipole array. The raw data from the Dipole-Dipole array was noisy when compared to the Wenner array, but after processing and the removal of bad data points, a clearer picture was able to be seen. The profile runs east along the road near Neal Hot Springs, with increasing proximity to the hot springs as distance along the profile increases. The data shows that the

proximity of the hot springs produces low resistivity results and this is explained by the high conductivity of the water.

DC6 indicated some negative SP anomalies associated with the high resistivity region (Figure 6-10). The localized high resistivity body located between 450-500m is possibly a spurious volcanic lava flow. An area of localized fresh water flow could also produce a high resistivity result. Further investigation would be required to define the source of this anomaly. A contact is clearly seen to the east of the profile, likely between volcanic rocks and sediments. At 800m, flat self-potential trend is seen; this corresponds to a region of no flow, thus the fault is sealed to the north by silica precipitation.

6.3.3 SP Map Interpretation

Self potential mapping is used to identify fluid flow pathways and the location of structures. All measurements from DC1-6 were used to generate a semi variogram. The variogram characterizes the spatial continuity or roughness of a data set. The variogram analysis consists of the experimental variogram calculated from the data and the model is then fitted to the data. The experimental variogram is calculated by averaging one half the differences squared of the SP values over all pairs of observation with the specified separation distance and direction. This was plotted as a two dimensional graph as shown in Figure 6-14. Different mathematical functions were tested to fit the variogram model with the data. In this case the Spherical function gave the best results and this was used to draw the self potential map using Kriging based on the fit of the semi-variogram (Figure 6-14). The faults, which lead to the horst-graben structures in the area, act as the dominant flow path leading to the upwelling of thermal waters. This is indicated by the self potential measurements which gave an estimate of the flux of upwelling thermal water.

Observations:

To the south of the study area, a positive SP anomaly is observed with a clear upwelling trend along the fault zone (Figure 6-15). SP anomalies ranged from ~5 to 35 mV. At the hot springs, the SP anomaly is almost flat ~0 to 10mV. To the north, the SP response decreases; ~-5 to -55 mV. Overall, the conductivity at Neal Hot Springs was relatively high (~0.1 s/m).

Interpretation:

It is postulated that the decrease in SP anomalies to the north is due to possible sealing of the fault. At the faults, a clear positive SP anomaly is observed. Upwelling of water occurs along the fault plane. Pressure build up within fractures can lead to cracking and subsequent increase in permeability along the fault. However, since the water is silica rich, precipitation of silica within the fractures and subsequent blockage of the faults may result to the north. Breccias were found to be associated with the fault plane.

A distinct and confined negative anomaly was observed to the northwest. Different interpretations were postulated for this effect – ground water recharge, and the effect of the rock properties in the area being the main two hypotheses. The resistivity and SP anomalies used in collaboration indicated that this negative anomaly can be due to the properties of the surrounding rocks in that region.

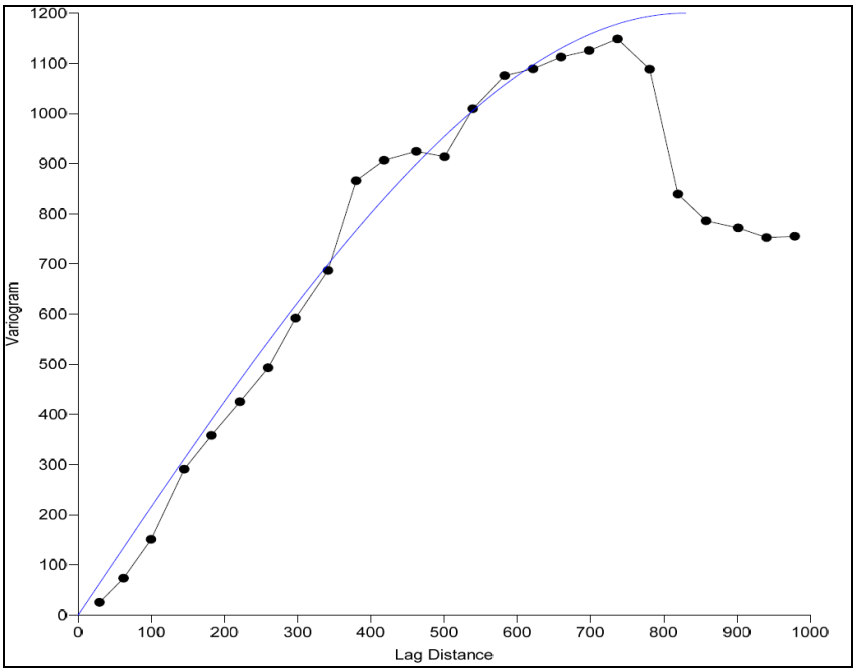

Figure 6-14 Best Fit Semi-variogram Which was Used to Create the SP Map Using Kriging

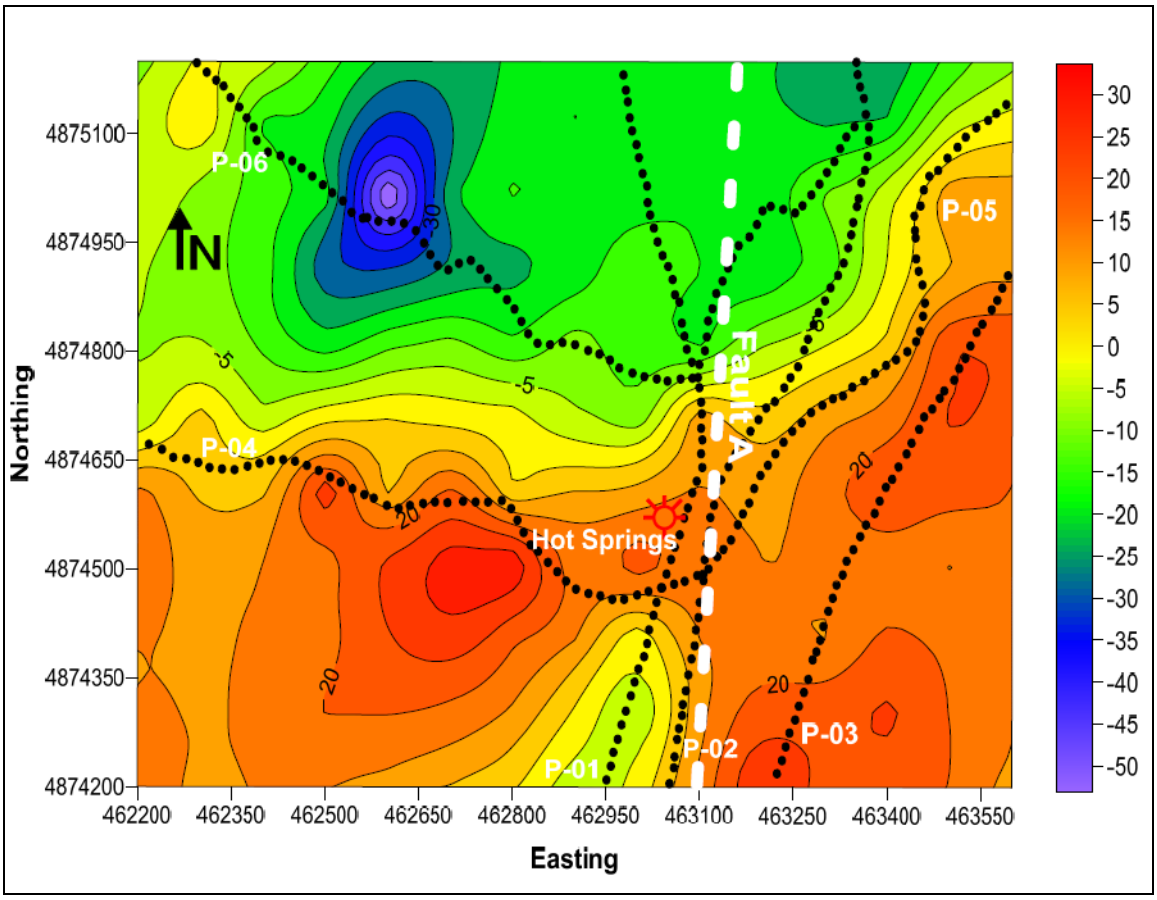

Figure 6-15 Self Potential (SP) Map of the Area of Investigation in mV

6.3.4 Resistivity Map Interpretation

Resistivity mapping is also used to identify fluid flow pathways and the location of structures. A semi-variogram (Figure 6-16), which best fits the data, was used to produce a resistivity map at a depth of 50m. A distinct change in the resistivity marked the boundary fault A, which bounded the horst structure.

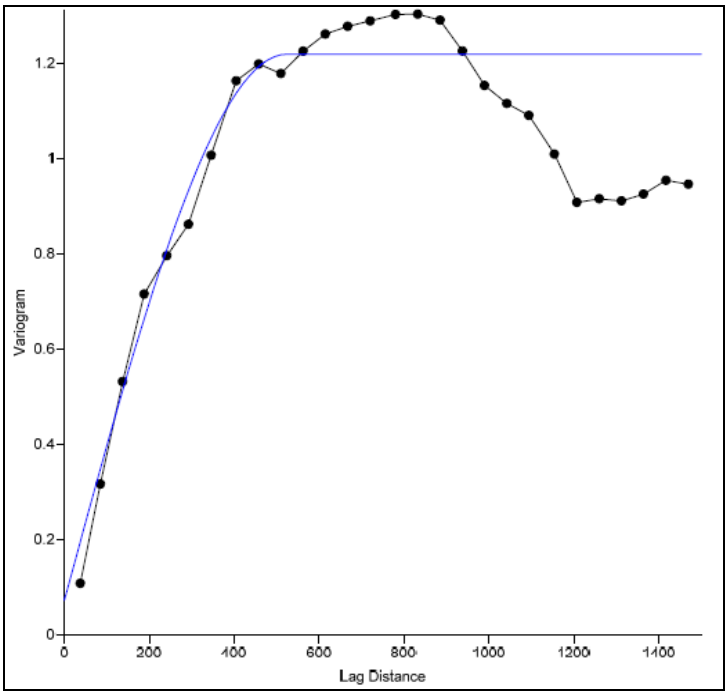

Figure 6-16 Best Fit Semi-variogram Which was Used to Create the Resistivity Map Using Kriging at 50m

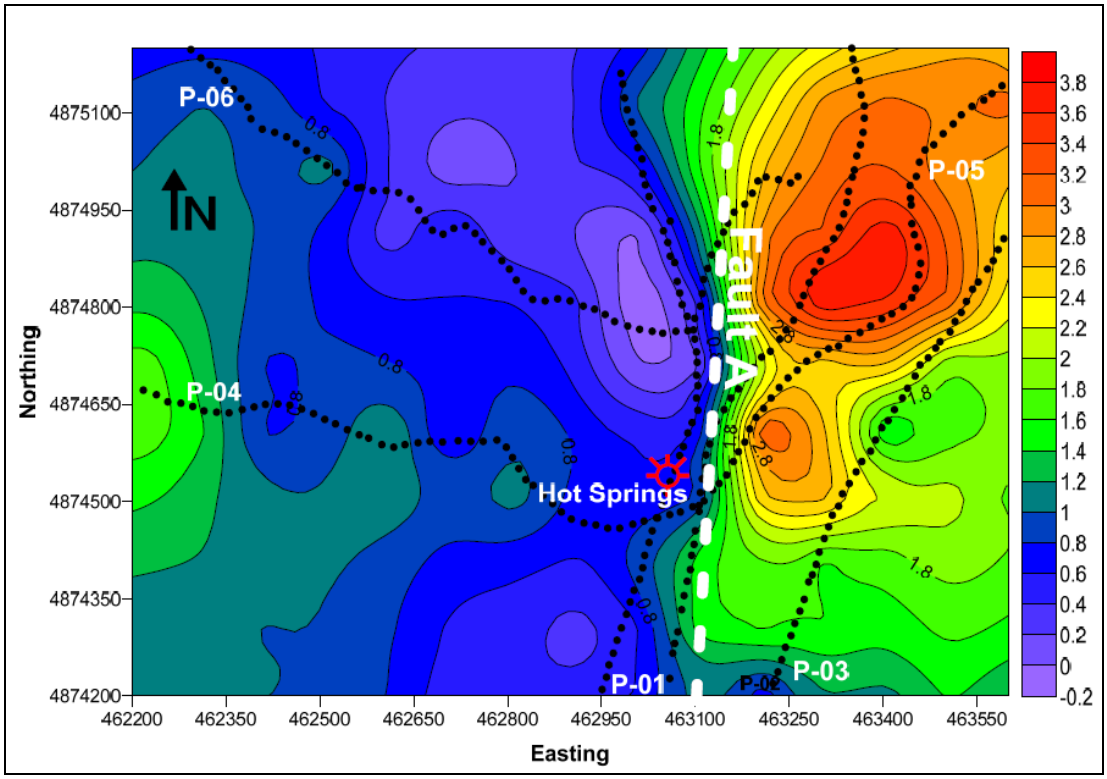

Figure 6-17 Resistivity Map at a Depth of 50m

Interpretation

The map in Figure 6-17 reveals the fault that has been postulated to exist in the area. The diagram indicates that the fault runs to at least 50m depth. To the West is low resistivity material, and to the east are higher resistivity materials. The former are assumed to be wet, sedimentary rocks and the latter are assumed dry volcanic rocks. The major fault that was postulated to exist in the area is revealed. The trend is clearly north-south.

6.3.5 3D Model Interpretation

Method

The resistivity, UTM coordinates, and depth of the layer from each profile was compiled into a single Excel spread sheet. MATLAB code was provided by Marios Karaoulis to create a 3D interpretation of the resistivity data. The Excel file was uploaded into MATLAB and the color bar was altered to best fit the resistivity values found. The results can be viewed in Figure 6-18.

Result

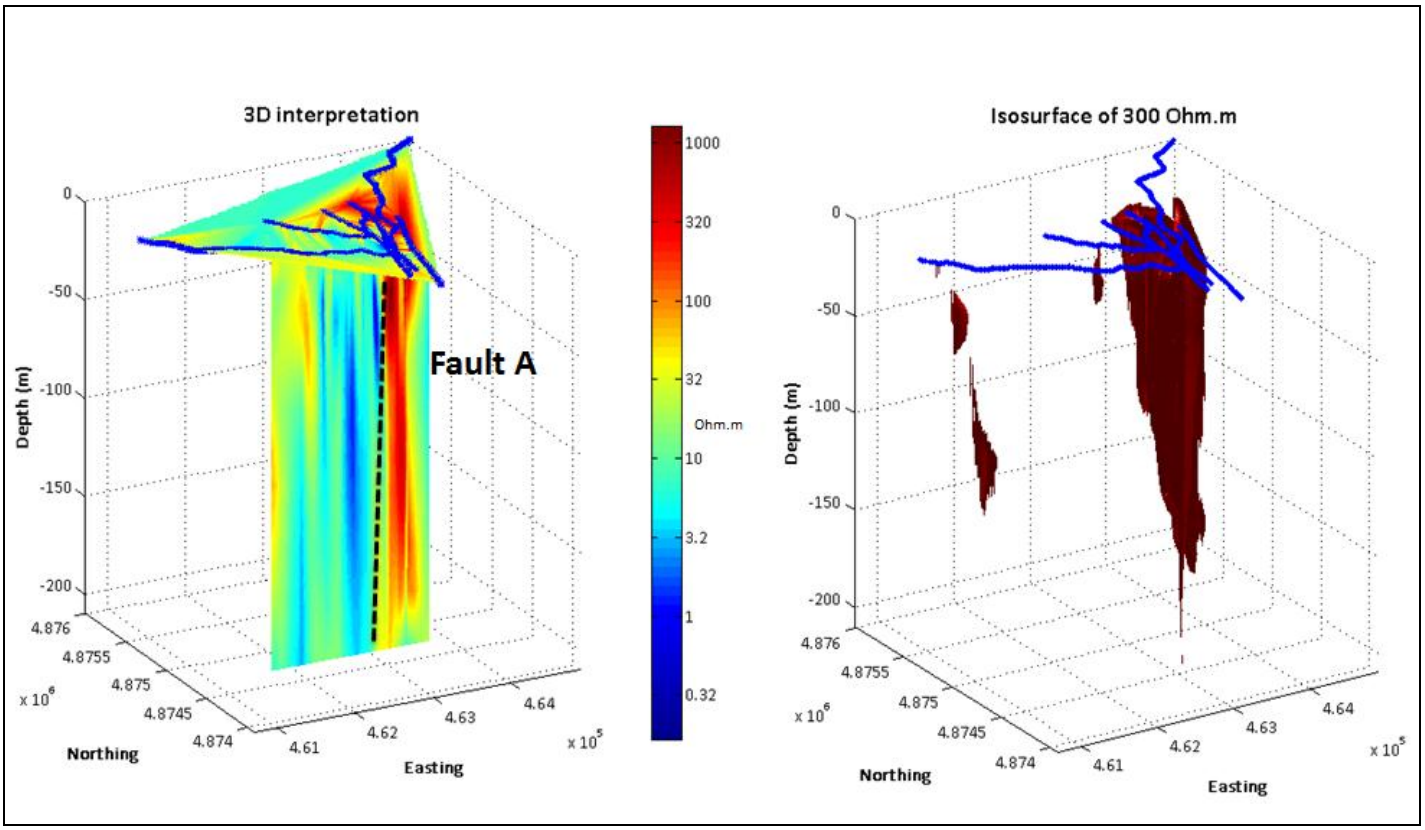

Figure 6-18 3D Resistivity Model with 300 Ohm.m Isosurface Displayed

Interpretation

The fault is delineated in this model by high resistivity values (~300 Ohm.m) corresponding to volcanic material and reveals it to have a near vertical orientation. In the immediate vicinity west of the fault there is material with resistivity values of 5-10 Ohm.m. This is the sedimentary material. Adjacent to this is a streak of lower resistivity material (<1 Ohm.m) starting from 20-30m below the surface and extending to beyond 100m depth. This possibly represents warm and porous sediments along a smaller fault that does not outcrop at the surface. The fault has acted as a conduit for the flow of water.

To the east of the major fault, on the other side of the horst, there is potentially a further large fault. The two larger faults taken together would describe a horst structure. However, this hypothesis is not conclusive due to the lack of available data east of the identified major fault. Thus the presence of a horst structure is merely a suggestion here that requires further investigation in order to be substantiated.

The red anomaly in the 3D model is displayed as an isosurface. It corresponds to material with resistivity values of 300 Ohm.m. The western edge of this defines the fault location. The vertical extent of the fault cannot be distinguished due to the limited amount of data available. It is suggested that further surveys with a greater number of electrodes, and thus a greater depth of penetration, be used to analyze the trend of the fault deeper in the subsurface. The geological observations made in the project indicate that the fault may be listric.

6.4 Recommendations

Following the analysis of the SP/DC data, a few recommendations are appropriate. Extending the profiles will give more data east of the hypothesized horst structure, thus enabling further definition of the structural geology. Achieving deeper penetration will help define where the fault tilts towards production Well 8. This could be done via surveying using a greater number of electrodes or carrying out a seismic survey in the area across the fault and the well.

7. Deep Seismic Data

7.1 Acquisition

Three deep seismic lines were acquired between the 20th and 25th of May: lines DS10, DS20 and DS30. These are summarized in Table 7-1 below.

Table 7-1 Deep Seismic Survey Lines

Line I.D.	Shot Direction	Date Acquired	No. receiver stations	No. shot stations	Receiver station no.s	Shot station no.s	Line Length
10	W-E	05/20/11-05/23/11	406	403 (shots 1-415)	1001:1406	1004:1406	12km
20	S-N	05/24/11-05/25/11	201	82 (shots 1-82)	2000:2200	2122:2203	6km
30	N-S	05/25/11	137	41 (Shots 83:123)	2000:2136	2122:2202/2	4km

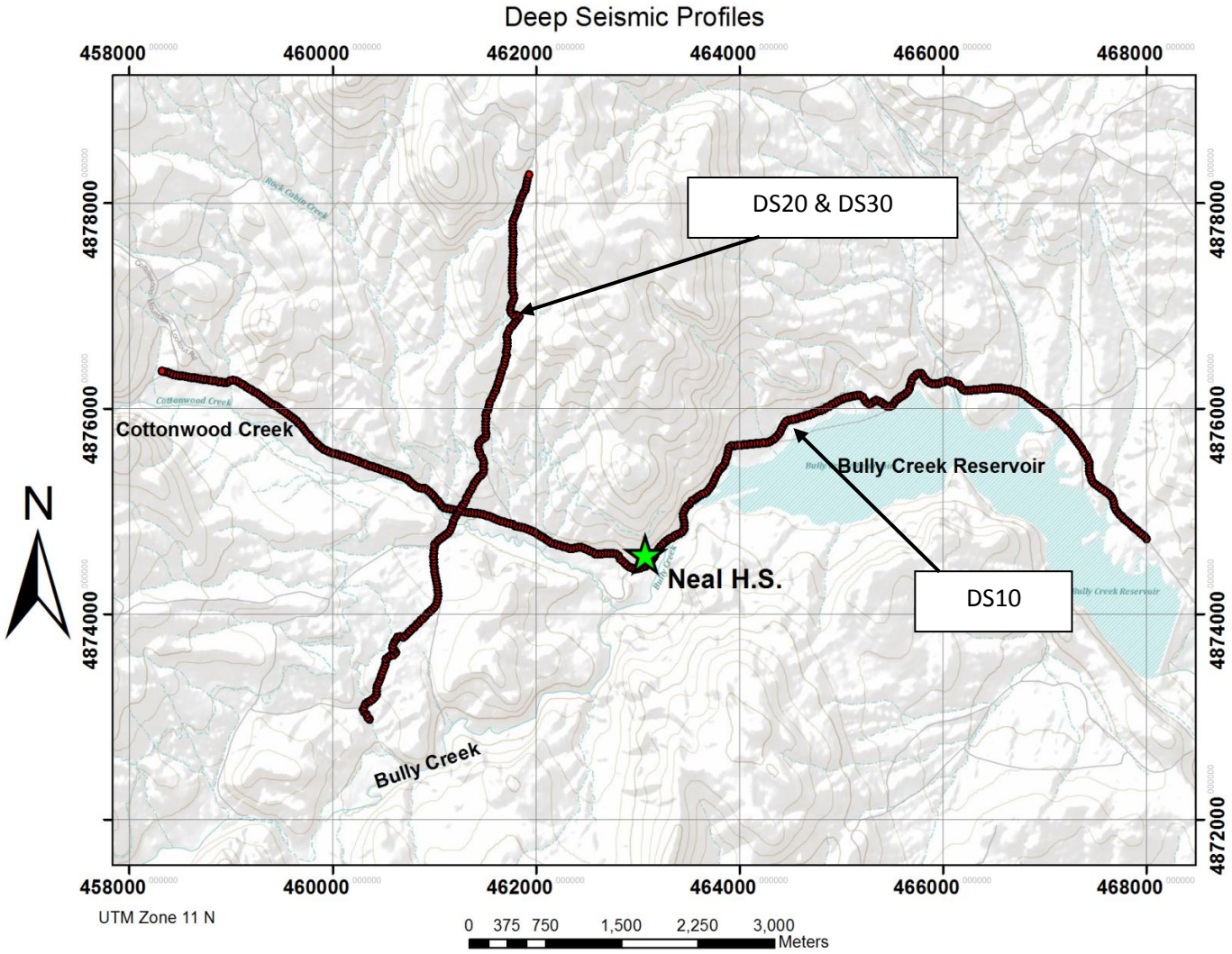

Figure 7-1 Seismic Survey Lines at Neal Hot Springs

Line 10 was orientated East-West and was approximately 9780m long. An end-on, double offset rollalong survey was implemented using Vibroseis trucks. The rear Vibroseis was a distance of 3 channels (90m) from the first recording channel and the lead Vibroseis was a distance of 80 channels (2400m) in front of the last recording channel. Figure 7-2 demonstrates this acquisition process. The acquisition parameters for DS10 are summarized in Table 7-2.

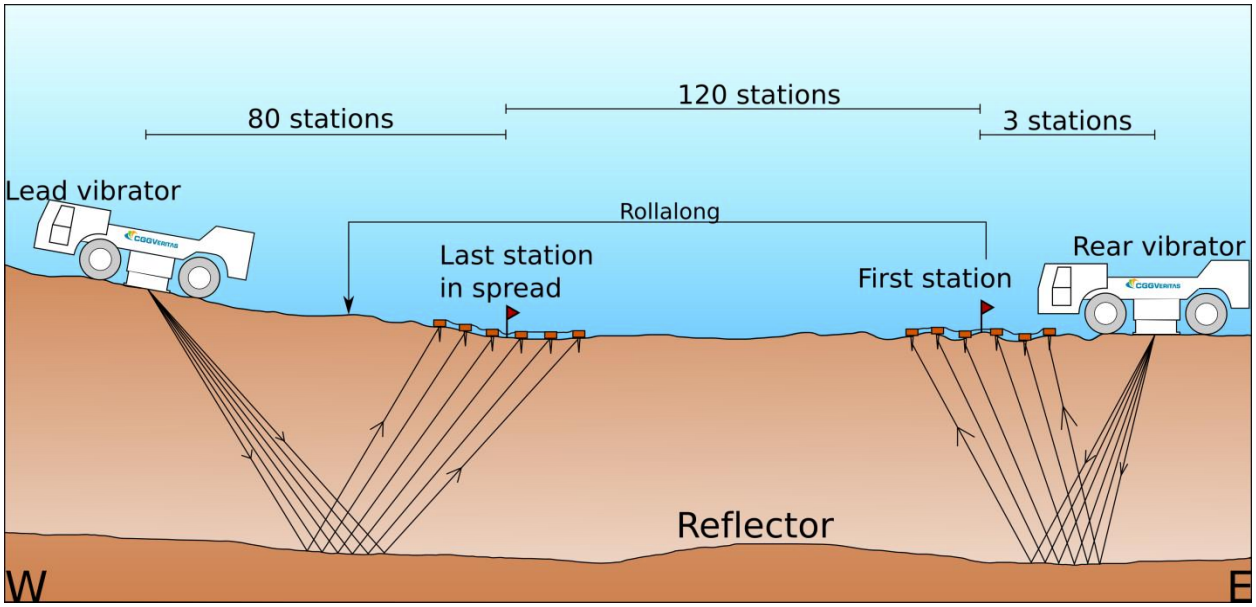

Figure 7-2 Acquisition Diagram for DS10. Represents a rollalong double offset survey with two Vibroseis trucks putting energy into the ground one after another.

Table 7-2 Deep Seismic Survey Parameters for Line 10

Shot interval	30m
Group interval	30m
Group composition	6 geophones, 5m interval
Spread	120 active groups + 30 inactive groups
Acquisition	End on, roll over spread
Min./max offset	90m/2400m
Fold	60

DS20 and DS30 were along the same array, approximately perpendicular to DS10. Figure 7-3 illustrated the Vibroseis acquisition for DS20 and DS30. DS20 was acquired South-North and DS30 North-South.

A single source, end-on, rollalong methodology was used to acquire DS20, with two Vibroseis trucks vibrating simultaneously approximately 20m apart, centered on the shot point. Shot points and receiver stations were at 30m intervals, and the receiver spread was rolled over between shots, the shot point remaining 90m offset from the end of the spread. The acquisition parameters for Line 20 are summarized in Table 7-3.

A dual source walkaway technique was used to acquire DS30. DS30 employed a static receiver spread with receiver stations at intervals of 30m. Shots were made at increasing offset from the receiver spread at intervals of 60m. The acquisition parameters for DS30 are summarized in Table 7-4.

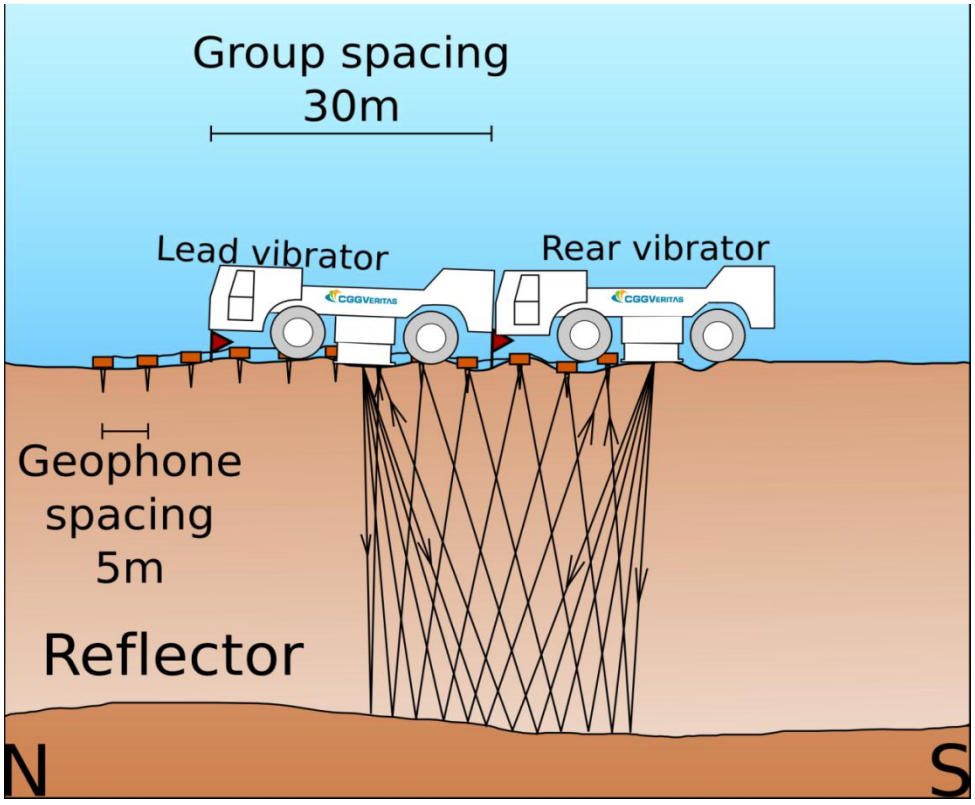

Figure 7-3 Acquisition Diagram for Lines 20 and 30 in a N-S and S-N Orientation

Table 7-3 Deep Seismic Survey Parameters for Line 20

Shot interval	30m
Group interval	30m
Group composition	6 geophones, 5m interval
Spread	120 active groups + 30 inactive groups
Acquisition	End on, roll over spread
Min./max offset	90m/3690m
Fold	60

Table 7-4 Deep Seismic Survey Parameters for Line 30

Shot interval	60m (alternate stations)
Group interval	30m
Group composition	6 geophones, 5m interval
Spread	137 active groups
Acquisition	Static spread, increasing source offset
Min./max offset	0m/6060m
Fold	Variable

A total of 120 channels were recorded for each shot point, except Line DS30 where 137 channels were recorded per shot point. Shot points and receiver stations were spaced at 30m intervals. Each receiver group was comprised of 6 geophones at a spacing of 5m. The same source type, geophone types, topside recorder and recording software were used for all lines as indicated in Table 7-5 below. The sweep and record parameters were the same for each line, shown in Table 7-6 below.

Table 7-5 Deep Seismic Survey Equipment

Source Type	Vibroseis
Receiver type	Geophone
Recording Software	Sercel SN428
Recorded Data Format	SEGD

Table 7-6 Sweep and Record Parameters

Sweep Length	10s
Sweep frequency	8-80Hz, upsweep
Record	6000ms
Sample interval	2ms
Sweep stack	5-15 sweeps (dependent on data quality)
Noise threshold	5%

The data were sampled at 2ms with a Nyquist frequency (f_N) of 250Hz. The use of geophones in stacked groups of six attenuated noise. The group array design, with stations at 30m intervals, was designed to attenuate ground roll in the data; the wavelength of the ground roll is approximately 30m (as the dominant source frequency is close to 40Hz and the velocity of the immediate subsurface is averaged at 1200m/s). As the group interval is 30m, the frequency of the ground roll falls at the spatial Nyquist frequency, and is aliased as DC noise (with a frequency of 0Hz). An anti-alias filter was also applied to remove high frequency noise. Further steps were taken during processing to improve the signal to noise ratio.

Data quality issues were encountered in acquisition, largely attributed to high amplitude, ongoing noise adjacent to the survey lines. In particular, channels 1280 to 1324 on DS10 did not record a shot point due to a construction site next to the survey at those channels. Shot points were also missed on DS20 due to drilling (of geothermal well bores) being carried out at two sites in close proximity to the survey line.

Other issues included time constraints; due to the necessary completion of survey activities on the 25th of May 2011, the shot point interval of DS30 was increased from 30m to 60m, reducing the effective fold on the line. Shot points were also missed DS10 due a malfunction of one the Vibroseis vibrators on the 22nd of May 2011.

7.2 Processing

Seismic processing suppresses noise contaminating the recorded data, improves the signal to noise ratio and ultimately migrates the observed reflections to the accurate position of the causative reflector. The final image is intended to accurately image the 2D subsurface structure. Further information with respect to rock properties and vertical and lateral subsurface variation can be derived on the basis of the estimated rock velocities and reflectivity.

The processing flow applied to the data acquired at Neal Hot Springs is summarized in Figure 7-4. The processing steps completed at the time of reporting include: filtering, amplitude recovery, velocity analysis, statics correction, deconvolution, and application of NMO corrections and stacking. A brute stack for line DS10 has been produced; it is intended that the data undergo further, iterative processing stages in order to attenuate noise and improve the resolution and accuracy of the image. It is also intended that lines DS20 and DS30 be similarly processed.

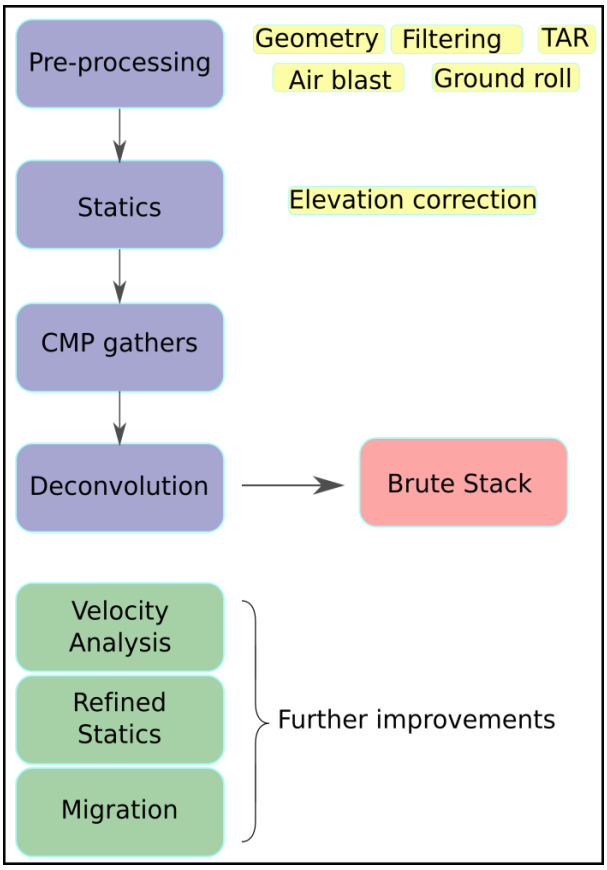

8

Figure 7-4 Summary of Deep Seismic Processing Flow

7.2.1 Issues with Land Processing

Processing of land seismic data carries additional issues to those encountered in marine data processing. There are frequently more sources of high amplitude, broad frequency noise, which require careful attention during processing. Noise can be coherent or incoherent, with random noise being uncorrelated between traces, and varying spatially and temporally. Coherent noise has some predictable behavior, such as periodicity, and includes multiples and refractions.

Ground roll and air waves, in particular, are sources of noise to be addressed in land seismic data processing. Ground roll is a shear wave that propagates along the air-Earth interface. Ground roll is low frequency and has a relatively low group velocity. As discussed in Section 7.1, the geophone array was designed to attenuate ground roll. However, this array filter is imperfect, and ground roll required further attenuation during processing. The air wave was low velocity and was also addressed by filters during processing.

Source and geophone coupling was a major issue in the data acquired at Neal Hot Springs due to the variable nature of the topsoil in which the geophones were planted, the inexperience of the survey team, and the variable terrain over which data were acquired. Poor coupling may be due to excessive tilt on the planted geophones, stiff topsoil preventing optimum planting of the geophone, or a poorly consolidated surface dispersing energy exerted by the Vibroseis. Poor source coupling degrades the amplitude and bandwidth of the source signal. Poor geophone coupling degrades the amplitude of the recorded signal.

Application of accurate geometry is crucial so that the data, and consequently interpretation, location is known. The geometry of land surveys is frequently complicated compared to marine surveys, the end-on array of which can be referenced to the vessel position. When processing the Neal Hot Springs data, the survey geometry was modeled as a crooked line for the purposes of calculating CMP positions. Modeling the survey array as a crooked line required a position for every shot and receiver station to be surveyed. The model takes into account the angular relationships between the shots and their receivers, and is more accurate than assuming the shot and receiver stations fall on a straight line.

7.2.2 Pre Processing

7.2.2.1 Geometry

The raw data were recorded in the SEGD file format, useful for acquisition over large arrays. The data were converted to SEGY format in Seismic Unix, useful for data exchange.

The field observation logs were used to match the live receiver arrays and associated recorded traces to the relevant shot points, review issues that occurred in the field, and match the shot and receiver stations to the surveyed DGPS positions. A geographical position, including longitude, latitude and elevation, was assigned to each shot point and receiver. This geometry was applied to the data in Promax 2D.

7.2.2.2 Filtering

The data were imported into Promax 2D, where the seismic processing was carried out. The data were zero phase, as the autocorrelation of the recorded data

with the known Vibroseis sweep reduces the source signature to a zero phase spike. This autocorrelation is carried out in the field as the data is recorded. This is the diversity stack, which contains the stacked sweeps carried out at each shot point.

A zero phase Butterworth band pass filter was applied to the seismic data, as described in Table 7-7.

Table 7-7 Butterworth Bandpass Filter Parameters

Bandpass Filter	
Type of Filter	Single Filter
Type of Filter Specifications	Butterworth Bandpass
Phase of Filter	Zero
Percent zero padding for FFT's	25
Apply a Notch Filter	Yes
Notch Filter Frequency	60
Width of Notch Filter	4
Automatic Notch Frequency Search	Yes
Maximum Notch Frequency Variation	4
Butterworth Filter (freq-slope) Values	5-12-50-60
Re-apply trace mute after filter	Yes

Electrical noise was observed in the data at a frequency of approximately 60HZ, as seen in Figure 7-4. A notch filter, with a 4 Hz target bandwidth between 58 and 62 Hz was applied to remove this noise. Tests showed that wider filters produced greater noise attenuation at the required frequency notch than narrower filters.

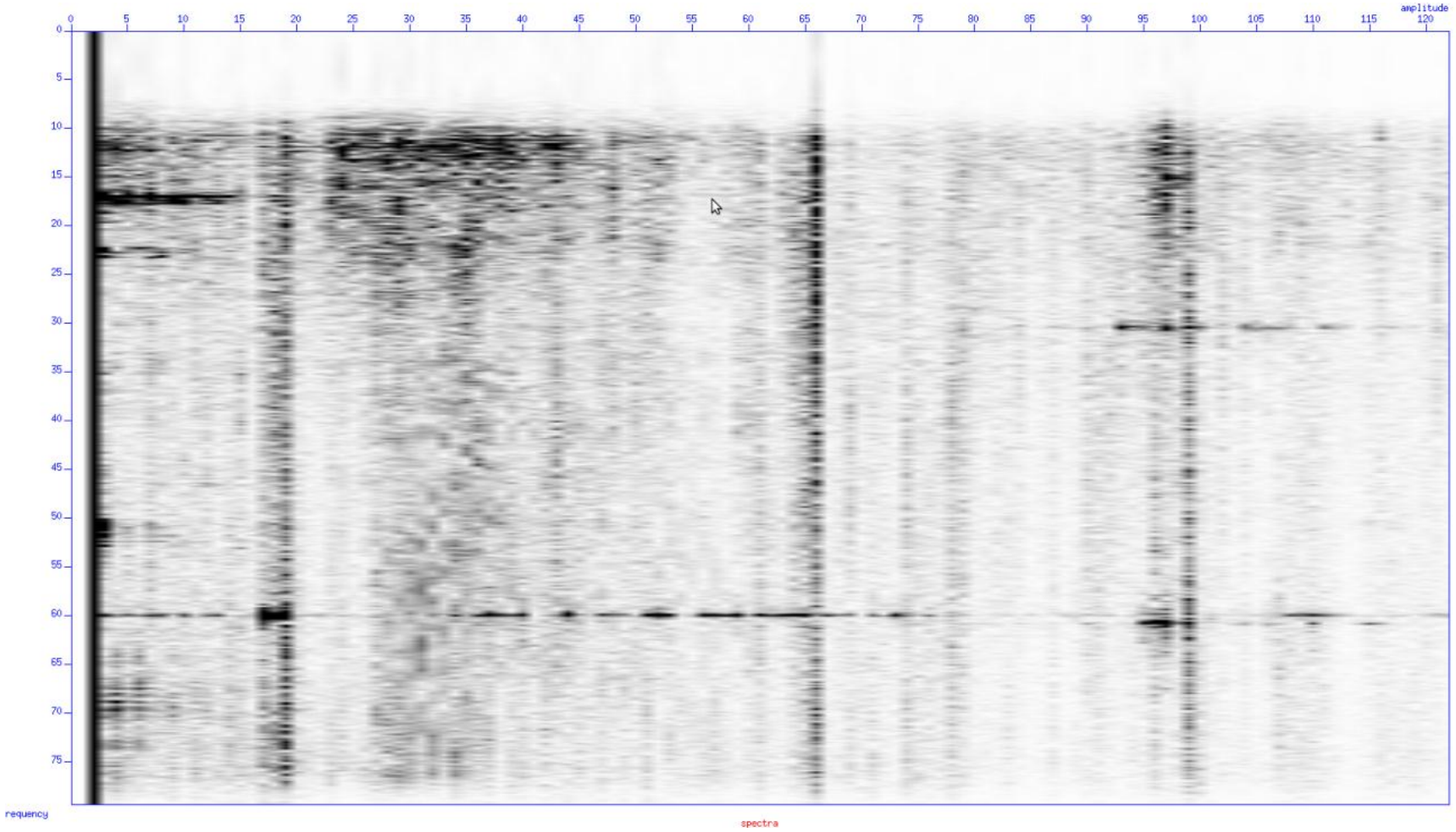

Figure 7-5 Noise Present in the Data at 60 Hz due to the Power Line Cable

7.2.2.3 True Amplitude Recovery

True amplitude recovery is intended to remove the decay of signal amplitude with increased travel time due to spherical divergence or inelastic attenuation. A single time-variant gain function was applied. The time variance of the gain function applied was described as a dB/s curve rather than a power of time curve. This function applied a constant scalar correction that amplified traces as a function of travel time. The parameters applied, shown in Table 7-8, were found to be optimal for balancing the amplitudes of the deep and shallow reflections.

Tests found that greater scalar correction constants resulted in greater enhancement of amplitudes at deeper zones relative to amplitudes of shallower zones, particularly observed in the comparison of a section processed with a 4 dB/sec constant to that with a 6 dB/s constant. A constant of 6dB/s over-amplified amplitudes of deeper reflections; 4dB produced a more balanced section.

Table 7-8 True Amplitude Recovery Parameters

True Amplitude Recovery	
Apply dB/sec Correction	Yes
dB/sec Correction Constant	2
Apply time raised to a power correction	No
Apply Function to Data	Apply
Maximum Application Time	0
Normalization Reference time	0

7.2.2.4 Air Wave Attenuation

The air wave is a direct wave travelling in the air between the source and receiver. It contains no subsurface information and is regarded as noise. The air wave is observed in the shot gathers as high amplitude noise with a velocity of 330m/s, as seen in Figure 7-6. This was muted by an automated Air Blast Attenuation operator. This operator weakens the amplitudes of “anomalous energy” in each input trace on the basis of three primary parameters: pilot velocity, noise amplitude threshold, and energy envelope width, seen in Table 7-9. Signal falling out with these parameters is unaffected by the operator, as seen in Figure 7-6. The filter parameters

applied to the data, including the frequencies defining the targeted boxcar bandwidth, are shown in Table 7-9.

Table 7-9 Air Blast Attenuation Operator Pararmeters

Air Blast Attenuation	
Approximate Velocity of Energy to be Attenuated	330
Start time (ms) at Zero Offset	0
Type of Energy Attenuation	Muting
Automatically Search/Detect Noise	Yes
Maximum Air Blast Energy Envelope Width	500
Filter to Apply to Enhance Air Blast Energy	35,50,70,80
Percentage to Expand Picked Air Blast Energy Envelopes	50
Minimum Detected Air Blast Energy Envelope Length	10
Air Blast Picking Amplitudes Ratio Threshold	2

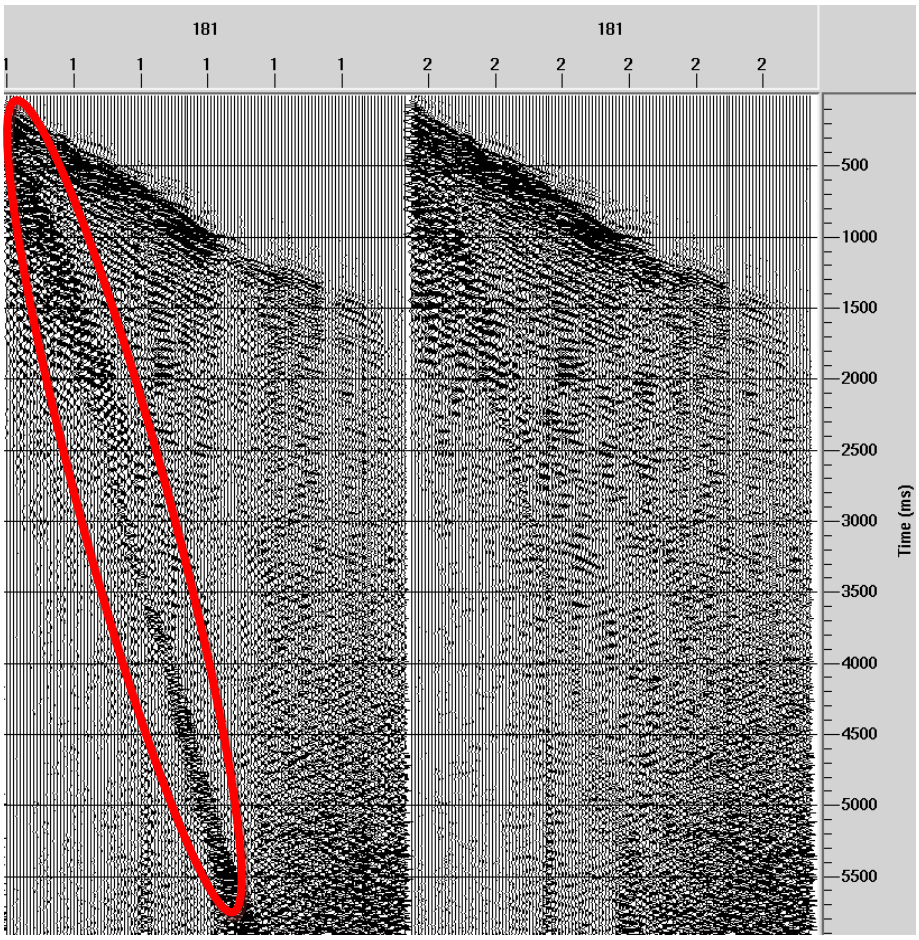

Figure 7-6 Example of the air blast, the dark straight line highlighted in red on the left panel, and how the record looks after attenuation on the right panel.

7.2.2.5 Surface Wave Noise Attenuation

The surface waves, or ground roll, generally have high amplitudes and low velocities. This was filtered from the Neal Hot Springs data by low frequency filtering in the frequency domain, based upon velocity and frequency of the noise. Frequencies and velocities of the selected cut-off values, seen in Table 7-10, were unaffected by this operator. The filter parameters applied, including the target velocity (identified by the across-trace dip of the noise), are shown in Table 7-10.

Table 7-10 Surface Wave Filter Parameters

Surface Wave Noise Attenuation	
Velocity	800
Trace Spacing	30
Low Frequency (Hz)	5
High Frequency (Hz)	25
Blend Width (Hz)	50
Set Trace Mix Limit	No

7.2.3 Static Corrections

Static corrections were applied to correct for the effects of topography and the near surface on seismic p-wave travel time. Static corrections are a highly important step in the processing of land data and were applied iteratively to maximize the accuracy of the corrections. Without static corrections, the data would not optimally stack and the final image of the subsurface would be skewed. Static corrections are frequently applied in 3 stages; field statics, refraction statics, and residual statics, in order of increasing precision.

Static corrections apply a bulk time shift to each trace based upon the position and elevation at which they were recorded relative to a particular datum. At this stage, the Neal Hot Springs data were processed with only field and refraction statics. Figure 7-7 shows a schematic of the ray paths demonstrating the importance of static corrections.

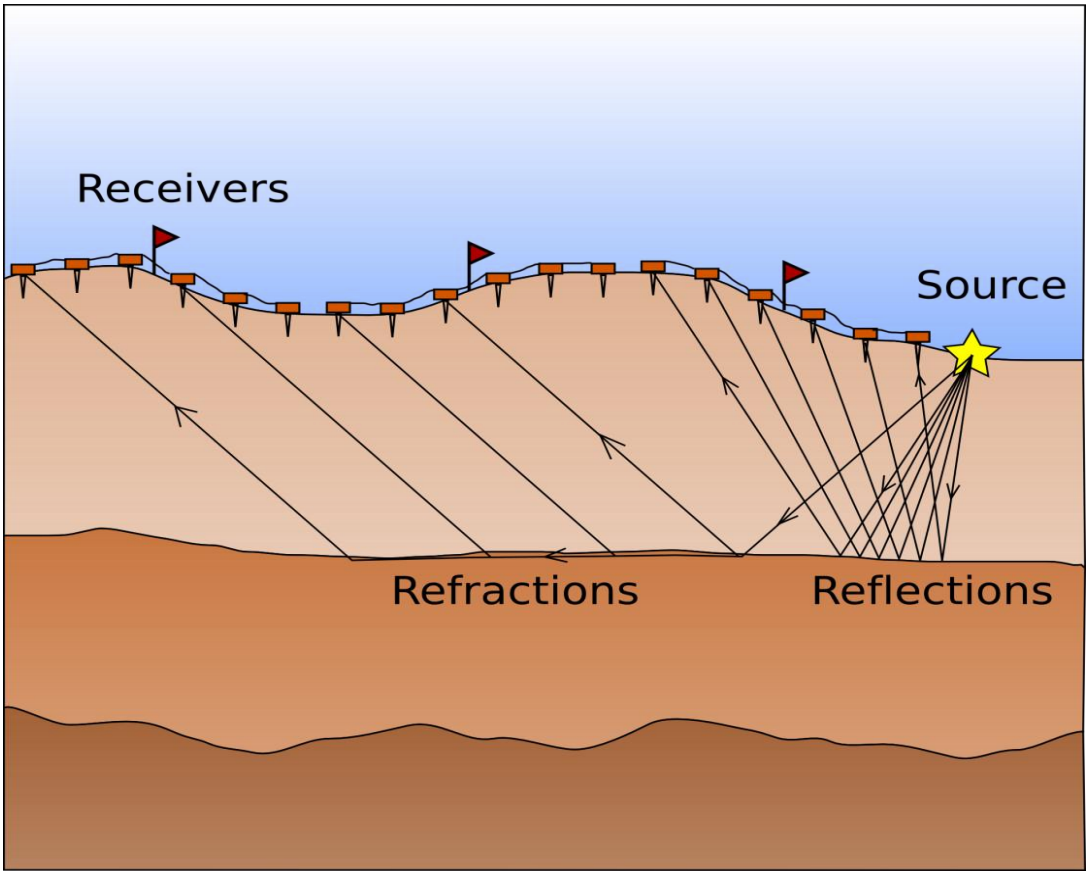

Figure 7-7 Reflection and Refraction Raypaths, illustrating the need for statics and how both reflections and refractions can be used to determine the velocity and thickness of the near surface layer.

7.2.3.1 Field (Elevation) Statics

Field statics, or elevation statics, are the coarsest static corrections. They correct for varying source and receiver elevations. A time shift was applied to each trace, based upon the elevation of the receiver and source relative to a chosen datum.

In addition to the surveyed source and receiver elevation data, calculation of the time shift required a characteristic p-wave velocity for the near surface medium between receiver and chosen datum.

For the purpose of field statics, the near surface velocity was assumed to be constant. Although the near surface is known to be strongly variable in the Neal Hot Springs survey area, it was considered that a representative value could be identified. The near surface velocity was derived from analysis of direct arrivals, given the unavailability of up-hole times from local wells. Analysis of the direct arrivals is shown in Figure 7-8.

The p-wave velocity of the near surface was found to be approximately 1800m/s. A datum of 800 meters above mean sea level was chosen. The static correction/time shift was applied to all traces on this basis.

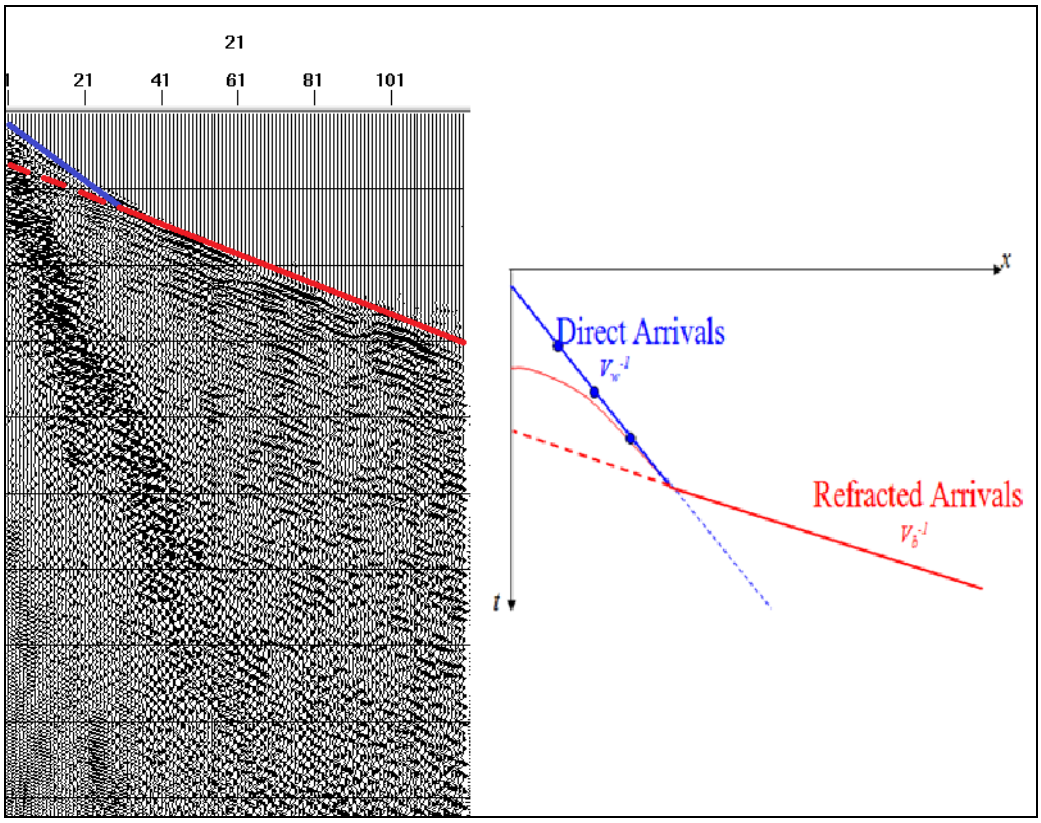

Figure 7-8 Direct Arrivals on Shot Record and Schematic t-x Plot

7.2.3.2 *Refraction Statics*

Refraction statics were applied after field statics. Refraction statics sought to further refine the statics corrections, with particular consideration given to the variability in velocity through the near-surface weathering layer.

In addition to refining the statics corrections, refraction statics also provide a near-surface velocity model. This can be used to image the near surface if required, as it was in this case. The near-surface velocity model was built following analysis of the first-break refractions, which were clearly visible on most raw shot records.

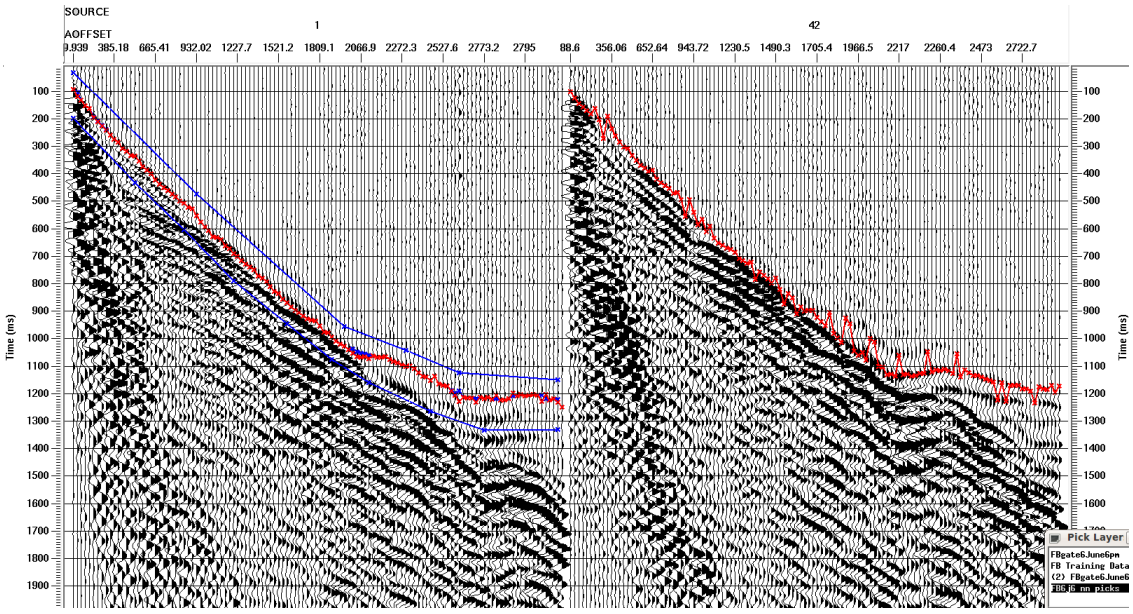

Figure 7-9 Picking First-breaks Using the Neural Network

First-break refractions in this instance were picked as shown in Figure 7-9. First-breaks were picked across all shot records using a neural network. They are illustrated above in red. Picks were constrained by a guide corridor illustrated above in blue, set manually at defined intervals.

There are several methods available for the calculation of refraction statics. In this case, the parameters necessary to model the near-surface, and therefore apply the eventual static shift, were calculated by an iterative Gauss-Seidel least squares inversion. In order to simplify this procedure and provide a stable inversion, the velocity through the weathered layer was assumed to be constant at 1200m/s. Parameters modeled by the least squares inversion were the bedrock velocity and the thickness of the weathered layer. VSP data could be used to further improve the velocity model.

With the bedrock and weathering velocities obtained, along with an interpolation of the weathering thickness at each receiver location, the near surface model was constructed. This allowed the bedrock horizon to be depth converted and a rudimentary model of the near-surface layer constructed. The results are shown in Figure 7-10 below, where the refraction statics velocity model can be used to see the sharp transition to high velocities over the proposed igneous horst block.

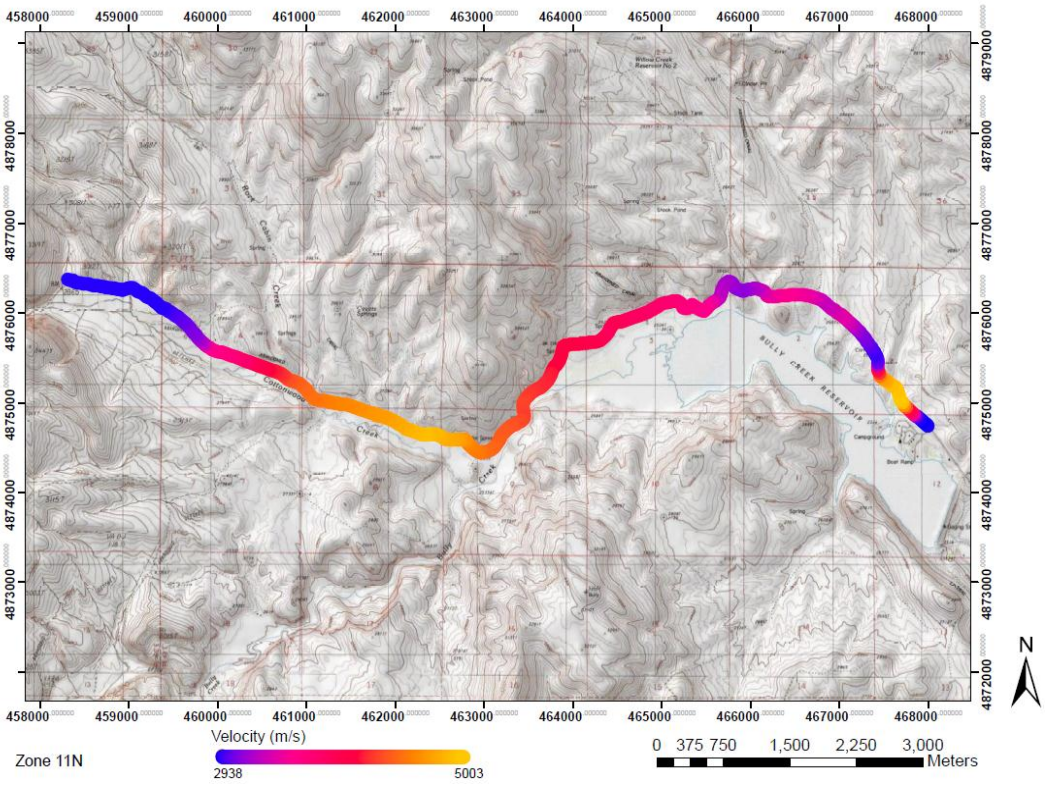

Figure 7-10 Plan View of the Velocities Acquired from the Refraction Statics, showing a sharp transition to high velocities over the proposed horst block

7.2.4 CMP Gathers

The Neal Hot Springs data were processed with the CMP method. The CMP method improves the signal to noise ratio as a function of the number of traces (with multiple source-receiver offsets) sharing a common reflection point. In order to perform the CMP sort, the supplied acquisition geometry in Figure 7-11 was used to assign each trace to a unique geometric midpoint on a shot-by-shot basis. With the crooked nature of the lines that were acquired, this resulted in a series of midpoints which did not lie along a straight line. This problem would normally be addressed with crooked line binning; however, in this instance the midpoints were not binned but were assigned using simple inline geometry.

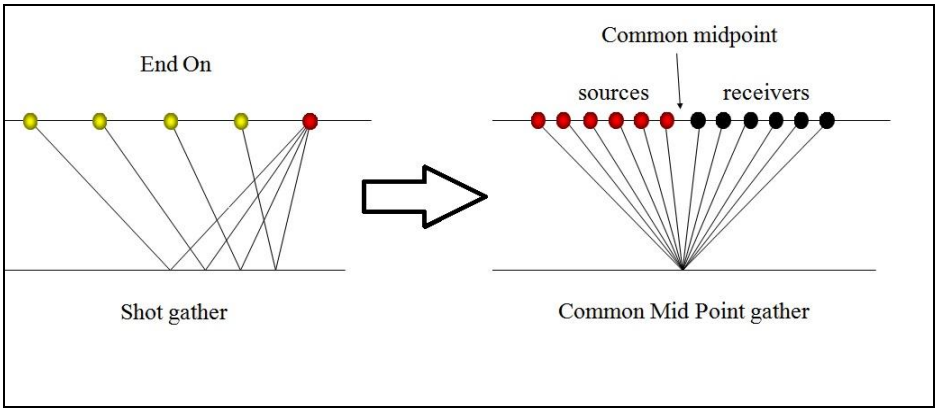

Figure 7-11 End-on Shot Gather Compared to Common Midpoint Gather [*H Jakubowicz, 2011*]

7.2.5 Deconvolution

Source signature deconvolution was not applied, as following autocorrelation of the data with the known Vibroseis source signature, the source signature is already a suitably compressed zero phase source signature.

A predictive, or “gapped” deconvolution was applied. This operator aimed to remove some of the shorter period multiples and reduce the number of reverberations present in the data at this early processing stage. Several predictive lags and operator lengths were tested in order to determine the optimal parameters with which to perform the predictive deconvolution. The tests and results of the deconvolution can be seen in Appendix B.

To target multiples and avoid interfering with the source signature, a minimum predictive lag of 35ms was chosen. This was based upon analysis of the minimum phase source signature, and the assertion that the predictive lag should never be

lesser in time than the second zero crossing of the source signature [*Jakubowicz, 2011*]. The parameters of the predictive deconvolution filter applied are summarized in Table 7-11.

Table 7-11 Predictive Deconvolution Filter Parameters

Type of deconvolution	Minimum phase predictive
Decon operator length(s)	120
Operator prediction distance(s)	35.0
Operator “white noise” level	0.01
Window rejection factor	2
Apply a bandpass filter after decon:	No
Re-apply trace mute after decon	Yes

7.2.6 Brute Stack

With each trace within the recorded data assigned to a suitable CMP, an initial or “brute” stacking was performed on the data. This gave a preliminary insight into the subsurface geology and a basic benchmark against which future stacks could be compared after further processing. The brute stack seen in Figure 7-12 was created using a single function velocity field that will be substantially iterated and improved upon at a later time.

The brute stack also illustrates numerous areas of the data in which noise, including multiples and reverberations, were still present. This noise decreases the temporal resolution of the image. The brute stack is one of the main results of the seismic acquisition at this stage, and is discussed in more detail in Section 7.3.

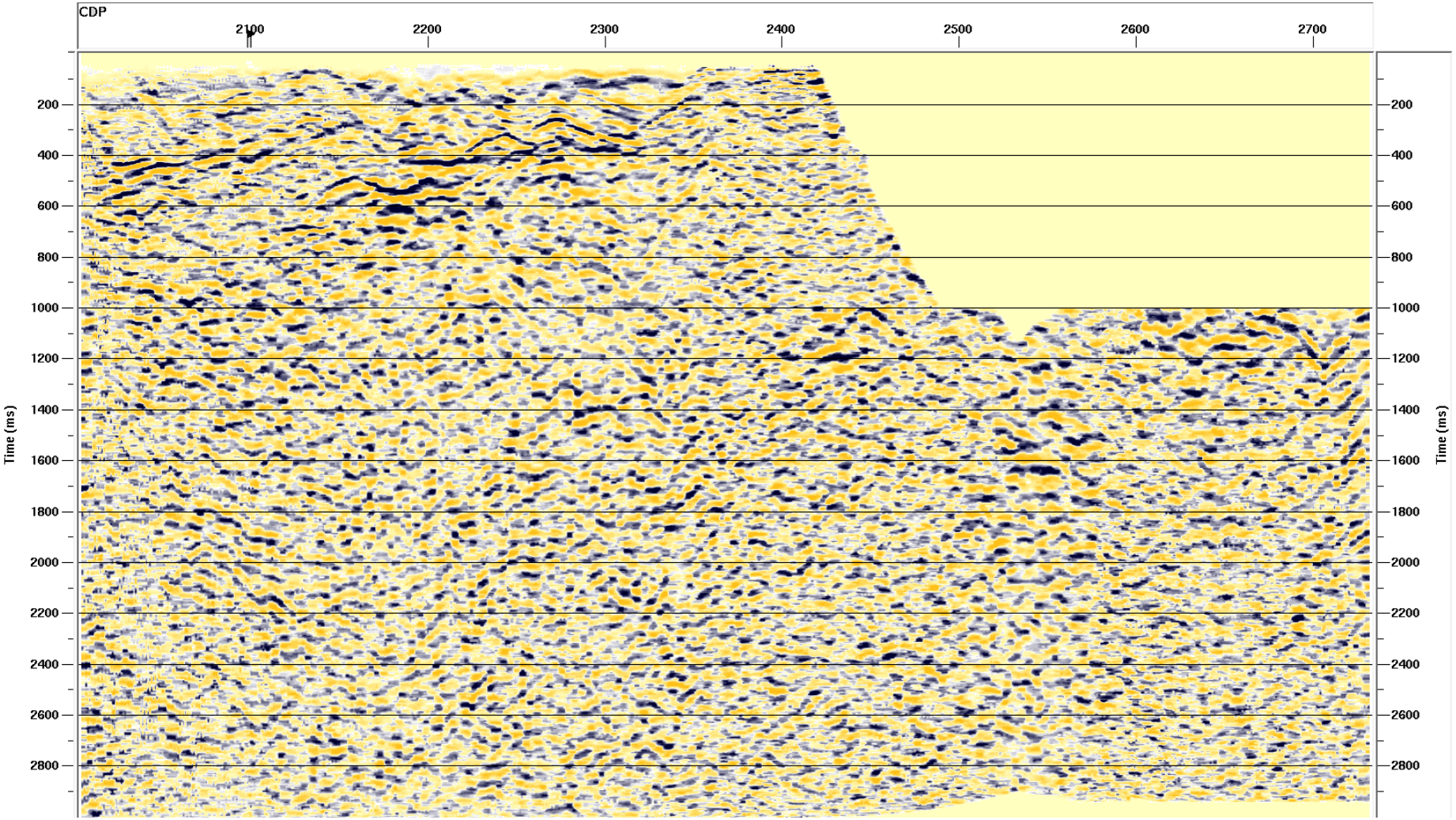

Figure 7-12 (Boise state) Brute stack

7.2.7 Further Improvements

7.2.7.1 Velocity Analysis

In order to attenuate noise and build a more refined stack, an initial velocity analysis would have been performed after the brute stack. This velocity analysis would primarily be used to correct for the effects of normal moveout (NMO).

Application of NMO corrections using velocities identified by a velocity analysis would improve the semblance between traces in each CMP gather, improving the signal-to-noise ratio achieved after stacking the data and refining the seismic image.

7.2.7.2 NMO Correction and Semblance Analysis

For a hyperbolic reflection event in a CMP gather (Figure 7-12 (Boise state) Brute stack), the difference between the two-way time at a given offset and the two-way zero-offset time is called normal moveout [*Yilmaz, 2001*].

Normal moveout is a function of offset and velocity. The offsets are known, and therefore the time correction required to flatten a reflection event constrains the stacking velocity to be picked during a velocity analysis. These stacking velocities are indicative (but not accurate) of the RMS velocities of the subsurface.

A CMP semblance spectrum can be calculated to aid velocity picking. This is discussed in further detail in Appendix B.

7.2.7.3 NMO Stretch Muting

Following NMO corrections, an NMO stretch mute would be applied. As the NMO correction is hyperbolic rather than linear, the correction caused the traces to stretch; the degree of stretch increasing with offset. If included in the stack, these far offsets smear the image. A front mute would therefore be applied to each of the CMP gathers to negate this effect. This would increase the resolution of the stack, but reduce the fold of the data, potentially also having a negative impact on the quality of the stack.

7.2.7.4 Stacking

After applying NMO corrections and an NMO stretch mute, the data would be restacked with the picked stacking velocities. It is expected that this stack would be significantly improved compared to the brute stack obtained in the project, with the single function velocity field.

However, despite multiples being attenuated by predictive deconvolution and stacking, it is expected that energy associated with non-primary reflection events would still be present within the data at this stage. Further to this, spatially aliased energy and numerous diffractions would still be present within the stack, along with reflections being mapping to the incorrect spatial locations. These should be addressed by further processing.

7.2.7.5 Migration

As the subsurface at Neal Hot Springs is known to feature dipping interfaces, the CMP will not overlie with the reflection point at depth. In order to accurately image subsurface reflectors, reflected energy must be 'migrated' to the correct reflection points.

The data would have required migrating in order to properly image and understand the subsurface geology, thus satisfying the main aim of this 2D survey. The process would have produced a significantly improved final stacked image of the subsurface geology

As is the case with all 2D surveys, with dip information only being available in the plane of the survey, undertaking an accurate migration would have been problematic. In particular, reflection points would have been required to lie within the plane of the section if they were to be correctly mapped. This would not always have been the case. This problem was further compounded by the crooked nature of the 2D line. However, completing a migration of the data acquired would give the best chance to see an accurate image of the fault that was the target of the survey.

7.3 Results

7.3.1 Refraction statics velocity model

Following on from processing, a refraction statics velocity model was generated which can be displayed and interpreted.

Figure 7-13 shows the velocity profile of seismic survey DS10 overlain on the topographic map of the Neal Hot Springs area. These velocities were calculated from the refraction statics model generated from the shot records. The profile shows a range of velocities from 2938 – 5003 m/s with the highest velocity at the center of the traverse. This

velocity profile is interpreted to indicate that the survey line bisects two antithetic, listric faults, with the maximum throw at the center of the peak in the subsurface velocity, decreasing away from the center. The antithetic faults are interpreted to bind a relatively elevated horst block, comprised of high velocity volcanic deposits, within the survey. This interpretation of the refraction statics model is consistent with the geological interpretation of the survey area. The area shown in yellow represents a horst block comprising older Miocene strata consisting of predominantly high velocity basalt and volcanic deposits. The younger Miocene strata, shown in red-blue, are comprised of sediments which typically have relatively low velocities.

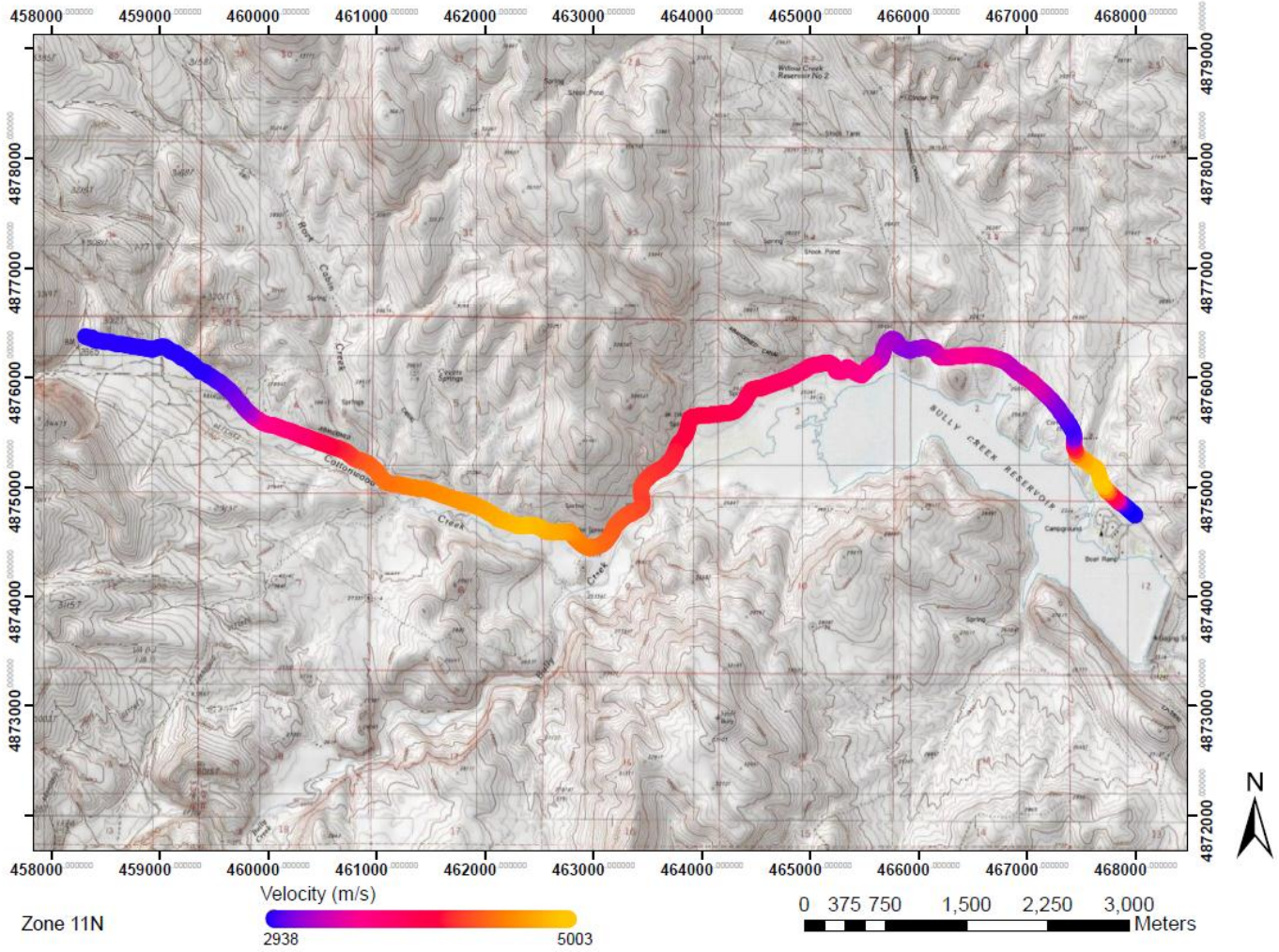

Figure 7-13 DS10 survey with line overlain by 2D velocity profile of the near-surface

7.3.2 Elevation Profile of First Refractor

An elevation profile of the first refractor was also generated which conforms to the geological hypothesis. Regardless of the ambiguity of the inversion result, the general trend of the profile shows the highest elevation is over the proposed horst, and decreases away from the horst towards the ends of the survey line.

Figure 7-14 shows the elevation profile of the first refractor, the top Miocene, basalt formation. Below (not to scale) is a schematic cross section of the geology from Raynolds [*2011*]. Between stations 1200 and 1300 there appears to be an elevated structure present that is interpreted to be the horst. Above this first refractor is a sedimentary/weathered near surface layer. The elevation profile of the first refractor is shown in Figure 7-15.

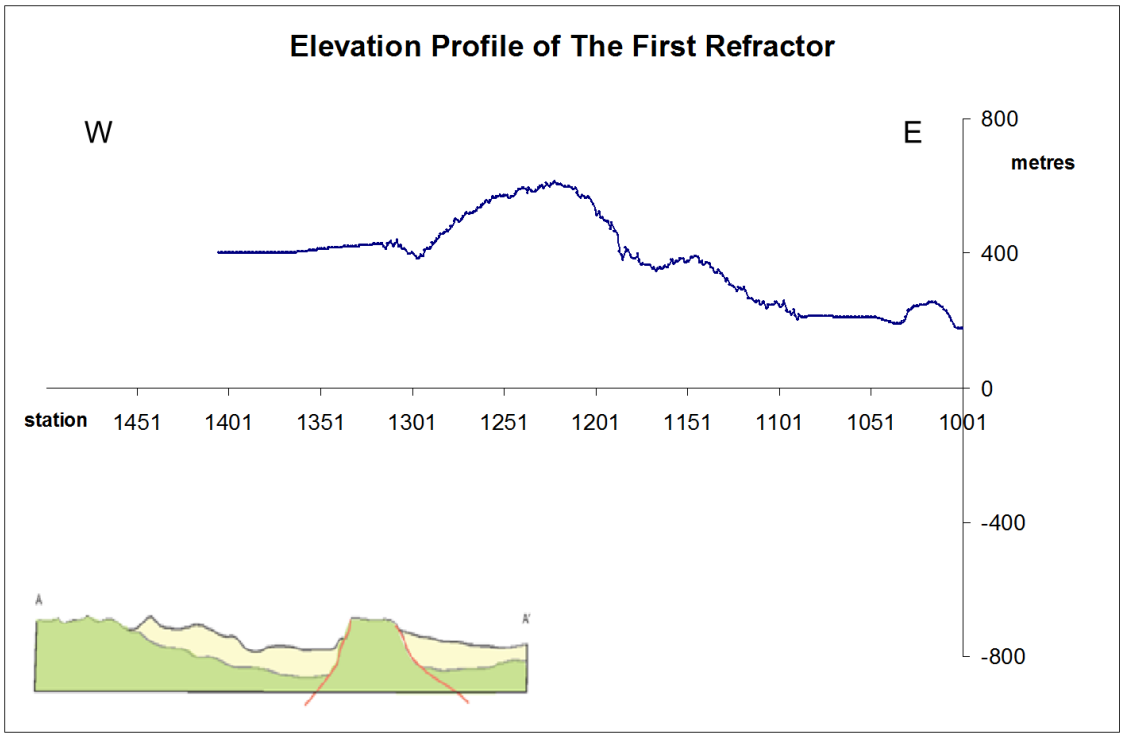

Figure 7-14 Elevation Profile Interpreted from the Refraction Static Velocity Model (top) Plotted Above a Schematic Cross Section of the Horst Structure

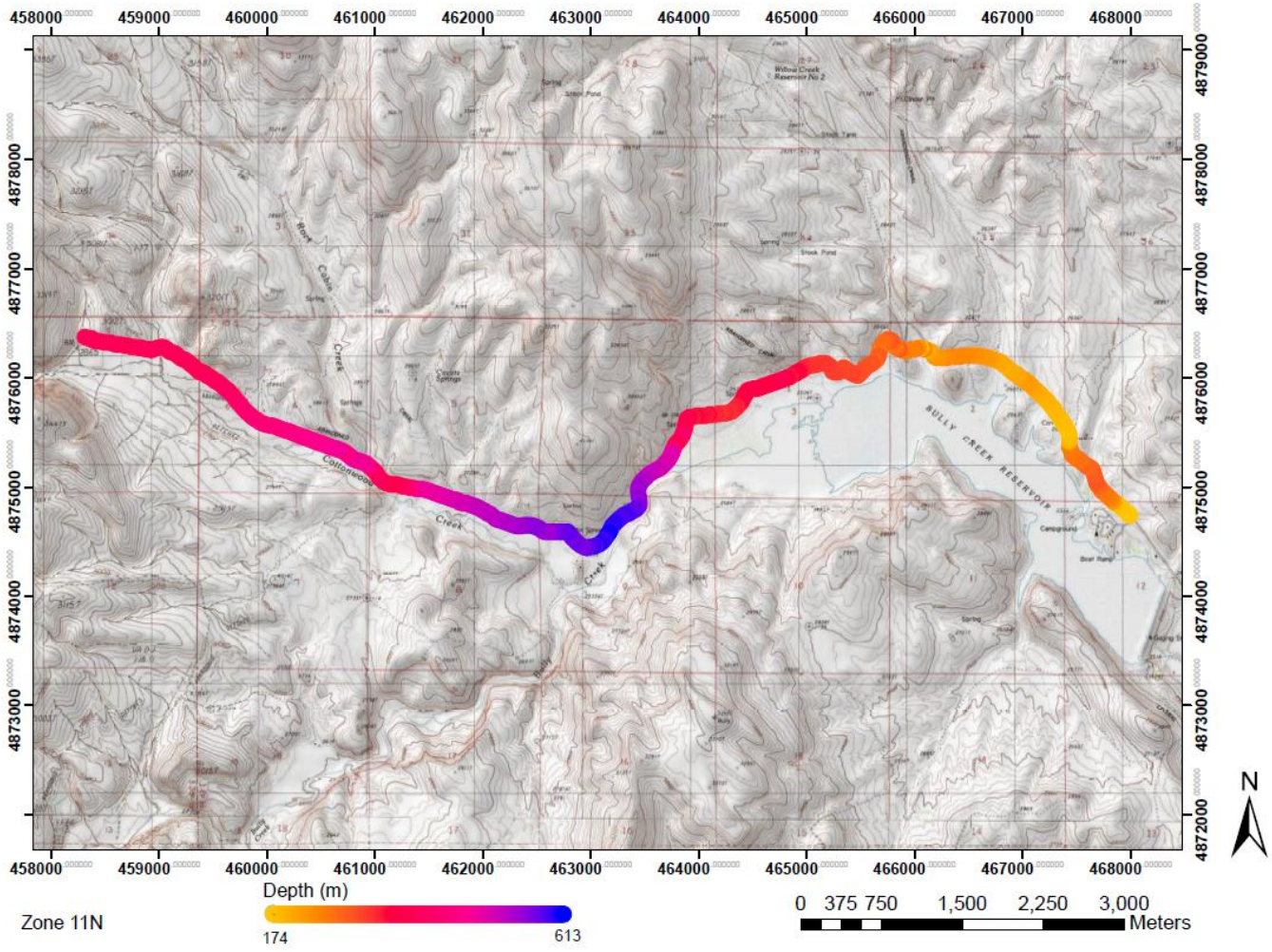

Figure 7-15 Elevation Profile Along DS10

7.3.3 Integration with Gravity

The profile of the reduced gravity data over the seismic traverse was superimposed onto the elevation profile of the first refractor. Consistency between the two datasets was observed. As shown in Figure 7-16, the profiles track each other; areas of high gravity correspond with areas of high elevation. As discussed, the area of high elevation is interpreted to be the location of the horst block.

The interpreted horst comprises older, basaltic, Miocene strata. Igneous rocks, including basaltic lava flows, are high density compared to sedimentary rocks (like the younger Miocene strata). Accordingly, as is observed, high gravity values are expected to be observed over the horst block, and low gravity values over the younger Miocene sediments.

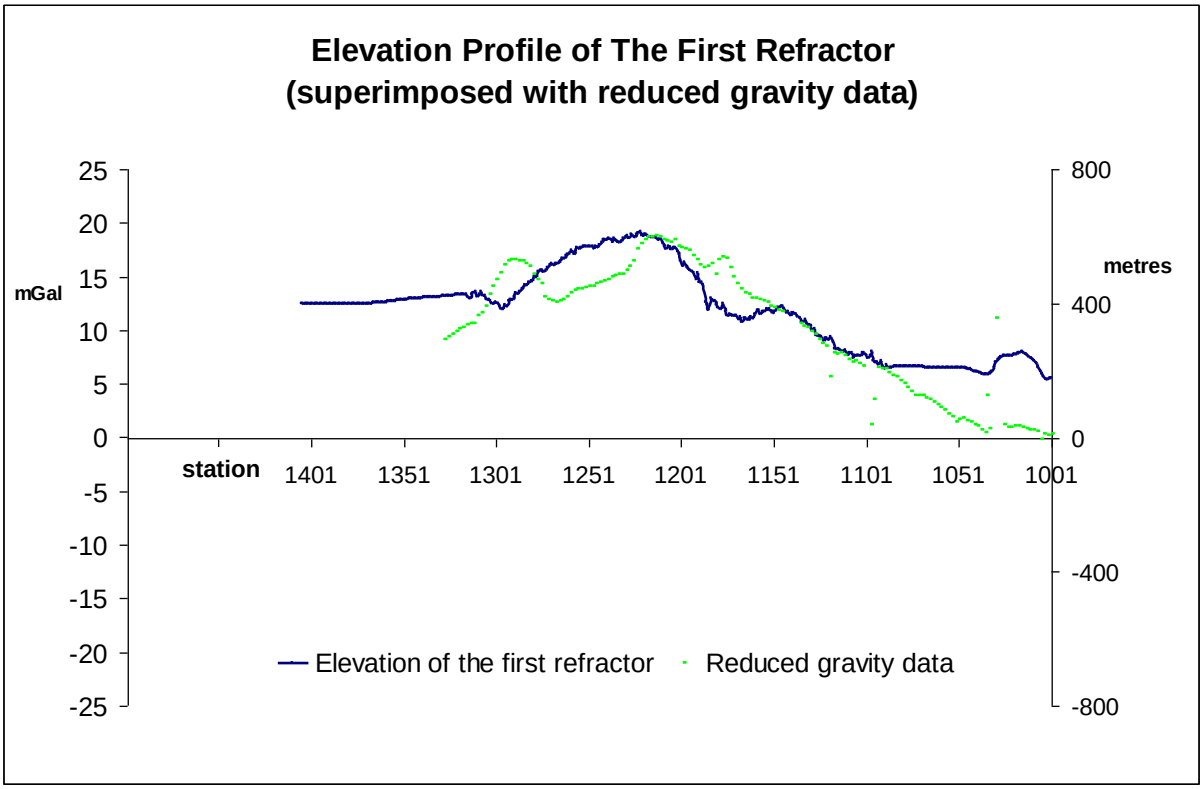

Figure 7-16 Elevation Profile of the First Refractor with the Reduced Gravity Data Super Imposed

7.3.3.1 Uncertainties in refraction results

There are multiple sources of uncertainty in the generation of the refraction velocity model which have a potentially large impact on the accuracy of the output. These include first-break picking, weathering layer thickness and velocity. However, the consistency of the model with the reduced gravity data and the geological interpretation of the area suggests that the trend exhibited by the model is correct.

7.3.4 Brute Stack Interpretation

A preliminary interpretation of the brute stack was produced, illustrated in Figure 7-17. It is possible to resolve some of the features that were targeted by this source. The interpretation is consistent with the geological interpretation of the Neal Hot Springs survey area that was based upon field observations. The horst structures identified are also consistent with the refraction velocity model discussed.

This interpretation is preliminary and qualitative only; exact values should not be taken from this result. It is expected that the interpretation will change significantly as the image is further processed, as outlined above. Accordingly, dip values are not accurate on this interpretation, although the general structure can be seen.

As seen in Figure 7-17, a number of near-offsets are missing from the data to the west of Neal Hot Springs. Accordingly, the fault is considered to be the main conduit for hydrothermal fluid flow to the surface, and the causative fault for the Neal Hot Springs, cannot be seen in the near surface information. However, it is considered that further processing will allow improved observation of this feature, especially in the deeper data.

E W

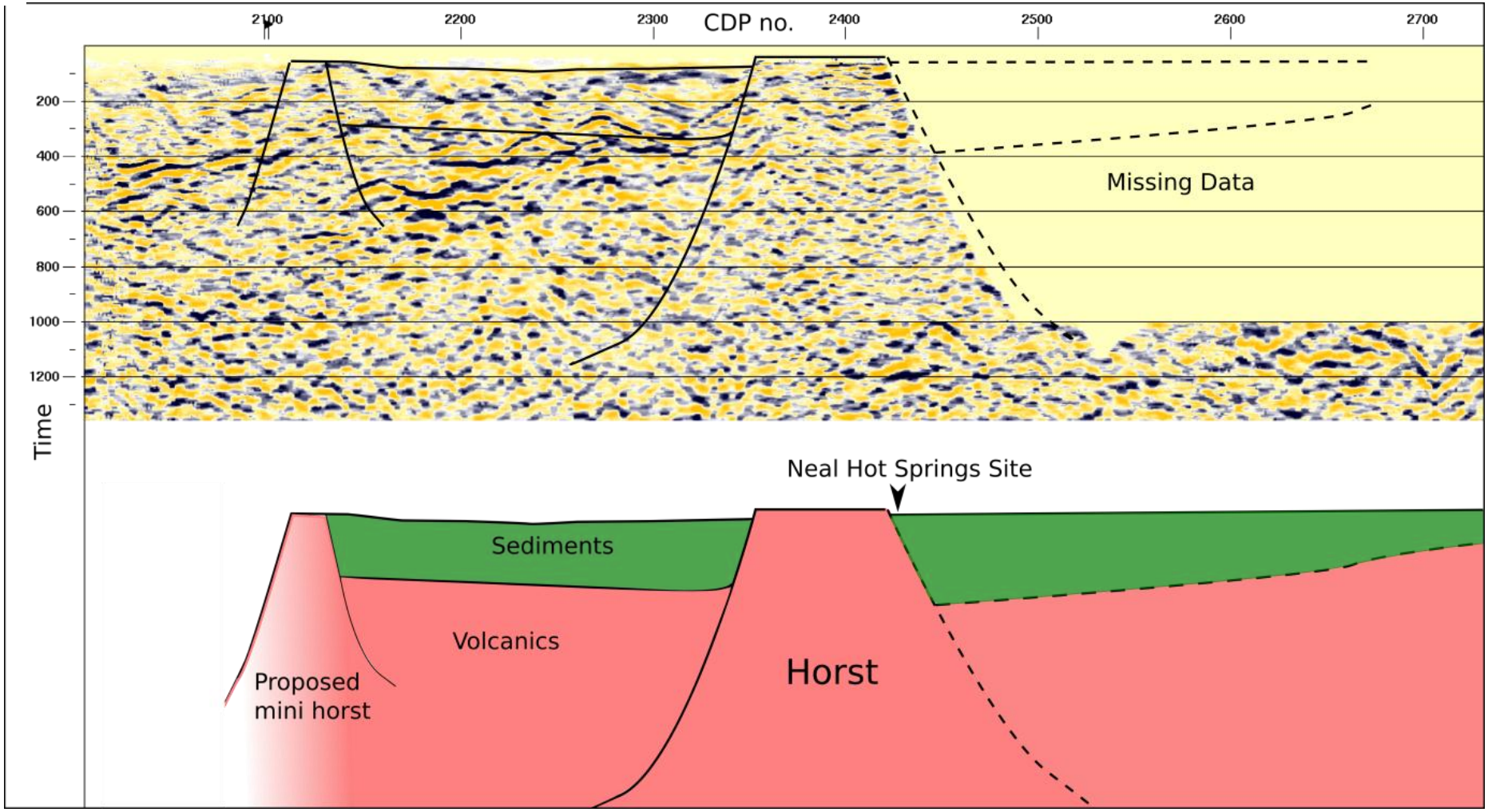

Figure 7-17 Brute Stack, processed by BSU with a simple interpretation based on the data processed thus far.

8. Vertical Seismic Profile

8.1 Acquisition

Vertical Seismic Profiles (VSPs) are localized seismic surveys carried out within a well bore over known depth intervals from the surface. As the data are acquired with time and depth information, high resolution, localized well data in depth can be correlated with low resolution, regional seismic datasets in time, and the interval velocities of the near surface can be estimated to produce a near surface velocity model. Knowledge of the interval velocities is critical for converting seismic interpretations into depth, and useful for inferring subsurface lithologies and understanding the rock distribution of the subsurface.

VSP data are typically recorded using multi-component receivers, which measure displacement in three mutually orthogonal planes (i.e. in the vertical and two horizontal directions). The horizontal receivers provide information that can be used for geophone re-orientation analysis or shear wave analysis in deep seismic data, while the vertical receivers are primarily for P-wave analysis

Three VSPs were acquired at well sites TG-99 (it should be noted that 'TG-99' is used for survey reference purposes only; US Geothermal has no official name for this well, which is adjacent to well TG-2), TG3 and TG19, as shown in Figure 8-1. The parameters for each survey are shown in Table 8-1. Both a 60kg accelerated weight drop and Vibroseis seismic sources were used. The accelerated weight drop made contact with a metal plate on the ground to generate P-waves in the ground. Two receiver arrays were used; a linear array of geophones located on the surface, and a sonde. The VSP survey geometry is summarized in Figure 8-2.

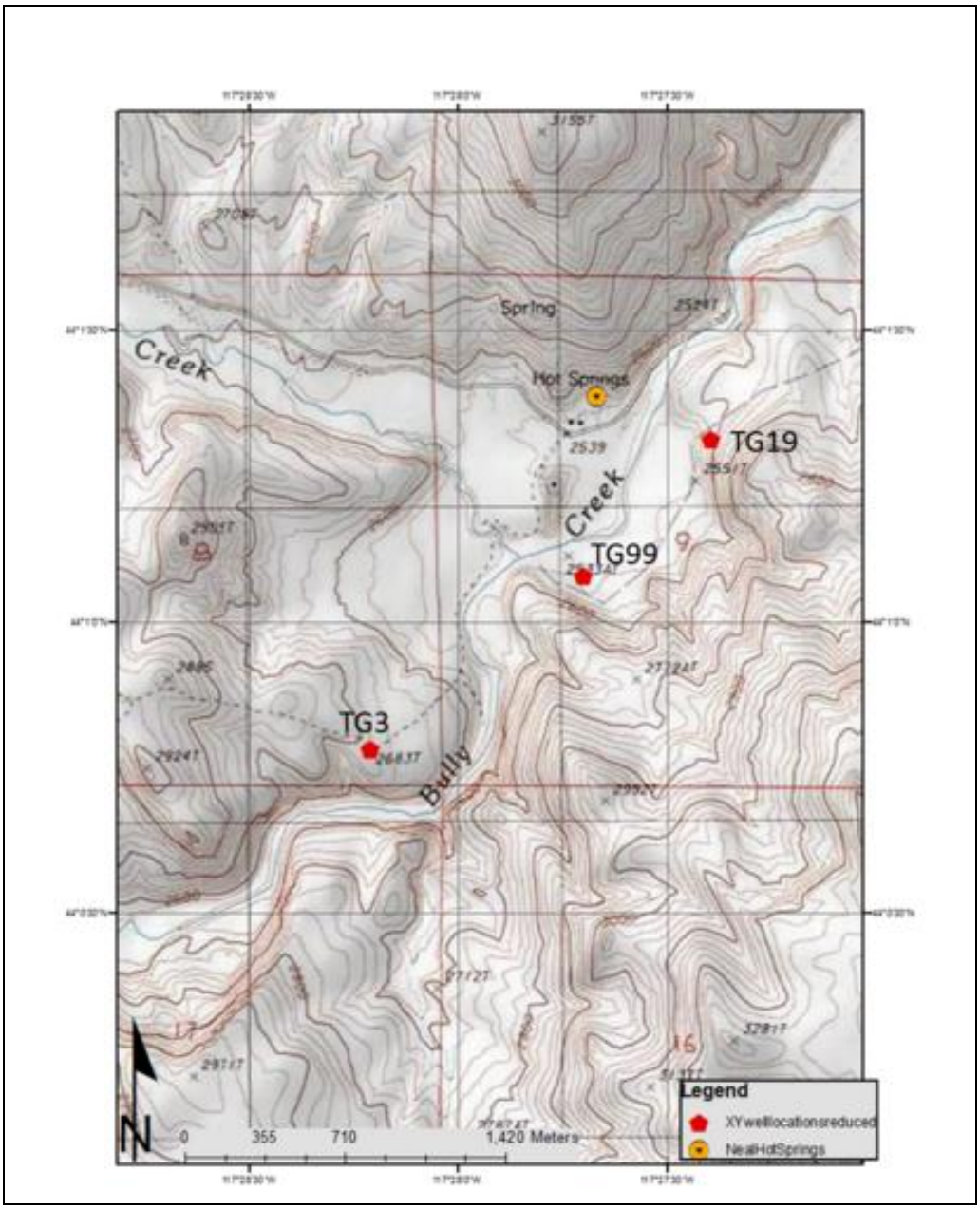

Figure 8-1 Well Bore Locations Surveyed by VSPs

Table 8-1 VSP Survey Parameters

Well Location	TG99	TG3	TG19
Min/Max VSP Depth	0/39m	0/490m	0/185m
Cased/uncased	Cased	Cased	Cased to 270ft depth
Hydrophone Interval	0.5m	2m	0.5-1m
Geophone Interval	1m	1m	1m (24 channels)
Offset of near geophone from source	3.1m		3.1m

Source distance from hole	3.7m		6.3m
Source type	60kg accelerated weight drop	60kg accelerated weight drop and Vibroseis	60kg accelerated weight drop
Height of well head from surface	0.6m		0.3m
No. strikes stacked per shot	3	1	3-5

The geophones in the linear array were spaced at one meter intervals and measured only the up-going wave field (as the surface imposes a boundary condition such that the down-going wavefield is negligible). The sonde measured the down-going and the up-going wave field. Geoids were used to digitize the analogue signal from the receivers, sampling the signal at a rate of 0.25ms. 48 channels were recorded on the geoids; channels 1-24 were designated to the surface geophones, channels 25, 26 and 27 recorded VSP measurements from the sonde, and the remainder of the channels recorded only noise.

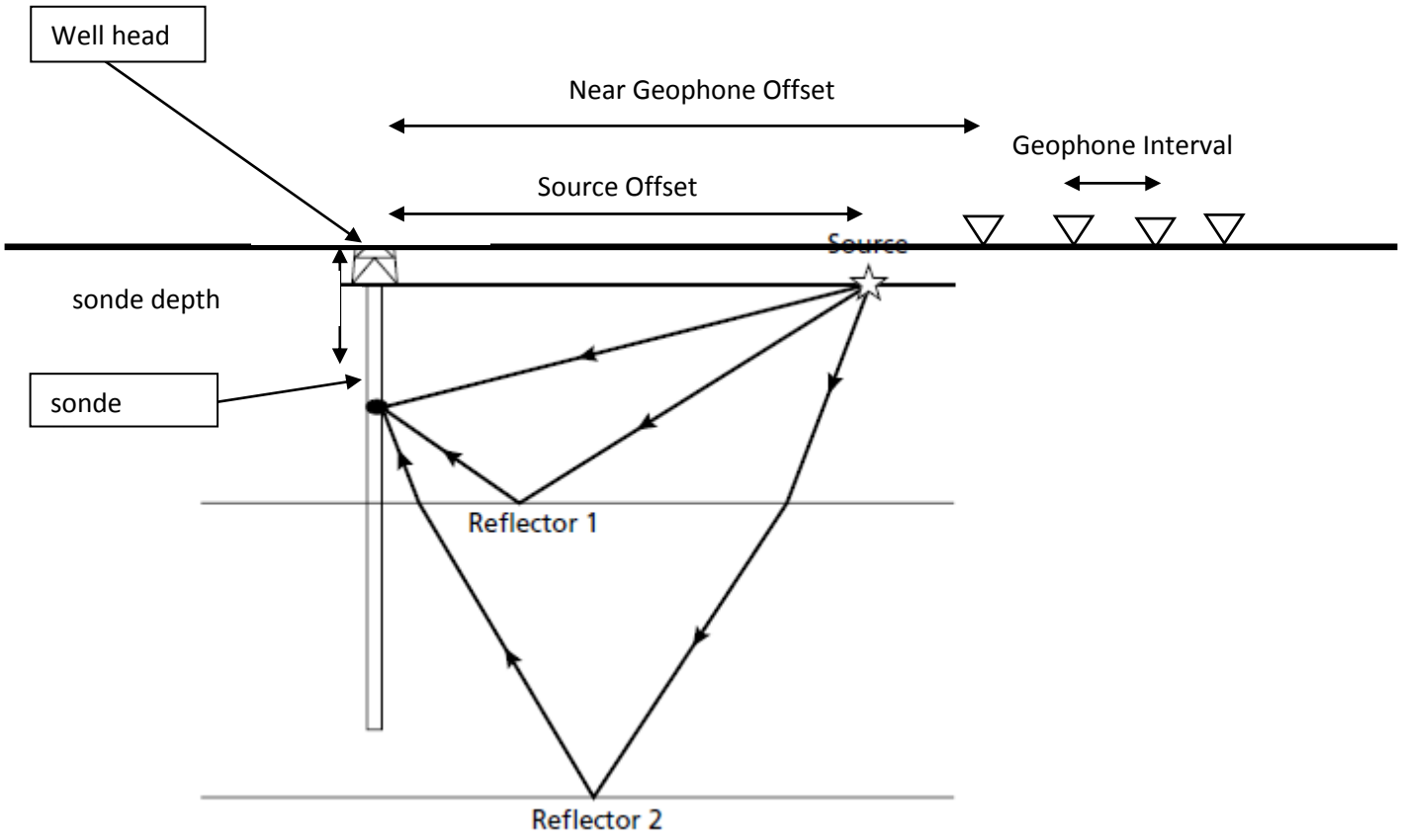

Figure 8-2 VSP Array [*Kearey, Brooks and Hill, 2002*]

Data quality issues were encountered where the holes were cased, as the casing denigrated the amplitude of the seismic signal, reducing the signal noise ratio. This particularly affected the data acquired at TG-3; the water wave was the most significant arrival recorded, despite use of both the high frequency accelerated weight drop and high energy Vibroseis sources due to high water pressure in an additional well casing. In addition, at TG-19, despite the maximum borehole depth being approximately 500m, the maximum depth recorded by the sonde was 184m due to the presence of a layer of mudstone which obstructed deeper measurements. Due to coupling issues when surveying well TG-99, only the vertical component of displacement at the surface geophones was recorded due to poor ground coupling preventing valid measurement of the horizontal components of displacement. A VSP had been planned to be acquired at well location TG-5, however, this could not be done as the well bore was too narrow for the sonde to be placed in the hole.

8.2 Processing

As the data obtained from well TG-3 were of very poor quality due to the presence of an additional casing, only the data from well locations TG-99 and TG-19 have been processed at this stage. Processing of the VSP data was undertaken by BSU. It was also intended to isolate the refractions measured by the surface lain geophones and process these data as a refraction survey to further investigate the subsurface, but this had not been completed at the time of reporting.

The raw VSP records from wells TG-99 and TG-19 are shown in Figure 8-3 and Figure 8-5 respectively. It is seen that the records are dominated by the down-going wave-field. The first arrivals in the raw data are the down-going direct arrivals. These were picked and plotted as a function of travel time and sonde depth in order to identify discontinuous variations in subsurface velocity, potentially associated with lithological variation across an interface, and continuous increases in velocity with depth potentially associated with compaction. Preliminary velocity models were produced on this basis, as discussed in Section 8.3.

Rapid changes in velocity in the subsurface, which may be identified in the first-break arrivals in the raw VSP data, are indicative of rapid changes in the strength of the subsurface. Rapid changes in strength are frequently associated with changes in lithology.

The VSP data for wells TG-99, TG-3 and TG-19 were processed in Seismic Unix. The down-going wave-field was filtered out by discriminating on the basis of multi-channel apparent dip. The down-going wave-field is regarded as noise, comprising the direct arrivals and multiples. The up-going wave-field comprises the primary reflections and multiples. The resulting records, for wells TG-99 and TG-19 respectively are shown in Figure 8-4 and Figure 8-6. The plots show the near-well reflectors as a function of travel time and sonde depth.

Where the vertical and horizontal components of displacement were both measured, both the P-wave and S-wave velocity were estimated from the picked first arrivals of the horizontal and vertical components respectively. The Poisson's ratio for the sampled subsurface was calculated from the ratio of these velocities as per Equation 8-1. The lithology of the subsurface could be inferred from the value of the Poisson's ratio obtained from these velocities.

Equation 8-1 Calculating Poisson's Ratio from P and S wave Velocities

$$\frac{\beta}{\alpha} = \frac{\sqrt{1-2\sigma}}{2(1-\sigma)}$$

Where: β = shear (S) wave velocity ($m.s^{-1}$), α = compressional (P) wave velocity ($m.s^{-1}$), σ = Poisson's ratio

Further processing of the VSP data may be undertaken, including application of a statics correction and producing a corridor stack that may be correlated with the deep seismic data. However, this had not been completed at the time of reporting.

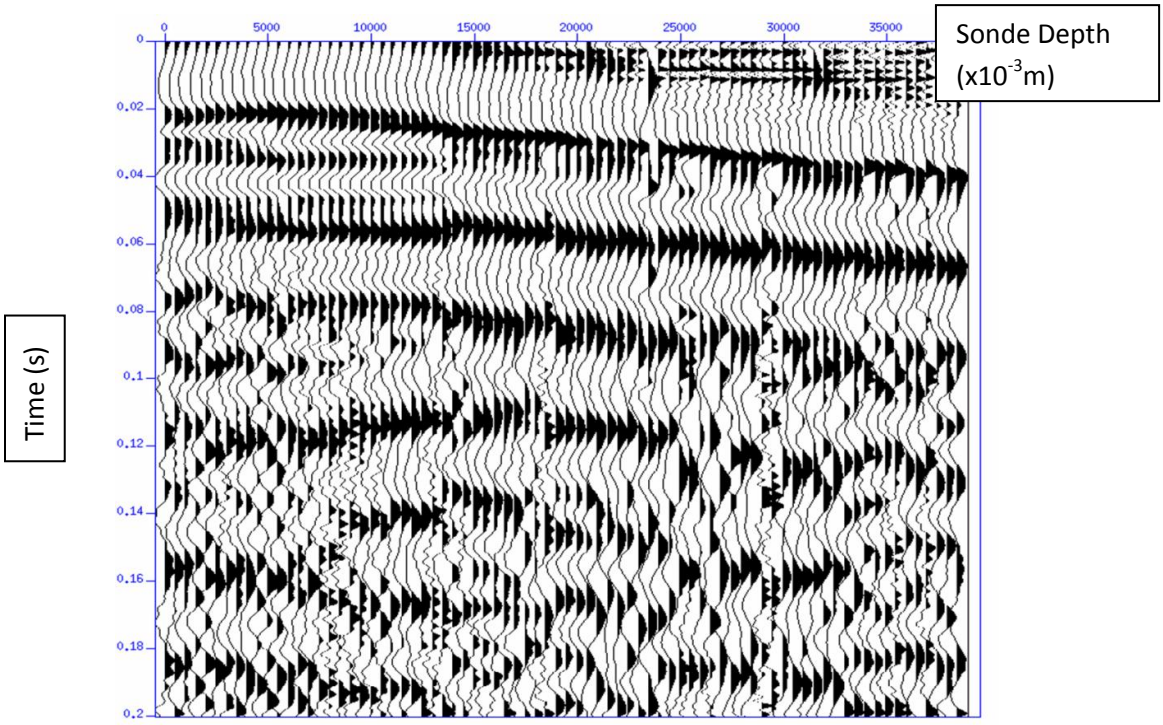

Figure 8-3 Raw VSP Record for TG-99 (0-39m depth)

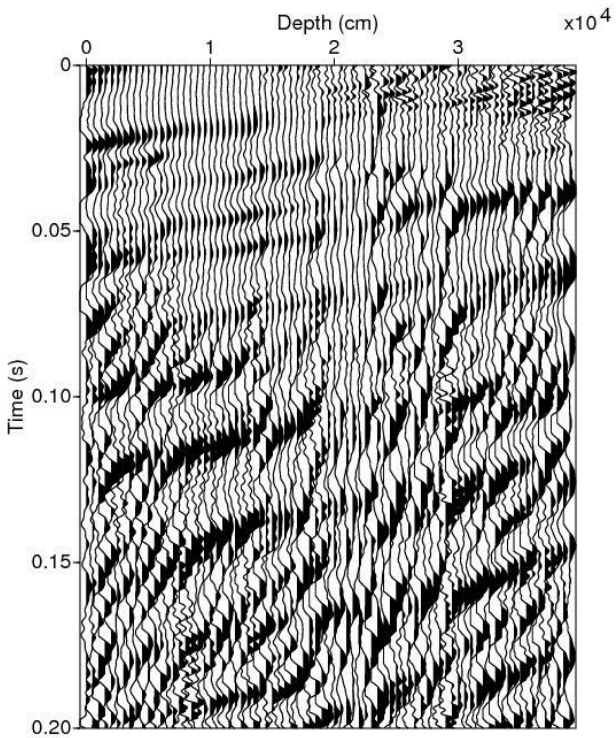

Figure 8-4 Filtered VSP Record for TG99

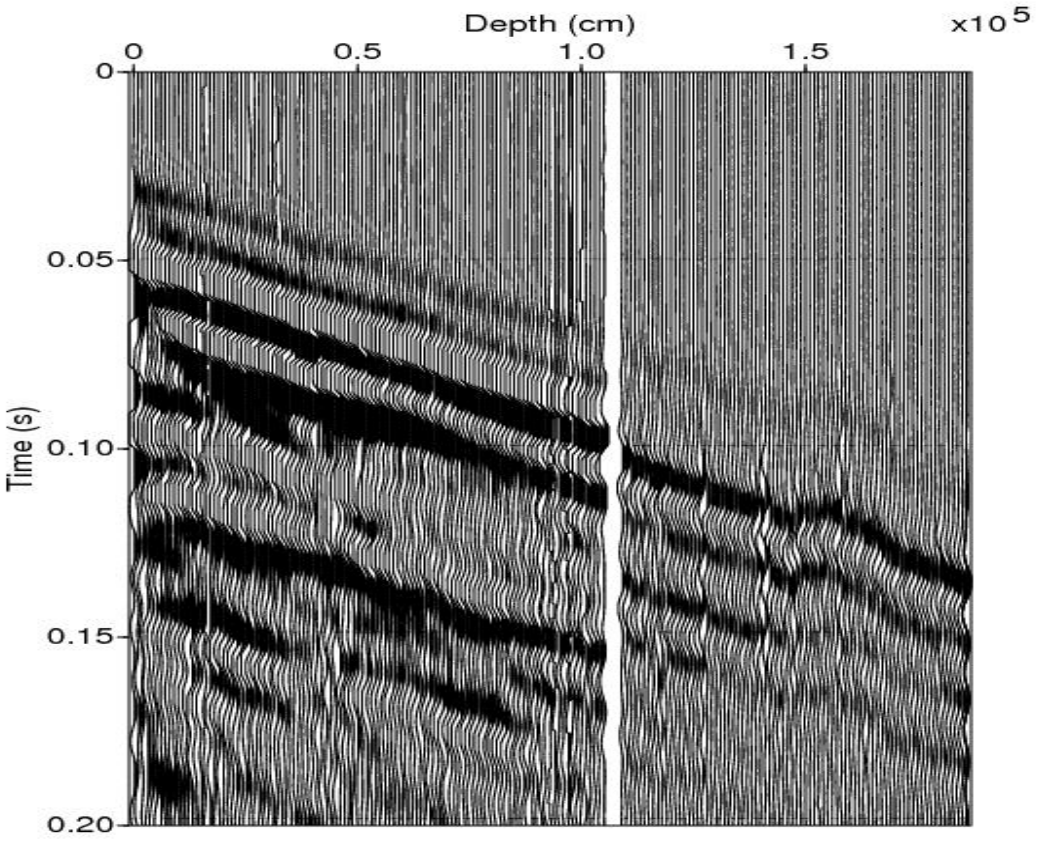

Figure 8-5 Raw VSP Record for Well Location TG-19

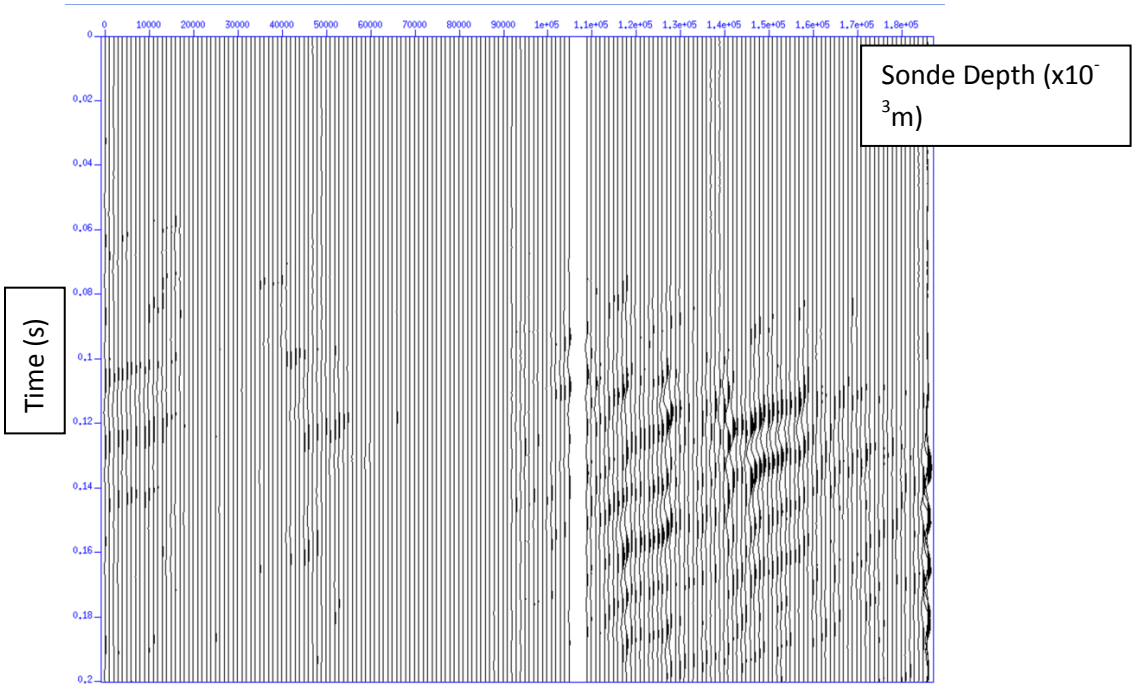

Figure 8-6 Filtered VSP Record for Well Location TG-19

8.3 Results

8.3.1 TG-99

A graph showing the time of the picked first-breaks (the direct arrivals) against depth for well TG-99 is shown in Figure 8-7. One large change in velocity is observed at 13.4m below the well head; the material above this point has an apparent velocity of ~2750m.s^{-1}. It is known that the velocity of sound in PVC piping is ~2500m.s^{-1}. This response in the direct arrivals is interpreted to be noise in the well casing. It is possible that this velocity exceeds that of the adjacent subsurface, and the signal from the subsurface reflectors has been overtaken by this noise. The underlying layer in the interpreted velocity model, seen in Figure 8-7, has an apparent velocity of approximately 1720m.s^{-1}. This is not significantly greater than the velocity of sound in water, which is approximately 1500m.s^{-1}. This layer is interpreted to be unconsolidated and water saturated sediments. The interface between the two velocities may be due to a break in the PVC casing, or other change in the casing, such as thickness or composition.

Strong variations in velocity, including layers of higher velocity overlying layers of lower velocity are expected in this area, due to interbedded water-lain sediments and volcanic flows. It is possible that the change in velocity coincides with an interface between high velocity volcanic rock and low velocity sediment, but the interpretation made above is considered more likely as geological observations made in the area and mud logs from wells within the survey area suggest that the depth of subsurface sampled by the VSP does not penetrate the first interval of volcanic rock. A mud or well log for this well is not available, as it was drilled for arable purposes rather than subsurface exploration. However, if a well log for a closely adjacent well should come available, this interpretation should be re-evaluated.

At well location TG-99, both the vertical and horizontal components of displacement were measured by the surface-laid geophones. The first arrival times of the P-waves (compressional, vertical component) and S-waves (shear, horizontal component) with depth were picked and plotted. The velocity of the P-waves was found to be ~1590m.s^{-1}; the velocity of the S-waves was ~456m.s^{-1}. On this basis, the Poisson ratio for the subsurface was 0.45.

A Poisson ratio of 0.45 falls within the range of ratios corresponding with stiff mud [*Sheriff and Geldart, 1995*]. This corresponds the interpretation made on the basis of the velocity model seen in Figure 8-7, and also with geological observations made in the field; the area is likely to be a paleo-lacustrine environment, and features thickly deposited lacustrine sediments that have been eroded by ongoing fluvial processes. The lacustrine sediments are terrigenous and clastic, and predominated by mud to silty mud, which are likely to become more consolidated with increased burial depth, and demonstrate increasing strength or stiffness.

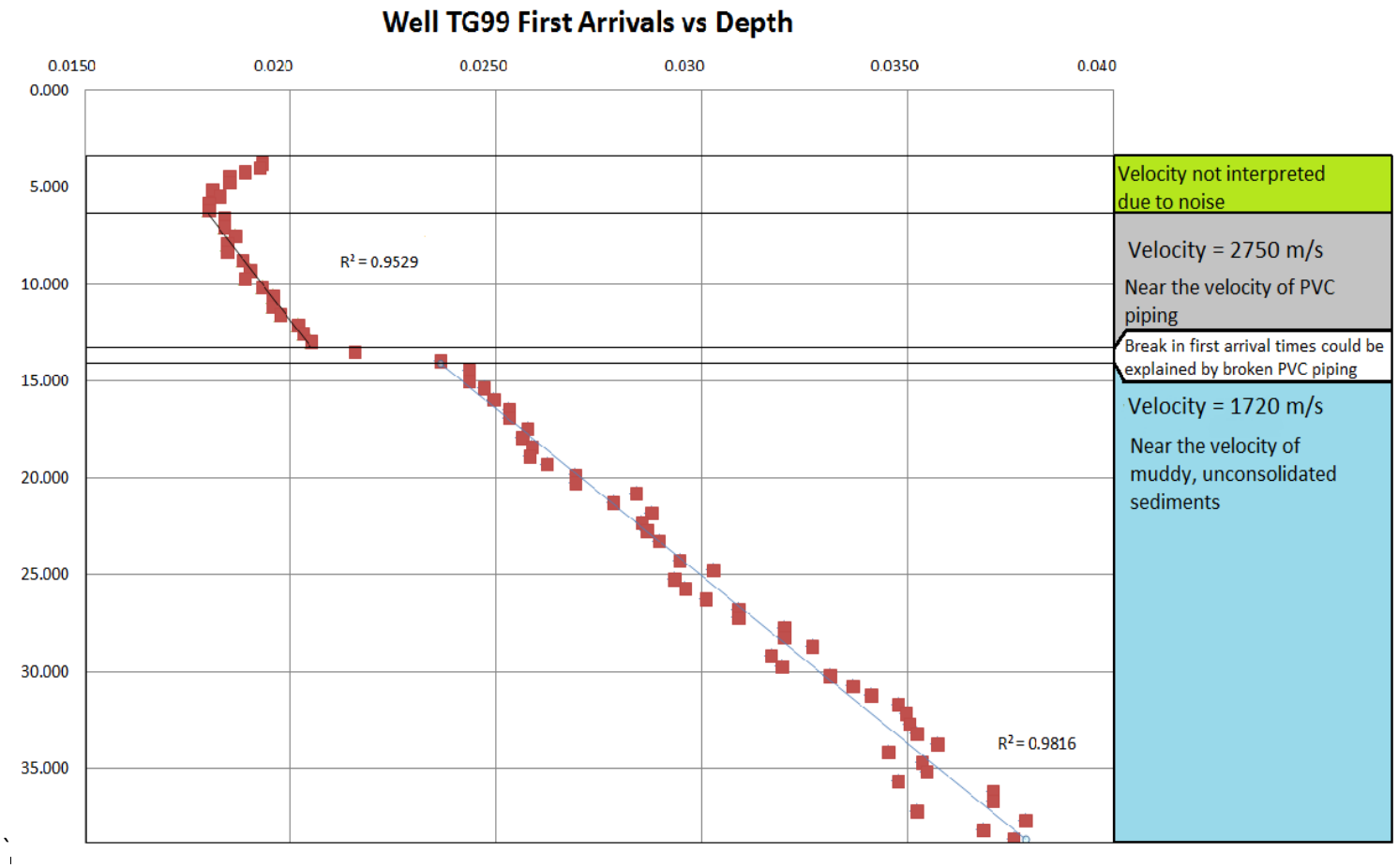

Figure 8-7 Graph showing First Arrival Time against Sonde Depth for the Vertical Component (P-waves) at Well Location TG99

8.3.2 TG-19

A graph showing the time of the picked first arrival against depth for well TG-19 is shown in Figure 8-8. The gradient of the time-depth relationships of the first-breaks has been used to construct a velocity model, also seen in Figure 8-8. Similarly to well TG-99, one interface is observed, at ~150m below the well head. The upper layer has an apparent velocity of ~2500m.s^{-1}. Similarly to TG-19, this is interpreted to be noise in the PVC well casing. The underlying layer has an apparent velocity of ~1600m.s^{-1}, and is interpreted to be water saturated unconsolidated sediment. A noisy interval in the picked travel times of the first-breaks is observed, for which a realistic, consistent velocity cannot be identified. This area may coincide with a break or other feature in the casing, but the precise cause of this noisy section is currently unknown.

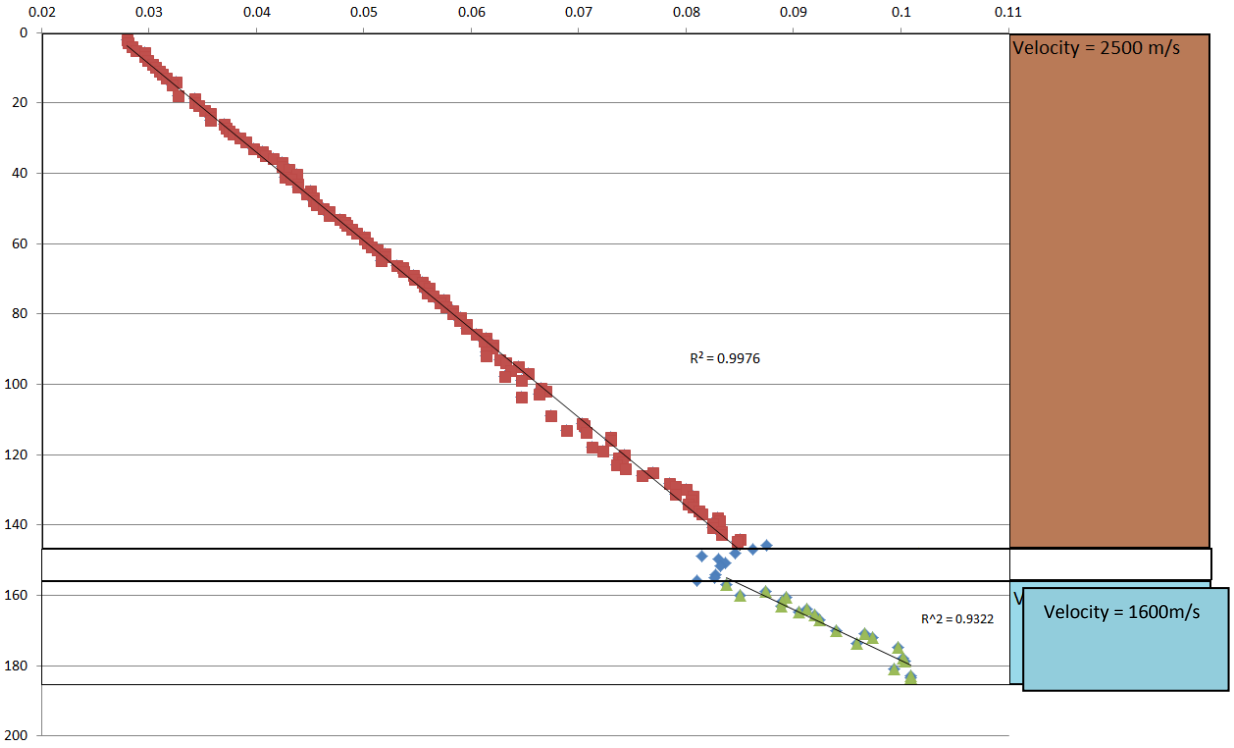

Figure 8-8 Graph Showing First Arrival Time Against Depth Recorded In-Well TG-19

9. Shallow Seismic Data

9.1 Acquisition

The locations of the shallow seismic surveys are shown in Figure 0-1. Three lines were surveyed: HS01, HS02 and HS03. The survey equipment, survey parameters, and survey geometry applied to each survey line were the same, and these are detailed in Table 0-1, Table 0-2 and Table 0-3 respectively. The length of each survey line, shot numbers and receiver numbers are detailed in Table 0-4.

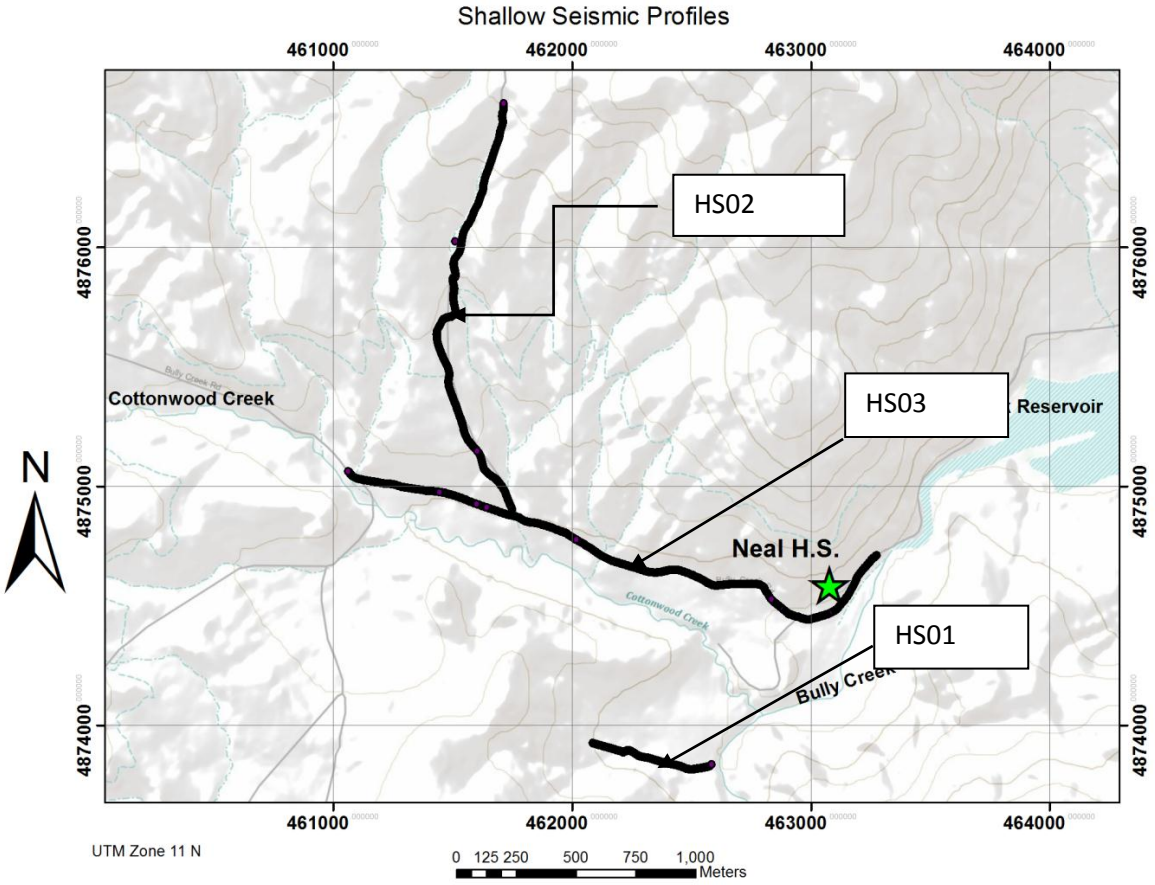

Figure 0-1 Map Showing Location of Hammer Seismic Surveys

The survey was carried out over a split, rolled over, spread of geophones. 96 live channels were laid at 5m intervals. Shots were made every 5m from the first shot station 2.5m before the first geophone. The shot device was a 60 kilogram accelerated weight drop which is show in Figure 0-2 Accelerated Weight Drop Source.

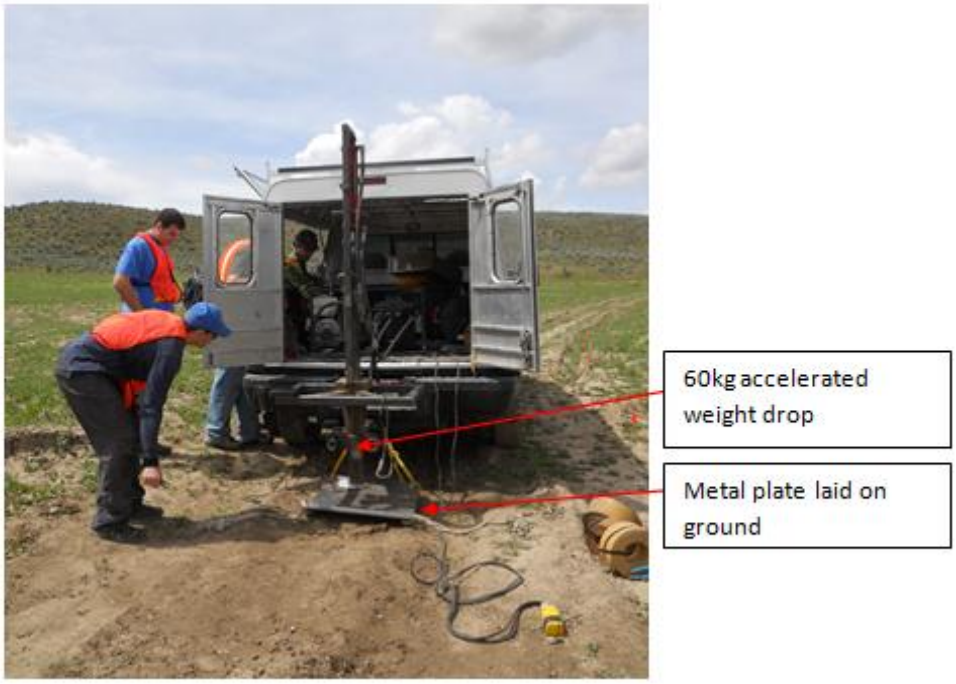

Figure 0-2 Accelerated Weight Drop Source

48 geophones (half the array) were rolled over to the front of the array once the shot preceding the geophone at the end of the array was completed. Shot stations were midway between receiver stations (i.e. 2.5m from adjacent geophone) and laterally offset approximately 2m from the receivers as the geophones were laid adjacent to the road along which the hammer seismic source was run. The array described is illustrated in Figure 0-3.

The array was not designed to filter ground roll from the recorded dataset (unlike the deep seismic array); however, it was intended to filter out ground roll upon data processing. Shot stations were confined to roads or areas where there was no agricultural growth. Line HS01 was particularly affected by these restrictions, as seen in Table 0-4, where multiple shots are missed at the start of the spread due to the line extending over a growing field.

Table 0-1 Survey Equipment

Source	60kg accelerated weight drop (truck mounted)
Receiver Type	8Hz geophones
Digitizers	Geodes mounted every 24m
Topside Recorder	PC
Recording Software	Seismodule Controller

Table 0-2 Shot and Record Parameters

Record Length	0.5s
Shot Stack	3-5 strikes (dependent on data quality)
Sampling Frequency	2ms
Recorded File Format	

Table 0-3 Survey Geometry

Shot Interval	5m
Group Interval	5m
Group composition	1 geophone
Spread	96 active groups
Acquisition	Split spread, 48 channels rolled over every 48 shots
Min./Max. Offset	0m/480m
Fold	48

Table 0-4 Survey Lines

Line I.D.	Shot Direction	Date Acquired	No. Receiver Stations	No. Shot Stations	Receiver Station No.s	Shot Station No.s	Line Length
HS01	W-E	05/19/11	175		1001-1175		870m
HS02	S-N	05/21/11-05/22/11	384	2001-2384	2001-2384	384	1915m
HS03	E-W	05/23/11-	524	3001-3524	3001-3524	524	2615m

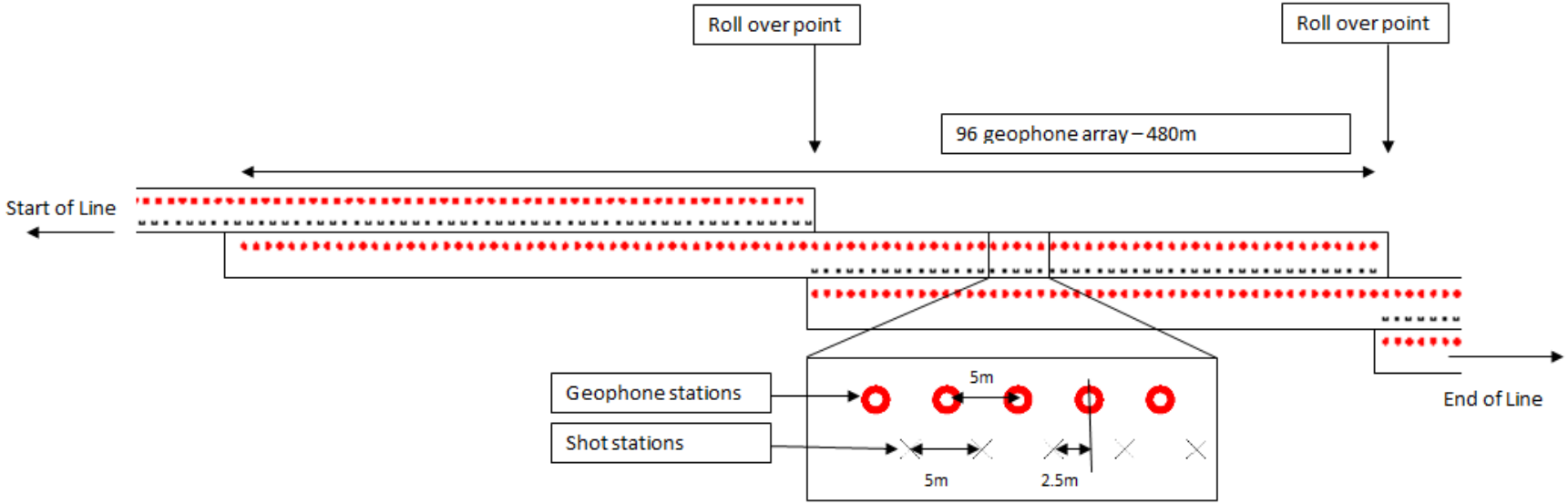

Figure 0-3 Array Design for Shallow Seismic Survey

9.2 Processing

As Lines HS02 and HS03 correspond with the main and cross lines surveyed with a large proportion of other geophysical methods over the course of the field camp, these lines were prioritized during processing. The processing was undertaken by BSU using Promax.

The raw SEGY files were uploaded into Promax. The data were filtered to attenuate noise, including ground roll. Sample raw shot gathers, filtered to remove ground roll, are shown in Figure 0-4. The survey geometry was subject to quality control, and applied to the data. The shot gathers were subject to a further quality control; bad shots (e.g. due to poor timing or excessive noise on the spread) were eliminated from the dataset. The data were then binned into CMP gathers.

A velocity analysis was carried out, NMO corrections were applied and the data were stacked. This process was carried out iteratively to optimize the semblance between common reflections in the CMP gathers and therefore optimize the signal-noise ratio. Interval velocities were calculated from the stacking velocities, and the data were migrated, producing final images.

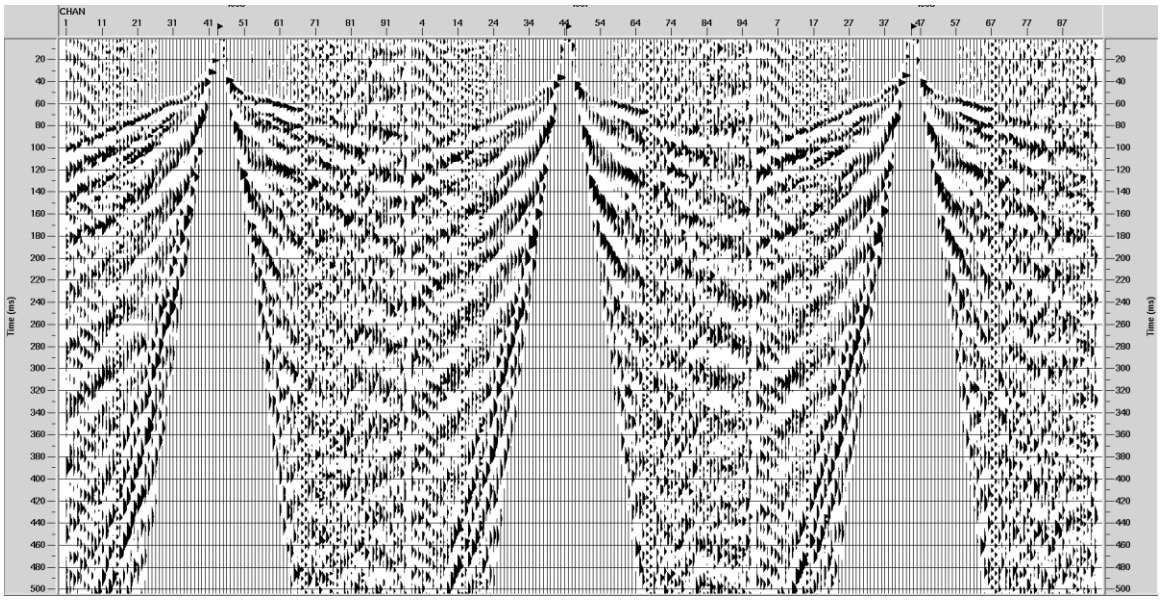

Figure 0-4 Raw Shot Gathers from Shallow Seismic Survey

9.3 Quality Control

Source coupling issues were encountered where the ground was irregular, which reduced the area of the plate in contact with the ground, which therefore reduced the proportion of energy transmitted to the subsurface. In addition, irregular terrain caused the distance between the hammer and plate to vary, causing the force exerted by the hammer on the plate to decrease where the distance was short. These issues were addressed by applying a minimum amplitude threshold at the recorder. If a shot within a stacked shot failed, to induce a sufficiently high amplitude response from the subsurface, the shot was retaken.

Three shots were stacked at the majority of shot points. Where source and receiver coupling issues were encountered, due to more poorly consolidated terrain, 5 shots were stacked at each shot point to improve the signal-noise ratio of the recorded data.

Reduced receiver coupling due to tilted geophones and difficult ground conditions was also encountered. However, this is regarded to have a negligible effect on the data once processed. Noise issues due to wind and ambient noise (e.g. vehicles, other survey activities including Vibroseis shots) were identified. Noise was a particular issue for line HS03, which was carried out on the main road running though the main Neal Hot Springs location; survey and construction traffic was frequent here. These issues were adequately addressed by normalizing and stacking shots during acquisition; and frequency filtering during processing. Additionally, the frequency band within which the majority of useful data were acquired is outside the frequency spectrums of these sources of noise.

9.4 Results

At the time of reporting, brute stacks for survey lines HS02 and HS03 are available, shown in Figure 0-5 and Figure 0-7 respectively. It is intended that both these sections, and the data from line HS01, undergo further processing to improve the images. However, preliminary interpretations of large scale features can be made on the basis of these initial data displays.

Both HS02 and HS03 are expected to cross the westerly fault plane bounding the horst block, predicted on the basis of the geological interpretation seen in Figure 3-7.

The brute stack for line HS02, shown in Figure 0-5, clearly shows dipping uppermost sediments on-lapping onto apparently sub-horizontal strata. The surface of the on-lap may be the target fault plane, as indicated in Figure 0-6. However, the low resolution of the data prevents offset horizons being observed, so this surface cannot be conclusively identified as the fault plane. Further refinement of the seismic stack is required to confirm this interpretation.

The brute stack for line HS03 is shown in Figure 0-7. The Neal Hot Springs are expected to immediately overlie the fault plane or an associated fracture, as these provide a conduit for the fluid flow observed at the surface. However, while a lateral discontinuity in the amplitude of the first reflector is observed at approximately CMP 6150, which may be associated with lateral offset of the horizon over the fault plane, the image is too poor to confirm this. The amplitude variation may also be associated with decreasing fold and roll off towards the end of the line, poor amplitude balancing during producing, or missing near-offset traces in this area. The possible fault plane is not observed in any subsequent reflectors, although these are indistinct in this section, which may mask any real structural offset. The stack of HS03 is too poor resolution to interpret a justifiable location of the fault plane. Further processing and data refinement is required to produce an interpretation of the HS03 profile.

South

North

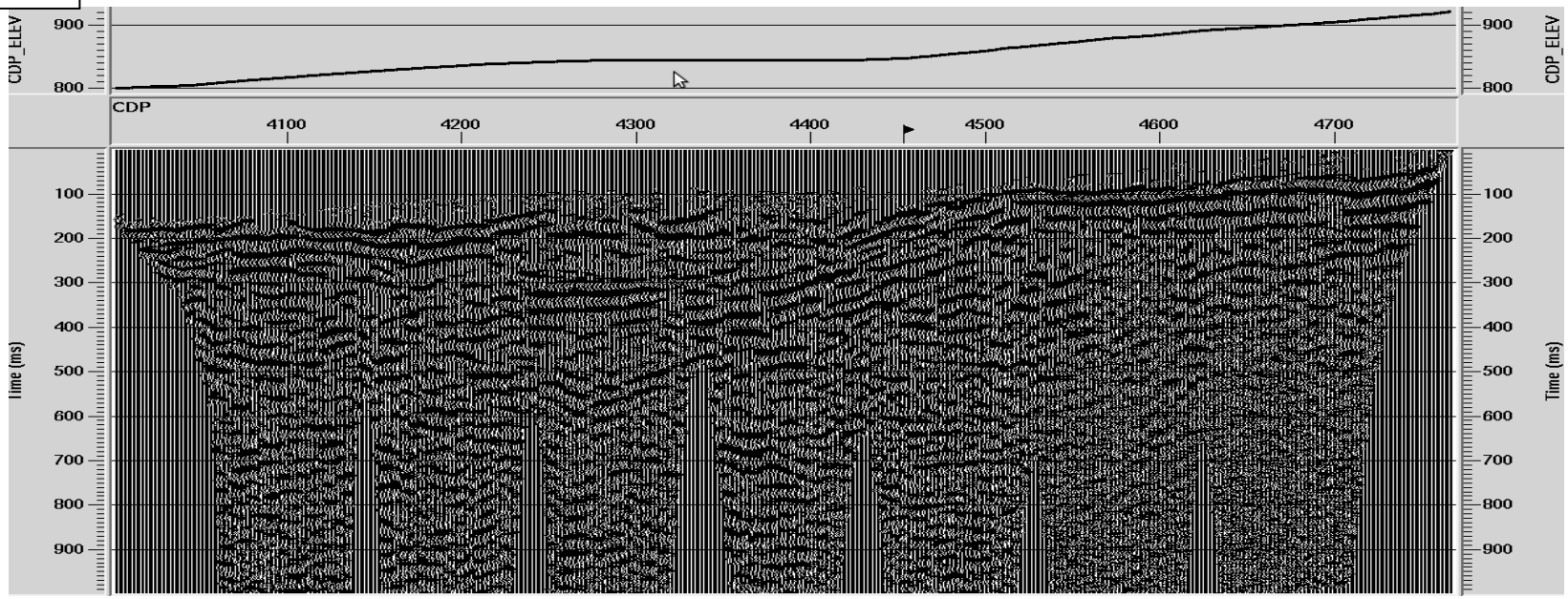

Figure 0-5 Brute Stack of Line HS02 (N.B. CDP/CMP interval is 2.5m)

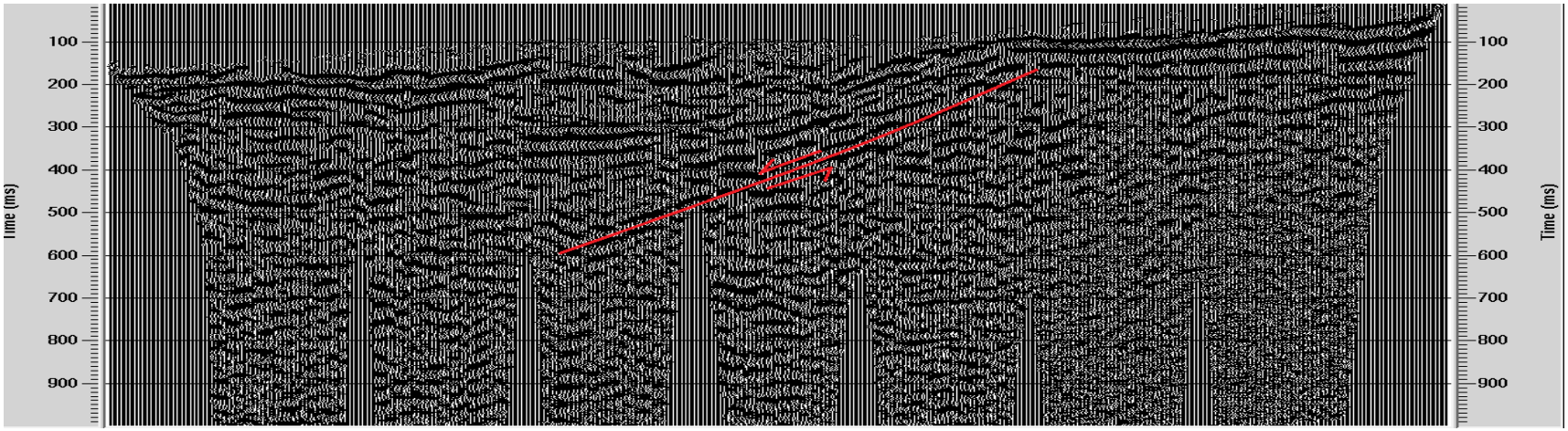

Figure 0-6 Brute Stack of Line HS02 showing Interpreted Fault Plane

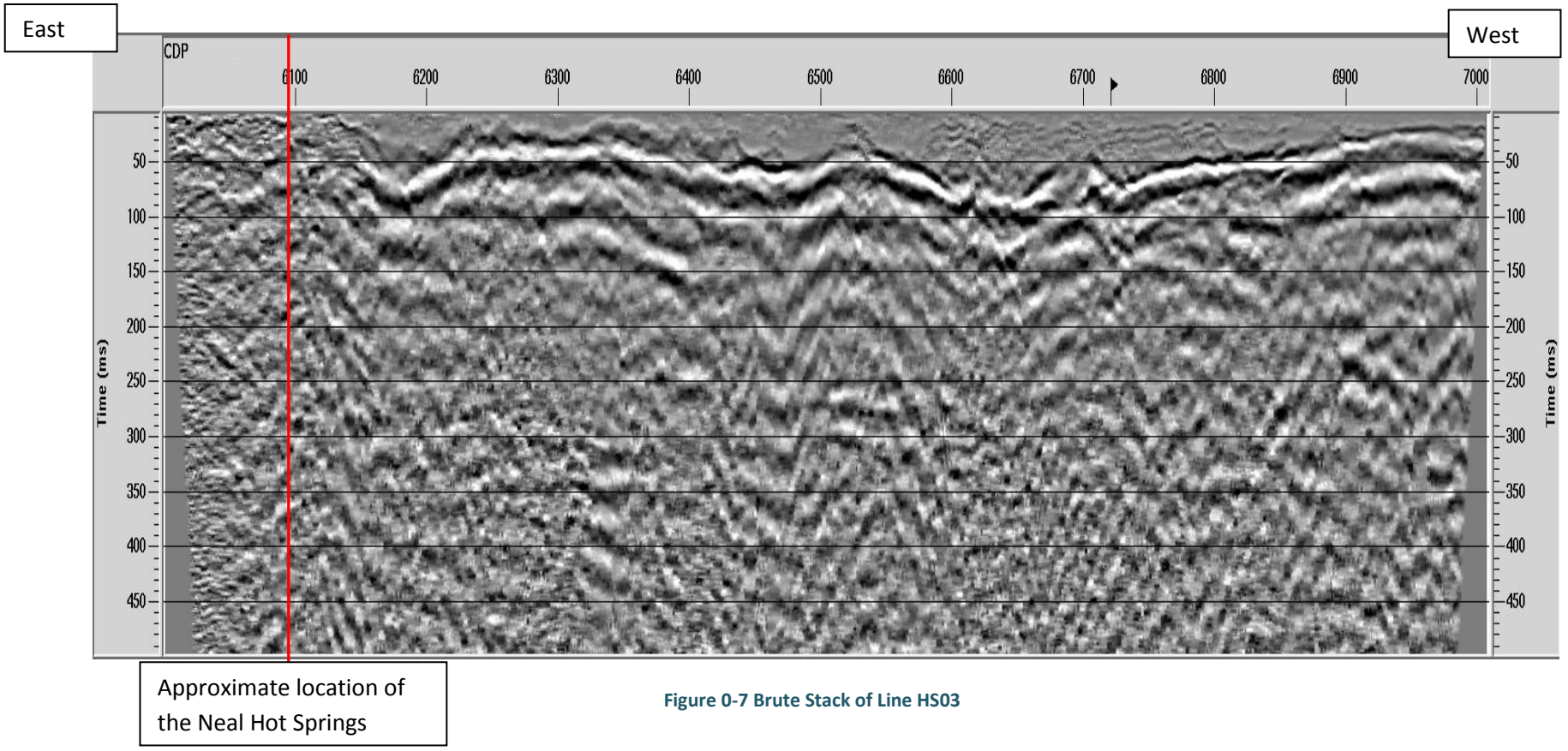

Figure 0-7 Brute Stack of Line HS03

10. Warm Spring Site

10.1 Introduction

As part of the field session, students had the opportunity to design and implement a survey. A lower temperature spring, found near the road to the northeast of Neal Hot Springs, was the target area chosen for the student-designed survey site. This spring was named the Warm Spring (WS) and it lies in a stream system with a temperature of approximately 30°C. The location of the site of investigation is illustrated in Figure 10-1.

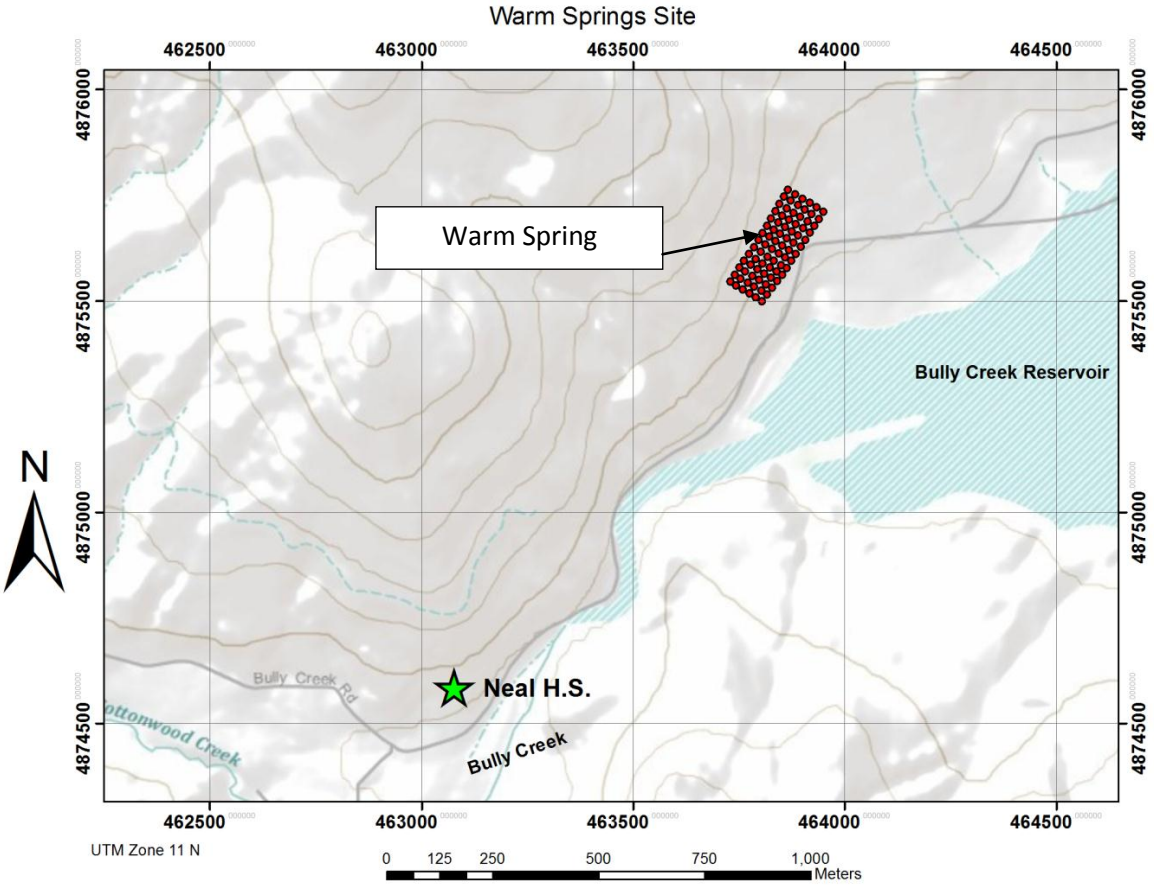

Figure 10-1 Location Map of the Warm Spring site

On investigation of the hillside to the northwest of the Warm Spring, a large volcanic outcrop was found and identified as an intrusive body. Based on observations at the outcrop, there appears to be a fault which dips to the northeast, the opposite of the dip direction of the main fault at Neal Hot Springs. It is thought to be associated with the Eastern edge of the Horst block (Figure 10-2). Additionally, silicified rock outcrops near the Warm Spring site indicate the possibility of hot springs at the same location in recent geological history. A photograph of a sample from the field is shown in Figure 10-3. Therefore, the observed fault and hydrothermally altered rocks in conjunction with the presence of the Warm Spring gave justification for this site.

Figure 10-2 Location of the Warm Spring (WS) and the Associated Horst Structure

Figure 10-3 Silicified, Hydrothermally Altered, Rock

10.2 Objectives

- Map the fault.
- Discover how fluid flows in the subsurface to create the Warm Spring.
- Hypothesize a reason for the lower temperature of the Warm Spring compared to Neal Hot Springs.

10.3 Survey Design

Several geophysical methods were utilized to achieve the outlined objectives: electromagnetic, gravity, magnetic, self-potential, and resistivity surveying. A shallow point in the subsurface was chosen as the survey target, and a grid was setup accordingly. The design and size of the grid was based on the resistivity survey because of limited equipment. Forward modeling determined the depth of penetration for various surveys and allowed for the selection of appropriate parameters. The model assumed a fault filled with material of low resistivity, 20 Ohm-meters (Ohm-m), with volcanic rocks of high resistivity, 1000 Ohm-m, composing the footwall, and sediments of lower resistivity, 300 Ohm-m, as the hanging wall. Figure 10-4 and Figure 10-5 illustrate the forward modeling of both the Wenner and Dipole-

Dipole arrays using 28 electrodes spaced at 10m as well as the input synthetic model described above. The modeling predicts a depth of penetration of 46.7m for both arrays, an appropriate depth of investigation for the survey objectives. A maximum of six lines of each array could be surveyed in the time allotted.

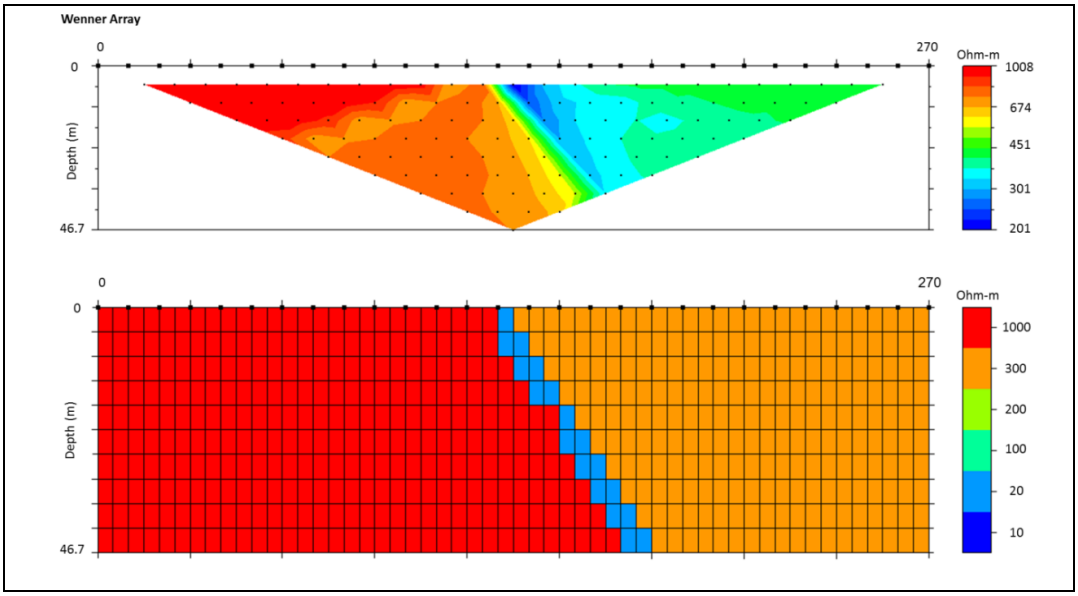

Figure 10-4 Forward Modeling of the Wenner Array. 28 electrodes, 10 m electrode spacing. Synthetic model represents a fault in the center with volcanic rocks to the left and sediments to the right, as hypothesized.

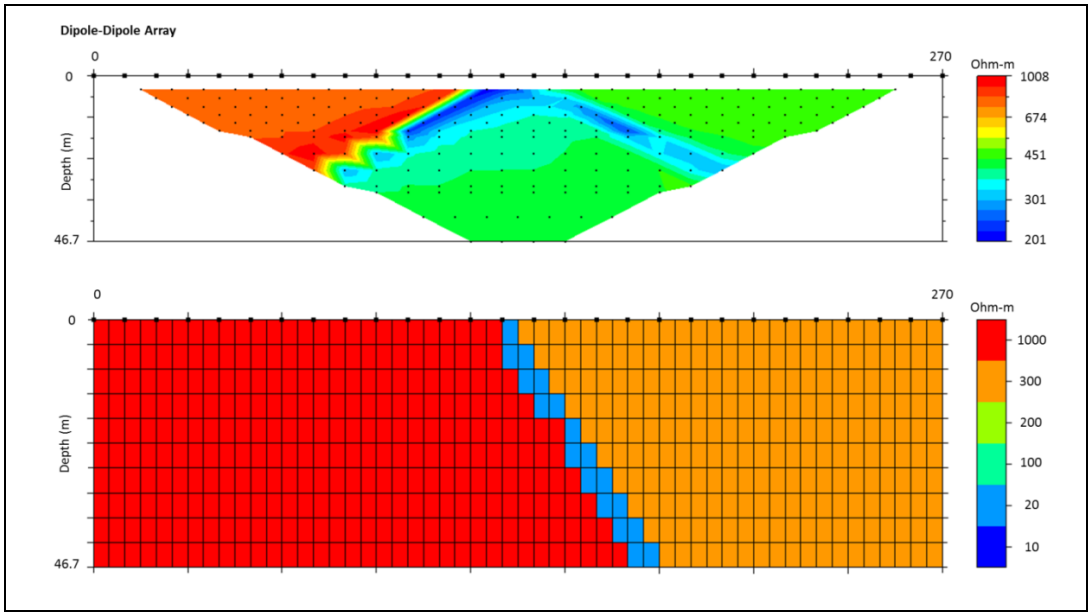

Figure 10-5 Forward Modeling of the Dipole-Dipole Array. 28 electrodes, 10 m electrode spacing. Same synthetic model used as above.

Originally, the grid was centered over the hypothesized fault. The 200 by 100 m grid shown in Figure 10-4 consisted of six lines spaced 20m apart, and oriented in a roughly northeast-southwest direction. Non-metallic flags marked in 20m increments, are depicted by blue dots in Figure 10-6. The electromagnetic, magnetic, and gravity surveys followed this grid. The additional yellow points in Figure 10-6 indicate an extension made to the grid for the resistivity and self-potential surveys. Each flag's location was recorded in UTM coordinates using a differential GPS, accurate to within 10m.

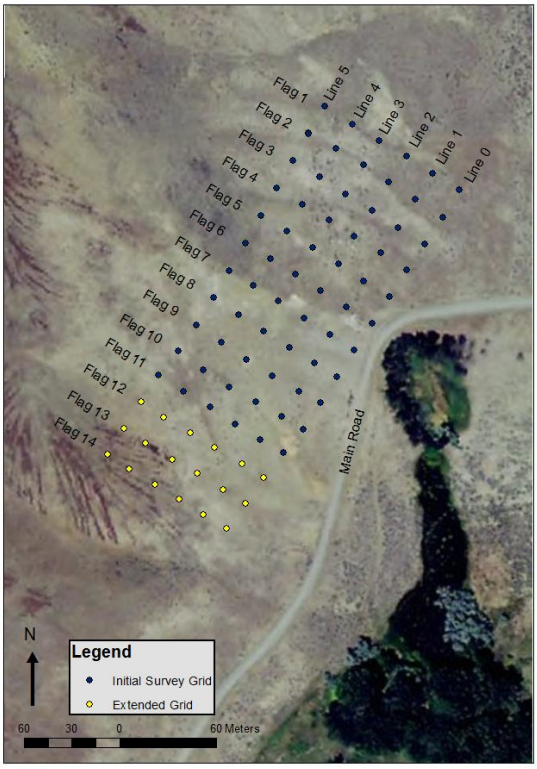

Figure 10-6 Grid Setup at the Warm Spring Site

10.4 Acquisition

The EM survey was performed using the Geonics EM31. Students covered the six flagged lines, collecting data continuously and marking each flag. Five additional lines centered between flagged lines made for a total of 11 lines. A metal fence cutting through the northern end of the grid shortened lines northwest of Line 3, as the metal would influence EM measurements.

The magnetic survey utilized a Cesium Magnetometer, and followed the same path as the electromagnetic survey. The magnetometer sensors, separated by 0.75m, were oriented with a vertical gradient. Throughout the survey, the top sensor was carried roughly 1.3m above ground, and the bottom sensor roughly 0.55m.

The gravity survey used the Lacoste and Romberg (L&R) gravimeter. Time restrictions limited readings to Lines 0, 2, and 4 and a 40m spacing (i.e. every other flagged point), where the L&R was leveled and counter readings were manually recorded.

The self-potential (SP) and resistivity surveys covered the extended grid. SP measurements were at flagged locations and midpoints between flags (10m increments), on all marked lines. The SP reference electrode was buried near Line 0. Only Line 0 was completed on the first day of surveying the Warm Spring. All equipment was packed up for the night, and the reference electrode was reburied on day two, in the same location, for completion of Lines 1-5.

The resistivity survey implemented the Super Sting R8 IP Earth Resistivity Meter. The survey followed a series of parallel lines. 28 electrodes separated by 10m were hammered into the ground and connected by a cable. Saltwater was poured into the ground surrounding the electrodes to make for better contact, and more conductive coupling with the ground. Because the forward modeling suggested that different arrays may produce different results, both Wenner and Dipole-Dipole arrays were used on each line. Once complete, the entire array of cables and electrodes was moved to the next line, where measurements proceeded.

10.5 2007 Gravity Data

A gravity survey was conducted in 2007 by Geothermal Inc. across the whole of the Neal Hot Springs site. It has been inverted using Gzinv3d which was created at UBC-GIF based on Li and Oldenburg, 1998 (Algorithm Teaching License was provided to CSM-CGEM for academic use only). As a result a regional density model has been created and is shown in Figure 10-7. This figure illustrates the location of the Warm Spring site in relation to the Neal hot springs. It shows the canyon that is present between the two sites (the low density area), which is interpreted as being part of the Horst structure and possibly a secondary fault within the greater horst structure. Figure 10-8 is the map view of the same model.

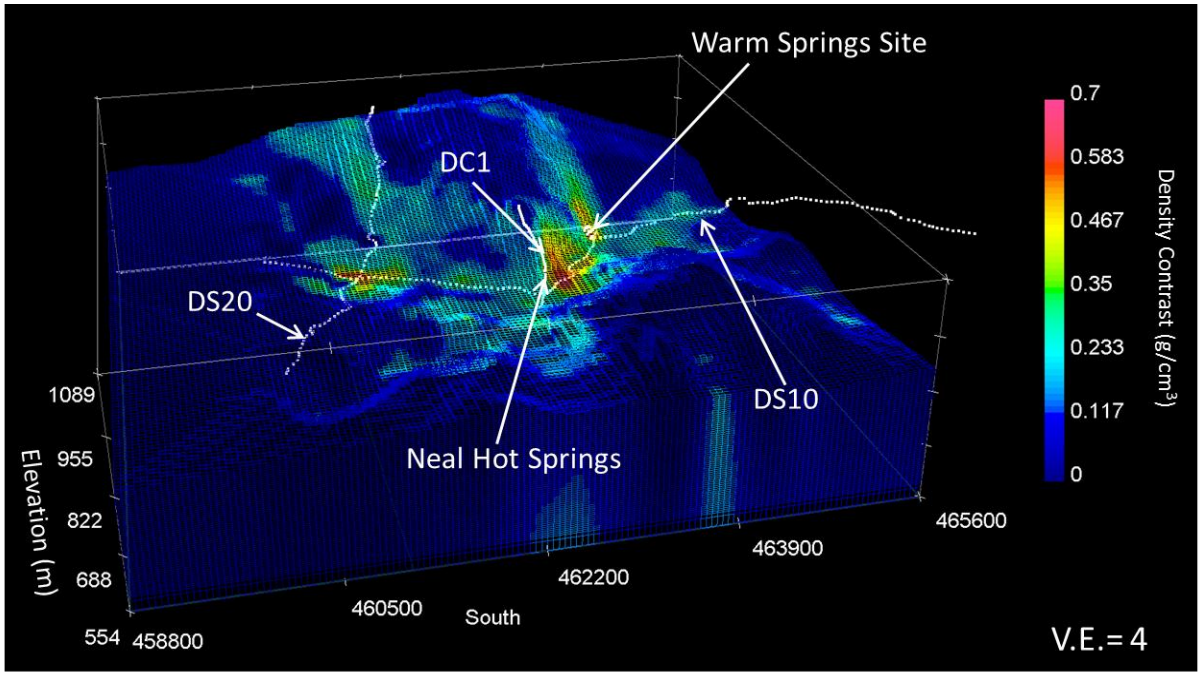

Figure 10-7 Regional Density Model. 3D inversion of 2007 gravity data [*Geothermal, Inc*.].Gzinv3d, created at UBC-GIF based on [*Li and Oldenburg, 1998*] Algorithm Teaching License provided to CSM-CGEM for academic use only.

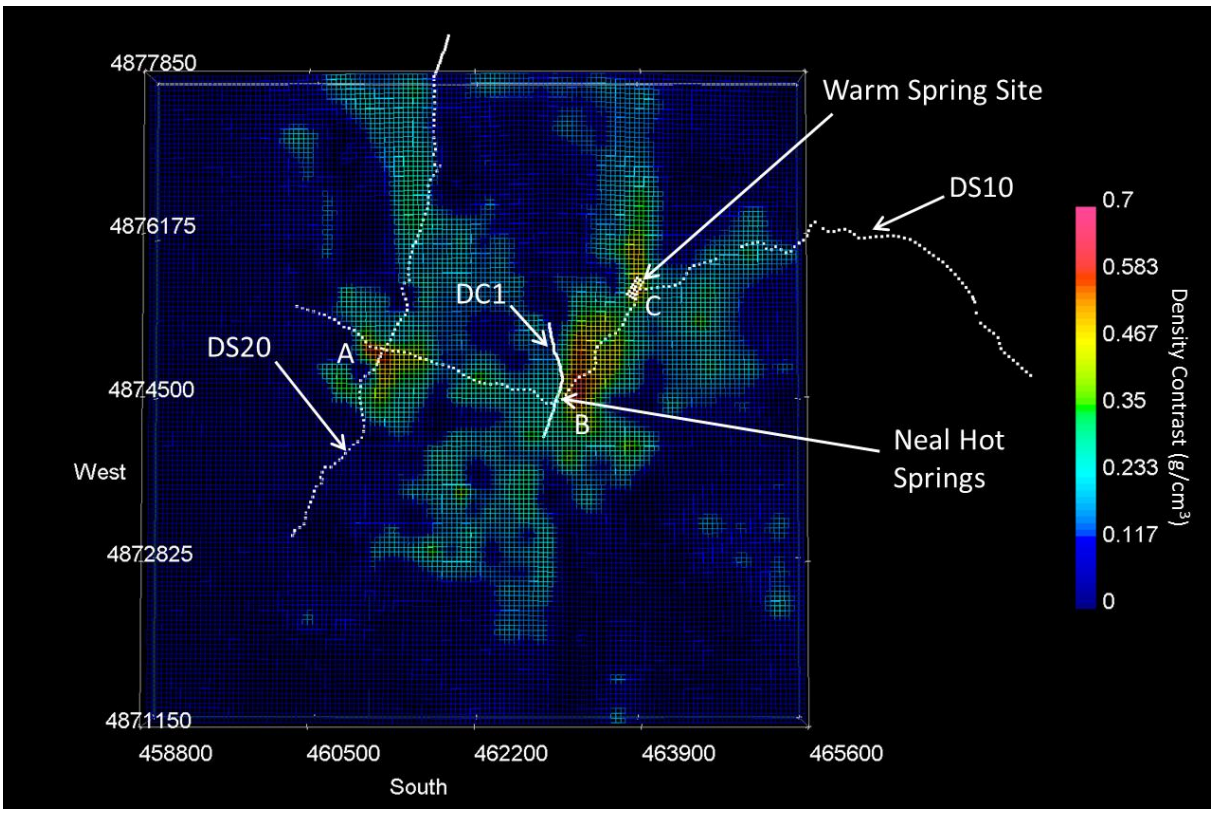

Figure 10-8 Regional Density Model in Map View. 3D inversion of 2007 gravity data [*Geothermal, Inc*].Gzinv3d, created at UBC-GIF based on [*Li and Oldenburg, 1998*] Algorithm Teaching License provided to CSM-CGEM for academic use only.

From the above two figures it is clear that although the Warm Spring grid was setup to be perpendicular to the observed feature in the field, there is a larger, regional density anomaly which runs approximately North-South. The grid has been placed to the Western edge of this North-South trending anomaly. It is expected therefore that there will be trends in this sense seen in the data as well as from the fault observed. Figure 10-9 is a cross-section through B-C as indicated on Figure 10-8. The high density contrast to the east of the Neal Hot Springs represents the volcanic rocks that outcrop in the canyon and form part of the Horst structure. There is then a drop in density contrast before an increase to a second, smaller anomaly at the Warm Spring site. It is the western edge of this that the grid is placed over.

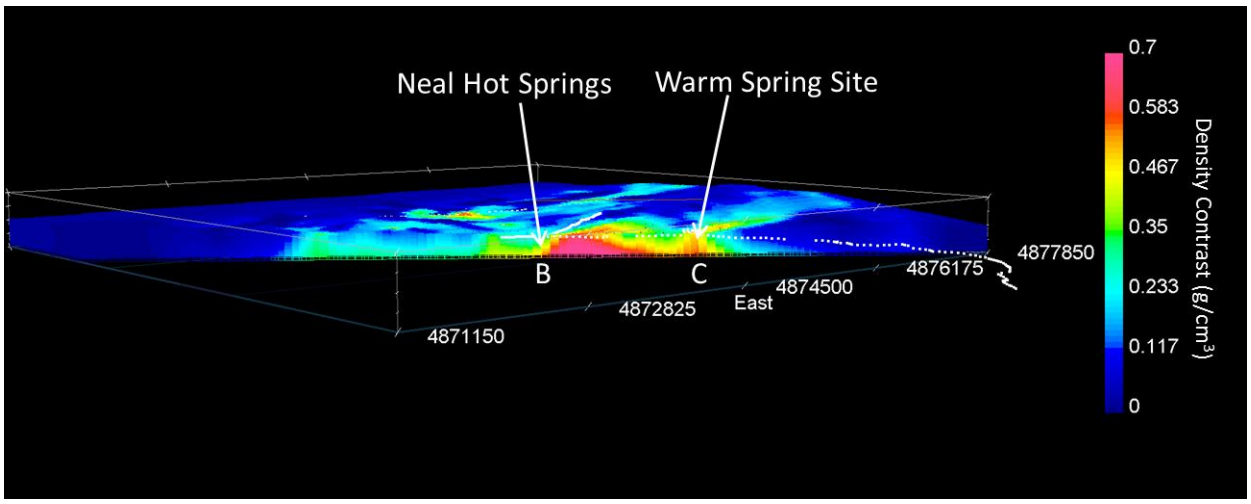

Figure 10-9 Cross Section through the density model between Neal Hot Springs and the Warm Spring Site. 3D inversion of 2007 gravity data (Geothermal, Inc.).Gzinv3d, created at UBC-GIF based on (Li and Oldenburg, 1998) Algorithm Teaching License provided to CSM-CGEM for academic use only.

These figures from the inversion of the 2007 gravity data provide a third target for the survey. The first is the observed fault, the second is the Warm Spring and the third is now the North-South trending density anomaly, connected to the main Horst structure.

10.6 Processing

10.6.1 EM-31

The electromagnetic data acquired at the Warm Spring was recorded using the Geonics EM31 instrument. The survey began at flag 11, line 0, and was obtained along each line with marks made every 20m, at each flag. Four of the survey lines were cut short because of the

presence of a metal fence in the survey area. Geonics Dat31W software was used to process the results. Initially, the data were organized as indicated by Figure 10-10.

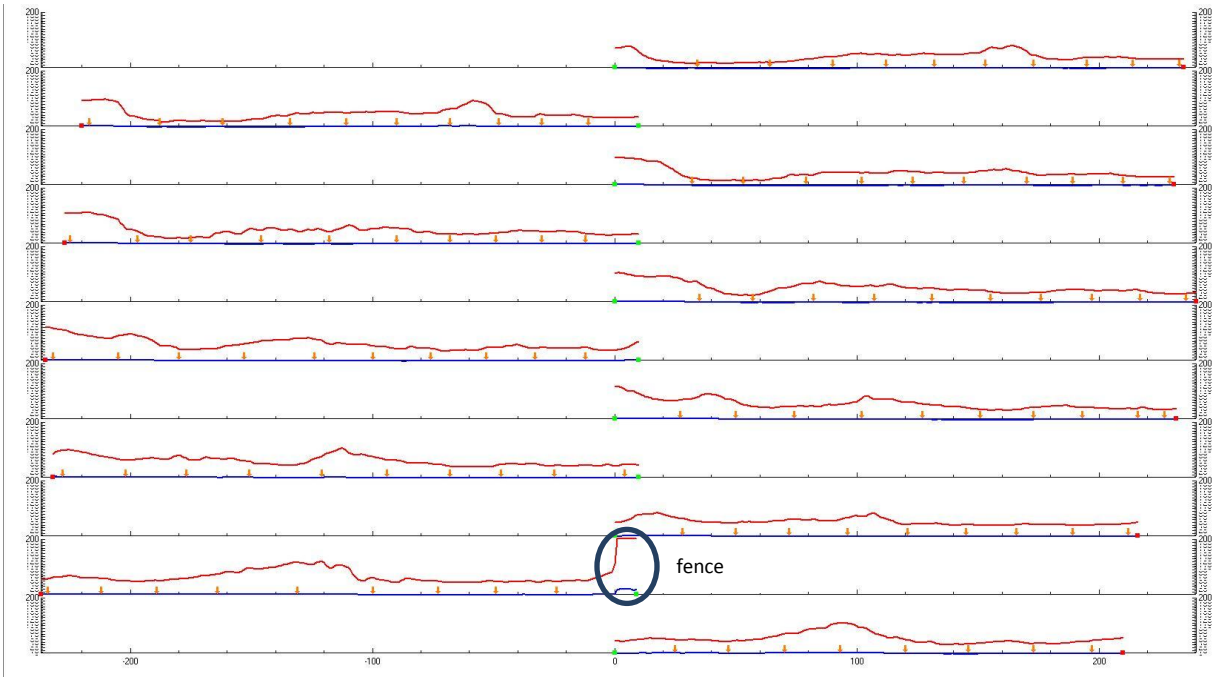

Figure 10-10 Initial EM31 Data Set

The lines were organized so they lined up at every mark of 10m. Each line began at the same point, but the last four lines were cut short due to the metal fence. The unusual jump in the data of Line 10 is because the survey got too close to the fence. Therefore, the data affected by the fence were not included in the mapping and overall survey. Figure 10-11 displays the adjusted lines.

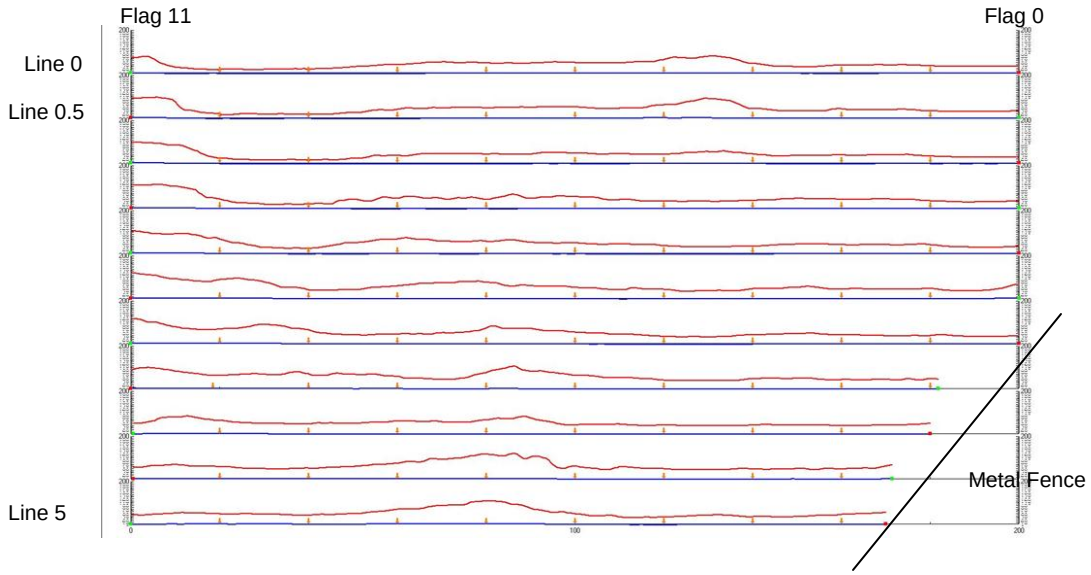

Figure 10-11 Adjusted EM Lines

Once the data were correctly formatted in xyz format, it was interpolated and plotted using Surfer 9. The gridded data show a large amount of heading errors resulting from the parallel-lined structure of the acquisition. These were corrected for by leveling and smoothing the grid. Next the data were re-gridded by the minimum curvature method. This was first plotted locally and then rotated 56 degrees counterclockwise using the CGEMaestro software. The plotted data are shown in Figure 10-12 and Figure 10-13.

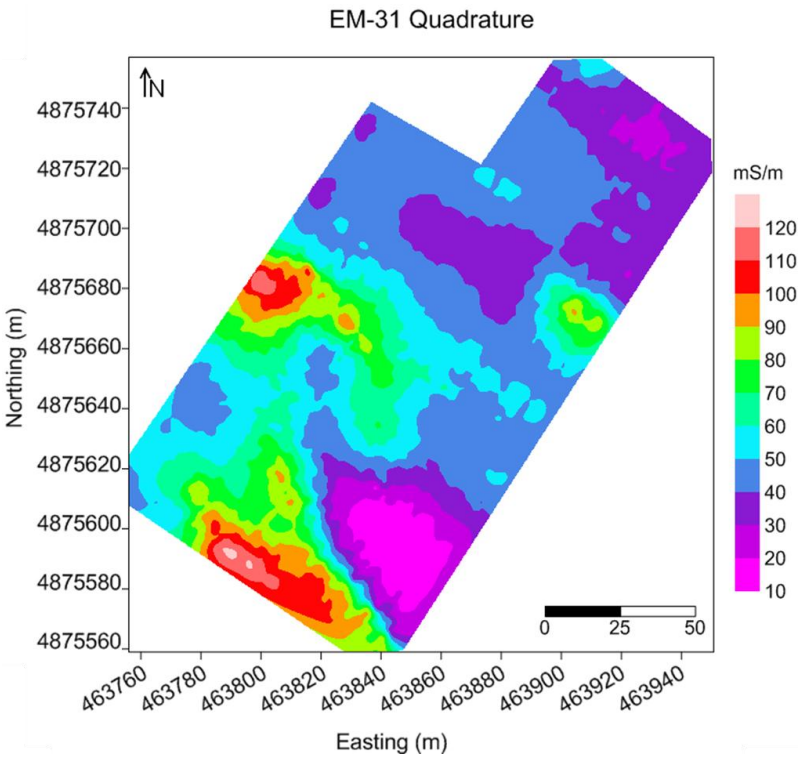

Figure 10-12 EM31 Shallow Survey Site Quadrature

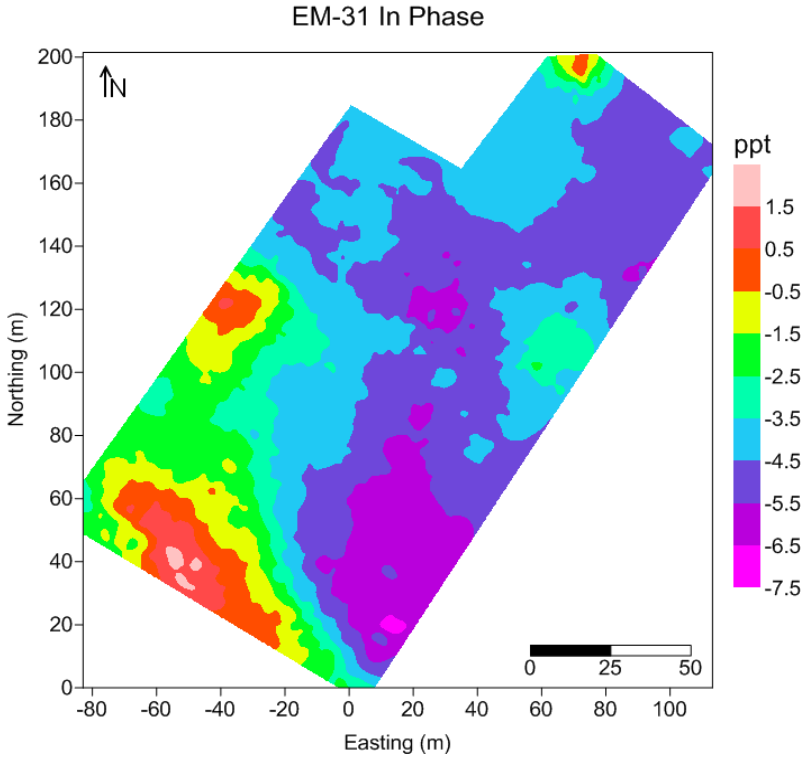

Figure 10-13 EM31 Shallow Survey Site In-Phase

10.6.2 Magnetics

The magnetic data acquired at the shallow site were recorded with a cesium vapor magnetometer. The data consist of 11 parallel lines forming a grid of 200m by 100m. Each line is 200m long, with mark points every 20m. The line separation is 10m. The first step in the processing was to re-order the data downloaded from the magnetometer to maintain consistency with the survey grid. This was done with the software MagMap2000 (Geometrics Inc.). Due to errors in the acquisition, the data initially looked as shown in Figure 10-14. This figure shows only 10 recorded lines instead of the 11 grid lines, and the first line is twice as long as the following lines. The start of the second line was not marked during the acquisition, producing this error. To amend this problem, the first recorded line was split into line 0 and line 1. Furthermore, some lines are shorter than others. Line 3 is shorter because a mark point had been missed during the acquisition. Lines 7 to 10 have been truncated because of the presence of a metal fence.

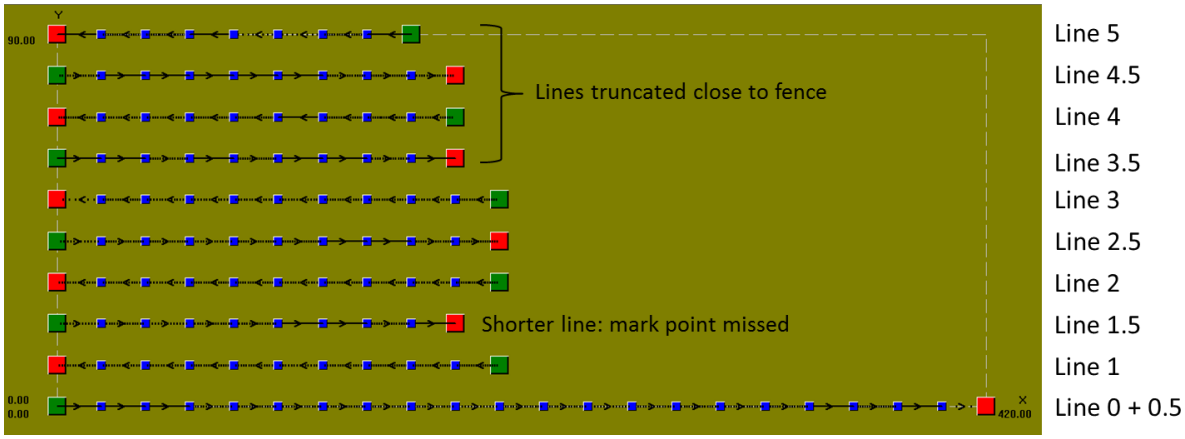

Figure 10-14 Data Ordering as Downloaded from the Magnetometer.

Based on the notes taken in the field, the acquisition grid was reconstructed as shown in Figure 10-15. Once the data were ordered, a diurnal correction was applied, based on the base station readings of that day (Figure 10-16). The base station was located at 44° 1.505” N, 117° 24.073”E.

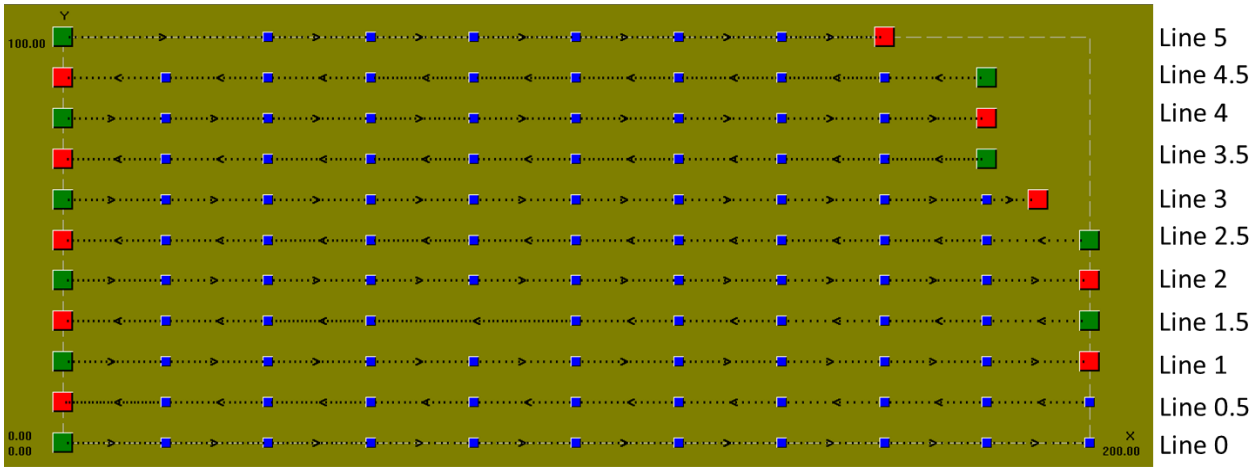

Figure 10-15 Magnetic Data Reorganized to Match the Survey Grid.

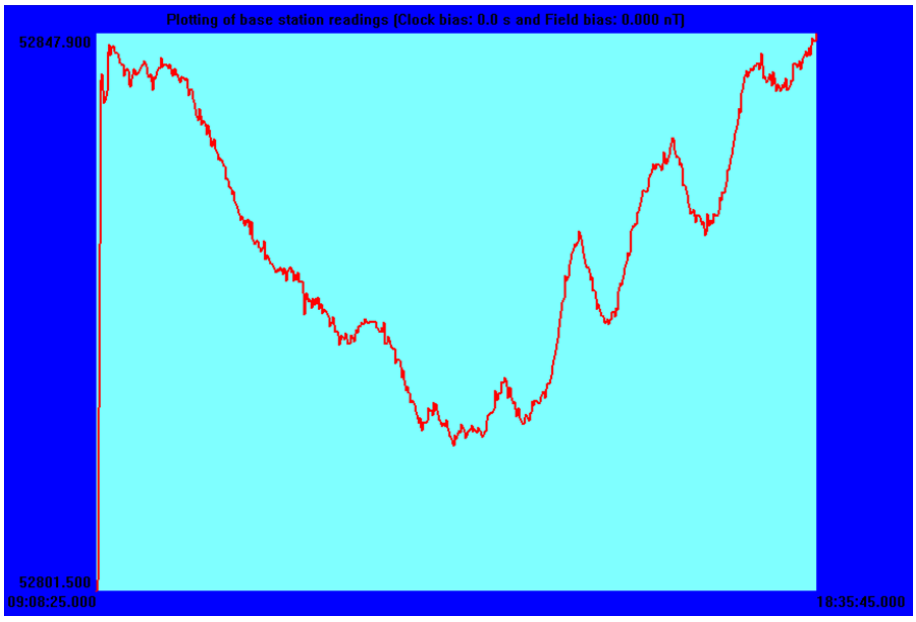

Figure 10-16 Magnetic Base Station Readings on 23/06/2011 in nT.

The data were then gridded and plotted using Surfer 9. The gridding was done using a minimum curvature gridding method and a grid spacing of 2.5m. In the first stage, the gridding was done on a local grid, with a length of 200m in the Easting direction and 100 m in Northing direction. Figure 10-17 shows the gridded total magnetic field measurements from the top-most sensor of the magnetometer. The orange dots represent the data-points. The strong anomaly at the two top-most lines probably results from the presence of a metal object at the surface, which was noticed during the acquisition.

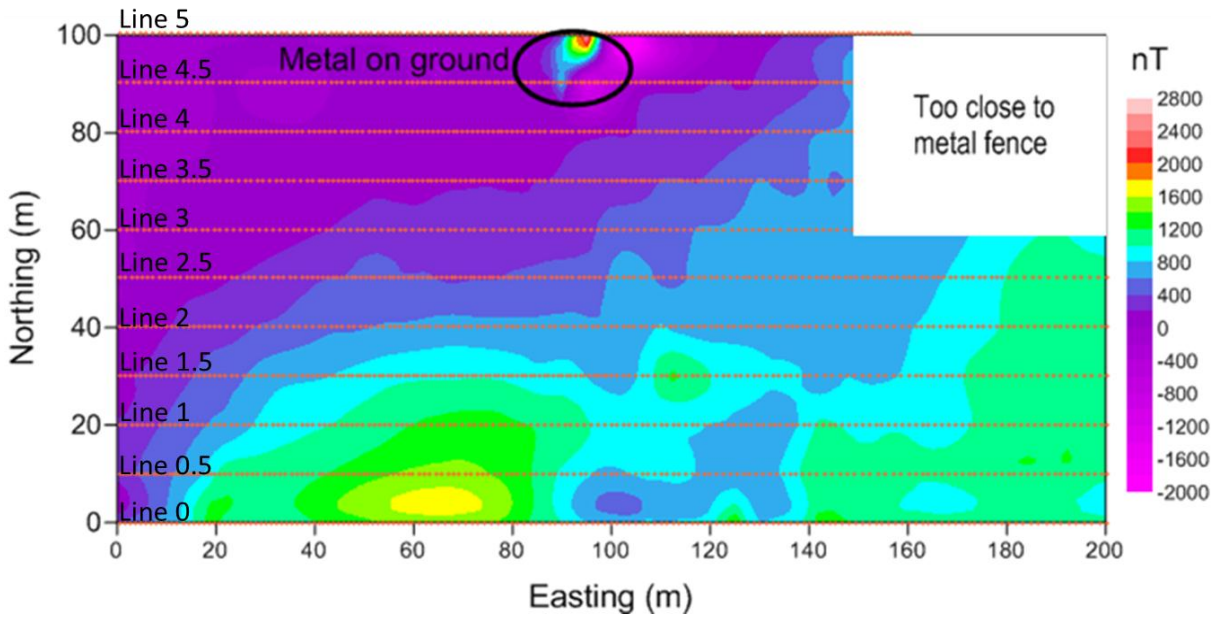

Figure 10-17 Total Magnetic Field Magnitude Measured from the Topmost Sensor of the Magnetometer. The orange dots represent the data-points.

After interpolation of the surveyed GPS coordinates the data were gridded with a coordinate grid. Figure 10-18 shows the results of this gridding for both the top and bottom sensor of the magnetometer. The data from the bottom sensor are slightly noisier than those from the top sensor. This is expected because the bottom sensor is situated closer to the surface and is hence more influenced by artifacts such as the presence of metal on the surface, changes in topography etc. Hence it was decided to continue only with the top sensor data.

Figure 10-19 is a plot of the vertical gradient of the total magnetic field, measured between the top and the bottom sensor of the magnetometer. The vertical gradient is hereby defined as the difference in intensity between the two sensors, divided by the distance between them. For a good gradient measurement, it is important to have no significant surface magnetic noise, as gradient anomalies tend to enhance the effect of shallow noise sources [*Breiner, 1999*]. Hence it is not unexpected that the vertical gradient map of the Warm Spring site is dominated by the effect of the metal object at the surface.

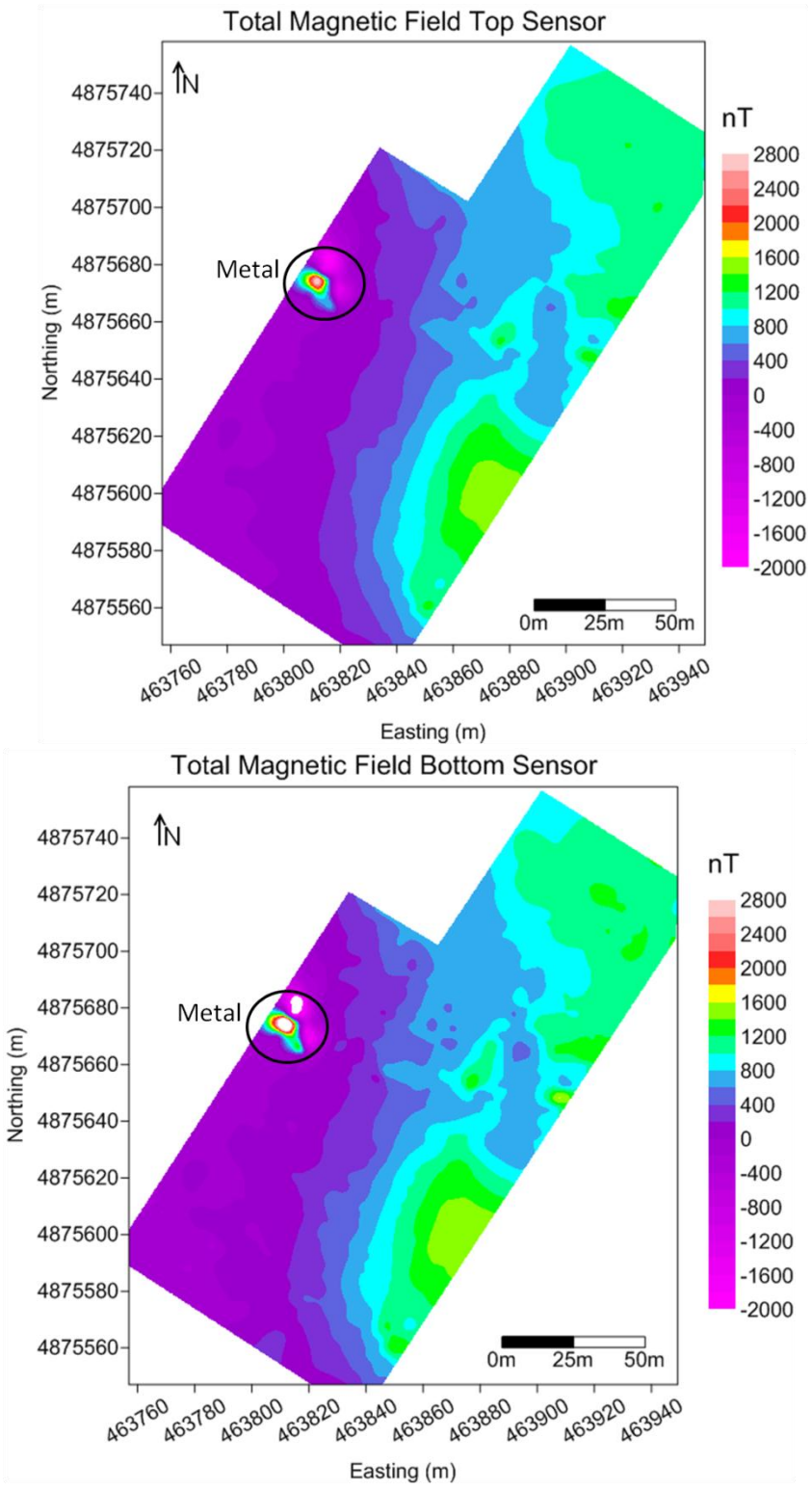

Figure 10-18 Gridded Total Magnetic Field Magnitude Measured with the Top and the Bottom Sensor of the Magnetometer. The bottom sensor data are slightly noisier.

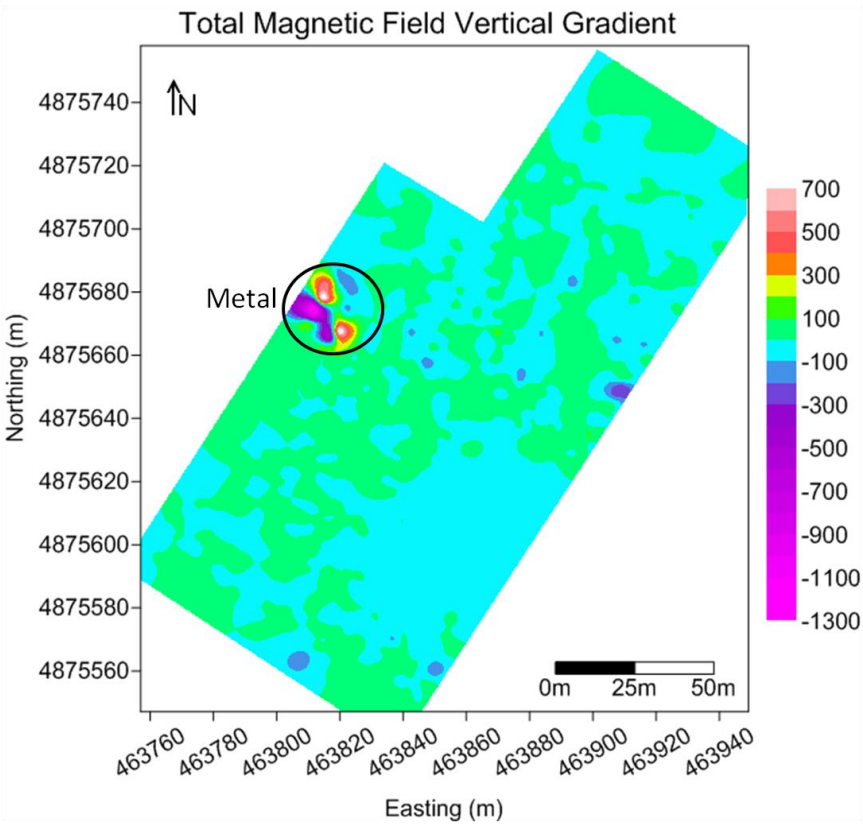

Figure 10-19 Grid of the Vertical Gradient of the Magnetic Susceptibility

10.6.3 Gravity

The gravity data collected at the Warm Spring site were processed and corrected simultaneously with the gravity data collected at the DS-10 line (see section 5.2.1 for more information on gravity processing). Hence the processing steps are not repeated in this section. Figure 10-20 shows the final processed gravity data over the Warm Spring site.

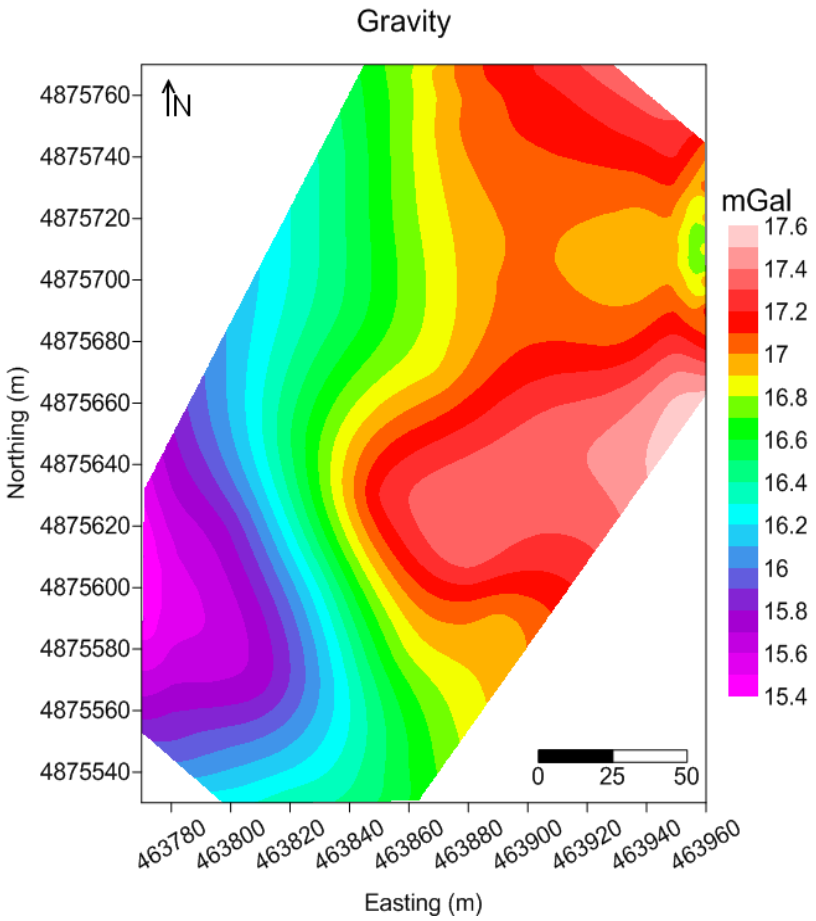

Figure 10-20 – Data from Gravity Survey of the Warm Spring

10.6.4 Self-Potential

A total of six SP lines with measurements every 10m were recorded as detailed in the survey design. The reference point was kept the same for all SP lines.

After completing the SP measurements, the raw SP dataset was processed and reconstructed with respect to the reference point. The SP measurement at the reference point

should ideally be equal to 0 mV. This was the SP value measured on the first day, when Line 0 was recorded. During the recording of the remaining five lines on Survey Day 2, the reference point reading was equal to -30 mV. The majority of the lines were recorded with respect to the reference value of – 30 mV, therefore a correction of -30 mV was applied to the first line only, i.e. Line 0.

After applying the above-mentioned corrections to the SP data, the data were presented in the form of graphs as a function of the distance or the altitude. These graphs are useful for the identification of discontinuities in the soil such as the circulation of fluids along faults, hydrothermal convection, etc. The program Surfer 9 was used to map the SP data after the initial evaluation of the graphs.

The creation of a data grid was the first step of SP data mapping. Acquisition of this data was inaccurate, so the resulting grid required conversion into an evenly spaced grid prior to mapping in Surfer. The Kriging method was applied to a file containing the SP measurements with the corresponding X and Y UTM coordinates to generate the corrected grid. The Kriging method is a statistical method for interpolation and correlation of data. For this purpose, a Variogram was generated using a Nugget Effect model, as shown in Figure 10-21.

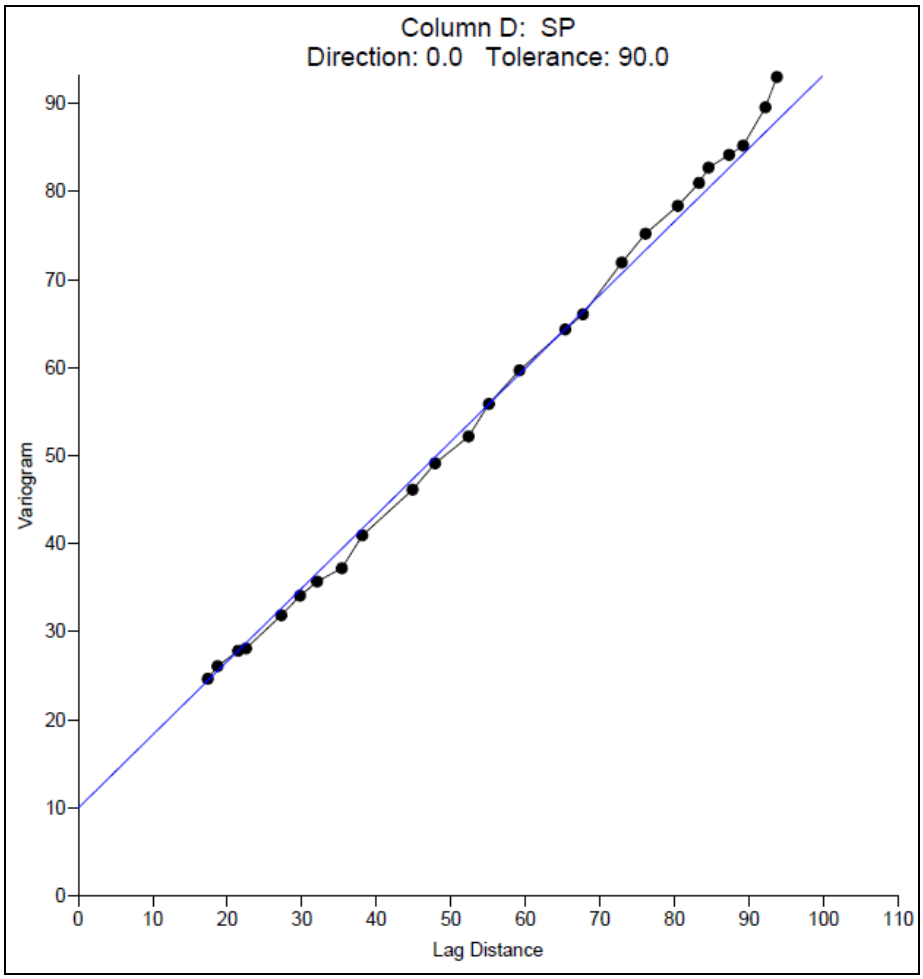

Figure 10-21 Variogram generated using Nugget model

After the creation of the grid, a map of the gridded data was plotted (Figure 10-22). The black crosses represent the SP measurement points overlain on the gridded data map. The portion of the map outside of the SP data point grid has been blanked. Additionally, a contour map has been generated to better visualize the distribution of the SP anomalies and to highlight the SP transitions (Figure 10-23).

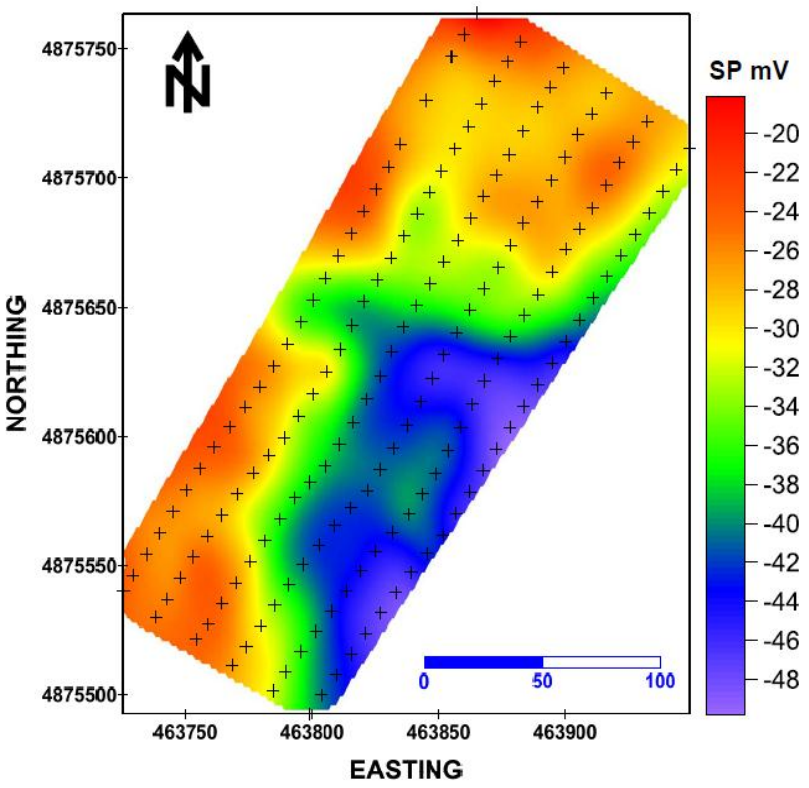

Figure 10-22 Image Map Overlain by Data Points

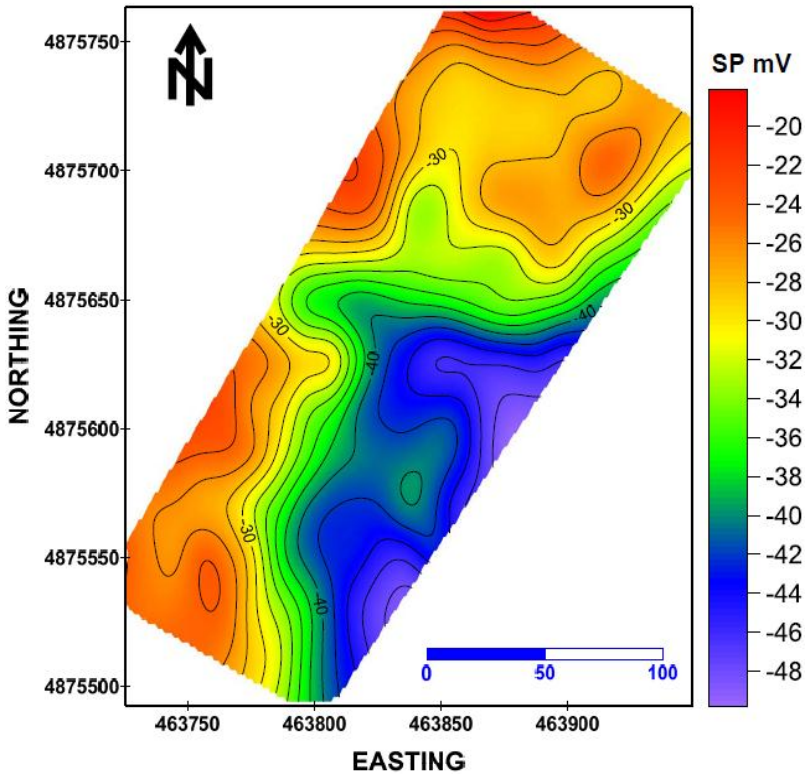

Figure 10-23 Contour Map of SP Measurements

The generated SP image and contour map can also be overlaid on a digital elevation model (DEM) as shown in Figure 10-24. This shows the distribution of the SP measurements with respect to the elevation.

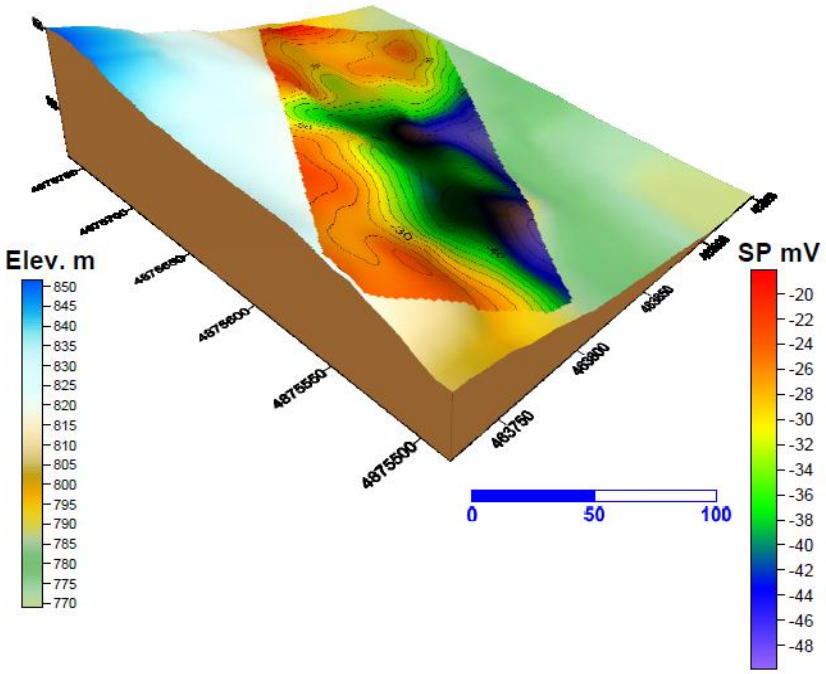

Figure 10-24 SP image map overlain on a DEM

10.6.5 Resistivity

Processing the DC resistivity data from the Super Sting initially involved rearranging it into a format readable by a specific inversion software package. The two programs used were RES2DINV and DCINV3D, and these two programs require different data organization. Advanced Geosciences Inc., the Super Sting manufacturer, produces its own software to invert the Super Sting data; however, this software was unavailable for the survey.

The first step of data processing was the evaluation of the STG files created by the Super Sting. All negative values were removed from the STG files; negative resistivity values have no physical meaning and therefore represent data acquisition errors. The data were then organized according to the format required by each program and converted to DAT files. Refer to section 6.2 for a description of the processing and inversion of the data with RES3DINV.

The format used by DCINV3D requires the use of a program, 'stgtodat', to convert the STG files to DAT files. The DAT files were then reformatted according to the DCINV3D manual (IPINV3D, 2000). DCINV3D requires a standard deviation value be calculated for each measurement (Equation 10-1). The value .001 was added to ensure that values with 0% error would be assigned a standard deviation number (IPINV3D, 2000). In addition to the data file, a topography file and a mesh file were required for use by the DCINV3D. The topography file used a local 270m-100m grid for a simpler inversion. The mesh file contained a dense, 2.5m to 5m cubic-celled, three-dimensional mesh in the center, representing the data acquisition area. Surrounding this zone was a looser mesh of padding cells using 10m intervals. These files were created according to the formatting parameters in the DCIP3D Manual (IPINV3D, 2000).

Equation 10-1 Standard Deviation

$$\sigma = \frac{V}{I} \times \%Error + .001$$

Where σ is standard deviation, V is voltage, and I is current

10.7 3D Inversion

Inversions were used to construct three-dimensional physical property models from the magnetic and DC surveys. An attempt was made to invert the gravity data, but time and data constraints prevented the success of these results. Inversion methods first incorporate a 3D discretized mesh model. This model is the basis of imaging the subsurface properties with inversion. A minimizing function (Equation 10-2) is then used to create an inversion model consistent with the geology and collected data. The regularization parameter, β, is arbitrarily chosen several times to run multiple inversions. These inversions generate an "L-Curve". The "L-Curve" separates the inversions which model the data noise, also known as the data misfit (ϕ_d), and the achieved model norm, ϕ_m. The most reasonable regularization parameter, indicated by the arrow in Figure 10-25, may now be modeled on the mesh. The choice of regularization parameter prevents the creation of an overly complex or simplistic geological model. Complex models result from the "L-Curve" fitting solely the data noise; simplistic models have "L-Curves" that follow the achieved model norm.

Equation 10-2 Error Minimization

$$\phi = \phi_d + \beta\phi_m$$

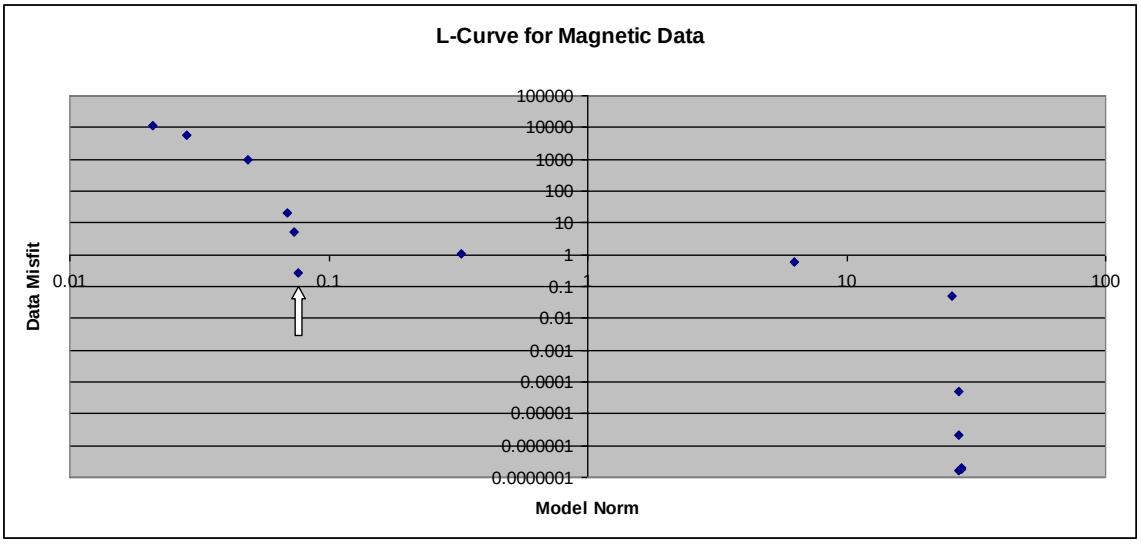

Figure 10-25 L-Curve for Magnetic Data

The 3D inversion software for interpretation of gravity, magnetic and resistivity data was created at the University of British Colombia's Geophysical Inversion Facility. The programs MAGINV3D [*Li and Oldenburg, 1996*], GZINV3D [*Li and Oldenburg, 1998*] and DCINV3D [*Li and Oldenburg, 2000*] were used for 3D generalized inversions formulated by Tikhonov regularization. These packages were made available to CSM-CGEM for academic purposes.

10.8 Results and Discussion

In this section, the results of the different methods applied on the Warm Spring site will be discussed and compared, followed by an overall conclusion.

10.8.1 EM-31

The EM-31 quadrature image (Figure 10-26) shows values of high conductivity at the SW side of the survey grid and values of low conductivity at the NE side. These features may indicate the presence of conductive sediments in the SW and resistive magmatic rocks at the NE side. Furthermore, two main structures have been recognized and interpreted as faults.

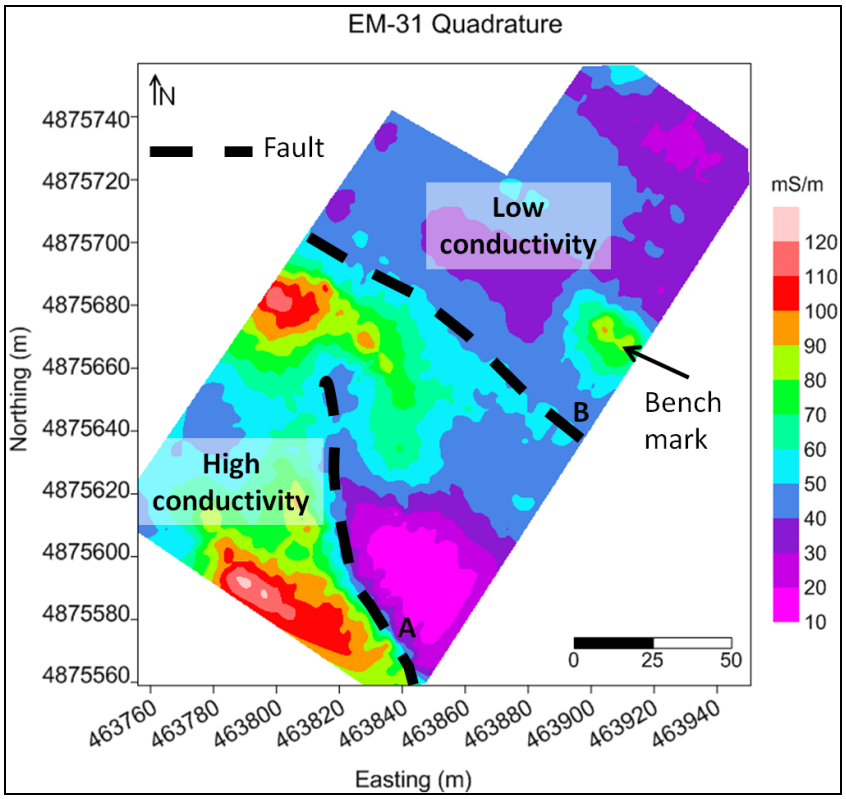

Figure 10-26 Interpreted Grid of EM-31 Data

10.8.2 Magnetic data

The total magnetic field magnitude grid (Figure 10-27) shows a low magnitude in the SW of the Warm Spring area and an increased magnitude towards the NE of the area. The two structural trends interpreted from the EM-31 data are also visible on the magnetic field grid. The 3D inversion of the total magnetic field data resulted in a 3D model of the magnetic susceptibility (Figure 10-28). The actual data points are located in the survey grid that is outlined by the blue box. The surrounding gridding cells are padding cells created during the inversion; therefore, their values are extrapolations. The 3D data show the same trends and features as the grid of the total magnetic field. This reinforces the interpretation of the sediments present at the SW side of the area and the magmatic rocks at the NE side. It also provides more confidence to the interpretation of fault locations.

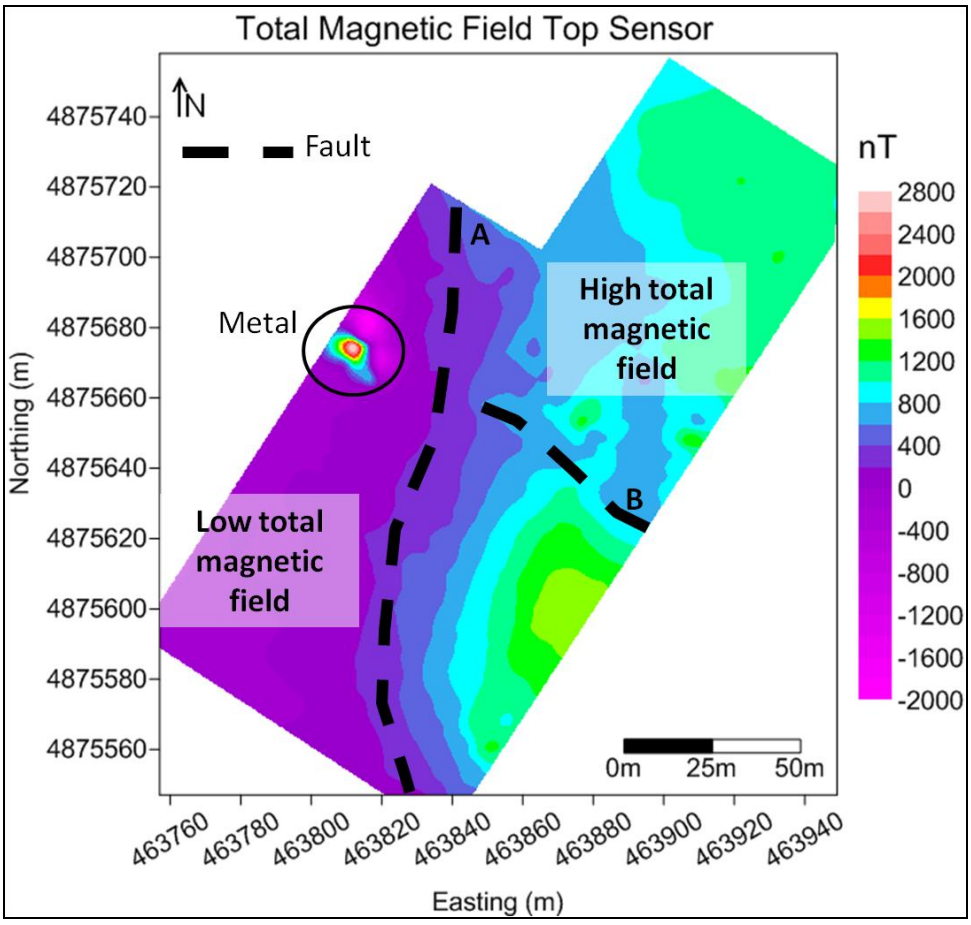

Figure 10-27 Interpretation of the Gridded Total Magnetic Field Data

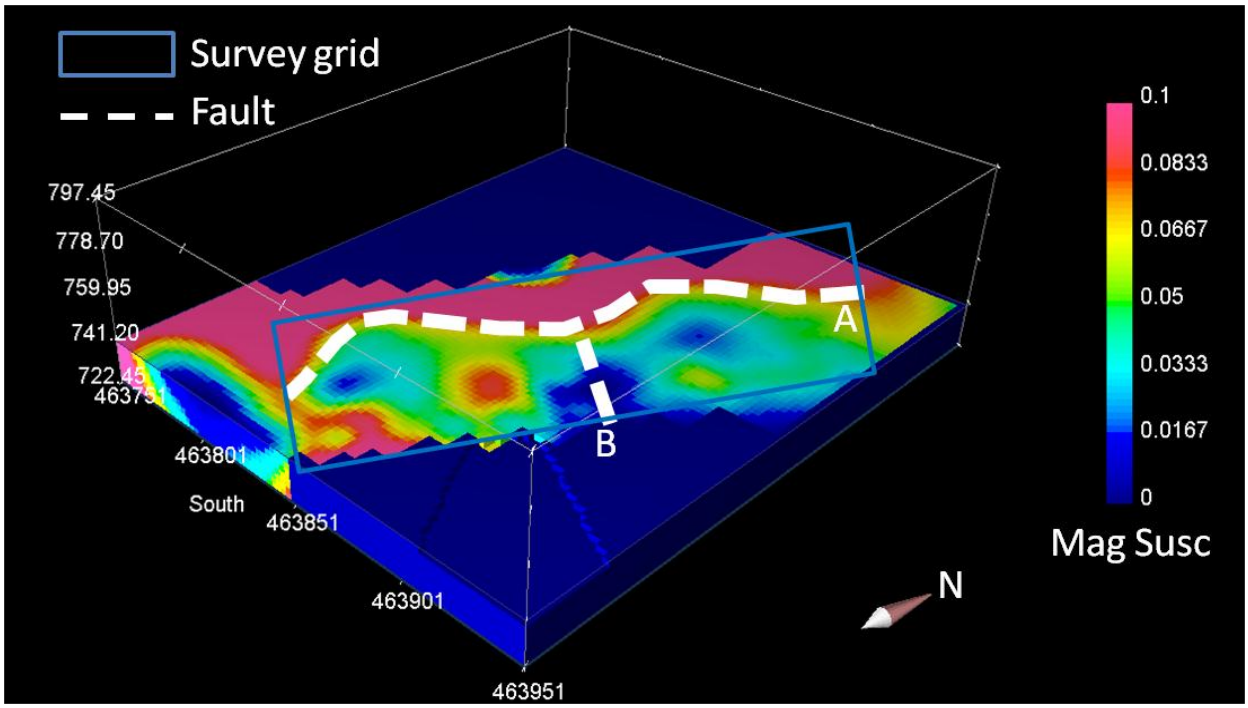

Figure 10-28 3D Inversion of the Total Magnetic Field Model. This shows the distribution of the magnetic susceptibility in S.I. units using MAGINV3D software [*Li & Oldenburg 1996*]

Figure 10-29 shows the surface of highest magnetic susceptibility at the bottom of the model. This surface dips towards the east, which is consistent with the observed topography and shows that the horst is bounded by an eastwards dipping fault.

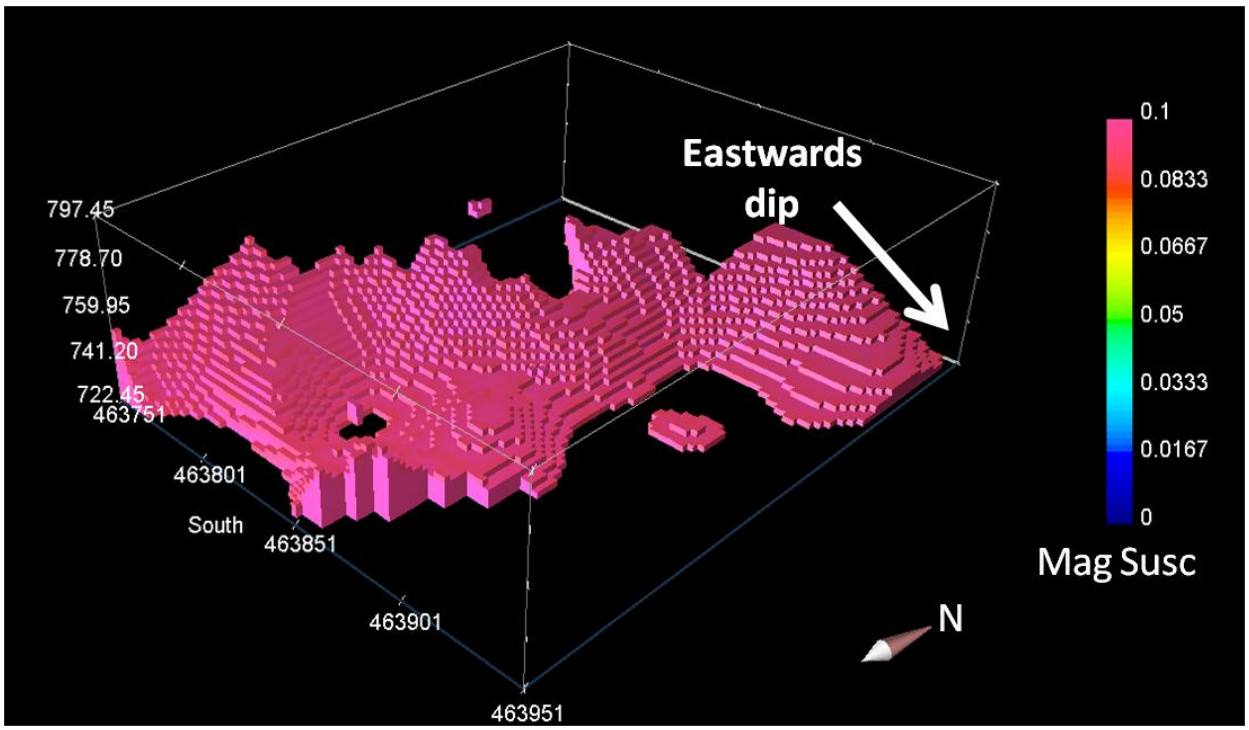

Figure 10-29 Extraction of the Model with a Susceptibility Larger than 0.09 using MAGINV3D Software [*Li & Oldenburg 1996*]

10.8.3 Gravity

Figure 10-30 shows the gridded gravity data recorded over the Warm Spring site. It is known from the regional gravity data acquired in 2007 by US Geothermal Inc. that the survey area is located on an overall high density anomaly. The data acquired over the Warm Spring site show a local variation, which consists of a lower density in the SW region compared to the NE region. This contrast in density coincides with the earlier interpretation of sediments present in the SW and magmatic rocks in the NE. The transition between these lithologies coincides with the location of Fault A as interpreted on the EM-31 and magnetic data.

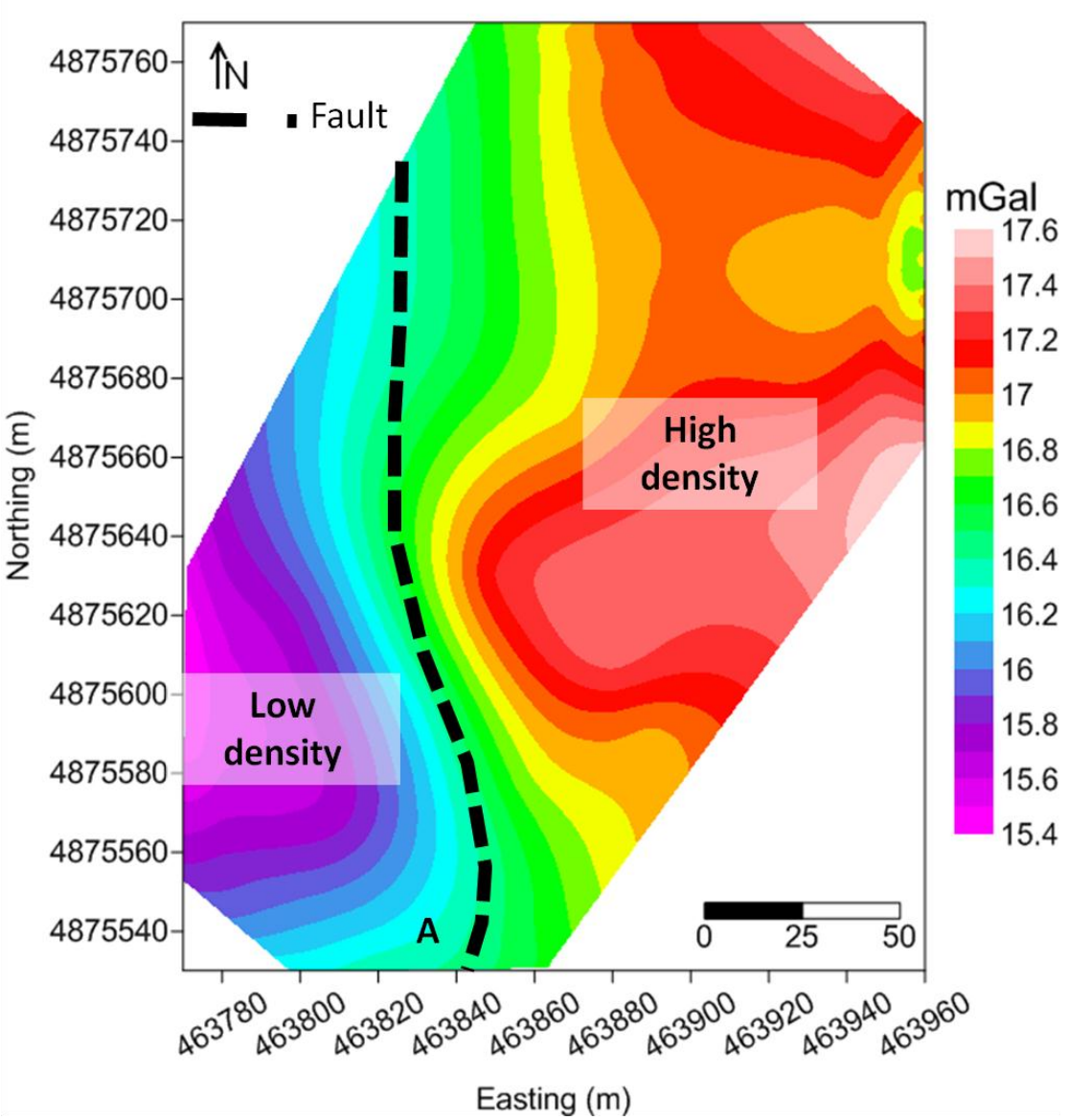

Figure 10-30 Grid of the Gravity Data Acquired Over the Warm Spring Site

10.8.4 Self Potential

The Self Potential grid was designed to observe the fluid movement along Fault A, the western boundary of the horst. The presence of a warm spring was the initial motivator to survey this locality; hydrothermal activity along a fault plane was predicted in the vicinity. Surface exposures of volcanic rocks coupled with silicified sinter deposits reinforced the initial theories as well as reveal the NW-SE strike of the fault.

The SP map (Figure 10-31) shows low SP values in the SW and NE and high SP values in the SE. The shallow depth of investigation makes it difficult to identify anomalies; however, two trends were extracted from the data. These trends may be artifacts of two faults with oblique orientations. Figure 10-32 shows anomalies of two types in the SP data. A small positive anomaly, Type-1, is the result of water upwelling along the fault plane. A negative anomaly, Type-2, has been attributed to ground water recharge.

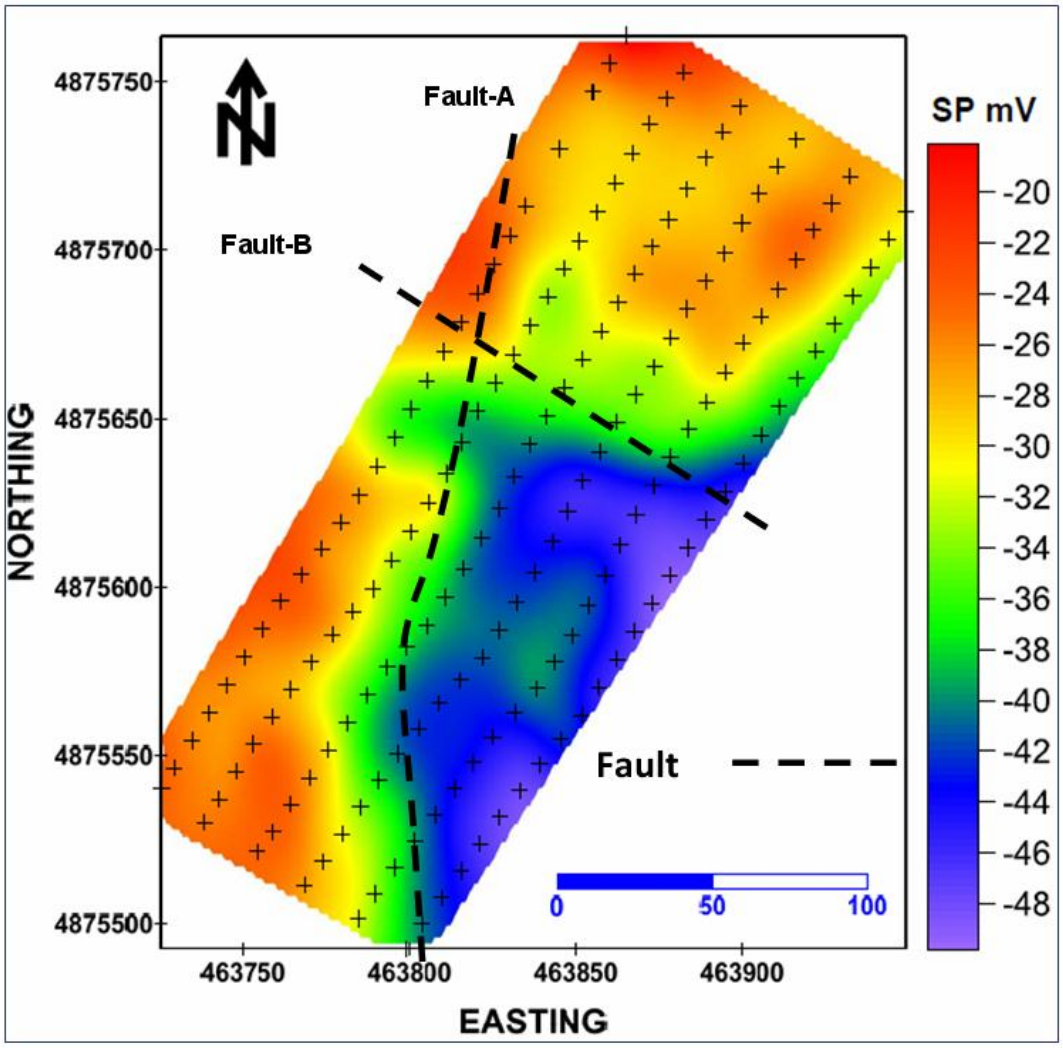

Figure 10-31 SP Map Showing Two Faults

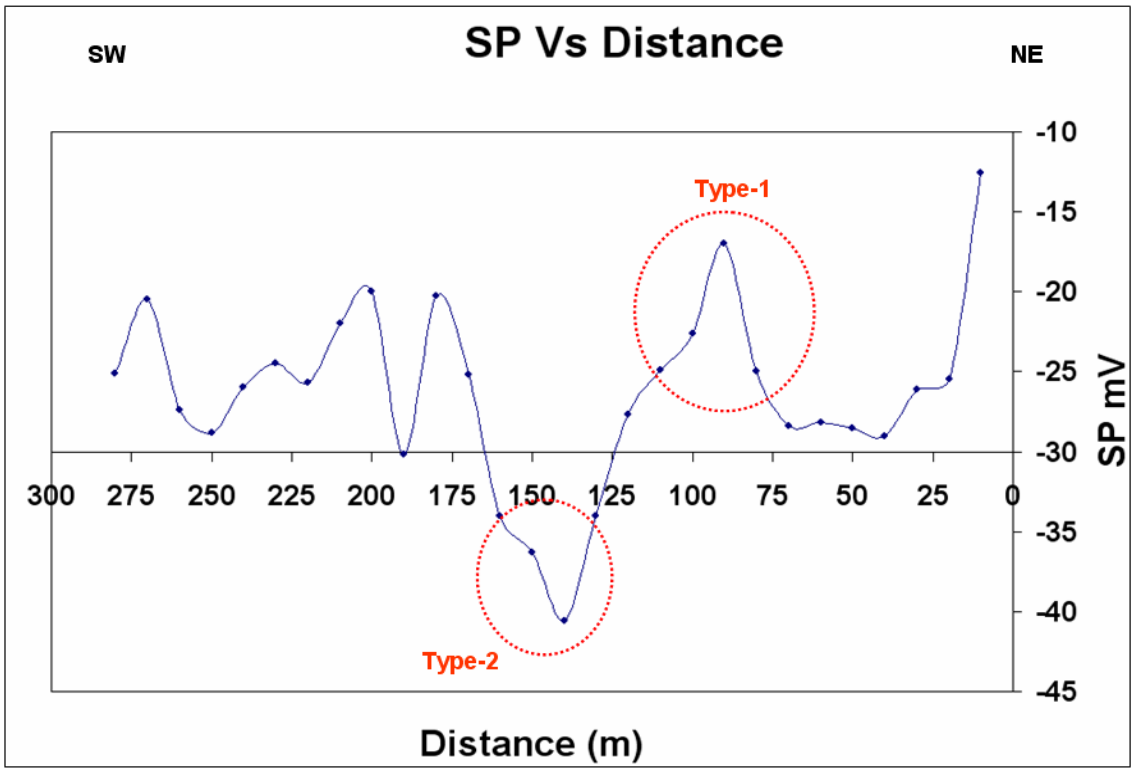

Figure 10-32 SP Anomalies Along 2D Profile 05

10.8.5 Resistivity

The surface conductivity map created from the resistivity data shows a region of high resistivity at the northeastern end of the grid and a conductive region in the southwestern end (Figure 10-33). Fault A is interpreted to run along the boundary between the conductive and resistive regions. In the orthographic view (Figure 10-34) the high resistivity region is seen to end at 10 to 30m depth. This implies that the resistive body may be overburden.

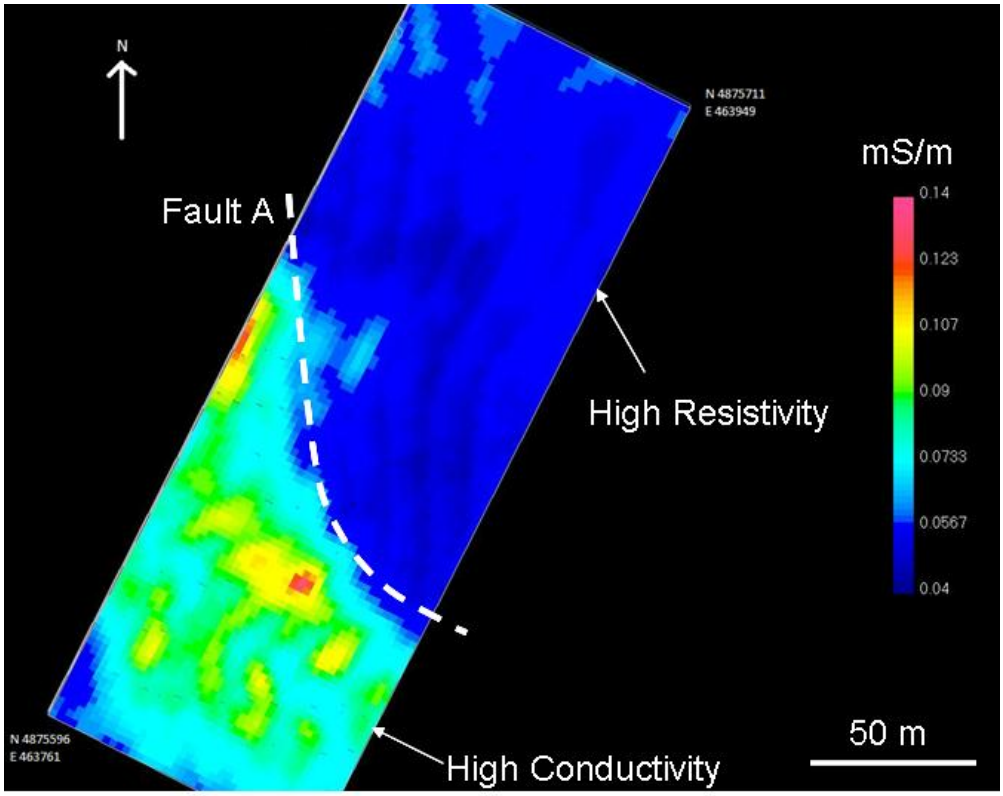

Figure 10-33 Surface Conductivity Map of the Shallow Survey Site

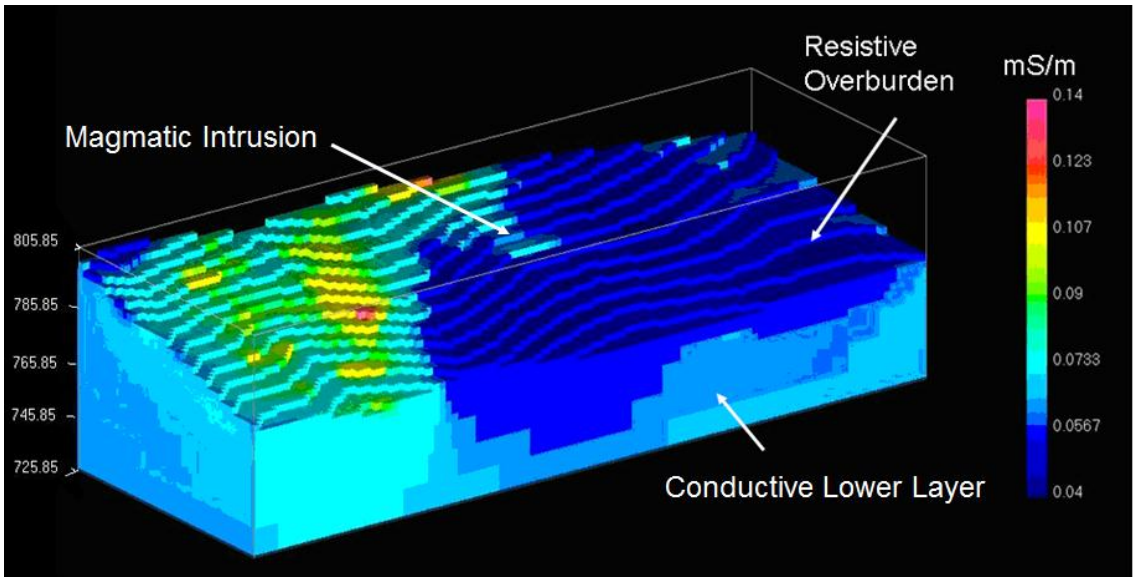

Figure 10-34 An Orthographic View of the 3D Conductivity Model

The conductivity data of the 3D model were compared against the conductivity data acquired by the EM31 (Figure 10-35). Though the grid size for the EM31 was significantly smaller, some distinct similarities are immediately apparent. Not only do the two methods

show similar conductivity contrasts between the northwestern and southeastern regions of the survey grid, but also they show the fault boundary at the same location. The only major distinction is a conductive region in the middle of the EM31 data that is not seen in the 3D model, though a smaller conductive feature in the 3D model (Figure 10-34) could correlate with the larger conductive structure in the EM31 data.

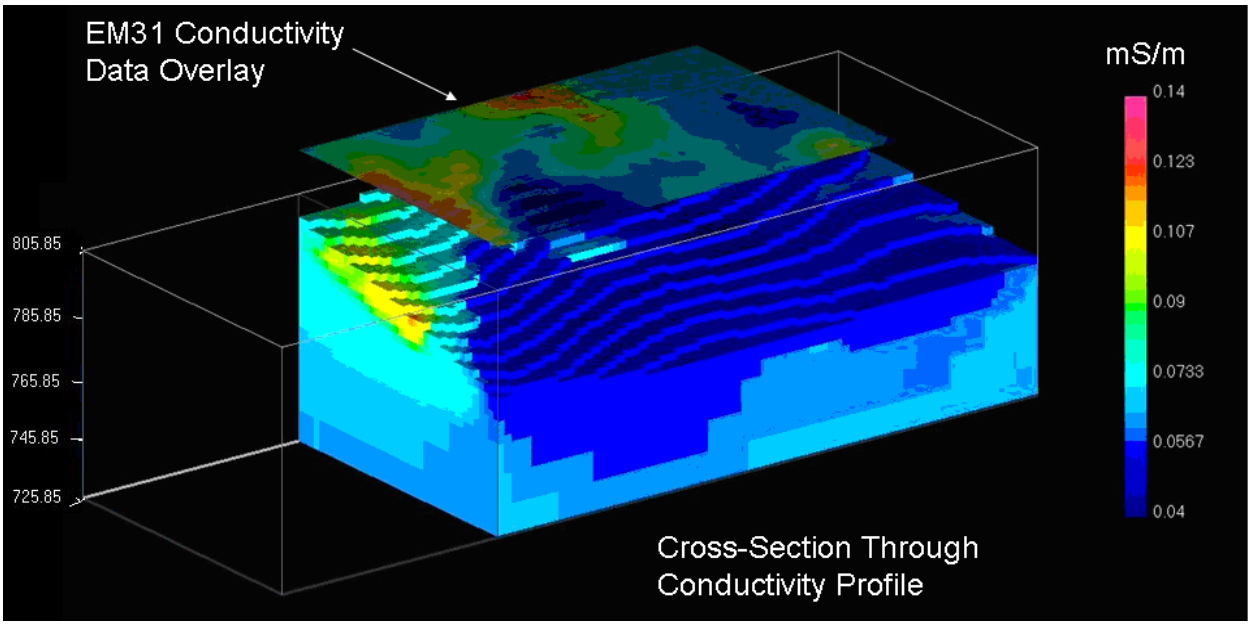

Figure 10-35 Cross-section through the Conductive Body is Overlaid by Data Taken from the EM31

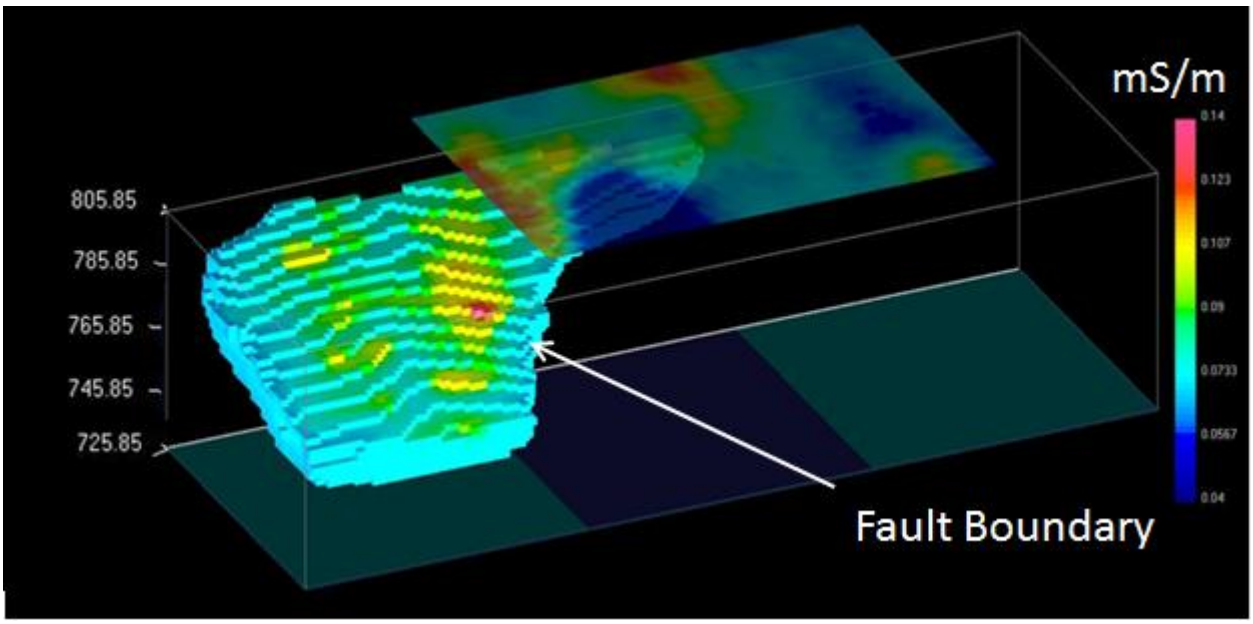

Figure 10-36 Cutoff Conductivity Profile with EM Conductivity Overlay

Figure 10-36 shows the shape of the highly conductive region as well as the correlation with the EM31 data. It appears as though the conductive region disappears with depth, though because of the limited depth of investigation of the Super Sting, this interpretation is questionable.

10.9 Conclusions

The different geophysical methods employed at the Warm Spring site yielded similar trends (Figure 10-37). Two faults were identified in the data: Fault A and Fault B. Fault A strikes NE-SW and dips to the east; it separates the sedimentary and igneous rocks. Fault B strikes NW-SE, extending locally from the intrusive body outcrop (refer to the geological map created by Mark Evans, section 3.2) to the Warm Spring. The survey grid was initially designed to investigate the physical properties associated with the predicted Fault B. However, the identification of Fault A correlates with geophysical data gathered in 2007 by US Geothermal Inc.

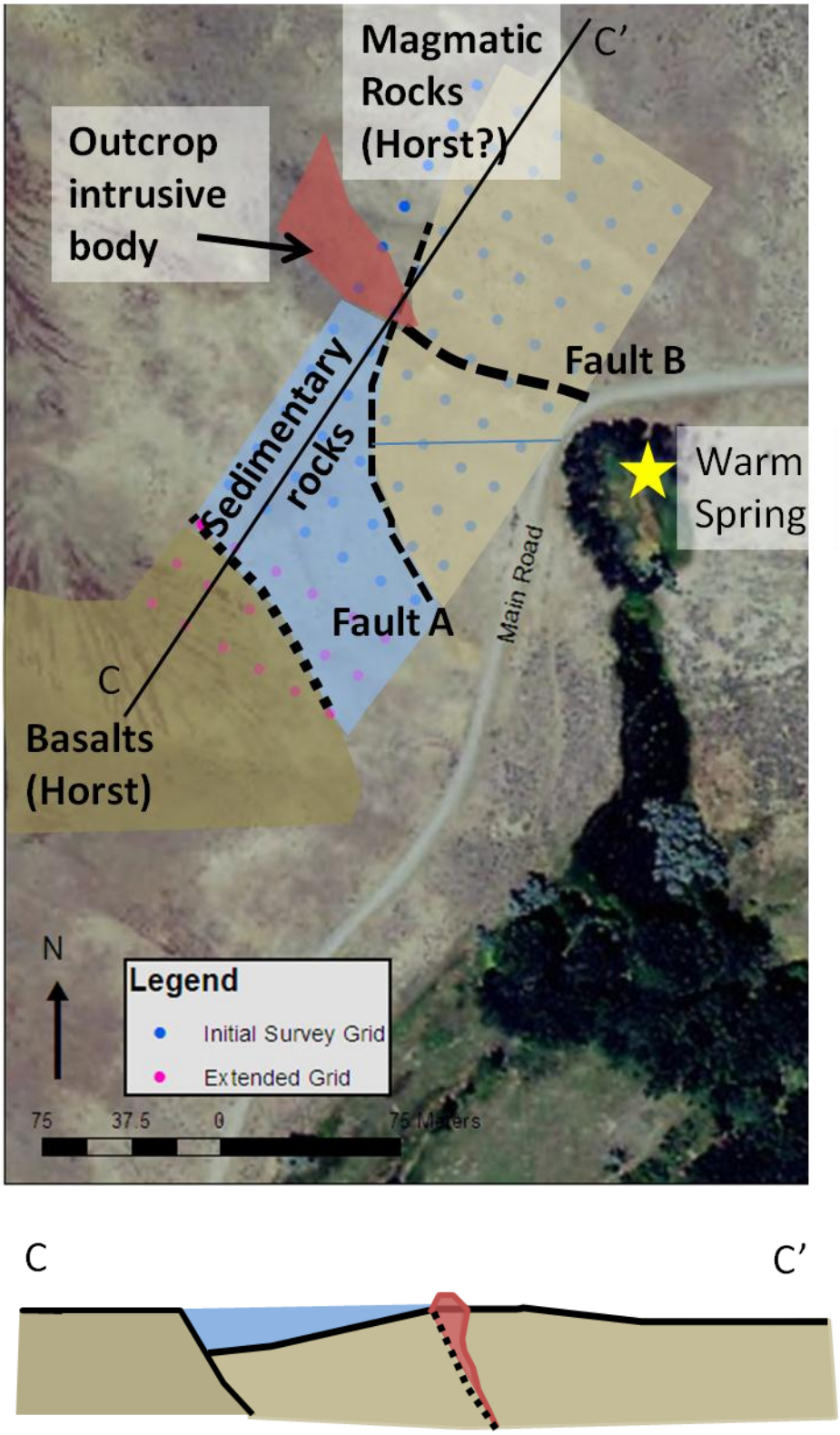

Figure 10-37 - Geological and Structural Interpretation Overlaid on an Aerial Photograph of the Warm Spring Survey Site

Furthermore there is potential fluid flow identified on the SP data, but this observation requires further analysis. Primarily because the observed anomaly was relatively small and the depth of investigation was limited.

It was not possible to identify the reason for the lower temperature of the Warm Spring compared to the Neal Hot Springs with the methods used. Distance from surface expression to heat source may have been a factor; however, this topic remains theoretical as the exact fluid pathways have not been defined.

Figure 10-37 indicates that the cross section developed from the surveys at the Warm Spring site is consistent with the anomalies identified by the 2007 US Geothermal survey. The cross section view is along the main line and the anomalies are evident in the other geophysical methods as well.

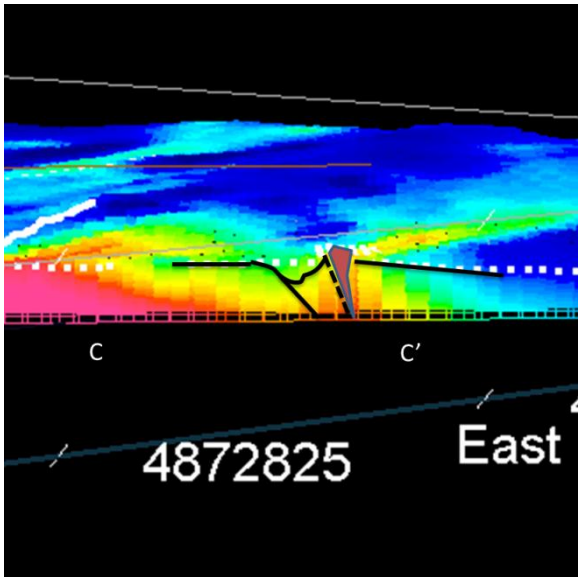

Figure 10-37 Cross Section from 2007 US Geothermal Survey, The overlay of the cross section developed from the Warm Spring survey

10.10 Recommendations

The Warm Spring survey could be improved in several ways. It is recommended to do a more detailed geological mapping of the area prior to the geophysical survey. This would make the geophysical interpretations easier and more consistent with the surface geology. Ideally the grid size should have been larger, providing a greater depth of investigation. This would have

made it possible to detect deeper fluid flow and the structural basement with greater confidence. Furthermore a larger gravity database would have enhanced the analysis of the gravity data and would have made a 3D inversion more accurate. Also, acquiring the SP data in a loop rather than a line scheme would have provided a closure of the measurements and a more accurate gridding. The Warm Spring survey site is located on an anomaly as indicated by the US Geothermal 2007 data. If the grid was extended, the anomaly could have been better defined relative to background levels and provided for a greater depth of investigation.

Finally it is recommended to spend time evaluating the collected data at the field location; this would render a first impression of the preliminary results and aid any decisions to adjust the grid or other parameters.

11. Additional Data

11.1 CSAMT

Controlled source audio magnetotellurics (CSAMT) devices use a high resolution electromagnetic sounding technique, which uses a fixed and grounded dipole as a source. The source dipole is used to transmit a controlled signal at a range of frequencies into the ground. The receivers, which are placed at a distance from the source, measure the induced electric and magnetic fields. The ratio of the horizontal electric (E_x) and magnetic field (H_y) values can then be used to calculate the resistivity structure of the subsurface [*Zonge, 1992*].

11.1.1 Acquisition

The setup for the CSAMT survey was designed as a multiple field reconnaissance survey. The source dipole was approximately 1 kilometer (km) long, with electrodes made of buried and layered tin foil saturated in salt water. The receiver array was set up parallel to the transmitter dipole, with 5 E_x channels and one H_y channel, with a receiver spacing of 50 meters. Measurements were taken at several different frequencies, ranging between 0.125 Hertz (Hz) and 8192 Hz, increasing by a factor of 2 for each successive measurement. The receiver channels themselves were devices called porous pots and essentially were ceramic pots with unglazed bottoms so that ions may travel through the bottom. The pots were filled with a copper sulfate ($CuSO_4$) solution, and an electrode. This setup allowed for effective communication between ground current flow and receiver current flow.

CSAMT acquisition began by connecting the source dipole, connecting the transmitter to the generator, and synchronizing the transmitter controller and the digital receiver. Next, CSAMT data acquisition took place in two separate lines of operation: with the source dipole operator and with the receiver array team. For the first measurement of a set, the source dipole operator's responsibilities consisted of powering on the generator, turning on the transmitter, setting the voltage and amperage of the current, and then transmitting the current. Subsequent measurements consisted of resetting the transmitter, changing the frequency of the current, resetting again, and then transmitting. Once at the receiver site, the

receiver array team began by laying out the cable spreads of 50 and 100 meter lengths, moistening the placement areas for the porous pots, placing and connecting the porous pots to the cables, connecting all cables to their respective channels, and starting the receiver software. Recording measurements consisted of setting the number of received iterations, the frequency band, starting the measurement, and then saving the results as long as the standard deviation of the reading was not excessively large.

Unfortunately, the CSAMT survey ran into multiple mechanical problems that inhibited users from collecting more than 200 meters of data. On the 20th of May, the original generator used to power the source dipole did not work, which led to no data being collected that day. On the afternoon of the 21st, the replacement generator began billowing smoke during operation. This occurred due to the large source amperage which the replacement generator could not support for an extended time. The current was reset to 4 Amperes (A), and later 2 A, which worked well for the rest of acquisition. The damage sustained during the 21st was significant, and on the 22nd, the secondary generator failed to operate. Table 11-1 shows the locations of the places where CSAMT data were able to be acquired, while Figure 11-1 shows the basic survey design for CSAMT.

Table 11-1 Locations of CSAMT Survey

Source dipole	Easting	Northing
1st transmitter electrode	0461197	4874874
2nd transmitter electrode	0460922	4873986

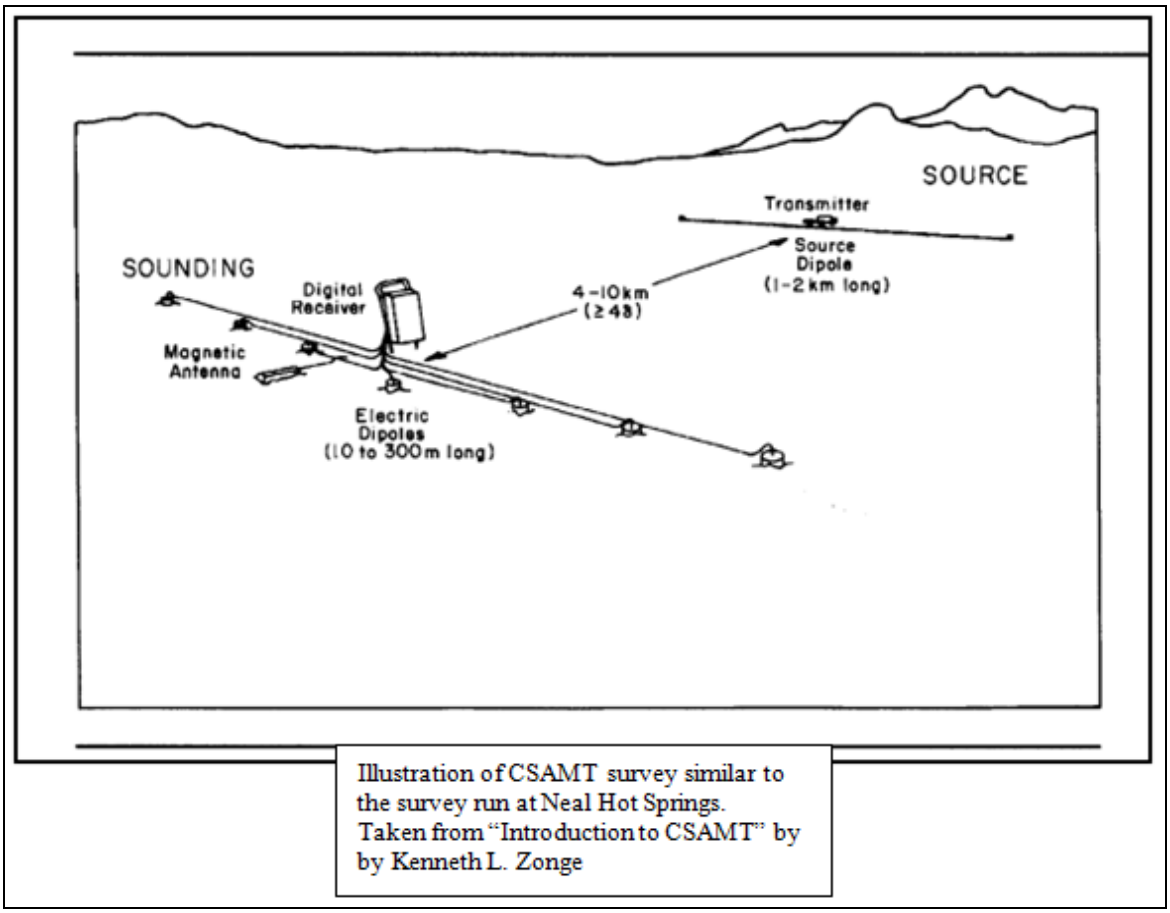

Illustration of CSAMT survey similar to the survey run at Neal Hot Springs. Taken from "Introduction to CSAMT" by by Kenneth L. Zonge

Figure 11-1 CSAMT Survey Design [*Zonge, 1992*]

11.2 Paleomagnetics

11.2.1 Acquisition

Measuring the magnetic properties of rocks provides information about the paleomagnetic field of the Earth, often from the time of the rock formation. Above a certain temperature, the Curie point, all remnant magnetic information is reset. When an igneous rock forms and cools below the Curie temperature (around 570°C in the rocks in this area), the magnetic information relating to the magnetic field at that time is stored. This time is often assumed to be at the formation of the unit, although in some regions a later burial or compressional phase could cause a resetting of the magnetic information if a higher Curie point is reached. In this area we surveyed igneous rocks, which demonstrate the thermal remnant

magnetization as described above. Other types of studies can be used in sedimentary rocks, depending on the purpose of the study.

Some of the many uses of paleomagnetic data are magnetostratigraphy (if the sequence is known locally), formation correlation, secular time variation, and for determining rotation about a vertical axis. However, in this study the primary objective was to obtain data to constrain potential field models (magnetic and gravity), and to correlate some of the igneous rocks if possible.

Three types of measurements were taken in the paleomagnetic survey. First, multiple measurements of in situ magnetic susceptibilities were made with a handheld meter. Next, a diamond tipped pipe drill was used to drill a cylindrical cut into the rock around the sample. The sample was oriented by azimuth and hade, using both a magnetic compass and a sun dial (see Figure 11-2 below). The core was marked with this information prior to separation from the rock face, so the in situ orientation is known. The cores are then tested in the laboratory for magnetic properties, including stage-by-stage demagnetization, which provides detail of the stages of magnetization and overprints. Last, a fist-sized hand sample of fresh rock is taken from the site for precise density measurements.

The samples and data were taken with the help of the United States Geological Survey (USGS). The results will be processed in the USGS labs, and are not currently available for this report.

Figure 11-2 Paleomagnetic Acquisition (Left) Demonstration of the Core Drilled by Jonathon from the USGS. (Right) The compass inclinometer used to measure the in situ orientation of the core samples.

11.3 Lacustrine Seismic Survey

11.3.1 Acquisition

A lacustrine seismic survey was carried out on the Bully Creek Reservoir adjacent to the Neal Hot Springs survey area. The principles of lacustraine and marine seismic reflection surveys are very similar to those discussed in Section 7 and Appendix A. A schematic of a typical marine survey is shown in Figure 11-3.

The fault zone that is anticipated to bisect the main survey area at Neal Hot Springs is likely to extend across the Bully Creek Reservoir, as indicated Figure 11-4. 9 survey lines, including 4 main lines traverse the reservoir. These lines are named A-I respectively.

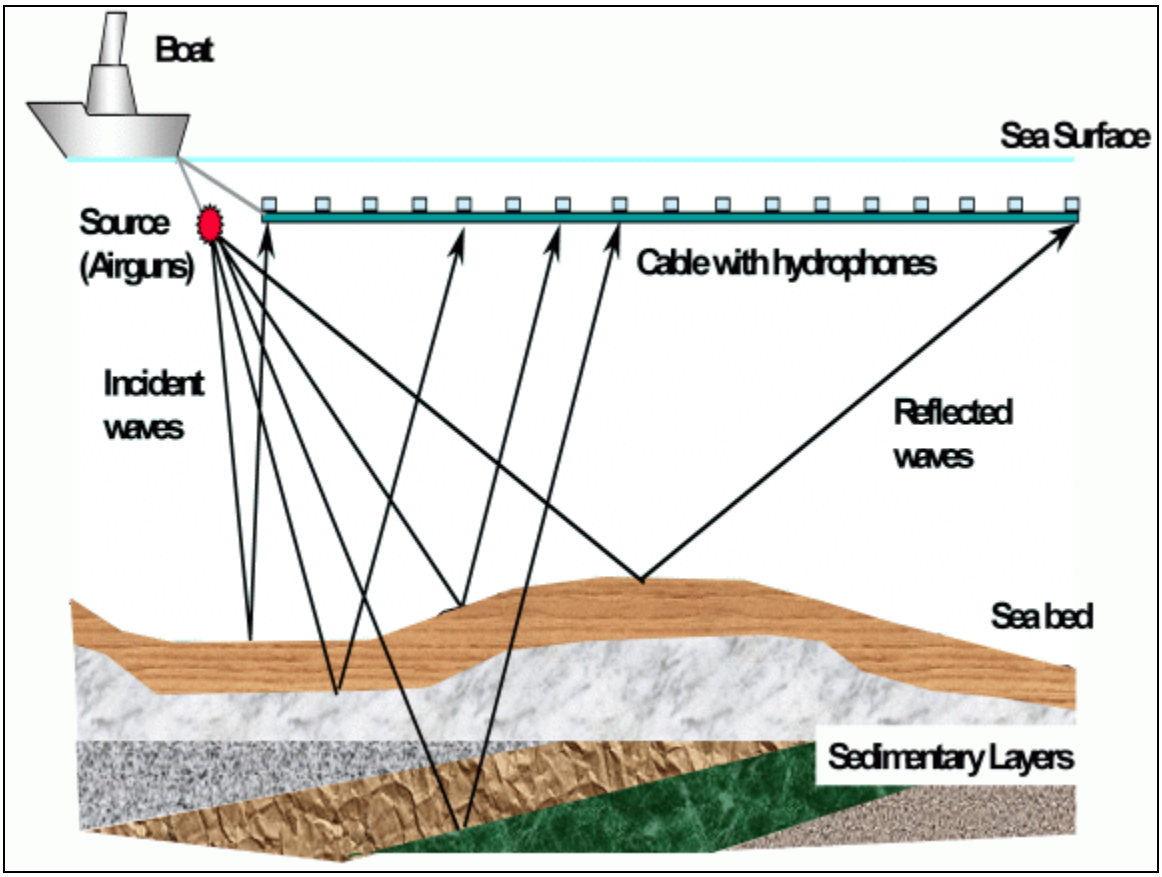

Figure 11-3 Schematic Diagram of 2D Marine Seismic Acquisition Configuration

The lacustrine survey employed a 12 channel hydrophone streamer towed behind a fishing boat. The depth of the streamer was controlled by 3 floats, mounted between channels 10 and 11, 11 and 12 and at the streamer tail. The group interval was 3m. A slide hammer source was used, which generated a low frequency signal and approximately 100 Joules of acoustic energy achieving approximately 50m penetration into the subsurface. The shot point interval was approximately 4s; 4227 shots were made over the course of the survey. The time of each strike was recorded automatically upon contact between the hammer and the plate mounted on the base of the boat. This contact also triggered the start of the shot record. The lacustrine survey parameters are summarized in Table 11-2.

A dual signal 50/250kHz Lowrance X-26 sonar unit was used to profile the reservoir bottom and record time, depth and GPS data throughout survey activities. The sonar system was stern-mounted on the vessel ~0.25m below the surface of the water. The system emits a seismic signal up to 250kHz in frequency (significantly higher than that of the slide hammer).

The majority of this energy is reflected from the resorvoir bed; as the high frequency signal attenuates very rapidly and achieves limited penetration of the subsurface (on the order of 20m in the course of this survey). The TWT of the reflected signal is recorded, allowing the depth to the reservoir floor to be profiled when converted with the appropriate water velocity (typically 1500m.s^{-1}).

Table 11-2 Lacustrine Seismic Survey Parameters

Group interval	3m
No. Channels	12
Shot point interval	4s
Near hydrophone-source offset	1m
Sample interval	2ms
Raw data format	SEGY
Acqusition software	Seismodule Controller

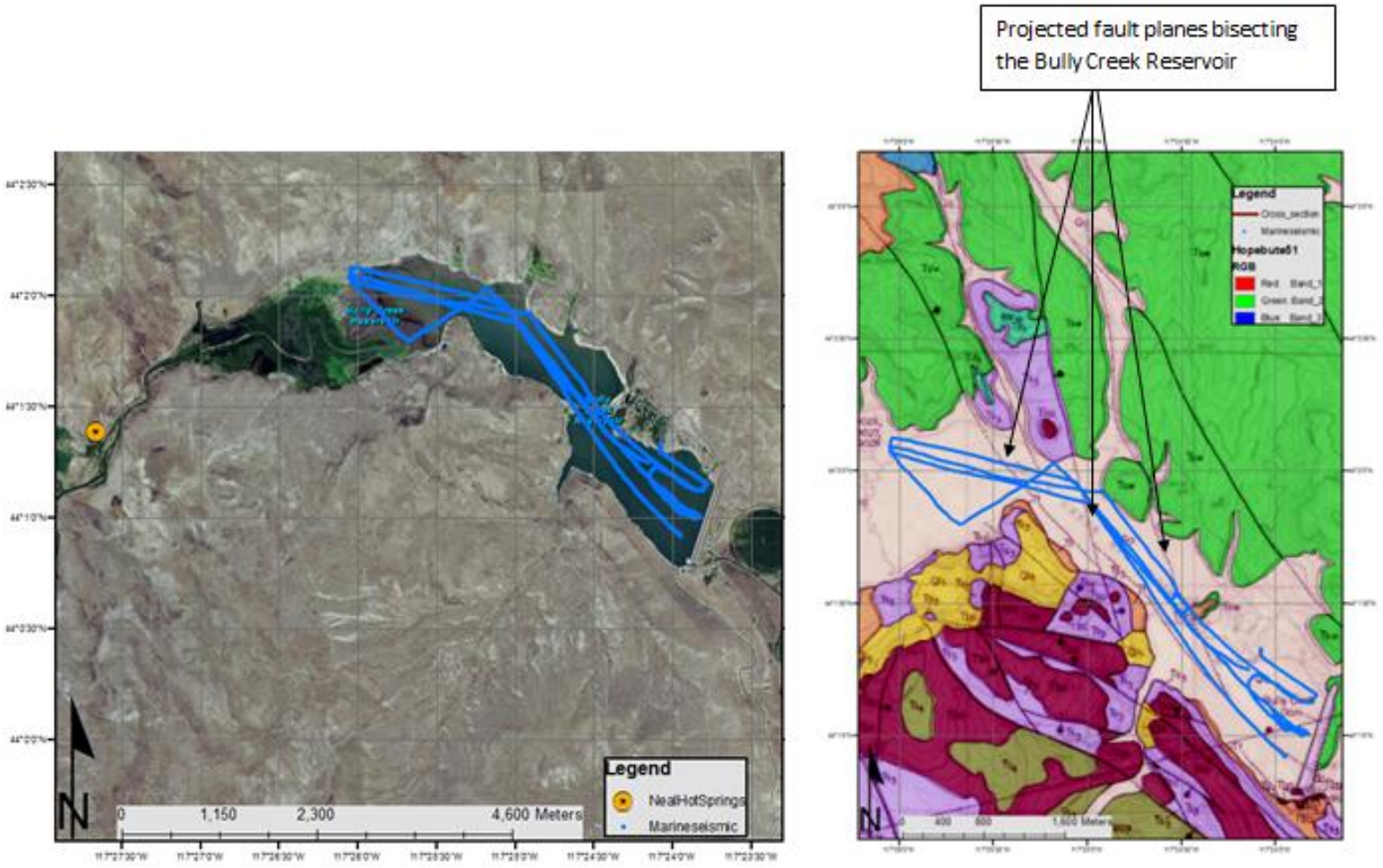

Figure 11-4 Lines Acquired by Lacustrine Seismic in Satellite Image and Geological Map

11.3.2 Lacustrine Seismic Preliminary Data

The seismic data acquired over lines A-I were processed by BSU. The data were filtered, subject to quality control, and single channel sections were built. Preliminary interpretations were made on this basis. It is intended that all the data from all lines acquired ultimately be fully processed to produce a stacked seismic section.

An extract from the brute stack of Line I is shown in Figure 11-5. An unknown object appears to be emplaced on the lake bed. A single, high amplitude horizon is clearly imaged across the section; this is likely to be the lake bed. The high reflectivity of this horizon causes the majority of the seismic energy to be reflected back to the surface, and the amplitude of any reflections from underlying interfaces to be relatively low. Consequently, it is difficult to observe whether the object arises from or penetrates to any significant depth in the subsurface.

Sonar and seismic profiles for Line C are shown in Figure 11-6. The seismic profile shows the first channel only, filtered to reduce noise in the data. However, as seen, this display poorly images the subsurface; the lake floor is observed indistinctly, but large scale features can be correlated with the higher resolution sonar profile. An expressive object on the lake floor is observed in both the seismic and sonar profiles. This is likely to be the same or similar to the object observed in Figure 11-5.

The poor signal observed in the seismic data is attributed to poor coupling of the source, effectively the base of the boat, with the water. It is possible that there was aeration under the boat due to the motion boat of the boat in the water, and this would significantly reduce the energy injected into the water by the shot. In addition, the shot was relatively low energy; where a similar source was used on land, at least three stacked strike were required per shot point in order for a sufficiently high amplitude signal to be measured. It is probable that the shot was too low in energy to achieve significant penetration below the lake floor. Further processing, including stacking of the data, may improve the signal to noise ratio and improve the resolution of the data and apparent penetration depth, but it is likely that issues with the data quality will persist.

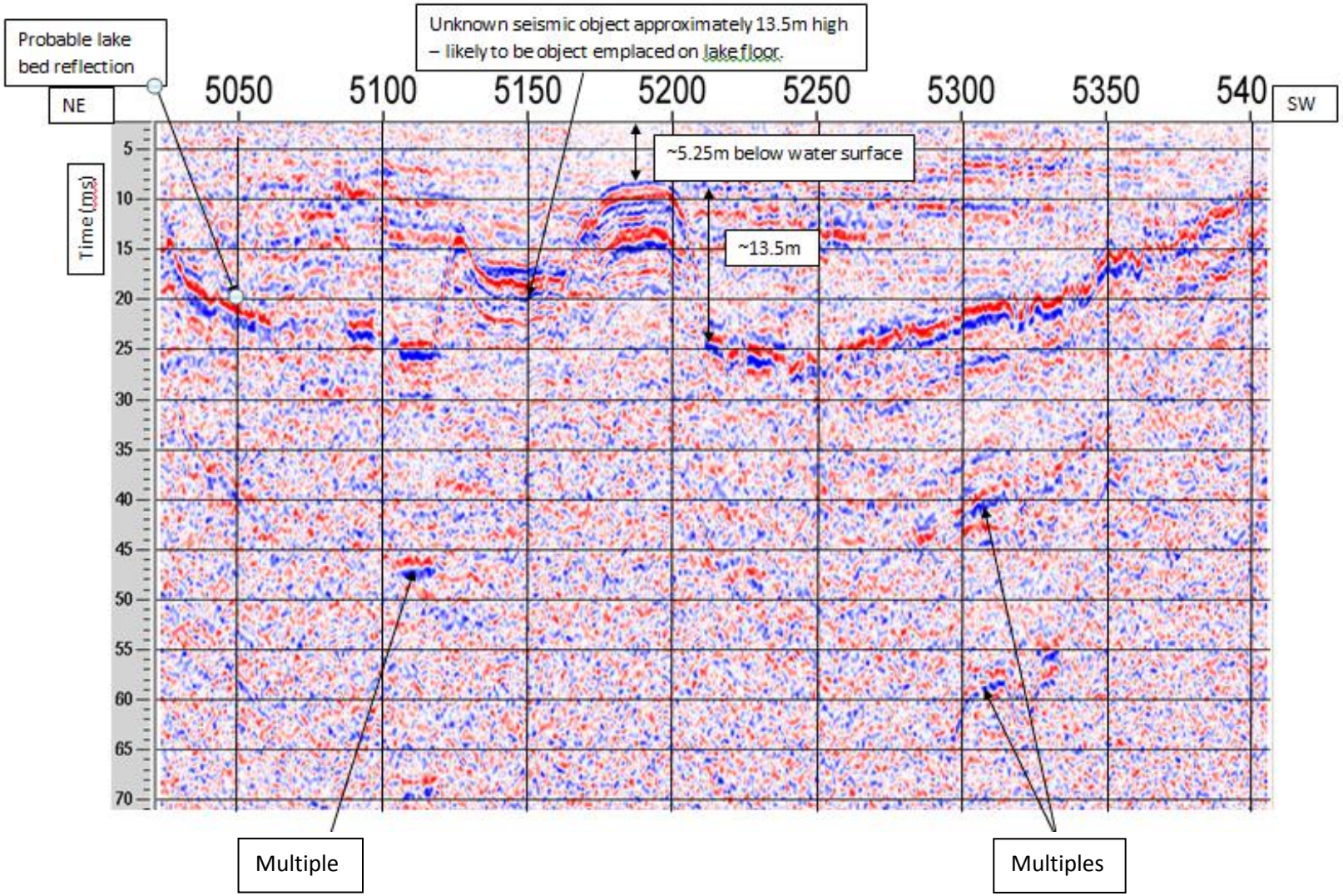

Figure 11-5 Single Channel (Channel 1) Displays for Line I

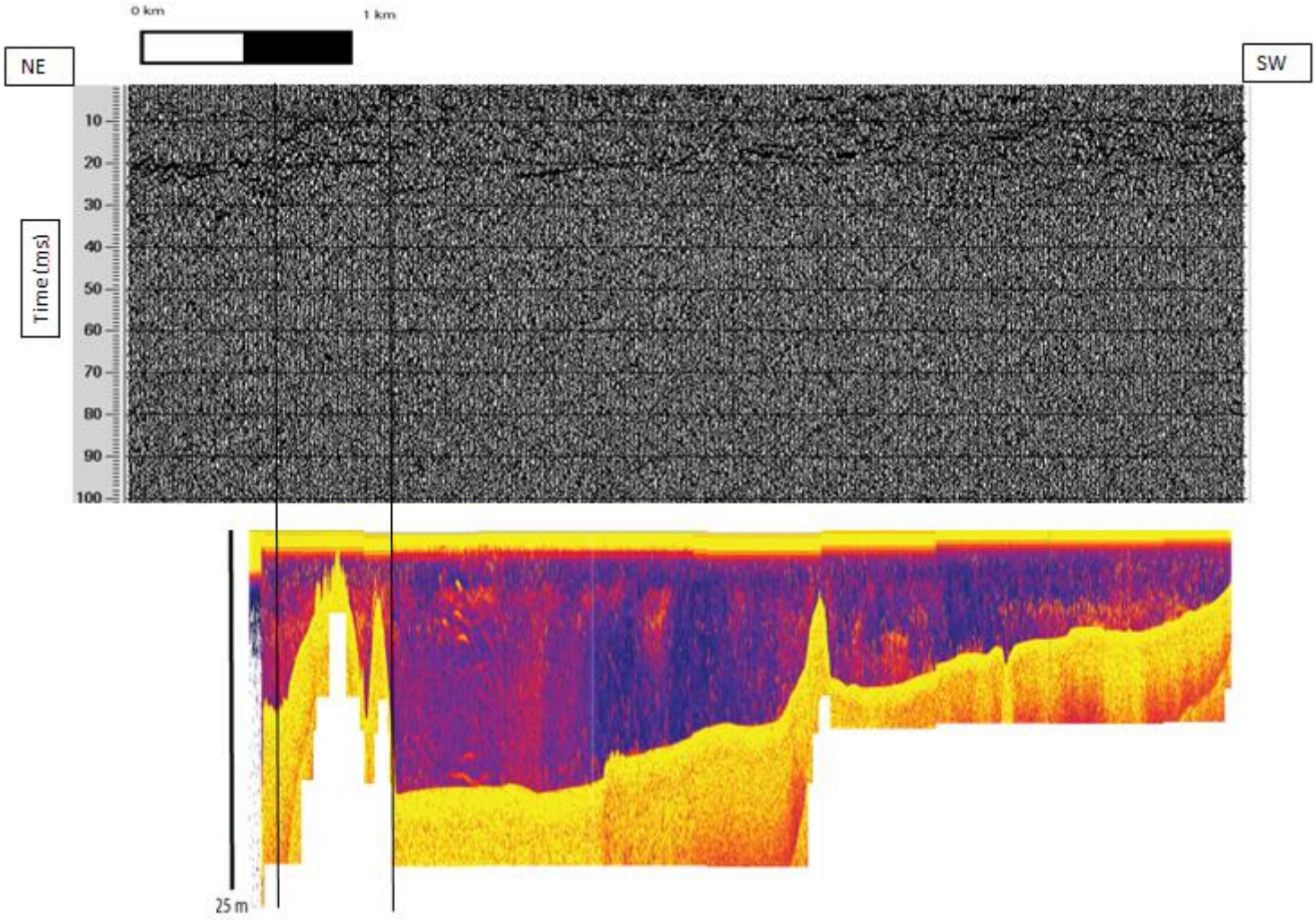

Figure 11-6 Seismic (above) and Sonar (below) Profile for Line C

11.4 Passive Seismic Survey

11.3.3 Passive Seismic Acquisition

Eleven passive seismic stations were placed around the Neal Hot Springs area. Each station was buried 1m below the ground surface at the locations listed in

Table 11-3 and indicated on the map in Figure 11-7. An additional passive seismic station was linked into the deep seismic trigger box, to allow correlation with the Vibroseis shots and the station records.

Table 11-3 Locations of Installed Passive Seismic Stations

Station	Latitude	Longitude
PS 1	44.0286	-117.4864
PS 2	44.0371	-117.4791
PS 3	44.0425	-117.4635
PS 4	44.0395	-117.4359
PS 5	44.0269	-117.4680
PS 6	44.0266	-117.4772
PS 7	44.0129	-117.4927
PS 8	44.0141	-117.4760
PS 9	44.0183	-117.4620
PS 10	44.0249	-117.4491
PS 11	44.0056	-117.4277

The passive seismic stations were comprised of a buried 3-component low frequency seismometer, a data acquisition system, a power regulator, a solar panel, and a 12 Volt battery. As seen in Figure 11-8, DGPS base stations were also placed at the passive seismic stations for the duration of field operations, these were used for survey positioning purposes. It was intended that the passive seismic stations remain in place for a duration of approximately 2 years. Table 11-4 details the equipment used at each station.

Table 11-4 Passive Seismic Equipment

Seismometer	Sercel L-22 low frequency land seismometer
Recorder	RefTek RT-130
Power	Solar panels and battery

Unlike the active seismic methods previously discussed, acquisition of passive seismic data does not incorporate a controlled source, and the data does not delineate subsurface structure or physical properties. Passive seismometers detect ambient noise (including motion due to earthquakes and tectonic activity), environmental noise, and anthropomorphic activity. Their primary purpose in this case was to detect noise associated with activity on the epithermal fault planes, gaining additional information regarding whether the faults remain active or are sealed. These data were used to trace fluid motion by mapping strength variation over time due to fluids interacting with the rock. It was also used to monitor subsurface motion or earthquakes due to pressure variation induced by extraction and re-injection of the hot brines from the epithermal system. Geothermal power generation can be associated with earthquakes generated because the rates and locations of extraction and injection may be inappropriate for the site; for example, where re-injection of the brines is carried out at too great a distance from the extraction well. Also, this may occur within a block isolated from the extraction well, such that that the pressure at the extraction well is unsupported, or where injection is carried out too fast, causing a localized pressure increase in the stratigraphy.

The noise recorded by a passive seismometer is typically at a significantly lower frequency than other seismic methods. Recorded noise is typically around 1Hz. The data were continuously recorded at a sampling rate of 250Hz (Nyquist frequency of 125Hz). This is the maximum frequency that can be recorded unaliased. Due to disk space, the data must be collected from the stations every 28 days. This will be carried out by Boise State University. A basic setup of the passive seismic stations is shown in Figure 11-8.

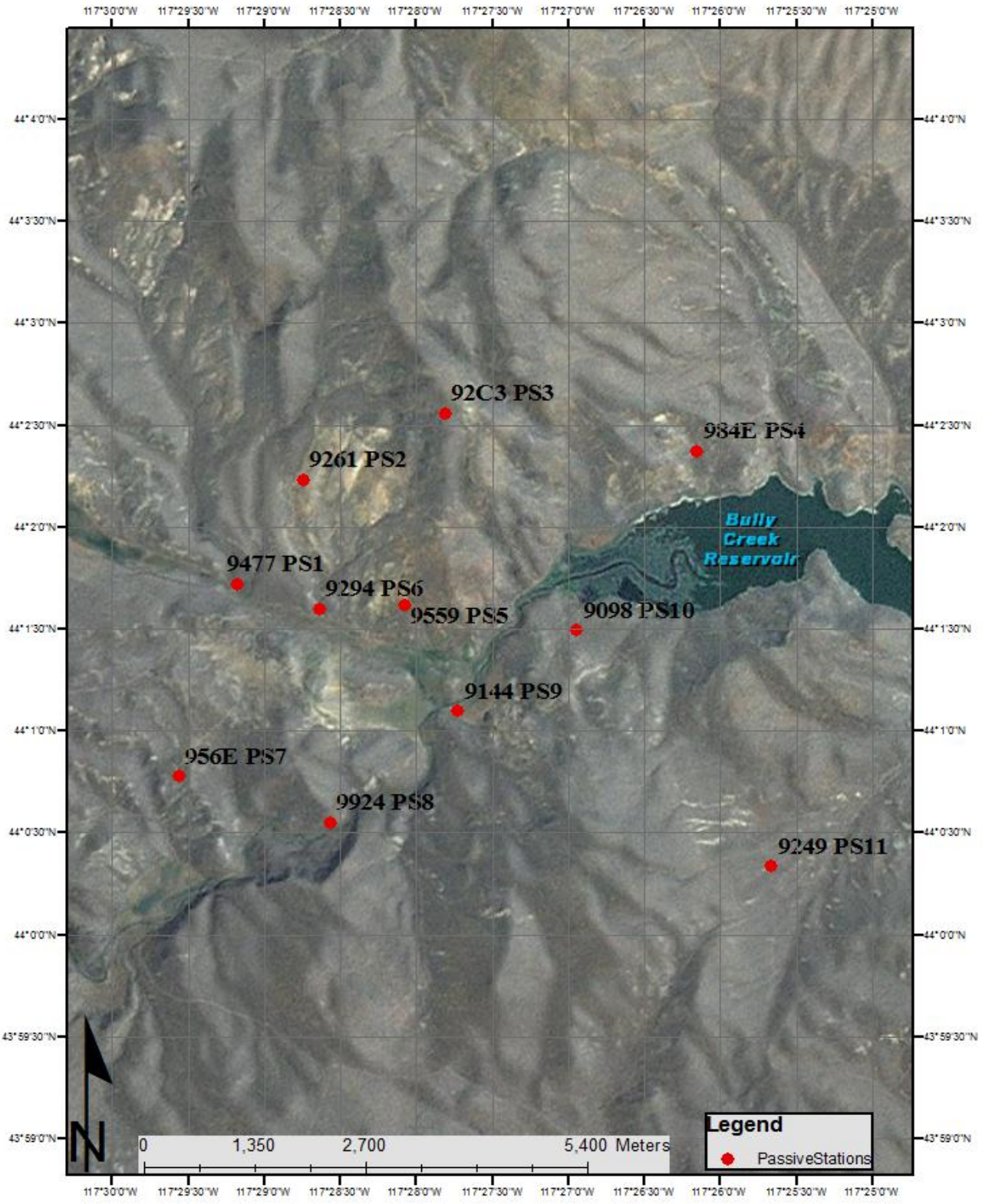

Figure 11-7 Map Showing Location of the Passive Seismic Stations

Figure 11-8 Passive Seismic Station and DGPS Base Station

11.3.4 Passive Seismic Preliminary Data

As the passive seismic array installed at Neal Hot Springs was intended to trace subsurface motion over extended durations, only preliminary results from seven stations are currently available.

During survey operations at Neal Hot Springs on May 20 2011, at 00:46:16 UTC[1] a 5.8 magnitude earthquake occurred near the east coast of Honshu, Japan. The surface waves generated by this earthquake were identified in the available data at all seven stations, as seen in Figure 11-9. The onset time across the seven stations is approximately 00:57:44; it can be seen that the waves took approximately 11minutes and 28 seconds to reach the site.

As seen in Figure 11-10, when data from two stations at the earthquake onset time are compared, the earthquake signature is largely consistent between stations, and the lower magnitude, higher velocity pressure waves can be differentiated from the higher magnitude, lower velocity surface waves. Figure 11-10 shows the comparison of the data for 2 stations.

[1] USGS[2011] http://neic.usgs.gov/neis/bulletin/neic_ldaf.htm

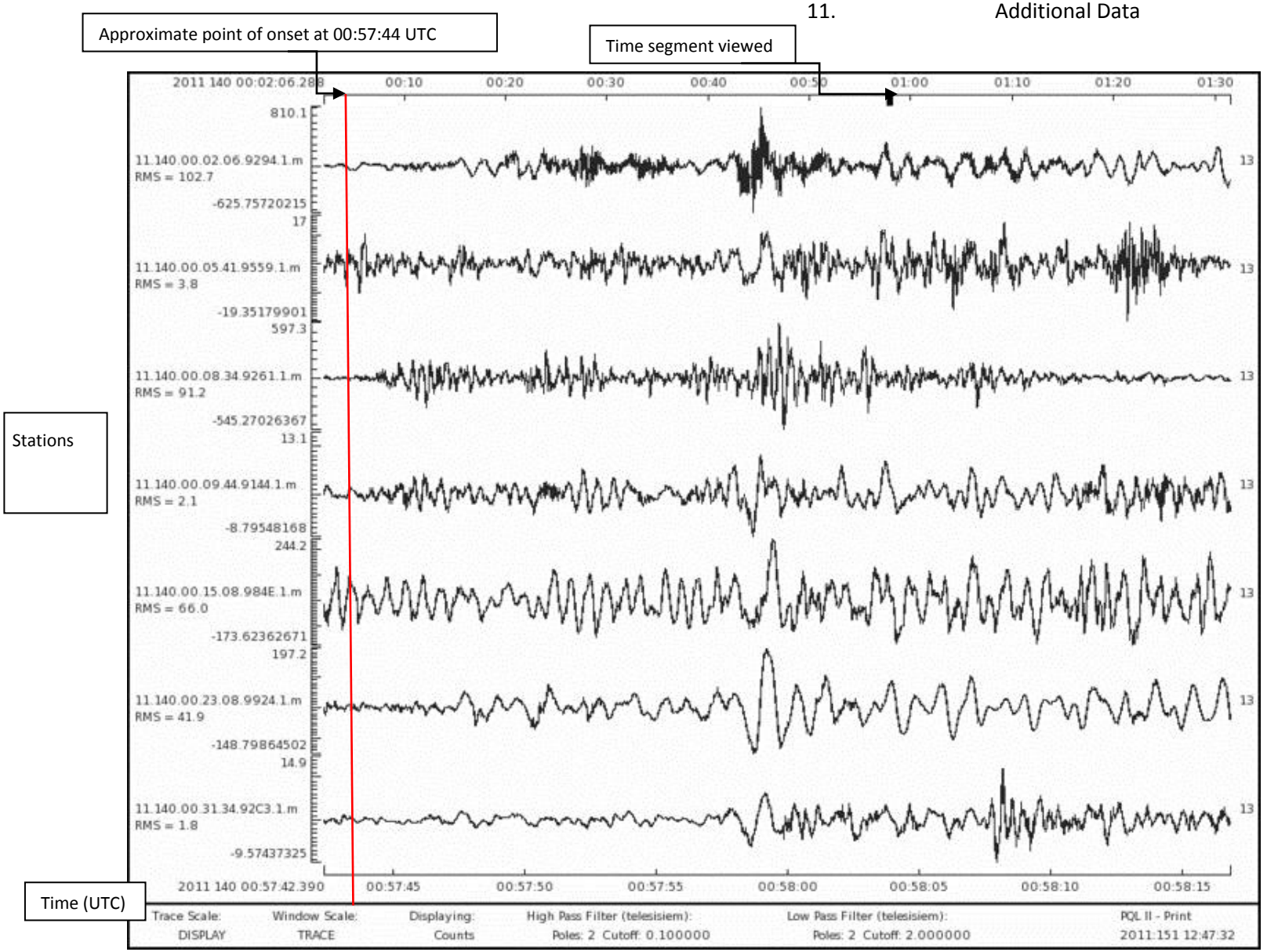

Figure 11-9 Data from 7 Stations recording Earthquake off East Coast of Honshu, Japan

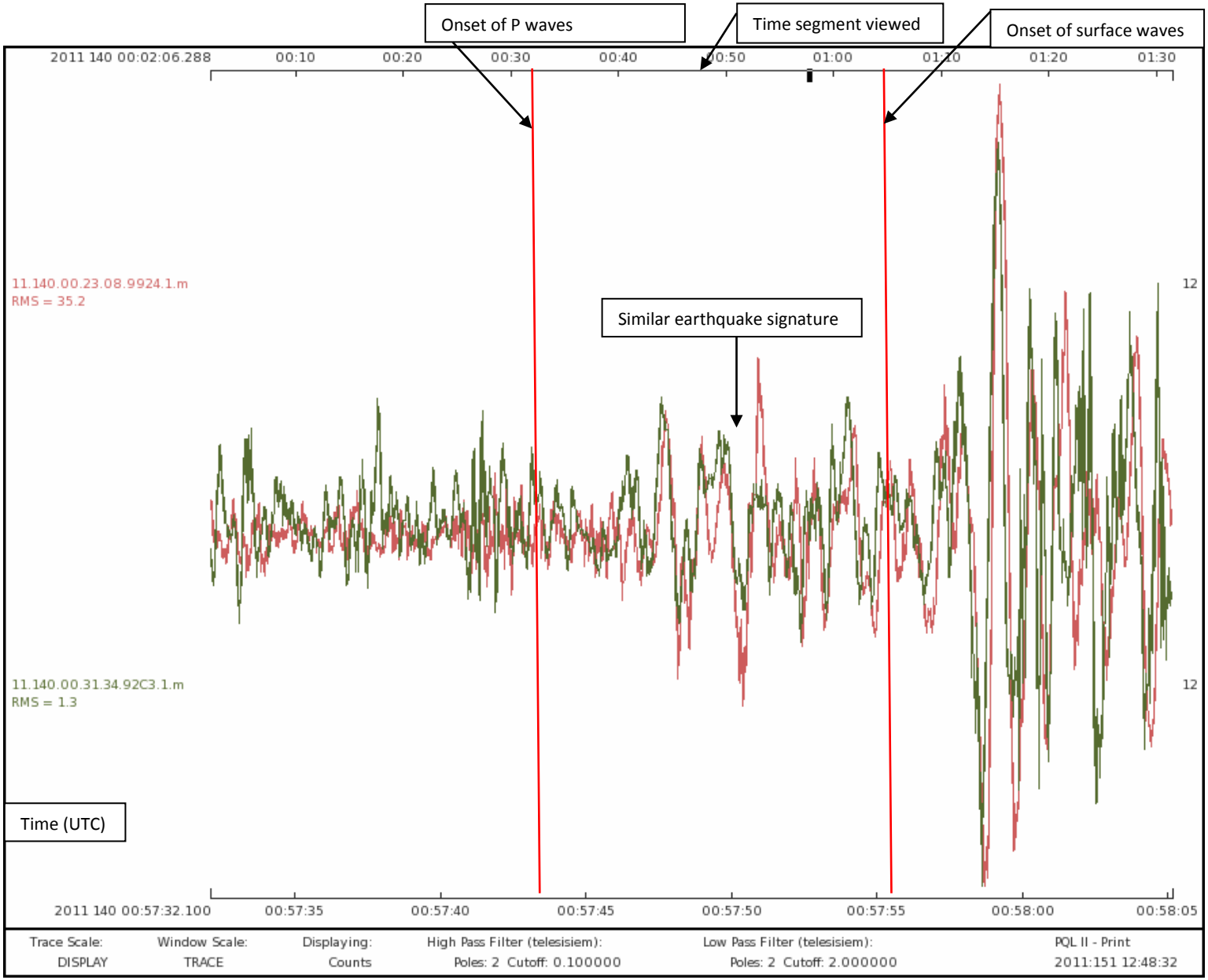

Figure 11-10 Data from 2 Stations Comparing Earthquake Signature and P and Surface Wave Onset Time

12. Data Synthesis

While every method surveyed a variety of locations surrounding Neal Hot Springs, the primary line that was analyzed and correlated between each data set was line DS10. The deep seismic, potential fields and DC resistivity/SP surveys all found similar results for line DS10. These results indicated the presence of a large igneous horst block flanking Neal Hot Springs to the east. The gravity and magnetic data were correlated and processed together to generate the cross section in Figure 12-1.

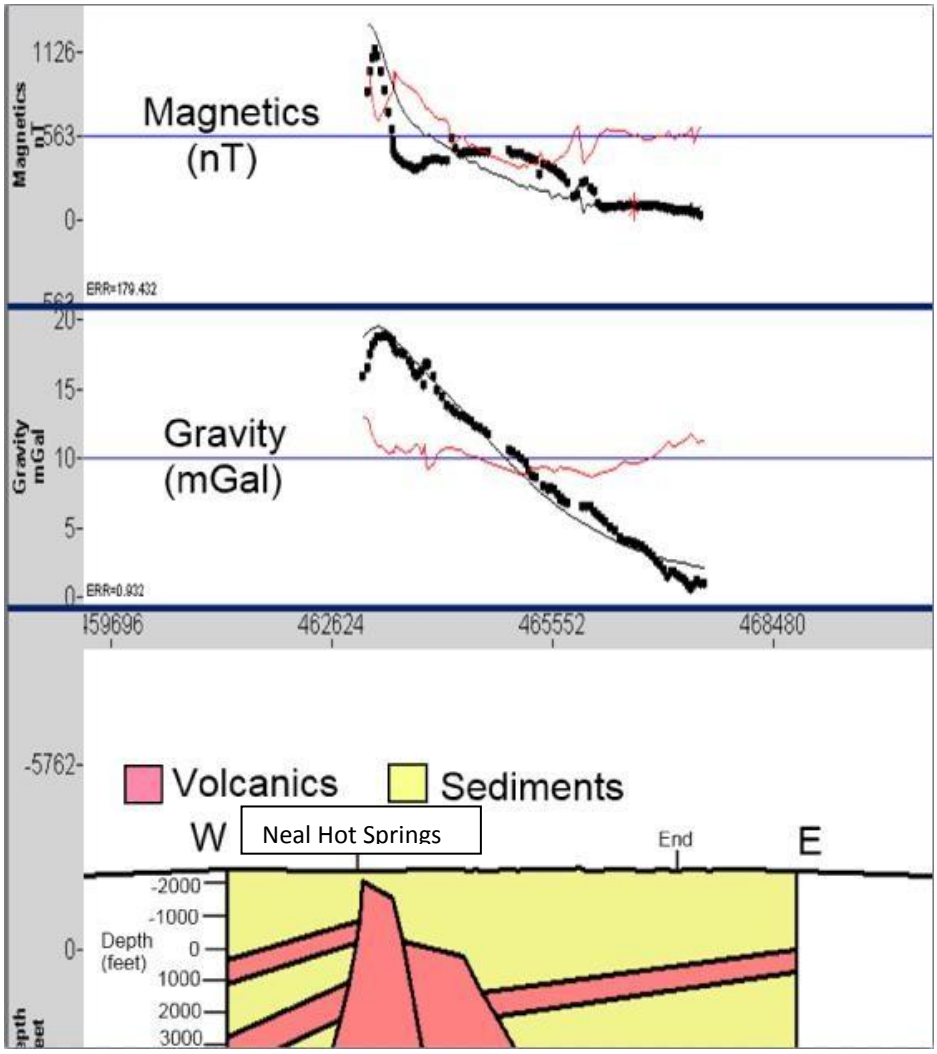

Figure 12-1 Gravity and Magnetics Data Correlated into a Cross Section on the Eastern Portion of Line DS10

Figure 12-1 shows the igneous horst block as a distinct feature surrounded by intermeddled sediments and volcanic rocks. This cross section, from the eastern portion of DS10, correlates very closely with the results from the FEM survey shown in Figure 12-2 below. Comparing Figure 12-1 and Figure 12-2, it can be seen that the higher density volcanic rocks on the gravity and magnetic cross section correlate with the higher resistivity (lower conductivity) section of the eastern DS10 line. This higher resistivity structure begins just east of Neal Hot Springs, and therefore represents the hypothesized horst block. Additionally, the east side of the high resistivity section correlates with results found from the Warm Spring survey. The interpretation from the Warm Spring site is shown in Figure 12-3

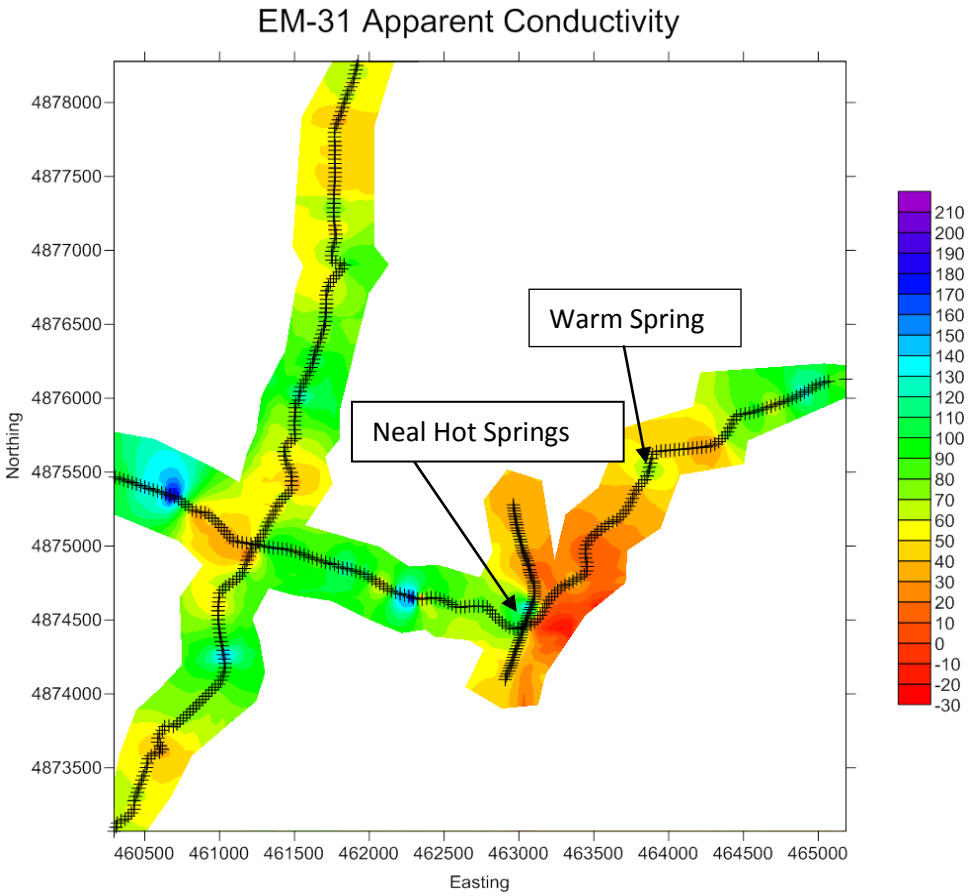

Figure 12-2 EM-31 Apparent Conductivity Survey Over the Neal Hot Springs Area

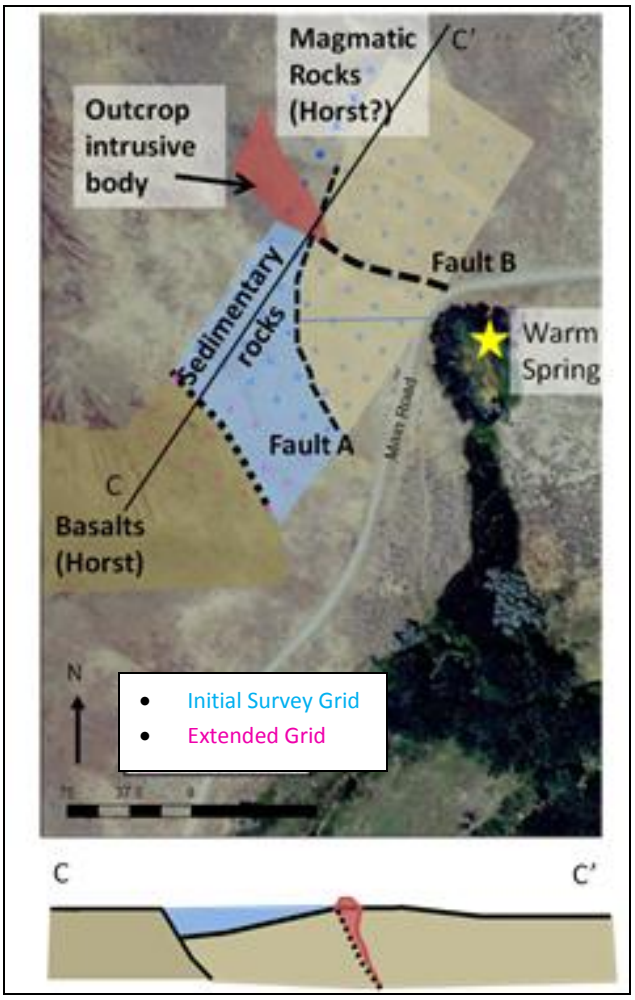

Figure 12-3 Warm Spring Site Schematic Generated from Results

The Warm Spring survey discovered the presence of two secondary faults that are part of the larger horst structure. The westernmost fault at the Warm Spring site, Fault A, is shown as being slightly downthrown and filled with sediments. This interpretation is supported by the FEM data as well the gravity and magnetic data. The FEM data in Figure 12-2 shows a slight decrease in resistivity at and just before the Warm Spring site, followed by an increase in resistivity before the larger and easternmost change in resistivity, which represents the end of the horst structure. A similar structure is seen in the gravity and magnetic model: the larger horst structure is faulted, causing the eastern block to be downthrown and filled with sediments. The second fault represented in the Warm Spring data was the structure initially targeted by this survey site, and is the structure actually believed to be associated with the Warm Spring.

The DC resistivity and SP models do not show the secondary fault within the horst block that the previous surveys demonstrated; however, the models do show the larger horst structure beginning just east of Neal Hot Springs and ending to the east of the Warm Spring. The SP data also show a general increase on the edges of, and within, the horst block. This indicates that there is water upwelling through the main fault at Neal Hot Springs as well as through smaller fractures located throughout the horst block and at the Warm Spring. The smaller fracture that is associated with the Warm Spring is shown in the Warm Spring interpretation in Figure 12-3 as Fault B. The modeling of the SP and DC resistivity data for the main line is shown below in Figure 12-4.

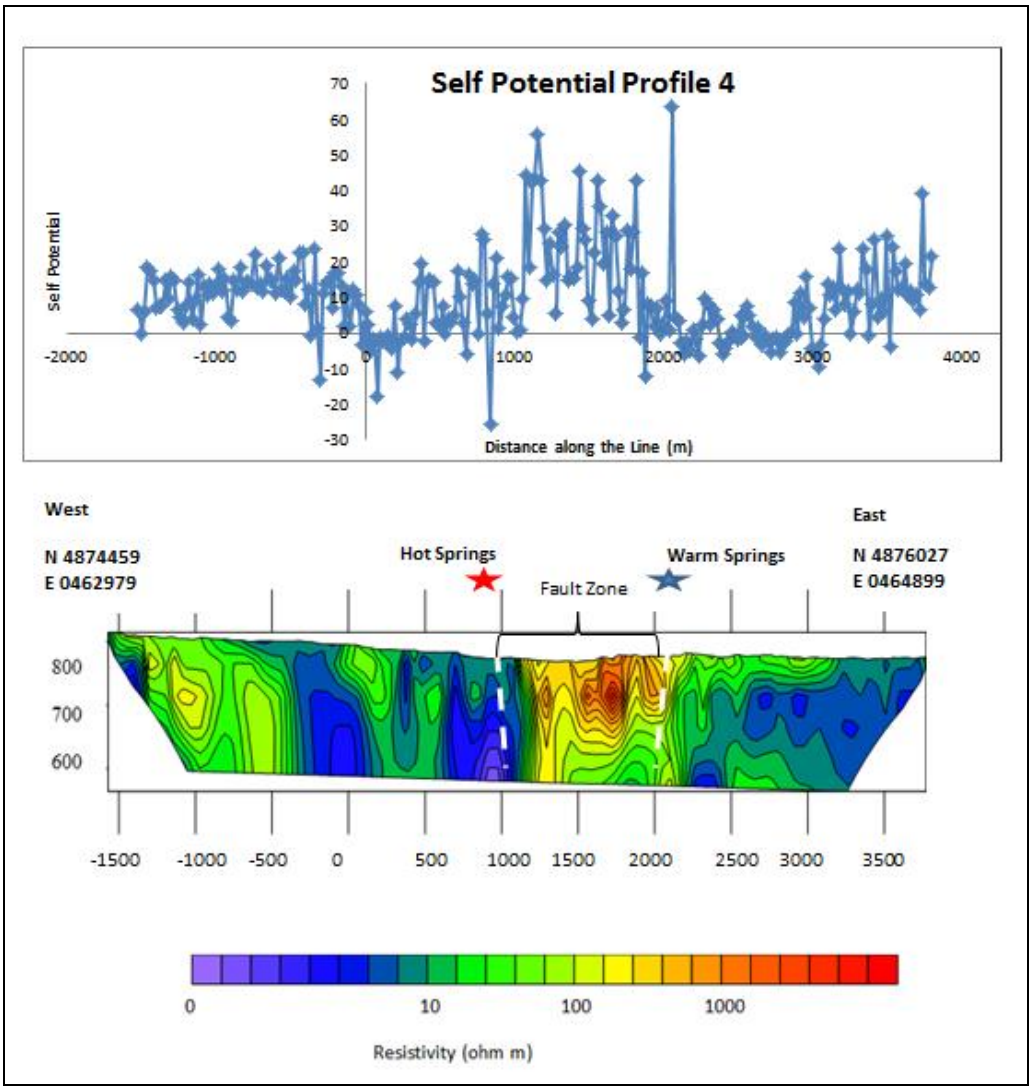

Figure 12-4 Self Potential and DC Resistivity Model Along DS10

The deep seismic data were not completely processed, so rough models were taken for initial interpretation. Figure 12-5 shows this model (it should be noted that it is oriented opposite of the previous profiles in this section). This model correlates fairly accurately with the general interpretations of the gravity and magnetic survey as well as the FEM survey. This data, however, does not show the secondary fault structure within the larger horst block.

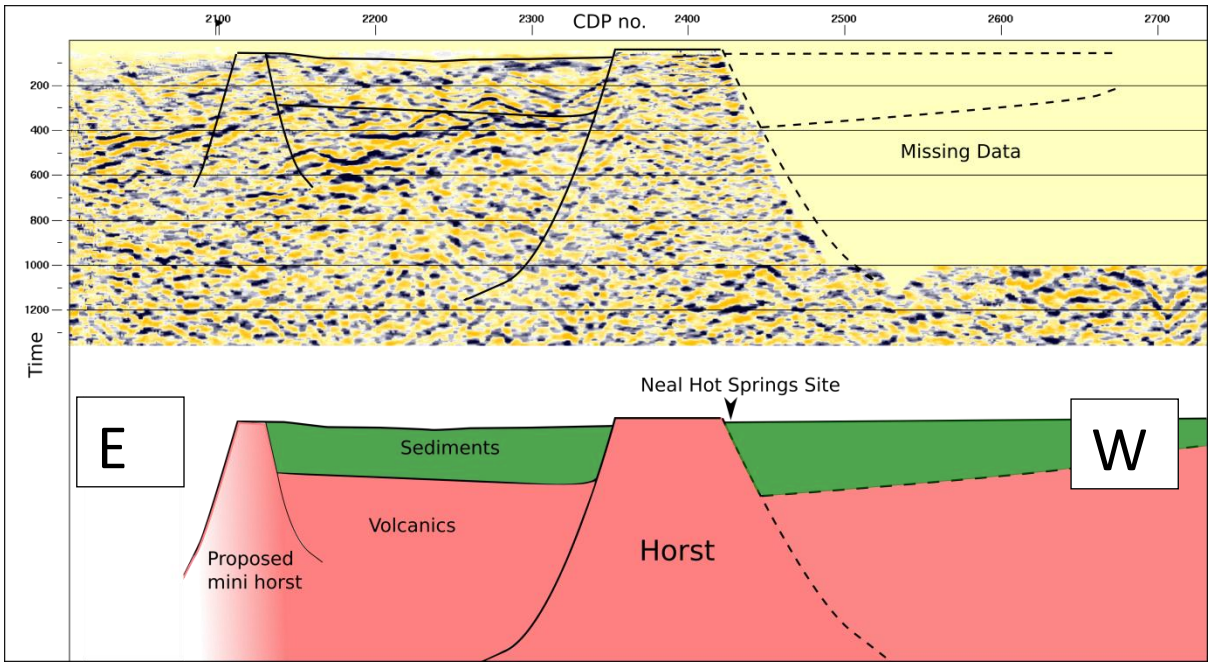

Figure 12-5 Initial Interpretation of Deep Seismic Data

The resistivity and SP data were also able to be correlated with the TEM data along line DC3, which is parallel to, but south of, the eastern portion of line DS10. This data shows the continuation of the fault that is on the western side of the horst block. Both the TEM and resistivity data show the low resistivity sediments to the west and the higher resistivity volcanic rocks on the east side of the fault. This fault is also represented by the positive SP anomalies along DC3. These anomalies are interpreted as places where ground water is upwelling through the fault zone, and although this area is not a hot springs, there may still be ground water flow in this area south of the hot springs.

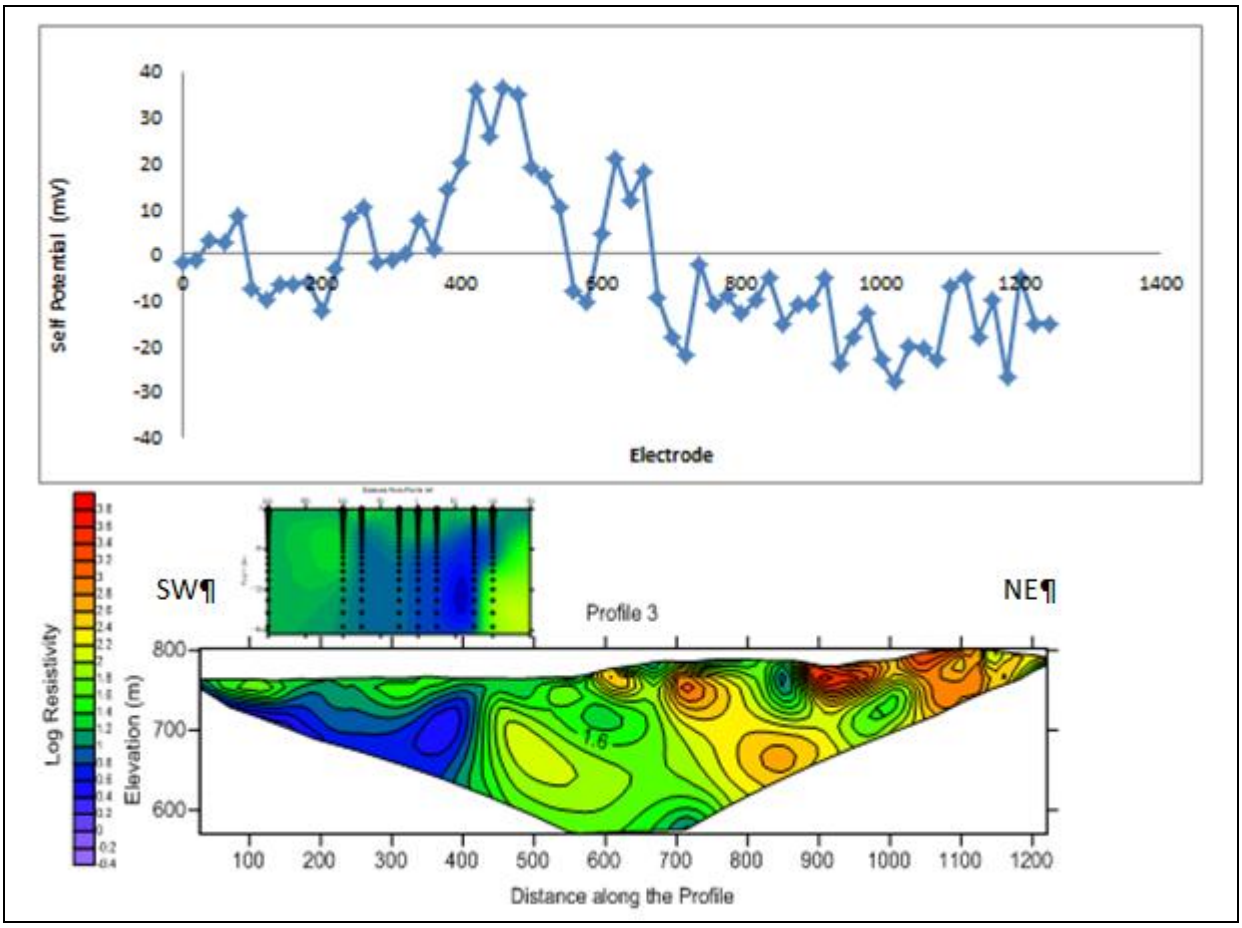

Figure 12-6 Correlation of TEM Data with Resistivity and SP Data Along Line DC3

There were several other surveys completed including passive seismic, lacustrine seismic, paleomagnetic, CSAMT, shallow seismic, and VSP. However, these methods did not provide conclusive information to help with the final interpretation. The methods, discussed above, that were useful all come to the same conclusion that there is a normal fault to the east of Neal Hot Springs. This normal fault represents the western side of a large horst structure that has a secondary fault within it. This secondary fault is just west of the Warm Spring and has caused the east side of the horst block to be downthrown and the top portion filled with sediment. Farther east of the Warm Spring site is the edge of the horst block which is shown in all surveys except the Warm Spring survey, which was too small of a grid to cover this fault structure.

13. Conclusions

13.1 Implications

Overall, a high degree of consistency was found between the qualitative interpretations of the datasets. The synthesized datasets appear to confirm the presence of a relatively elevated horst block bounded by two normal faults. The geology comprises volcanic rock intermeddled with lacustrine sediments. The faults postdate the deposition of the Miocene age rocks. The adjacent fault blocks have been significantly downthrown. The shallow geology of the adjacent fault blocks comprises lacustrine sediments of early Miocene age, while that of the horst comprises volcanic rock of late Miocene age; the overlying lacustrine and fluvial sediments have been eroded. The hydrothermal system associated with Neal Hot Springs is focused on the western fault; hot, conductive brine upwells along this conduit and adjacent, smaller scale fractures. Sinter, produced by the silicification of porous sediments by interaction with silica-bearing hydrothermal fluids, is indicative that the water temperature at depth is sufficiently high to strip silica from the bedrock at depth.

An additional hydrothermal system was identified on the eastern fault, referred to as the Warm Spring. It is unknown whether this system is in communication with that producing the Neal Hot Springs. The water upwelling to the surface is substantially lower in temperature than that at Neal Hot Springs. The cause of this temperature difference was not identified in the course of this study.

In addition, the data suggested the existence of further, possibly smaller scale, structures. These structures are not associated with any known surface expressions of hydrothermal activity. The deep seismic data suggested the presence of an additional horst structure to the east of the one hosting the Neal Hot Springs system. The Warm Spring survey suggested the presence of a fault intersecting the main eastern fault; this fault is understood to dip southwest, antithetic to the eastern fault hosting the Warm Spring.

It was found that SP and resistivity geophysical surveys are an effective means of identifying subsurface upwelling of hot water, such as that associated with hydrothermal systems. Seismic imaging proved to be useful for imaging subsurface structure, particularly where there are sharp variations in the mechanical properties of the subsurface. Passive fields and electromagnetic surveys were useful for identifying changes in subsurface composition, associated with lithological variation. A holistic interpretation was produced by synthesizing the data acquired by these survey methods. This interpretation exploits the strengths of each survey method and improves the accuracy and precision of the overall interpretation made.

After further processing, the data may be used to quantitatively evaluate the scale of the subsurface structures, including the dip of structural planes. Additional data acquisition is required to verify the true character of the fault.

13.2 Recommendations

The deep seismic data acquisition was confined to the main roads running through the area. Other survey methods, including gravity and magnetic surveys were carried out over the same lines in order that the results of these surveys could be compared and jointly interpreted. However, it would have been informative to also carry out magnetic and gravity surveys over the lines that the electrical (resistivity, SP and EM) survey methods crossed.

In order to be able to process the data as 2D profiles, the gravity and magnetic data were divided into two segments where the road turned a sharp corner. Unfortunately, this point coincided with the location of the Neal Hot Springs, the likely location of the western fault bounding the main horst block. As the results obtained from the deep seismic data remain preliminary, this survey cannot be used to tie these surveys together. A survey grid centered over the Neal Hot Springs area could have produced more valuable data.

Additional, fully processed VSP data from wells in closer proximity to the gravity and deep seismic survey lines would provide for improved density and velocity models. The VSP data acquired were significantly offset from the deep seismic survey lines, and further processing is required in order that the VSPs can be correlated with the seismic data.

It is recommended that, during further acquisition, each survey method have a common notebook for recording field measurements and additional observations. While the practice of keeping an individual field notebook is common practice and important, compiling data from disparate notebooks and reducing it to a common format became a time consuming process. Maintaining a common notebook in addition to personal ones would make this process more efficient, and reduce the risk of data being lost.

It is recommended that preliminary data processing be carried out in the field in order to improve the results and inform further survey activities while in the field. This would allow surface observations to be more rapidly and accurately tied in with the geophysical datasets. In addition, the data would be subject to quality control before leaving the field, allowing scope of reacquisition if an important dataset is found to be of poor quality.

It is recommended that further study be carried out in order to identify whether the hot, upwelling fluid is associated with a magmatic intrusion or the geothermal gradient. This may include measuring the surface heat flux over the survey area and forward modeling on this basis.

The flows used to process the shallow and deep seismic datasets should be refined in order to improve the resolution and accuracy of the seismic images, and allow the subsurface structure to be quantitatively evaluated. In order to refine the identified fault location along strike, additional surveys should be carried out to increase the survey density over the fault zone.

This study failed to identify the cause of the temperature differential between the Neal Hot Springs and the Warm Spring, although it is suggested this may be related to the depth of fluid penetration. In addition, it is unknown whether the two spring sites are in communication. Further surveys could investigate this.

The resistivity and SP data suggested that there was hot fluid upwelling on faults that did not propagate to the surface. This suggests the presence of sealed faults where this is the case, and unsealed faults where the springs are observed. This may indicate ongoing activity on the

fault planes hosting the hydrothermal system. This should be subject to further study; analysis of the passive seismic data over a long duration may be useful in this instance.

The passive seismic data has not been analyzed in depth in this report as it is intended to view the data over a long duration. When available, the data should be processed and interpreted with the aim of identifying fluid motion in the subsurface.

14. References

Blakely, R., 1995. *Potential Theory in Gravity and Magnetic Applications*, Cambridge University Press, p 135-136.

Boise State University, 2011. Geology NHS2011. [online] Available at: <http://pal.boisestate.edu/index.php/Geology_NHS2011> [Accessed 7 June 2011]. After Evans, (in review), USGS

Bowen, R. G., and D. D. Blackwell, 1975. The cow hollow geothermal anomaly, Malheur County,Oregon, The Ore Bin, 37(7), pp. 109–121.

Brantax, 2010. Geophysical Methods. [online] Available at: < http://www.brantax.com/en/site/98/> [Accessed 7 June 2011]

Bronicki, L. Y. and Yavne, I., Ormart Inc., 1990. Method of and Apparatus for Retrofitting Geothermal Power Plants. Sparks, NV, USA. Pat. 4996846.

Camp, V., Ross, M. & Hanson, W. 2003. Genesis of flood basalts and Basin and Range volcanic rocks from Steens Mountain to the Malheur River Gorge, Oregon, Geological Society of American Bulletin, 115(1), pp. 105-125.

Christiansen, R.L., Foulger, G. R. and Evans, J. R., 2002. Upper-mantle origin of the Yellowstone hotspot. Geological Society of America, 114(10), pp. 1245-1256.

Clutter, T.J., 2010. Neal Hot Springs Promises Oregon Commercial Geothermal Power. [online] Available at: <http://www.renewableenergyworld.com/rea/news/article/2010/10/neal-hot-springs-promises-oregon-commercial-geothermal-power> [Accessed 7 June 2011].

Couch, R., French, W., Gemperle, M., and Johnson, A., 1975, Geophysical measurements in the Vale, Oregon geothermal resource area, The Ore Bin, 37(8), pp. 125-129.

Cummings, M., Evans, J., Ferns, M. and Lees, K., 2000. Oregon-Idaho Graben stratigraphic and structural evolution of the middle Miocene synvolcanic, Geological Society of American Bulletin, 112 (5) pp. 668–682.

Duffield, Wendell A. and Sass, John Harvey, 2004. Geothermal Energy: Clean Power from the Earth's Heat. [online] USGS. Available at: <pubs.usgs.gov/circ/2004/c1249> [Accessed 7 June 2011]

Environmental Protection Agency (EPA), 2010. Vertical Incidence VSP. [online] Available at: <http://www.epa.gov/esd/cmb/GeophysicsWebsite/pages/reference/methods/Borehole_Geophysical_Methods/Surface_to_Borehole_Procedures/Vertical_Incidence_VSP.htm>. [Accessed 7 June 2011]

Geonics Limited, 2004. Electromagnetic Geophysical Instrumentation. [online] Available at: http://www.geonics.com/. [Accessed 7 June 2011]

Heiskanen and Moritz, 1967, Physical geodesy: San Fransisco, Freeman Press.

Hoekstra, P. and Blohm, M. 1990. *Case Histories of Time-Domain Electromagnetic Soundings in Environmental Geophysics,* in Vol 2., Geotechnical and Environmental Geophysics, S.H. Ward, Ed., SEG. Tulsa, OK.

Kearey, P. Brooks, M. and Hill, I., 2002. An Introduction to Geophysical Exploration. 3rd Ed. Oxford: Blackwell Science

Li, Y., 2011. Lab_EM3-1D TEM data Inversion. GPGN 302 Introduction to Electromagnetic and Seismic Methods. [Lab. Notes.] 2010 ed. Golden, Colorado: Colorado School of Mines

Loke, M. H. 2011. *Tutorial: 2-D and 3-D electrical imaging surveys;.* [Online] Available from: <http://www.geoelectrical.com/downloads.php> [Accessed 7/9/2011]

Milson, J. and Eriksen, A., 2010. Field Geophysics. 4th Ed. Chichester: John Wiley and Sons.

Powers, C. et. al., 2007. *Integration of Surface Geophysical Methods for Fracture Detection in Bedrock at Mirror Lake, New Hampshire***; <**http://water.usgs.gov/ogw/bgas/surface/>

Revil, A., Naudet,V. and Meunier J. D., 2004. The hydroelectric problem of porous rocks: Inversion of the water table from self-potential data, Geophysical Journal International, 159(2), 435– 444.

Reynolds, M., 1997. *An Introduction to Applied and Environmental Geophysics*. Chichester: John Wiley and Sons.

Sheriff, 1984*, Encyclopaedic Dictionary of Exploration Geophysics.* 2nd Edition, p141.

Sheriff, R.E., and Geldart, L.P., 1995. *Exploration Seismology*. 2nd Ed. Cambridge: Cambridge University Press.

Telford, W. M., Geldart, L.P. and Sheriff, R.E., 1990. *Applied Geophysics*. 2nd Ed. Cambridge: Cambridge University Press.

U.S.Geothermal Inc., 2007. *Neal Hot Spring Project*. [online] Available at: <http://www.usgeothermal.com/NealHotSpringProject.aspx> [Accessed 7 June 2011].

U.S. Geological Survey, 2011. *Preliminary Earthquake Report*. [online] Available at: <http://neic.usgs.gov/neis/bulletin/neic_ldaf.html> [Accessed 7 June 2011].

Ward, C. 2011. *Seismic Processing Report Line TRV-436 Taranaki Basin, New Zealand.*

Yilmaz, O., 2001. *Seismic Data Analysis*. 2nd Ed. Tulsa, OK; Society of Exploration Geophysicists.

Zonge, K.,1992. *Introduction to CSAMT*. After Northwest Mining Association, 1992. Practical Geophysics II. 2nd Ed. USA: Northwest Mining Association.

A. Appendix A: Theory

a. Potential Fields

i. Gravity

Gravity surveying is based on two of Sir Isaac Newton's principles: the Universal Law of Gravitation as well as his Second Law of Motion. The Universal Law of Gravitation describes the force generated by the distance between two known masses. The Second Law of Motion states that an object's mass multiplied by the acceleration due to gravity is equal to the force generated [*Reynolds, 2003*]. Equation A-1 and Equation A-2 display each of the laws described above.

Equation A-1 Universal Law of Gravitation

$$F = \frac{G \; x \; M \; x \; m}{R^2}$$

In Equation A-1, F: force, G: gravitational constant, M: primary mass (kg), m: secondary mass (kg), R: distance between masses (m)

Equation A-2 Newton's Second Law

$$F = m \; x \; g$$

In Equation A-2, F: force, m: mass (kg), g: acceleration due to gravity (m/s^2)

In theory, these equations show that gravity should be relatively constant over the surface of the Earth. However, the Earth is a dynamic and heterogeneous body with a mass that is not constant. Density changes in subsurface materials can cause small changes in the acceleration which can then be measured in gravity surveys. Anomalies found in gravity surveys are calculated by subtracting the regional field from the measured field at a specific location [*Reynolds, 2003*]. Positive anomalies are a result of high density bodies whereas negative anomalies are a result of low density bodies or cavities.

The gravity method is a fairly straight forward use of one of Earth's natural potential fields. However, it is only able to measure lateral changes and cannot measure changes as a function

of depth. Because gravity surveys only measure lateral changes, there is a certain amount of ambiguity when analyzing gravity data. Data must be interpreted to the best ability of the geophysicist as to what shape the object in the subsurface is and what depth it is at. Additionally, Earth's gravitational forces are affected on a larger scale by things such as rotational flattening, elevation changes, and tidal forces which must be accounted and corrected for when interpreting the data.

Regional gravity changes as well as changes caused by density variations in the immediate subsurface are often measured with a small gravimeter, but airborne gravity data can also be collected. When using a gravimeter, change is measured in milligals. Milligals come from the unit of gals which is defined as 1 cm/s^2. Some of the studies that gravity surveys are useful for include hydrocarbon exploration, location of ore deposits, regional changes in geology, and geodesy [Reynolds, 2003].

ii. Magnetics

The concept of magnetization is described by Ampere's Law which explains the relationship between a magnetized field and the flow of electrical current. This relationship is the key for enabling areas to be surveyed magnetically [*Telford et. al., 1990*]. Equation A-3 below demonstrates this relationship.

Equation A-3 Ampere's Law

$$\Delta H = (I\Delta l)x\frac{r_1}{4\pi r^2}$$

In Equation A-3, ΔH: magnetizing field, *I*: current (V), Δl: length of the conductor (m), r: distance from the object (m).

The relationship between current flow and magnetization is critical when completing a magnetic survey, because these two concepts are directly proportional to the magnetization intensity of an object. The magnetization intensity is how well molecules align in a magnetizable body when placed in a magnetic field. Magnetization intensity is also known as the magnetic polarization, because the molecules align based on their magnetic dipole, which aligns with the Earth's dipole and generates a magnetic field [*Telford et. al., 1990*]. The relationship between the magnetization intensity and magnetizing field is determined by an objects magnetic susceptibility, k and is shown in Equation A-4.

Equation A-4 Magnetic Susceptibility

$$M = kH$$

In Equation A-4, M: magnetization intensity (A/m), k: magnetic susceptibility, H: magnetizing field (A/m)

Magnetic susceptibility is the parameter that makes magnetic surveying possible. Every rock has a generalized susceptibility based on the amount of magnetic material within the rock. This susceptibility is measured by a magnetometer. In general, sedimentary rocks have a much lower susceptibility then igneous rocks, and metamorphic rocks are generally between the two, depending on the mineral content in the rock. The wide range of susceptibilities makes magnetics a feasible survey for looking at large scale changes in subsurface rock formations. However, magnetic surveying has two major drawbacks. The first is that it maintains ambiguity with depth and only measures lateral changes. Secondly, magnetic surveys are also affected by any conductive material in the area such as power lines and metal objects.

iii. Electromagnetics

There are two types of electromagnetic methods: time-domain electromagnetics (TEM) and frequency-domain electromagnetics (FEM). Both electromagnetic methods use Ampere's Circuital Law to describe the behavior of the magnetic field as the method controls it [*Geophysics Field Camp, 2010*]. This Law is shown in Equation A-5.

Equation A-5 Ampere's Circuital Law

$$\nabla \times \boldsymbol{H} = \boldsymbol{J} + \frac{\delta \boldsymbol{D}}{\delta t}$$

In Equation A-5, H: magnetizing field (A/m), J: free current density (S/m), D: electric displacement field (C/m^2), t: time (s)

1) Frequency Domain Electromagnetics

Frequency-domain methods use multiple frequencies and an artificial transmitter coil to generate an electromagnetic field. The frequency range can be from as low as 10Hz to as high as 10^{16} Hz. An alternating current in a small coil generates a magnetic field which then penetrates the surface and travels through the subsurface. This magnetic field is varied sinusoidally by the transmitter, and that variation generates an electric field, or eddy currents, in a conductive body within the subsurface. These eddy currents will then create a secondary

magnetic field which travels through the subsurface back up to the surface where it is detected by a receiver coil [*Reynolds, 2003*]. The induction of eddy currents in the subsurface is explained by Faraday's Law, Equation A-6.

Equation A-6 Faraday's Law

$$\nabla x E = \frac{\partial B}{\partial t}$$

In Equation A-6, E: electric field (N/C), B: magnetic field (A/m), t: time (s)

The receiver will also detect the portion of the primary field that traveled through the air providing a resultant field. In FEM surveys the transmitter never shuts off the current generating the primary magnetic field, therefore it will always be present in FEM data and must be corrected for. Figure A-1 shows a schematic of FEM surveying of the subsurface with the three loop system as well as the primary and secondary fields.

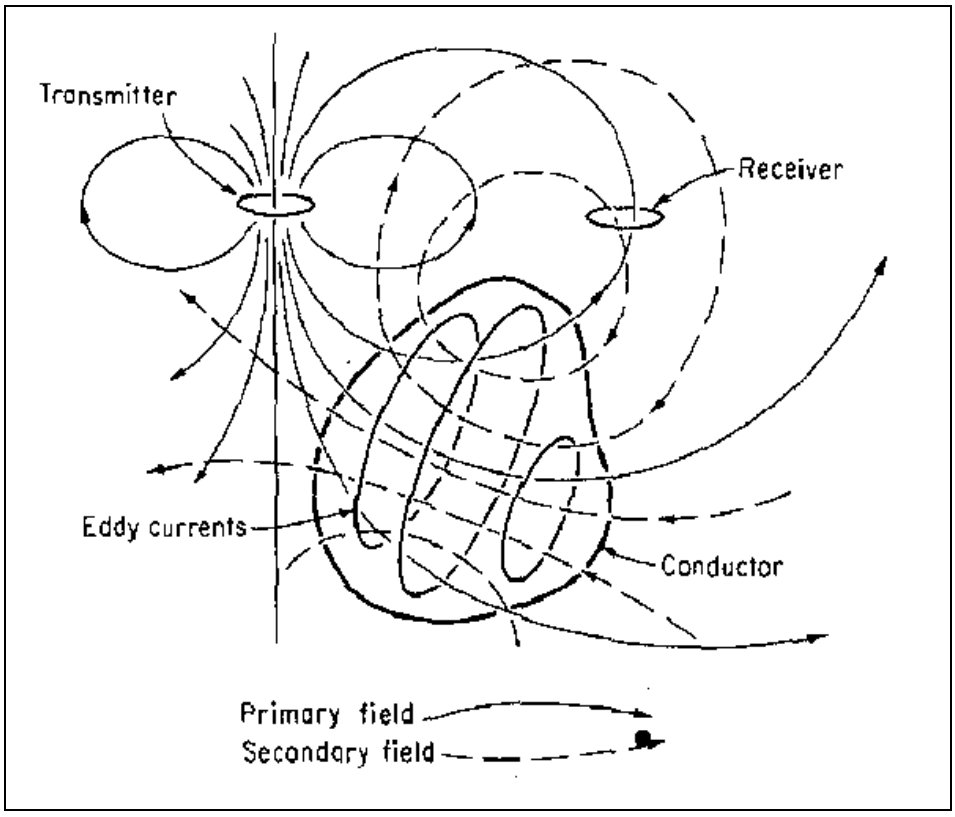

Figure A-1 Basic Schematic of EM Methods: Primary field induces a current in the conductive body, which generates its own secondary electromagnetic field that then induces a current in the receiver coil. [*Grant and West, 1965*]

10.1.2 Time Domain Electromagnetics

Time-domain methods maintain a single frequency throughout acquisition and measure variations in the electromagnetic current as it disperses through the ground with time. In TEM surveying a large transmitter loop surrounds a small receiver loop. The current is shut off in the transmitter loop while the receiver measures how quickly the induced magnetic field disperses through the ground. Faster dispersion represents resistive subsurface bodies while slower dispersion represents more conductive subsurface material. TEM surveys benefit from the fact that the primary field is turned off during acquisition and therefore does not need to be corrected for in the final data. The diagrams in Figure A-2 demonstrate the shutting off of the current to measure the induced field as it decays.

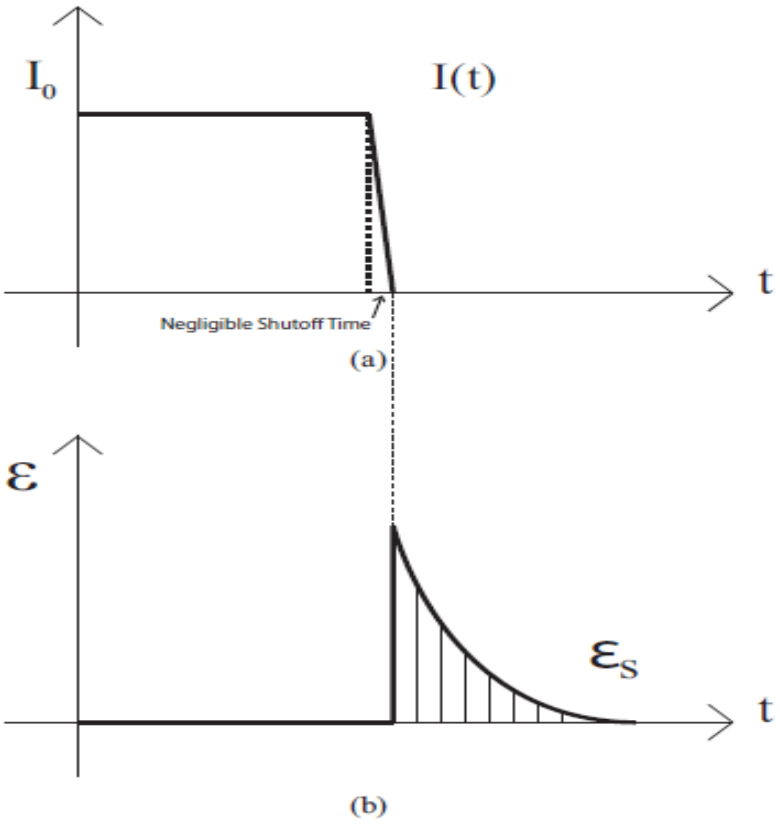

Figure A-2 Representation of Current and Voltage in Time Domain Electromagnetics: (a) demonstrates current versus time (b) demonstrates voltage versus time [*Geophysics Field Camp, 2010*]

Electromagnetic methods have several advantages over other methods, including the fact that processing EM data has a much simplified process. However, there are also several

draw backs. A major disadvantage of this method is that it can be inconclusive if a highly conductive layer is overlaying a smaller conductive body. Little or no primary field will be able to penetrate the conductive layer to gather information about the conductive body below. This can create ambiguity in the analysis, and therefore inversion must be done to gain a better understanding of the results.

iv. Controlled Source Audio Magneto Tellurics

CSAMT is a remote source electromagnetic method which uses a dipole separated over 1-2 km , which is much greater separation then other surveys. By placing the receivers away from the transmitter in this manner, we can assume that the magnetic field lines generated by the dipole are planar and horizontal waves at these locations, therefore the magnetic field only needs to be measured once along one receiver line. However, the electric field will change more rapidly, so it needs to be measured by each receiver [*Milson, 2010*].

Once this data is collected, the resistivity can be found since it is proportional to E and H. The artificial source allows for faster data collection and greater precision than the AMT and MT methods do, and it's depth of investigation ranges from 20-2000m. Frequencies range from 0.125Hz to 8000Hz, allowing for a large range of depths to be investigated.

b. Electrical Methods

i. Self Potential

The self potential (SP) method is one of the best equipped methods for mapping the flow of water in the porous subsurface. In basic principle, SP is a passive electrical method that measures the current in the ground from water flow. When ground water contains an excess of electrical charges, these charges are dragged along the pore walls which causes a polarization of charges. This process will create an electrical potential that is positive in the direction of ground water flow [*Revil et. al., 2004*]. This electrical potential is known as the streaming potential which describes the strength and direction of the flow. Figure A-3 shows a diagram of the charge build up due to ground water flow.

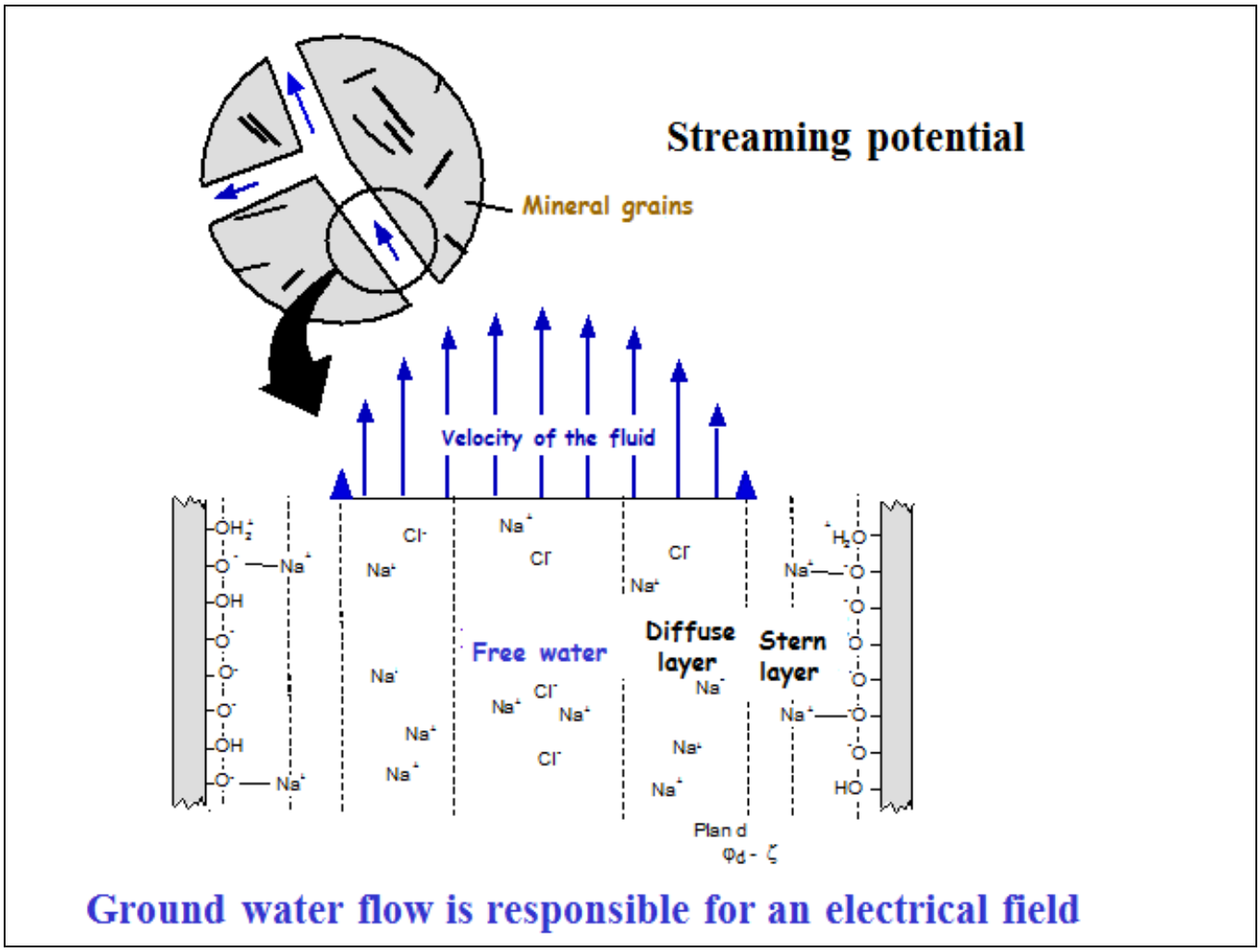

Figure A-3 Streaming Potential Measured by the Self Potential Method [*Revil 2011*]

The streaming potential can be measured using non-polarizing electrodes; in the case of the Neal Hot Springs area lead/lead-chloride electrodes were used. These electrodes are connected to a voltmeter that has sensitivity in millivolts. It is normal for measurements to be either positive or negative when completing the SP method; changes are only looked at in a relative sense. Positive changes in measurements generally indicate ground water flow towards the surface, while negative changes indicate water flowing away from the surface. Figure A-4 shows some basic anomaly types that may be seen based on variations in SP measurements.

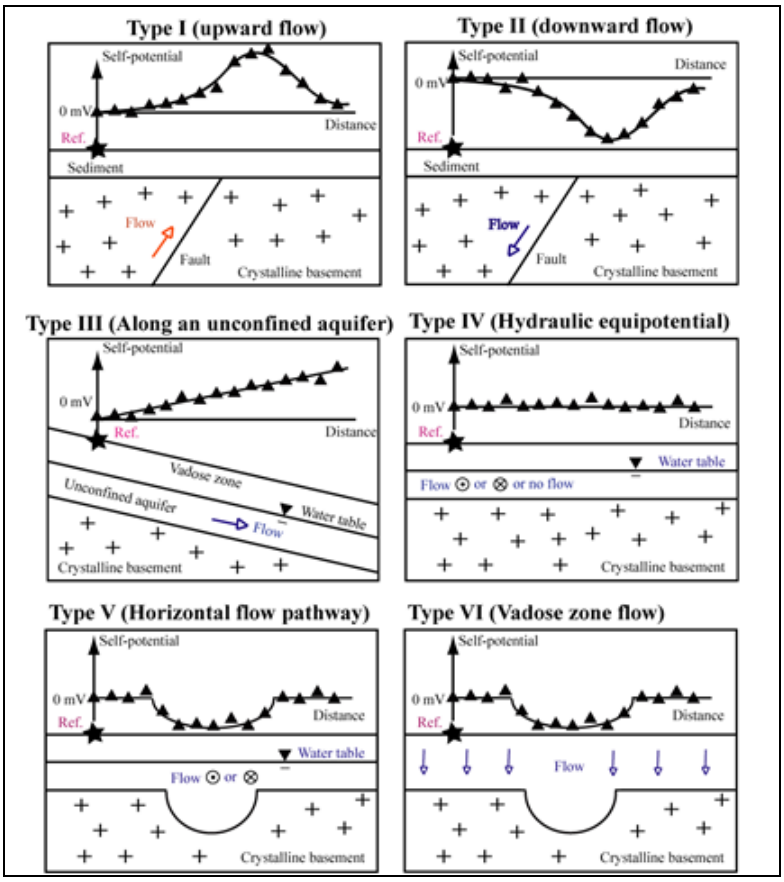

Figure A-4 General Types of Anomalies Detected by the Self Potential Method [*Revil 2011*]

The SP method is a fairly fast surveying technique that requires little equipment. It is effective at modeling ground water flow but it is fairly limited when identifying other anomalies in the subsurface that are not associated with ground water flow. One subsurface body that can cause a large negative anomaly is a sulfide mass within the subsurface, which could cause confusion when interpreting the data [*Milson, 2011*].

SP data can be presented in graphs as a function of the distance or as a function of the altitude. The study of this type of graph can be interpreted for localizing discontinuities in the soil (e.g. circulation of fluids along faults) and identifying hydrothermal convection. Usually this can be done by joining the results of other geophysical or geochemical methods. With an appropriate dataset, we can also present SP data in map form, interpolating between lines.

ii. DC Resistivity

The resistivity method employs an artificial source of current, which is introduced into the ground through point electrodes. The objective is to measure the potential at other specified electrodes. The current is also measured, making it possible to determine an effective or apparent resistivity of the subsurface. Resistivity measurements (Equation A-7[*Telford, 2004*]) are normally made by injecting current into the ground through two current electrodes and measuring the resulting voltage difference at two potential electrodes. The configuration of the four electrodes depends on the choice of array.

Equation A-7 Apparent Resistivity Formula

$$pa = k\,V / I \text{ or } pa = k\,R$$

In Equation A-7 k is the geometric factor which depends on the arrangement of the four electrodes, V is the voltage (V), I is the current values (A), *pa* is the apparent resistivity values, R is the resistance value from the resistivity meters (V/I)

To determine the true subsurface resistivity, an inversion of the apparent resistivity values using a computer program must be carried out. In this method, the center point of the electrode array remains fixed, but the spacing between the electrodes is increased to obtain more information about the deeper sections of the subsurface.

Igneous and metamorphic rocks typically have high resistivity values though the resistivity of these rocks is greatly dependent on the degree of fracturing, and the percentage of the fractures filled with ground water. Sedimentary rocks, which usually are more porous and higher water content, typically have lower resistivity values.

Wenner Array

The Wenner array is relatively sensitive to vertical changes in the subsurface resistivity below the center of the array. However, it is less sensitive to horizontal changes in the subsurface resistivity. The Wenner is good in resolving vertical changes (i.e. horizontal structures), but relatively poor in detecting horizontal changes (i.e. narrow vertical structures). The signal strength is inversely proportional to the geometric factor used (***2pa***, which is smaller than the geometric factor for other arrays) to calculate the apparent resistivity value for the array. The configuration of the Wenner array is illustrated below in Figure A-5. The four

electrodes are evenly spaced. Current is induced through electrodes A and B and the voltage is measured through electrodes M and N.

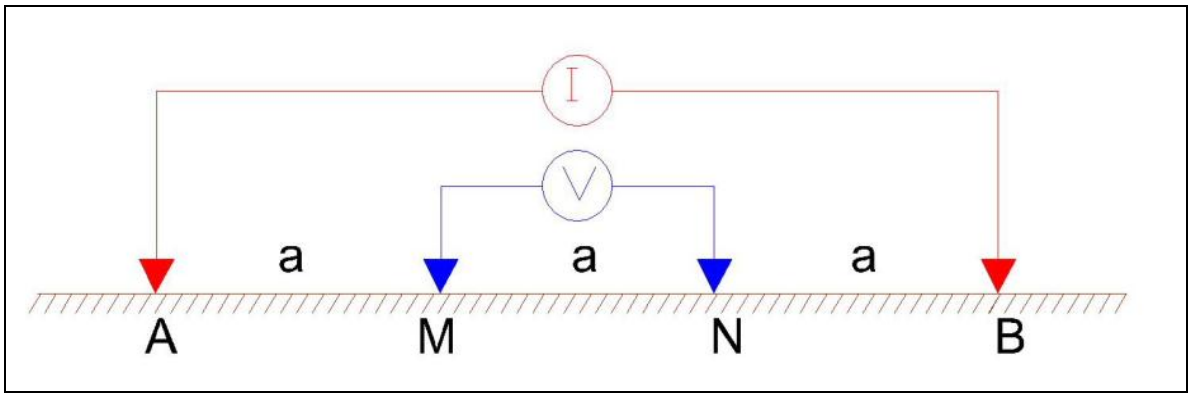

Figure A-5 Wenner Array Configuration [*Brantax Website*]

Dipole-Dipole

This array is most sensitive to resistivity changes between the electrodes in each dipole pair. Note that the sensitivity contour pattern is almost vertical. Thus the dipole-dipole array is very sensitive to horizontal changes in resistivity, but relatively insensitive to vertical changes in the resistivity. That means that it is good in mapping vertical structures, such as dykes and cavities, but relatively poor in mapping horizontal structures such as sills or sedimentary layers. It has a lower signal to noise ratio than the Wenner array. The configuration is illustrated below in Figure A-6, using the same convention as for the Wenner array.

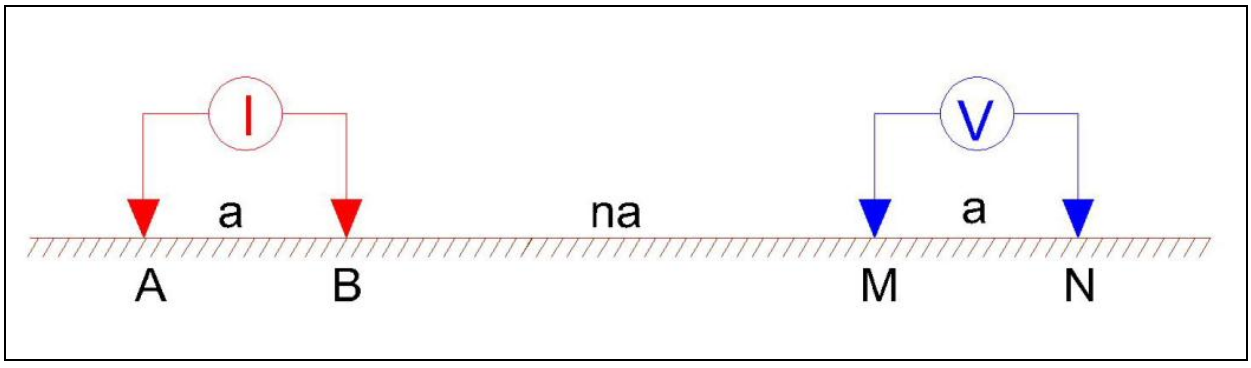

Figure A-6 Dipole-Dipole Array Arrangement [*Brantax Website*]

The distance between the two pairs of electrodes (na) is a multiple of the electrode spacing within the pairs (a).

c. Reflection Seismology

Seismic data is a recording of the Earth's response to a controlled seismic source. Seismic reflection surveys measure the seismic reflections received from subsurface interfaces following detonation of the source. The source primarily induces compressional waves (P-waves) over a broad frequency spectrum in the Earth's subsurface. The receivers primarily record the compressional waves reflected from subsurface interfaces. This is regarded as the signal; all other content of the record is regarded as noise. In the case of land seismic data, Vibroseis, or a truck-mounted vibrator, is a commonly used source. Geophones are used as receivers.

The objective of seismic reflection processing is to separate the primary reflections due to subsurface interfaces from all other recorded noise, including rays that have reflected multiple times (multiples). Processing also attempts to optimize the signal to noise ratio and image the subsurface effectively. The recorded traces are the convolution of the following, of which the Earth's reflectivity series is the desired information:

- Source signature
- Earth's reflectivity series
- Receiver signature
- Noise, e.g. ghost source, ambient noise, refractions, ground roll.

The ideal source wavelet is a spike or impulse at zero time, containing all possible frequencies. This is not possible to due to physical limitations; for example, the wavelet must be causal and have finite energy. In the case of a Vibroseis source for land surveying, the source wavelet is a known maximum phase wavelet, the autocorrelation of which is a spike at zero time. As the wavelet is known (unlike where dynamite or air guns are used as sources), it is correlated with the data in order to reduce the source signature to a band limited spike.

A broad range of frequencies is desirable as high frequency waves attenuate more rapidly with depth, but achieve higher resolution than low frequency waves, which penetrate more

deeply. In processing, the wavelet can be shaped with digital filters in order to optimize the data, and reduce the wavelet as close to the ideal as possible in order to optimize data resolution.

A typical processing sequence for land seismic data is illustrated below:

1) Demultiplex data and sort into shot gathers
2) QC shot gathers
3) Apply refraction mute
4) Filter noise and apply trace edits
5) Compensate for spherical divergence
6) Apply DBS (deconvolution before stack)
7) Apply geometry and bin to CMP gathers
8) Conduct static analysis and apply corrections
9) Conduct velocity analysis
10) Multiple attenuation (e.g. PRT)
11) Apply NMO corrections
12) Stack traces
13) Output brute stack. QC and iterate process to optimize stack.
14) Apply DAS (deconvolution after stack)
15) Multiple attenuation (e.g. predictive deconvolution)
16) Apply DMO corrections
17) Reiterate velocity analysis
18) Calculate interval velocities
19) Migrate
20) Output final stack

A primary tool for improving the signal to noise ratio is the common midpoint (CMP) method, by which records are made at multiple source and receiver offsets, which have the same midpoint between the source and receiver. In the case of a horizontal reflector, the subsurface reflection point of the traces is also in common, such that multiple responses from

the same reflection point are acquired, as shown in Figure A-7. These traces are gathered and ordered by source-receiver offset, producing a CMP gather, as shown in Figure A-8.

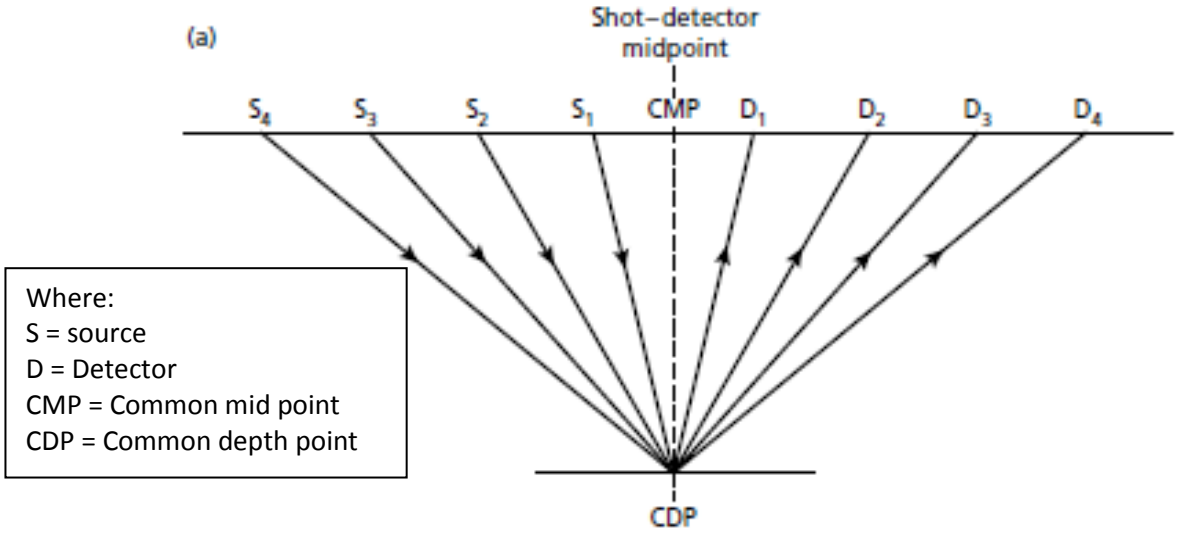

Figure A-7 Reflected Rays Comprising a CMP gather [Modified from Kearey, Brooks and Hill, 2002]

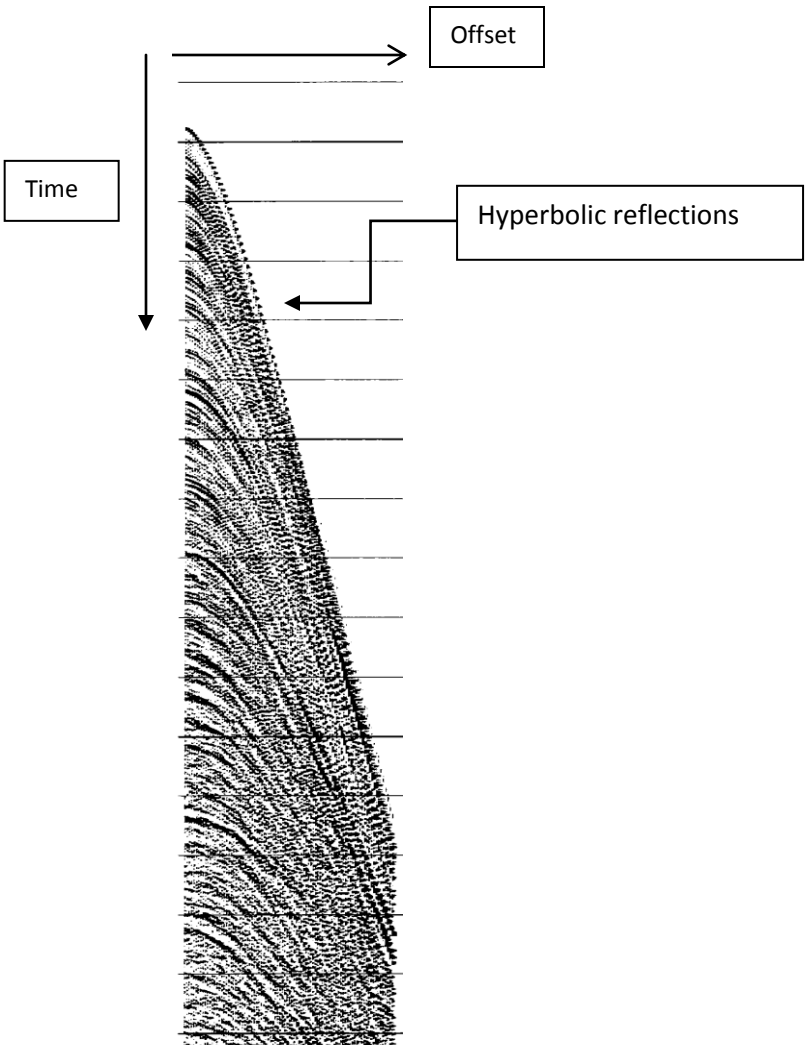

Figure A-8 Sample CMP Gather [*Modeified from Yilmaz, 2001*]

Normal moveout (NMO) corrections are applied to the CMP gather in order to correct for moveout due to increased travel time with increased source-receiver offset, approximating the data to zero source-receiver offset. NMO is hyperbolic, as seen in the CMP gather in Figure A-8Figure A-9, and is a function of subsurface velocity and source-receiver offset, as shown in tropy.

Equation A-8. NMO corrections 'flatten' the reflectors, as seen in Figure A-9. The traces are then summed, or stacked. The common reflections constructively interfere; the single to noise ratio increases as a function of the number of traces in the CMP gather, or fold.

It should be noted that the velocity indicated by NMO corrections is primarily an imaging parameter, being the velocity that produces the best correlation between traces in a CMP gather. This parameter tends to overestimate subsurface velocity as the zero offset reflection does not sample lateral anisotropy.

Equation A-8 Normal Moveout

$$t^2 = t_0^2 + \frac{x^2}{v^2}$$

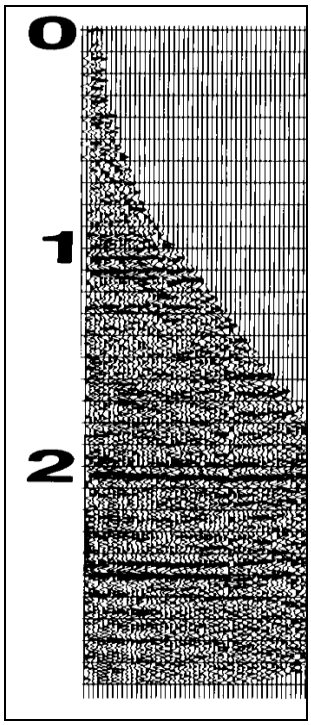

Figure A-9 NMO Corrected CMP Gather (from Yilmaz [2001])

Multiples are a form of noise in the dataset that are a result of waves being reflected from multiple interfaces in the subsurface before being received at the surface. In the data, they succeed a primary reflection, appearing as periodic duplicates of the primary. The predictable nature of multiples, and their slower velocity compared to simultaneously arriving primary reflections can be exploited in order to suppress multiples in the data. Short period multiples can be targeted by predictive deconvolution; long period multiples can be filtered by a variety of methods, including parabolic radon transform and F-K filtering.

Dip moveout (DMO) corrections are applied to the stacked dataset in order to remove the dependency of subsurface velocity on the dip of reflective interfaces, such that the stack is a true zero offset section, as the assumption that traces with a common midpoint share a common reflection point is only true in the case of horizontal interfaces.

Migration also compensates for the assumption that rays in the zero offset section are normally incident to the reflective interface; a lateral and vertical shift is applied to reflections, effectively moving the reflection over the spherical wave front intersecting the interface. It has the effect of moving the reflection down dip such that the position of the reflection correlates with that of the reflector.

The final stack is intended to represent the reflectivity of the subsurface in time, and allows interpretation of subsurface structure and possible lithology. Reflectivity is a function of density and velocity, and seismic data can be inverted in conjunction with further data in order to extract these from the data.

d. Vertical Seismic Profiling

Vertical seismic profiles (VSPs) have multiple applications, but in particular are a valuable means of obtaining seismic data with depth information, enabling improved correlation between localized well data (measured in depth). It can be useful for wire line logs and rock cores or cuttings, for regional scale seismic data, and also for generating local scale velocity models (which with additional information may be extrapolated over the scale of a seismic survey).

A VSP survey is conducted at a well site, using in-hole receivers, such as geophones, at known depths from the surface, and surface sources at known offsets from the well head. The in-hole geophones record the single way time of seismic waves travelling through the subsurface from the source.

Figure A-10 shows the survey geometry for an offset VSP, although VSP surveys may also comprise zero offset or ‘walkaway’ geometries. These methods are differentiated on the basis

of the source location relative to the well. In a zero offset survey, the surface source is placed vertically above the in-hole receivers; in an offset survey, the surface source is laterally offset from the in-hole receivers; and in a walkaway survey, the surface source increases in offset from the wellhead with successive shots. Offset and walkaway surveys have the advantage of allowing the survey to sample the subsurface radially from the well to a limited extent. VSPs are generally of higher resolution than regional seismic surveys due to reduced attenuation of the seismic signal due to the shorter travel path (one-way), and can provide structural information that cannot be observed in the well data, such as stratigraphic dip about the well. Offset and walkway VSPs can also inform more representative velocity models by sampling lateral anisotropy in the subsurface.

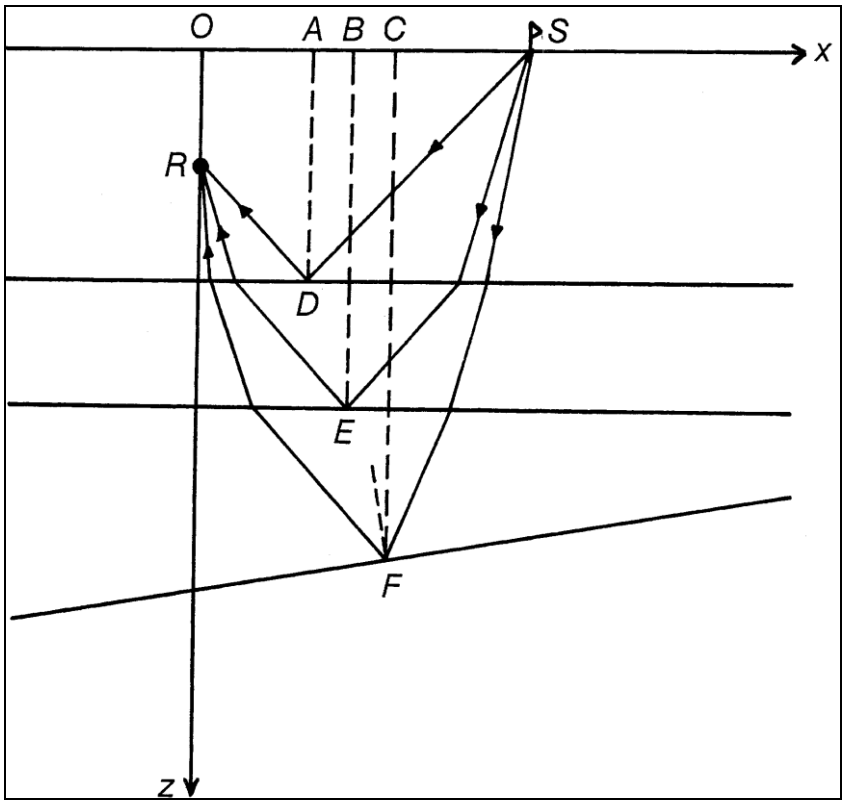

Figure A-10 Geometry for a VSP with Offset Source [*Yilmaz, 2001*] Where: S is the source location, R is the receiver location, O is the wellhead, x is offset, z is depth, D E and F are the reflection points on 3 subsurface reflectors.

As seen in

Figure A-11, the depth to a subsurface interface can be identified in the record of a zero offset VSP by the intersection of the downward travelling direct arrival and the upward

travelling primary reflection. These arrivals will be succeeded by upward and downward travelling multiples, seen in

Figure A-11. The gradient of the direct arrivals corresponds with the bulk velocity of the layer.

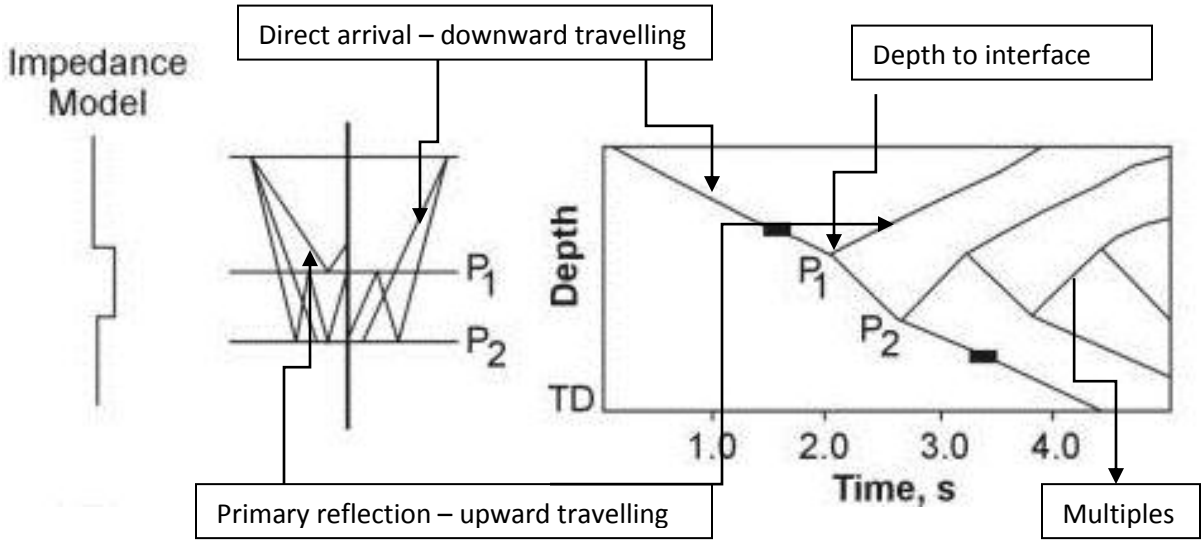

Figure A-11 Impedance Model, Ray Diagram and Model Zero Offset VSP Record for a 2 Layer Case [*EPA Website*]

VSPs require processing to isolate the signal from the noise, which includes separating the up-going reflections and down-going multiples (and direct arrivals). This can be achieved by applying a multichannel dip filter, such as an f-k filter. The data is then corrected for statics, or the decreasing travel time with increasing geophone depth; the data is corrected to a datum surface, for example, the surface or sea level, such that a reflection event appears flat in the data record, as seen in Figure A-12. The narrow corridor of the short-time arrivals in the data, indicated in Figure A-12, is stacked to generate a corridor stack. This portion is selected and is largely multiple free. The corridor stack can be used similarly to a synthetic trace to correlate seismic and well data.

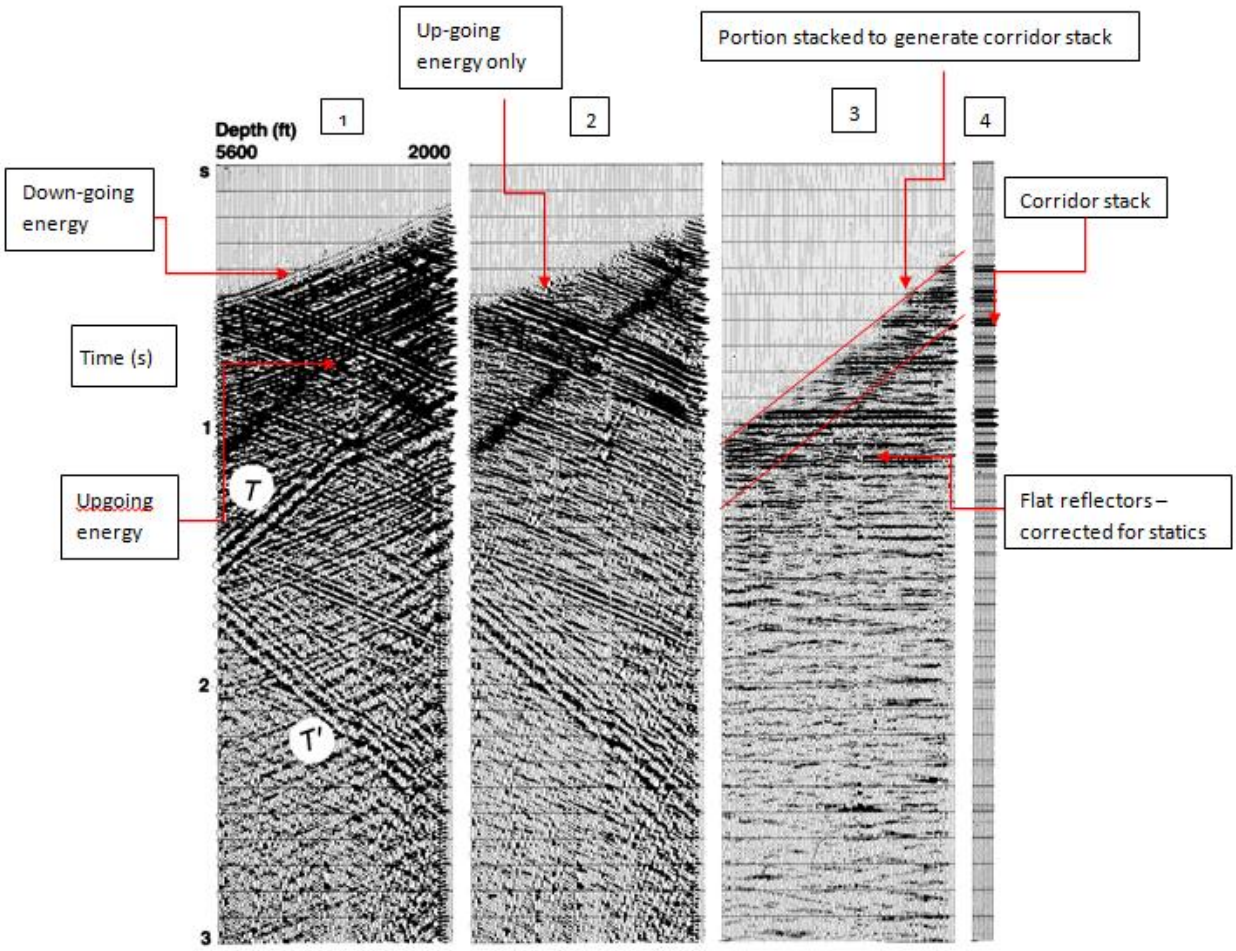

Figure A-12 Zero Offset VSP Data 1) prior to processing, 2) filtered to remove down-going energy 3) with statics corrections and noise attenuated 4) presented as a corridor stack [*Yilmaz 2001*]

B. Additional Tables, Equations, and Figures

a. Potential Fields

TABLE 1

MILLIGAL VALUES FOR LACOSTE & ROMBERG, INC. MODEL G GRAVITY METER #G- 491

COUNTER READING*	VALUE IN MILLIGALS	FACTOR FOR INTERVAL	COUNTER READING*	VALUE IN MILLIGALS	FACTOR FOR INTERVAL
000	000.00	1.02136			
100	102.14	1.02121	3600	3682.28	1.02563
200	204.26	1.02111	3700	3784.84	1.02579
300	306.37	1.02111	3800	3887.42	1.02593
400	408.48	1.02113	3900	3990.01	1.02607
500	510.59	1.02118	4000	4092.62	1.02620
600	612.71	1.02124	4100	4195.24	1.02631
700	714.83	1.02133	4200	4297.87	1.02640
800	816.97	1.02142	4300	4400.51	1.02648
900	919.11	1.02152	4400	4503.16	1.02657
1000	1021.26	1.02165	4500	4605.82	1.02665
1100	1123.43	1.02177	4600	4708.48	1.02673
1200	1225.60	1.02192	4700	4811.16	1.02680
1300	1327.80	1.02205	4800	4913.84	1.02688
1400	1430.00	1.02218	4900	5016.52	1.02696
1500	1532.22	1.02232	5000	5119.22	1.02701
1600	1634.45	1.02245	5100	5221.92	1.02706
1700	1736.70	1.02260	5200	5324.63	1.02709
1800	1838.96	1.02275	5300	5427.34	1.02712
1900	1941.23	1.02290	5400	5530.05	1.02712
2000	2043.52	1.02305	5500	5632.76	1.02712
2100	2145.83	1.02318	5600	5735.47	1.02706
2200	2248.14	1.02333	5700	5838.18	1.02698
2300	2350.48	1.02348	5800	5940.88	1.02688
2400	2452.82	1.02363	5900	6043.56	1.02676
2500	2555.19	1.02379	6000	6146.24	1.02663
2600	2657.57	1.02394	6100	6248.90	1.02649
2700	2759.96	1.02409	6200	6351.55	1.02633
2800	2862.37	1.02426	6300	6454.18	1.02616
2900	2964.80	1.02444	6400	6556.80	1.02597
3000	3067.24	1.02463	6500	6659.40	1.02576
3100	3169.70	1.02481	6600	6761.97	1.02557
3200	3272.18	1.02499	6700	6864.53	1.02537
3300	3374.68	1.02516	6800	6967.07	1.02515
3400	3477.20	1.02534	6900	7069.58	1.02495
3500	3579.73	1.02547	7000	7172.08	

* Note: Right-hand wheel on counter indicates approximately 0.1 milligal.

1-12-78
rp

Figure B-1 Lacoste and Romberg G-491 Gravimeter Conversion Table

i. Gravity Data Correction Equations

Bouguer anomaly

Equation B-1 Bouger Anomaly Correction for Ground or Ship Borne Surveying

$$Gb = Gf - 0.0419088 * [D * Hs + (Dw - D) * Hw + (Di - Dw) * Hi] | Gc$$

Gb: Bouguer anomaly (mgals), Gf: Free air anomaly, D: Bouguer density of the Earth (g/cm^3), Dw: Bouguer density of water (g/cm^3), Di: Bouguer density of ice (g/cm^3), Hs: Station elevation (m), Hw: Water depth (including ice) (m), Hi: Ice thickness (m), Gc: Curvature (Bullard B) correction, Hg: Ground (DEM) elevation at survey station location (m)

Latitude Correction

The latitude correction requires the theoretical gravity at the station location on Earth's spheroid. There are four optional formulas provided, and more formulas can be added by editing the file Gravity_Formulas.lst" in the geosoft/user/etc directory. Note that this file will be created the first time the GRBOUG GX is run. In each formula Gl is theoretical gravity and L is the station latitude.

Equation B-2 1930 Formula

$$Gl = 978049 * [1 + 0.0052884 \sin(L) * \sin(L) - 0.0000059 * \sin(2L) * \sin(2L)]$$

[*Blakely, 1995*]

Equation B-3 1967 (Sheriff) Formula

$$Gl = 978031.846 * [1 + 0.005278895 \sin(L) * \sin(L) + 0.000023462 * \sin(L) * \sin(L) * \sin(L)$$

[*Sheriff, 1984*]

Equation B-4 1980 Former Geosoft Formula (in previous Geosoft versions, this is referred to as simply the 1980 formula)

$$Gl = 978032.7 * [1 + 0.0053024 * (\sin(L) * \sin(L)) - 0.0000058 * (\sin(2 * L) * \sin(2 * L))]$$

(This expression was provided by a Geosoft user and is included for compatibility with older versions of Geosoft.)

Equation B-5 1984 Formula

$$GI = 978032.67714 * \frac{[1 + 0.00193185138639 * (sin(L) ** 2))}{sqrt(1 - 0.00669437999013 * (sin(L) ** 2)]}$$

[*Blakely, 1995*]

Free-Air Anomaly

The free air correction is calculated by subtracting the latitude correction (theoretical gravity) from the absolute gravity and adding a correction for the station elevation. The following formulas are defined in Gravity_Free_Air.lst in the Geosoft/etc directory where Gf is the Free air anomaly (mgals), Ga is absolute gravity (mgals), Gl is the Latitude correction, Hs is the station elevation (m), and L is the latitude of the station:

Equation B-6 Old Geosoft Formula

$$Gf = Ga - Gl + 0.308596 * Hs$$

Equation B-7 Sheriff Formula

$$Gf = Ga - Gl + 0.3086 * Hs$$

[*Sheriff, 1991*]

Equation B-8 Heiskanen and Mortiz Formula

$$Gf = Ga - Gl + (0.308767763 - 0.000439834 * (sin(L) ** 2) - 0.000000072124602 * Hs) * Hs$$

[*Heiskanen and Mortiz, 1967*] **This formula accounts for the non-linearity of the free-air anomaly as a function of both latitude and height above the geoid.**

ii. Time Domain Electromagnetics

6.1 PROTEM DIGITAL RECEIVER GATE LOCATIONS - 20 GATES MODE

(from end of trailing edge in micro seconds)

	<-- 285/237.5 Hz --->			<--- 75/62.5 Hz ---->			<---- 30/25 Hz---->		
gate	start	center	width	start	center	width	start	center	width
1	6.000	6.813	1.625	32.00	35.25	6.500	80.00	88.13	16.25
2	7.625	8.688	2.125	38.50	42.75	8.500	96.25	106.9	21.25
3	9.750	11.13	2.750	47.00	52.50	11.00	117.5	131.3	27.50
4	12.50	14.19	3.375	58.00	64.75	13.50	145.0	161.9	33.75
5	15.88	18.07	4.375	71.50	80.25	17.50	178.8	200.6	43.75
6	20.25	23.06	5.625	89.00	100.3	22.50	222.5	250.6	56.25
7	25.88	29.44	7.125	111.5	125.8	28.50	278.8	314.4	71.25
8	33.00	37.56	9.125	140.0	158.3	36.50	350.0	395.6	91.25
9	42.13	47.94	11.63	176.5	199.8	46.50	441.3	499.4	116.3
10	53.75	61.13	14.75	223.0	252.5	59.00	557.5	631.3	147.5
11	68.50	77.94	18.88	282.0	319.8	75.50	705.0	799.4	188.8
12	87.38	99.38	24.00	357.5	405.5	96.00	893.8	1014	240.0
13	111.4	126.7	30.63	453.5	514.8	122.5	1134	1287	306.3
14	151.7**	166.4	29.38	576.0	654.3	156.5	1440	1636	391.3
15	181.1	206.0	49.88	732.5	832.3	199.5	1831	2081	498.8
16	231.0	262.8	63.63	932.0	1059	254.5	2330	2648	636.3
17	294.6	335.2	81.25	1187	1349	325.0	2966	3373	812.5
18	375.9	427.7	103.6	1512	1719	414.5	3779	4297	1036
19	479.5	545.6	132.1	1926	2190	528.5	4815	5475	1321
20	611.6	695.9	168.5	2455	2792	674.0	6136	6978	1685
21*	780.1			3129			7821		

* end of gate 20
** a gap of 9.7 μs exists between GATE 13 and GATE 14 at u frequency

This table applies to both synchronization modes regardless of which of TEM37(67), TEM47 and TEM57(MK-2) transmitters is used, provided that correct Tx model is selected in HEADER (2.4).

7.5/6.25 and 0.75/0.625 Hz proportional to 75/62.5 Hz.
3/2.5 and 0.3/0.25 Hz proportional to 30/25 Hz.

GEONICS PROTEM-47D operating manual 3.0

Figure B-2 Time Gate Locations [*Geonics PROTEM-47D Operating Manual, 2006*]

iii. Deep Seismic Data

Seismic Processing

SEGD is a file format standard developed by the Society of Exploration Geophysicists used for acquisition of large systems.

A Butterworth filter is defined by 2 frequencies and 2 roll off slopes defining a boxcar: the low cut-off frequency-low slope-high cut-off frequency-high slope, otherwise referred to as (F1-db/Octave1) – (F2-dB/Octave2).

Predictive Deconvolution

The predictive deconvolution mainly targets short-period multiples with avoid touching the signature [*Jakubowicz, 2011*]. It aims to collapse a long, ringy wavelet into a shorter energy source wavelet. This will improve the resolution of the primary reflections by the key assumption that genuine reflections come from an earth reflectivity series can be considered random and therefore not predictable [*Yilmaz, 1987*].

The white noise was added to data during the processing to stabilize the deconvolution calculation, while an autocorrelation function performed on the trace after deconvolution represented the wavelet in the data use to determine self-similarity and QC the remaining multiples. The autocorrelation function was accomplished by choosing the design window including operator length and gap length.

Gap or predictive lag is the preserved signature period [*Jakubowicz, 2011*] which is typically chosen to be larger than the desired source wavelet length, and less than the period of the shortest multiple [*Warner, 2011*]. The shorter gap can cause to be data distorted as the reflection will be deleted and a non-spectral balancing as the low and high frequency noise will be boosted up, However, the longer the gap length, the lower the resolution of the reflections.

Operator length is the effective deconvolution length operated. Increasing the operator length removes multiples but can eliminate reflections.

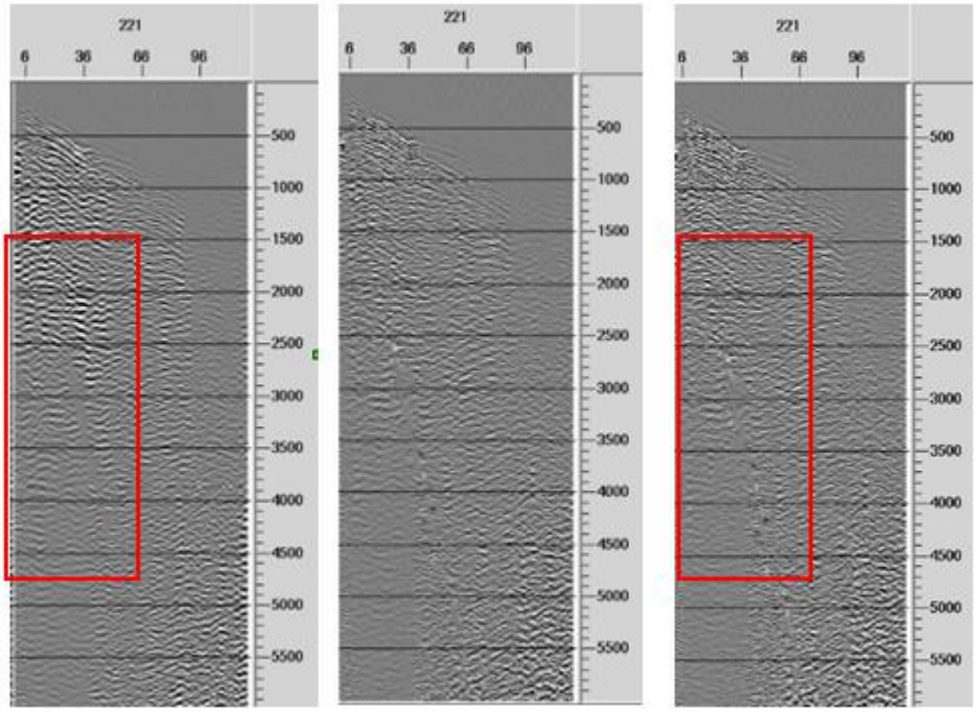

Figure B-3 The Result of Deconvolution at Shot Number 221; before processing on the far left, with 100 operator length and 1% noise in the mid and 120 operator length with 0.01 % white noise adding in the far right.

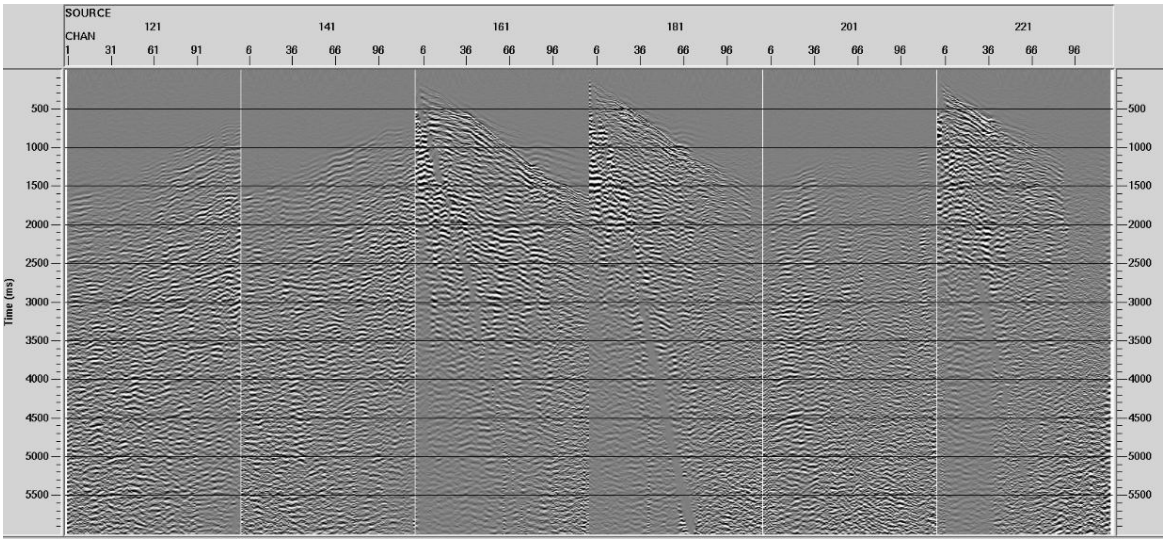

Figure B-4 Pre-stack Gather Before the Predictive Deconvolution was Applied

The reverberation reflections (short period multiples) were suppressed. Long ringing wavelet was collapsed on the autocorrelation window which increases S/N ratio and improves the resolution.

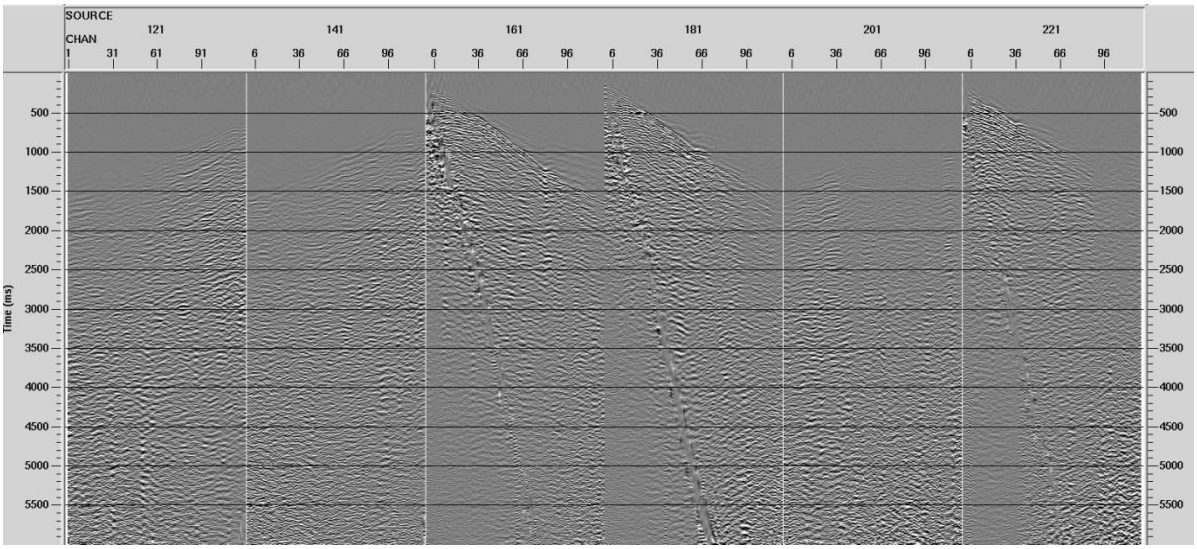

Figure B-5 Pre-stack Gather After Doing the Predictive Deconvolution using Operator Length of 120 ms, 35 ms Gap Length and 0.01 % White Noise Adding

This is generated through stacking with a range of constant velocities. In a horizontally layered subsurface with more than one reflection event, these velocities represented the RMS p-wave velocity through the different media above the reflection event.

Velocity Analysis

A CMP semblance spectrum can be calculated to aid velocity picking. The stacked traces generated by each of the velocities are displayed side by side to form the semblance spectrum. Cross correlation is utilized which measures similarity and semblance can be described as the normalized output to input energy ratio. Normalized, or energy normalized cross correlation brings out weak reflections. The output from one type of velocity analysis is a table of numbers as a function of velocity vs. two-way/zero offset time. Velocity time pairs are selected from these spectra based on maximum coherency peaks. These velocity functions are then spatially interpolated between analysis points across the entire profile.

To perform the correction, the semblance spectra of each CMP were analyzed and through processes of trial and error, optimal stacking velocities were picked so as to attain an accurate NMO correction – flattening primary reflection events within the gathers.

For the purposes of a first pass velocity analysis, velocities can be manually picked through the high amplitude peaks on the CMP semblance spectra.

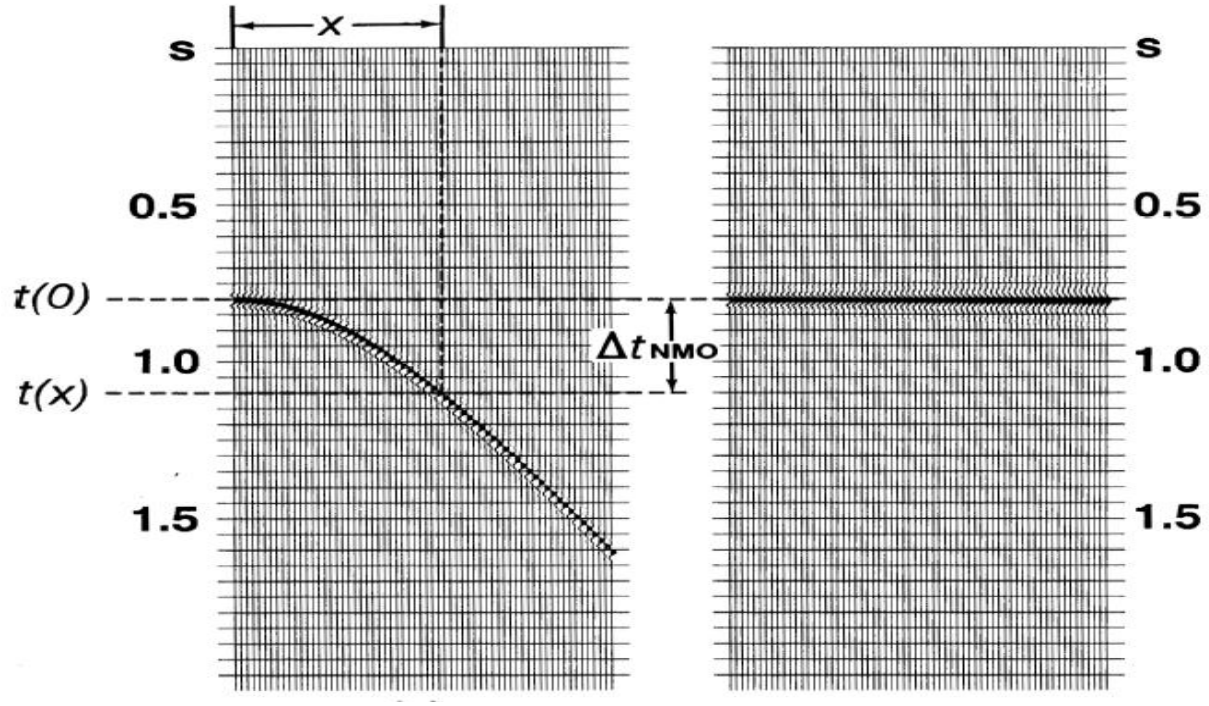

Figure B-6 (left) CMP Gather With Single Reflection Event before NMO Correction. Hyperbolic behavior Is a result of source receiver geometry and layer velocity. (Right) Reflection event flattened after NMO correction [*Yilmaz 2001*]

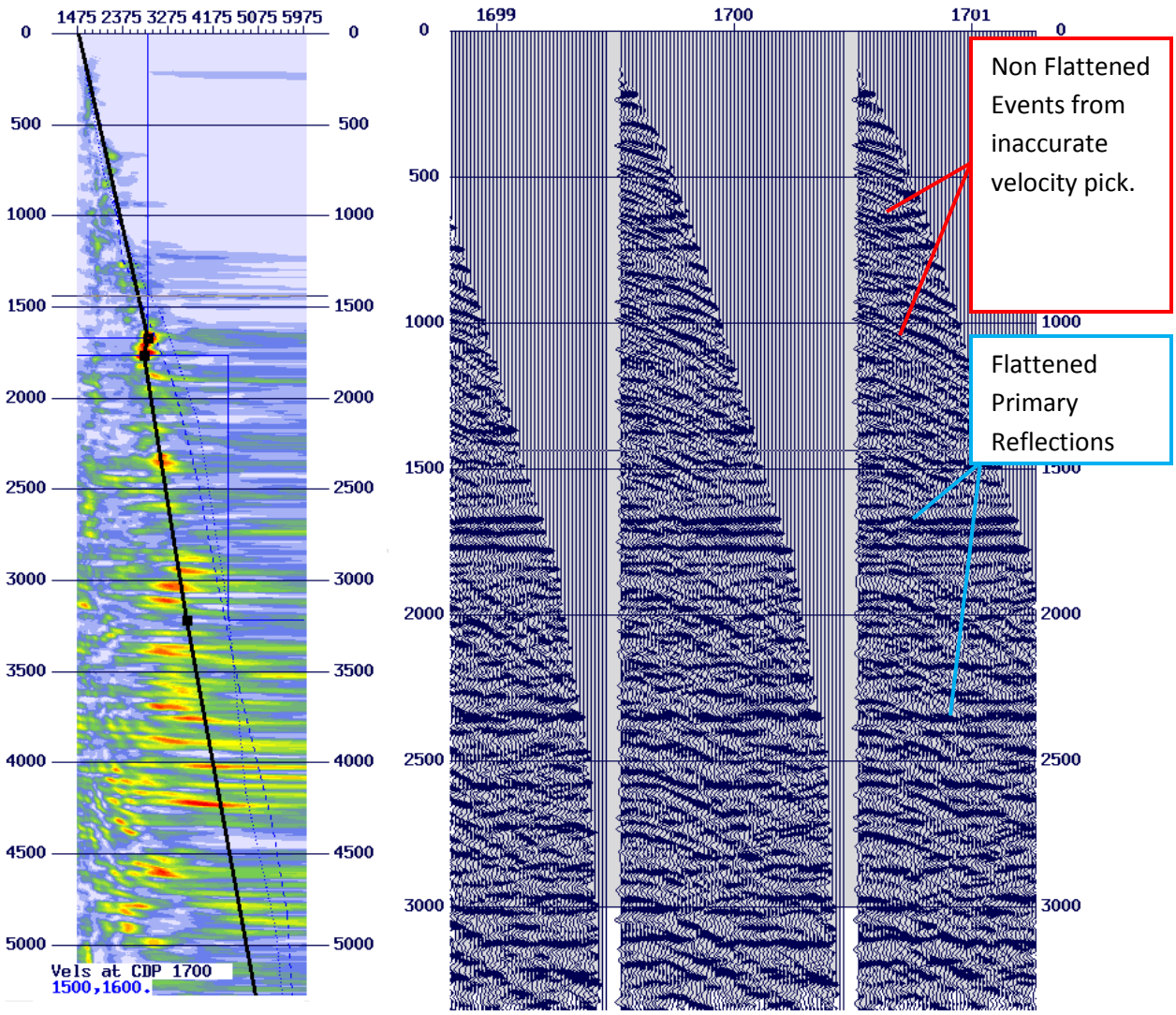

Figure B-7 Semblance Spectrum: with each velocity pick on the semblance spectrum the software calculates a relevant moveout correction and displayed the corrected cmp gather. This is used in the picking of accurate velocites.